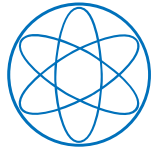




Technische Universität München

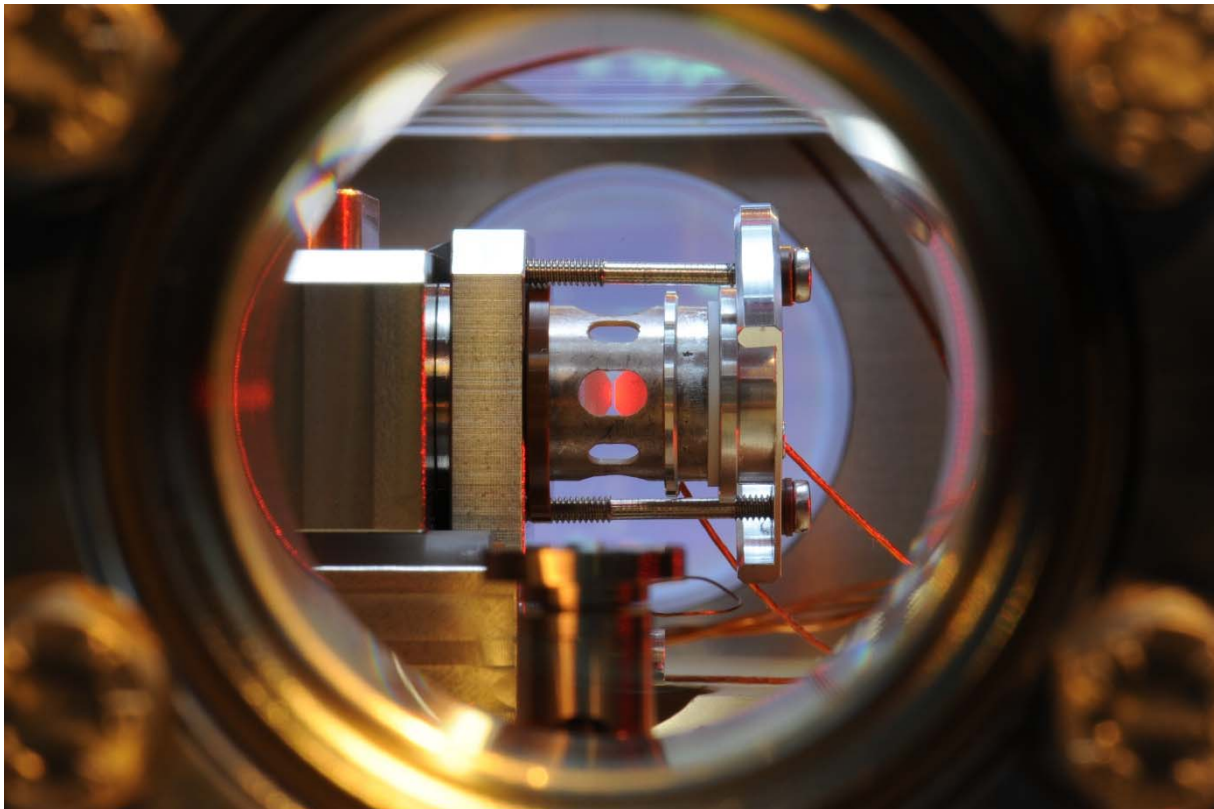


Physik-Department



Atomic Antiresonance and Parametric Feedback in a Strongly Coupled Atom-Cavity Quantum System

Christian Sames



Dissertation

Max-Planck-Institut für Quantenoptik, Garching und
Physik-Department, Technische Universität München

April 2016

Cover Illustration

Side view photography of our cavity, in which a single atom strongly interacts with the single mode of the resonator. The cavity is embedded into a vacuum chamber and the picture is taken through one of the viewports. The mirrors of the cavity are illuminated with a diffuse, red laser beam – for artistic reasons.

Technische Universität München
Max-Planck-Institut für Quantenoptik

Atomic Antiresonance and Parametric Feedback in a Strongly Coupled Atom-Cavity Quantum System

Christian Sames

Vollständiger Abdruck der von der Fakultät für Physik der Technischen Universität München zur Erlangung des akademischen Grades eines

Doktors der Naturwissenschaften (Dr. rer. nat.)

genehmigten Dissertation.

Vorsitzende(r): Prof. Dr. Wilhelm Zwerger

Prüfer der Dissertation: 1. Hon.-Prof. Dr. Gerhard Rempe
2. Prof. Dr. Rudolf O. Gross

Die Dissertation wurde am 30.05.2017 bei der Technischen Universität München eingereicht und durch die Fakultät für Physik am 16.02.2018 angenommen.

für meine Eltern

Abstract

A system composed of a single two-level atom interacting with the single mode of a quantized electromagnetic field is one of the most fundamental systems to study quantum optical effects. These effects become visible if one enters the regime of strong coupling, in which the exchange rate of the energy quantum between the two constituents is large compared to the decay rate of the cavity field and the atomic polarization; this thus permits a coherent exchange of the energy quantum. Here we trap a single rubidium atom at the antinode of a high-finesse optical Fabry-Perot cavity to fulfill this condition. The new apparatus that has been set up in the course of this thesis features, among others, improved detection efficiency, macroscopic length variability as well as excellent side access. Field programmable gate arrays (FPGAs) are put in place and coded to meet the high requirements in data acquisition and real-time processing on the nanosecond timescale.

The timespan during which the atom is strongly coupled corresponds to the period where the atom is exactly positioned at the anti-node; it is hence necessary to accurately trap the atom and avoid any residual motion, i.e. reduce its temperature, as much as possible. We capture individual atoms by utilizing an intracavity dipole trap. A weak, near-resonant probe beam, which passes through our system, carries information about the atomic trajectory. We process this information to alter the depth of the dipole trap in such a way to counteract the atomic motion. With this feedback loop we are able to significantly enhance the time the atom remains in the cavity and furthermore can show that the temperature of the atom is reduced. By making full use of the processing power of FPGAs, the feedback routine can not only be applied to radial oscillations of the atom, perpendicular to the cavity axis, but also to the two orders of magnitude faster oscillations along the cavity axis. This marks an important step towards a full three-dimensional control of the atomic trajectory in real-time.

We have extended our detection setup, consisting of single photon counting modules for intensity measurements, with an alternative heterodyne detection of the transmitted probe beam allowing a full reconstruction of the optical field. We employ this measurement technique to determine the amplitude and phase of the transmitted probe beam while we scan its frequency over the resonances of the coupled system, also known as normal modes. This permits to reveal a new feature between the normal modes, which is hardly visible in any intensity measurement and solely depends on the properties of the bare atomic resonance – despite being strongly coupled to the cavity. This feature corresponds to an antiresonance as the behavior in phase and amplitude is opposite to that at the resonance. Moreover, we are able to imprint a phase shift of 140° on the transmitted probe beam by employing a single rubidium atom, which is the highest value reported to date for any single emitter. This behavior can become useful for quantum computation experiments, as single emitters can show a strong nonlinear behavior on the single-photon level. In addition, the results provide a technique for gaining information on single emitters in complex quantum networks or in systems where the constituents cannot be disassembled and investigated individually – which to date remained inaccessible.

Zusammenfassung

Ein System bestehend aus einem einzelnen Zweiniveaumatom, welches mit der einzelnen Mode des quantisierten elektromagnetischen Feldes wechselwirken kann, bildet eines der fundamentalsten Systeme, um quantenoptische Effekte zu untersuchen. Diese Effekte werden sichtbar, wenn man das Regime der starken Kopplung betritt, in dem der kohärente Austausch eines Energiequants zwischen den beiden Partnern groß gegenüber der Zerfallsrate des Resonatorfeldes sowie der atomaren Polarisation ist; dies ermöglicht somit einen kohärenten Austausch eines Energiequantums zwischen den beiden Partnern. Hier betreten wir diesen Bereich, indem wir ein einzelnes Rubidium-Atom an dem Schwingungsbauch eines optischen Fabry-Perot-Resonators höchster Güte fangen. Der während dieser Dissertation aufgebaute, neuartige, experimentelle Apparat besitzt, unter anderem, eine verbesserte Detektionseffizienz, eine makroskopisch veränderbare Länge der Cavity sowie einen großzügigen, optischen Seitenzugang. Außerdem werden so genannte *Field Programmable Gate Arrays* (FPGAs) eingesetzt, um die hohen Anforderungen des Datensammelns sowie deren Verarbeitung in Echtzeit auf einer Nanosekunden-Zeitskala zu gewährleisten.

Die Zeitspanne, während der das Atom stark an die Cavity gekoppelt ist, entspricht der Zeit, in der es sich exakt an einem Schwingungsbauch der Resonatormode befindet. Es ist daher notwendig, das Atom akkurat an dieser Position zu halten und seine Bewegung, d.h. seine Temperatur so gut wie möglich zu reduzieren. Wir fangen und halten die einzelnen Atome mittels einer Dipole-Falle im Inneren des Resonators. Ein schwacher, nahresonanter Laser, der *Probe Laser*, wird eingesetzt, um das System zu untersuchen. Dieser wird von unserem System transmittiert und enthält danach Information über die atomare Trajektorie. Wir verarbeiten diese Information und passen dementsprechend die Tiefe der Dipole-Falle an, um dieser Bewegung entgegenzuwirken. Durch diesen Regelkreis sind wir in der Lage, nicht nur die Zeitspanne, die das Atom innerhalb des Resonators verweilt, signifikant zu erhöhen, sondern darüber hinaus auch seine Temperatur abzusenken. Indem wir die Rechenleistung der FPGAs ausschöpfen, können wir diesen Regelkreis nicht nur auf die radialen Oszillationen anwenden, sondern diesen auch auf die um zwei Größenordnungen schnelleren Oszillationen des Atoms entlang der Resonatorachse ausweiten. Dies ist ein wesentlicher Schritt hin zu einer kompletten dreidimensionalen Kontrolle der atomaren Trajektorie in Echtzeit.

Wir haben unseren bisherigen Detektionsaufbau, bei dem mittels Einzelphotonenzähler eine Intensitätsmessung durchgeführt wird, um eine alternative Heterodyne Detektionsmethode des transmittierten Probe-Strahles erweitert. Dies erlaubt eine vollständige Rekonstruktion des optischen Feldes. Wir verwenden diese Methode, um die Amplitude und Phase des transmittierten Probe-Strahles zu messen, während wir seine Frequenz über die Resonanzen, bekannt als Normal Moden, des gekoppelten Systems scannen. Zwischen diesen Normal Moden können wir ein neues Merkmal identifizieren; dieses ist in normalen Intensitätsmessungen kaum ersichtlich und wird lediglich von den Eigenschaften des nackten Atoms geprägt – trotz dessen starker Kopplung an die Cavity. Das Verhalten der Phase und Amplitude an dieser Position ist entgegengesetzt zu dem an einer Resonanz und kann daher als Anti-Resonanz identifiziert werden. Des Weiteren sind wir damit in der Lage, einen Phasenversatz von bis zu 140 Grad auf den transmittierten Probe Strahl aufzomodulieren – dies ist der bis dato höchste berichtete Wert eines einzelnen Emitters. Insbesondere für Quantencomputer-Experimente könnte dies sehr nützlich werden, da einzelne Emitter starke nicht-lineare Eigenschaften bereits auf der Einzelphotonen-Ebene zeigen können. Darüber hinaus bietet dieses Verfahren eine

Möglichkeit, Information über die Eigenschaften eines einzelnen Emitters innerhalb eines komplexen Quantennetzwerkes, welches nicht zerlegt werden kann, zu erhalten – diese Möglichkeit blieb zuvor unzugänglich.

Contents

Abstract	i
Zusammenfassung	ii
1. Introduction.....	1
1.1. Cavity Quantum Electrodynamics.....	1
1.2. Cooling an Atom via Feedback	2
1.3. Heterodyne Measurements	3
1.4. This Work.....	4
2. Theory	7
2.1. Quantum Theory of the Atom-Cavity System.....	7
2.1.1. Jaynes-Cummings Hamiltonian	8
2.1.2. The Dressed States	10
2.1.3. Hamiltonian for a Driven System.....	11
2.1.4. Dissipation and Master Equation	12
2.1.5. Analytic Solution for Weak Excitation	13
2.1.6. Intracavity Photon Number and Atomic Excitation.....	14
2.1.7. Saturation Intensity of a Single Atom.....	16
2.2. Theory of Heterodyning	17
2.2.1. The Local Oscillator.....	17
2.2.2. Homodyne Detection Process	18
2.2.3. Shot Noise	20
2.2.4. Heterodyne Detection of a Coherent State.....	20
3. Experimental Setup.....	23
3.1. Single Rubidium Atom.....	24
3.2. High-Finesse Optical Cavity	25
3.2.1. Basic Definitions	26
3.2.2. Geometry.....	27
3.2.3. The Mirrors	28
3.2.4. Parameters	29
3.2.5. Inch-Worm Motor	31

3.3.	Laser System.....	33
3.3.1.	Probe Laser.....	33
3.3.2.	Repumper	35
3.3.3.	Trapping Laser	36
3.4.	Magneto-optical Trap (MOT) with Atomic Fountain	38
3.5.	Vacuum Chamber	39
3.5.1.	Lower Chamber.....	40
3.5.2.	Upper Chamber	41
3.5.3.	Vibration Isolation.....	42
3.6.	Excitation and Detection	43
3.7.	Cavity Lock	45
3.8.	Experimental Sequence	46
3.8.1.	Preparation & Magneto-Optical Trap (MOT).....	46
3.8.2.	Molasses & Atomic Fountain.....	47
3.8.3.	Catching the Atom	47
3.8.4.	Experimental Data-Acquisition.....	47
3.8.5.	Cleaning-Up	48
3.9.	Experimental Control	48
4.	Field Programmable Gate Arrays (FPGAs).....	51
4.1.	Deployment of FPGAs in the Lab	52
4.2.	FPGAs under the Hood.....	53
4.3.	Intellectual Property (Programming/Coding).....	55
4.3.1.	Very High Speed Integrated Circuit Hardware Description Language.....	56
4.3.2.	National Instruments: LabVIEW FPGA	56
4.4.	Deployment 1: Signal Processing in Photon Counters.....	57
4.4.1.	Deserialization.....	58
4.4.2.	Feedback.....	60
4.4.3.	Monitoring.....	61
4.4.4.	Overview and Specifications.....	61
4.5.	Deployment 2: Signal Processing in Heterodyne Systems.....	63
4.5.1.	Direct Digital Synthesis of Radio Frequencies	63
4.5.2.	Real-time Processing of the Heterodyne Carrier.....	64

4.6.	Deployment 3: Locking of a Cavity	66
4.6.1.	Introduction	66
4.6.2.	Under the Hood	68
4.6.3.	Performance	69
4.6.4.	Increased Storage Time	70
4.7.	Deployment 4: Digitizing and Monitoring of Signals	72
4.8.	Conclusion	72
5.	Control of Atomic Motion	73
5.1.	Introduction	73
5.2.	Harmonic Approximation	74
5.3.	Measuring Atomic Motion	76
5.3.1.	Correlation Measurement	76
5.3.2.	Fourier Analysis	79
5.3.3.	Parametric Heating	81
5.4.	Anharmonic Oscillator	83
5.5.	Feedback on a Single Atom	86
5.5.1.	Basic Idea	86
5.5.2.	Bang-Bang Feedback	87
5.5.3.	Radial Parametric Phase Feedback	91
5.5.4.	Axial Parametric Feedback	103
5.6.	Conclusion	106
6.	Heterodyning	107
6.1.	Setup of the Optical Down-Conversion	108
6.2.	Technical Implementation and Electric Down-Conversion	110
6.2.1.	Schematics of the Heterodyne Detection Signal Paths	110
6.2.2.	Phase drifts	111
6.3.	Vacuum Noise	113
6.4.	Beat Node	116
6.4.1.	Choice of Local Oscillator (LO) Frequency	117
6.4.2.	Comb-beat vs. Heterodyne Phase	121
6.5.	Sample Heterodyne Trace	122
6.6.	Feedback Implementation	123

6.6.1.	Radial Oscillation	124
6.6.2.	Axial Oscillation	125
6.7.	Switching Measurements.....	126
6.7.1.	Implementation.....	127
6.7.2.	Phase Sensitive Switching Measurement.....	128
6.7.3.	Qualification and Post-selection.....	129
6.8.	Super-Rabi Color Measurement	133
7.	Free-space Atomic Antiresonance	137
7.1.	Theoretical Perspective.....	137
7.2.	Influence of Physical Parameters on the Spectrum	138
7.2.1.	Cavity Amplitude and Atomic Polarization Decay Rate	138
7.2.2.	Atom-Cavity Detuning.....	139
7.3.	Pendulum Example.....	140
7.4.	Antiresonance in Cavity Quantum Electrodynamics.....	142
7.5.	Optical Control of the Antiresonance Phase Shift.....	145
7.6.	Bare Atomic Resonance in Strongly Coupled Systems.....	147
7.7.	Future Antiresonance Applications	148
7.8.	Saturation Measurements	149
7.8.1.	Saturation by High Probe Beam Intensity.....	149
7.8.2.	Controlled Saturation by Separate Saturation Beam.....	151
8.	Summary and Outlook	155
9.	List of Own Publications	159
	Awards	159
	Own Publications Prior to this Thesis.....	160
10.	Appendix	161
10.1.	Mirror Specifications	161
10.2.	Photon Counting Socketed CLIP	163
10.3.	FPGA Photon Counting Protocol.....	165
10.4.	Simple FPGA-VGA Connector	168
10.5.	High-Speed FPGA Digital-to-Analog-Converter	170
10.6.	Heterodyne Detection	171
10.6.1.	Spectral Filtering of Signal.....	171

10.6.2.	Resolution and Video Bandwidth.....	172
10.6.3.	Filter Response in the Time and Frequency Domain	174
10.6.4.	Visibility	180
10.7.	Coupled Electronic Oscillators	182
10.8.	Symbols Used in Drawings.....	185
11.	References	187
	Danksagung.....	201

1. Introduction

While quantum mechanics has become an essential part in our understanding of nature, the quantumness of nature is not directly visible in our everyday life. In order to be able to study and control these quantum effects, one needs to build small model archetype systems.

The path to explanation of quantum mechanical effects was paved by a series of important discoveries. They comprise the observation of cathode ray by Michael Faraday [1] in 1838, the suggestion of Ludwig Boltzmann that energy states could be discrete in 1877 [2], [3] as well as the observation of the photoelectric effect by Heinrich Hertz in 1887 [4]. The first quantum hypothesis describing the quantized energy exchange between the electromagnetic field and matter was postulated by Max Planck in 1900 [5]. This work explained the spectrum of black-body radiation and also mentioned the proportionality between energy and the (optical) frequency

$$E = h\nu . \quad (1.1)$$

Subsequently, the proportionality constant h was named “Planck constant”. A few years later, in 1905, Albert Einstein postulated that light itself is made of individual quantum particles and explained the photoelectric effect [6]. Later, these energy quanta came to be called “photons”, a term introduced by Gilbert N. Lewis in 1926. This explanation started a series of discoveries and laid the origin for the area of quantum physical description. A rigorous mathematical description of this field was achieved around 1925 by Werner Heisenberg, Max Born and Pascual Jordan [7]–[9] by employing a matrix formalism. These publications also coined the expression “Quantum mechanics”.

1.1. Cavity Quantum Electrodynamics

The heart of quantum theory lies in the description of electrodynamic process between light and matter – a field termed “quantum electrodynamics”, abbreviated with QED. Typically, this description is a fairly sophisticated theory and will usually be treated in a perturbative way for calculations. In order to be able to formulate an exact description, Jaynes and Cummings investigated around 1960 the theoretically most simple system [10], i.e. a single two level emitter coupled to a single mode of the electromagnetic field. Initially intended only as a theoretical description, first experimental realization already followed two decades later [11].

Here, a single atom is placed at or near the antinode, i.e. the maximum field, of the mode of an optical resonator. The resonator supports a resonant mode of the electromagnetic field, causing a standing wave pattern to form, which locally enhances strength of the electric field. Described differently, the single photon sees a few thousand mirror images of the single atom, like in a chamber of mirrors. Thus, the interaction between the single atom and the mode itself is enhanced in such a way that interactions on the single-atom, single-photon level become

observable. If the interaction strength, g , is strong enough and surpasses the decay rate of the atomic polarization, γ , and the decay rate of the cavity field, κ , then the system is said to be in the strong coupling regime. This is achieved by reducing the mode volume of the resonator, leading to an increase in g , and decreasing its losses, lowering κ . In this regime the excitation is jointly shared by the systems' constituents, manifesting in vacuum Rabi oscillations. The characteristics of the individual components vanish, giving rise to a collective behavior of the coupled system. Experimentally, this can be observed as the emergence of an avoided crossing in the spectrum between the resonator mode and the atomic excitation. In the past years a variety of systems emerged; these include Rydberg atoms in microwave cavities [11], [12] and Alkali atoms placed in optical Fabry-Perot resonators [13]–[17] or placed in the evanescent field of microtoroidal resonators [18]. In addition systems with “artificial atoms” emerged, featuring quantum dots placed into semiconductor microcavities [19]–[22] or photonic crystal cavities [23] as well as superconducting qubits in microwave resonators [24]–[27]. In all these systems the two constituting “particles” are well known and hence permit an exact description of the system. However, as simple as the system may be, a broad variety of effects emerges that can be studied. These include employing the strong coupling matter light interface for quantum computing [28], [29] and quantum communication [30] or quantum state preparation [31].

1.2. Cooling an Atom via Feedback

The experimental realizations mentioned above necessitate an isolation of the system from its environment; this ensures that the quantum coherence is maintained over relevant timescales. For a long time this requirement posed an insurmountable challenge. The first pioneering work tackling this challenge consisted in trapping and cooling of ions in 1980-1981 [32], [33]. While this work relied on charged particles, the first cooling of neutral atoms to very low temperatures was enabled by the invention of laser cooling [34]–[37]. This also made it possible to observe atoms in a magneto-optical trap (MOT) [38]–[40] as well as in dipole traps [41], [42]. Besides isolation and cooling of single atoms, the strong coupling to an electromagnetic mode also required the capability to manufacture ultrahigh reflective mirrors and combine them to tiny, high-finesse resonators. In this case the finesse can be approximated by the reciprocal value of the per-round-trip power loss multiplied by 2π . In the optical domain a milestone of such a system showing the normal-mode spectrum of a beam of atoms in an optical cavity was realized in 1992 [13]. However, atoms inside the atomic beam were too fast to be studied individually. A combination of the technologies of high-finesse cavities and laser cooling methods enabled to capture atoms inside the cavity and hence allowed to extend the time a single atom could interact with the cavity mode [43]–[45]. The coupling depends heavily on the overlap, i.e. the position, of the atom and the mode of the intracavity field. As the transmittance of a near-resonant probe beam through the cavity is governed largely by the coupling strength, information about the spatial position of the atom, even below the standard diffraction limit [46], can be derived. Extending the time the atom spends inside the cavity also permitted to examine effects of the radiative force stemming from few-photon light fields [47], [48]. Forces

generated by single intracavity photons were even strong enough to control the motion of a single atom. An experimental realization yet showed that this permitted to capture a single atom by only one intracavity photon [49] while simultaneously tracing its motion [50]. This seeded the idea to use this information for real time feedback on the atomic motion and was first realized by Fischer et al. in 2002 [51], [52]. The radial symmetry of the fundamental cavity mode only allowed to observe the radial distance of the atom from the center of the cavity. This limitation was lifted by the work of Horak et al. (2002), Maunz et al. (2003) and Puppe et al. (2004) [53]–[55]. Higher order transverse modes permitted to obtain information about the angular motion of the atom perpendicular to the cavity axis. While implementation of feedback permitted an increase in storage time of almost 30% in the initial work of Fischer et al., advances in the experimental setup permitted to achieve an increase in storage time by feedback of more than a factor of eight as shown by Kubanek et al. [56], [57]. The improvement mainly stems from adding a repumper beam, keeping the atoms in the cycling transition, as well as a more efficient feedback algorithm in combination with faster electronic circuitry. The new setup built during this thesis with an asymmetric cavity, optimizing the photon flux, in combination with even faster electronics permitted to further increase the average storage time to more than 1 second [58], which corresponds to an improvement by a factor of 30 compared to the case where no feedback is applied. The long storage time additionally enabled us to show that the feedback actually led to a cooling of the atom and not only to an improvement of the localization of the atom. Further optimizing the experimental and electronics setup enable us to harvest the full power of fast electronics [59]. In combination with a refined feedback algorithm, taking into account the history of the atomic motion, this permitted us to increase the average storage time of the atom to up to two seconds. It also allowed for the first time to control the fast axial motion of the atom by external feedback [60].

1.3. Heterodyne Measurements

The most common way of gaining information about optical QED systems consists of measuring the emitted photon flux with gated avalanche photodiodes sensitive to single photons. However, these devices only permit an intensity measurement, where no information about the electric field can be derived. This limitation can be overcome by a heterodyne measurement technique. The etymological origin of the word “heterodyne” lies in the Greek words “hetero” (“other”) and “dyne” (“force”); this already signals that another force than that of the received signal is used to derive the relevant information. This “other force” is the local oscillator signal. In brief, heterodyning is a technique, which is employed to frequency-shift signals into a new frequency range, which is easier to access. The frequency components of the two input signals are combined in a nonlinear signal-processing device such as a vacuum tube, transistor or diode, usually called a mixer [61]. The fundamentals for this technique have been laid in the beginning of the 20th century. In 1901, Reginald Fessenden demonstrated a heterodyne receiver, also known as beat receiver, as a method of making continuous wave radiotelegraphy signals audible [62]–[64]. Yet, stability problems of the local oscillator caused his invention not to be applied much in the beginning: this changed when simple, stable

oscillators became available. In the acoustic domain heterodyning becomes directly audible in our daily life if two musical tones are just slightly detuned. The small difference in frequency causes a beat signal to appear in their amplitude, resulting from the superposition of the two tones in our ear. In addition, the basic principle of heterodyning is employed in all of today's communication and hence marks one of the highest peaks of achievements in wireless communication. This includes as an example radio and television receivers, radio transmitters, modems, networking infrastructure, satellite communication and set-top boxes, radar, radio telescopes, telemetry systems, cell phones or microwave relays. While heterodyning is most common in the radio frequency regime, it can also be applied in the same way to optical frequencies. Here, the superposition of two optical fields yields a mixing on a photodiode producing radio frequency signals; the resulting signal is sufficiently "slow" to be analyzed by standard electronic components. Despite this conversion process all amplitude and phase properties of the signal are preserved. If the properties of the local oscillator are well known, a full reconstruction of the optical field is possible. This is useful in quantum logic phase gates [65] with controlled phase shifts [66]. Matching the frequency of the local oscillator to the incoming light beam, also referred to as homodyning, permits to measure only one selected quadrature of the light. This way non-classical, squeezed light states from the atom-cavity system, which had been predicted theoretically [67], could be accessed experimentally [68]–[70]. In addition, we have been able to show quadrature squeezed light from a single atom excited by two photons [71]. Furthermore, the information gathered during a heterodyne measurement is sufficient to reconstruct the full quantum state of the signal [72]–[74]. This reconstruction is called optical homodyne tomography. Here, we employ the heterodyne technique to spectrally examine the strongly coupled atom-cavity system and reveal an antiresonance feature [75], which is experimentally inaccessible in an intensity measurement. This permits to gain important insights into strongly coupled systems and even to reveal properties of the individual constituents.

1.4. This Work

This work will start by giving a brief introduction into the theoretical concepts of cavity QED in Chapter 2. Afterwards, in Chapter 3, the new experimental apparatus, which has been built during this thesis, will be described. Besides improvements on the physical setup also a new electronic control system was introduced. This features field programmable gate arrays (FPGAs) as a unique way to deterministically execute real-time feedback. In Chapter 4 we will elaborate on how these chips work and how they are programmed – as achieving exceptional computational powers requires a sophisticated and complex way of coding, i.e. programming. FPGAs are put into practice to measure incoming photon clicks with a 1 ns resolution while performing fast real-time feedback as well as plotting and evaluating experimental data in real-time. The vast power of these devices also permits to integrate the full heterodyne measuring system including feedback on one chip. Chapter 4 will close by demonstrating how our improved FPGA based system actively stabilizes the length of the cavity down to 200fm.

The motion of the atom inside the cavity will be described in Chapter 5. The atom is trapped by a red-detuned dipole trap. The radial and axial oscillation of the atom inside the cavity is analyzed. It is monitored via a near-resonant probe beam sent through the coupled atom-cavity system. Varying the intensity of the trap, it is also possible to apply feedback on the measured atomic motion. We use a simple bang-bang strategy, which switches between two discrete values, allows to cool the radial oscillation of the atom and increases the average trapping by more than a factor of 30 times to above one second. This feedback strategy relies on the information gathered during less than one oscillation period. We integrated a more advanced parametric feedback strategy, which is even capable to increase average storage time above two seconds. Here, the feedback strategy accounts for the history of the atomic motion gathered during multiple periods and compares the phase of the atomic oscillation to the phase of a reference oscillator. By doing so, we are able to extend the scheme even to the two orders of magnitude faster axial oscillation.

Phase measurements of the transmitted light field are the main topic in Chapter 6 and 7. For this purpose, we built and characterized a heterodyne detection scheme, including an adapted feedback algorithm as well. The phase of a spectral scan of the transmitted probe beam yields, besides the two normal modes, a third feature, which has not been examined beforehand. This feature corresponds to an antiresonance of the system. The phase undergoes a reverse phase shift compared to the normal modes and the intensity drops to minimum. At this position, despite exciting the cavity-mode, the excitation is mainly held by the atom. We analyze the spectral properties of this antiresonance, which are hence fully governed by the atomic transition, even though the system is strongly coupled. The thesis will close by giving a conclusion and an outlook on possible extensions to this work in Chapter 8.

2. Theory

In this chapter a brief review of some of the theoretical concepts and methods, which are needed to analyze and describe the experimental data in this thesis, will be given. A single atom coupled to the single mode of a high-finesse optical cavity represents an archetype system of quantum mechanics. It paves the road to experimentally study the fundamental interaction of light and matter. The simplicity of the system is achieved by utilizing the basic unit of matter, a single atom, in combination with the simplest form of an electromagnetic field, a single mode. Despite its simplicity such a system still permits to reveal and study a magnitude of quantum effects. These effects range from the cooling of particles [76] over the generation of non-classical light fields [71] to quantum information processing [29], [30]. The first part of this chapter gives a summary of the most important theoretical concepts. A more detailed description can be found in [52], [77]–[81] or in textbooks [82]–[88]. The second part of the section is dedicated to introduce the theoretical frame work of a heterodyne detection scheme, which enables to reconstruct amplitude and phase information of electromagnetic fields on the single-photon level.

2.1. Quantum Theory of the Atom-Cavity System

In this chapter the theoretical concept of a strongly coupled atom-cavity system will be given. We will start by looking at the Hamiltonian in the Jaynes-Cummings model leading to the dressed states. Then we will add a driving of the cavity field and introduce dissipation. By doing so, we gain an understanding of the excitation strength held by the constituents of the strongly coupled system, i.e. the single atom and the cavity mode, permitting to explain nonlinear effects.

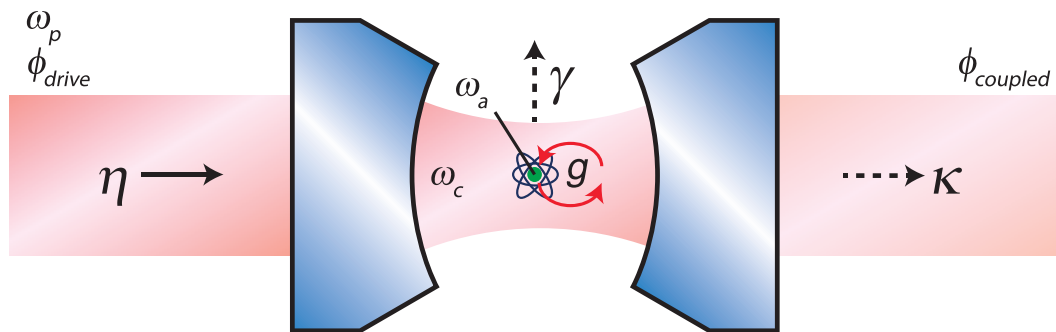


Figure 2.1: Schematic drawing of the atom-cavity system. The most relevant parameters to describe the system are illustrated. An atom is strongly coupled to the single mode of an optical cavity. The parameter g represents the coupling constant, i.e. half the rate at which the excitation is exchanged between the two constituents. The decay rates of the system, i.e. the atomic polarization decay rate and the cavity field decay rate, are given by γ and κ . They correspond to the half width at half maximum (HWHM) of the respective resonance at ω_c for the cavity and ω_a in case of the atom. The system is driven by the probe beam at the frequency ω_p with the strength η . For completeness the phase of the driving probe field, as it will become necessary in the next section, is denoted by ϕ_{drive} . The phase of the field emitted by the coupled system is denoted by $\phi_{coupled}$.

A system comprising of a single atom and a single mode of the electromagnetic field as it will be studied throughout this thesis can be characterized by a few basic parameters as they are sketched in Figure 2.1. These include the resonance frequencies of the single constituents, i.e. the cavity mode and the atomic resonance, which are given by ω_c and ω_a , respectively. Typically, we chose frequencies to be only a few MHz apart. The coupling of the atom to the cavity mode is determined by the coupling constant g , which corresponds to half the vacuum Rabi frequency, i.e. the rate at which the excitation oscillates between the atom and the cavity mode [12]. Two decay channels for the coupled system have to be considered. The atomic polarization decays at a rate of γ by emitting photons into free-space i.e. into other modes than supported by the cavity. The cavity field inside the resonator decays at a rate of κ by emitting photons that are matched to the cavity mode on both sides of the resonator (in the illustration decay to only one side is shown). The system is driven by a weak probe beam, which is centered at the frequency ω_p . The electromagnetic field of this beam drives the system. If the empty cavity is driven on resonance $\omega_p = \omega_c$, a driving of strength η leads to an intracavity photon number of

$$n = \frac{\eta^2}{\kappa^2}. \quad (2.1)$$

As it will be eluded in Section 2.1.5, the driving amplitude needs to be weak in order to avoid a saturation of the single atom. In Section 2.2 a framework will be presented which permits to study the light field; here, the phase of the driving field ϕ_{drive} as well as the emitted field by the coupled system $\phi_{coupled}$ will be of importance.

2.1.1. Jaynes-Cummings Hamiltonian

In this section we will start by considering the Jaynes-Cummings model [10] in which the steady state of a coupled atom-cavity system will be considered. The Hamiltonian will hence consist of a cavity, an atomic, as well as an interaction part. These three constituents will be described briefly.

2.1.1.1. Single mode electromagnetic field

The quantization of the electromagnetic field is described by the quantum mechanics of a harmonic oscillator. In case the light field is restricted to a single mode an optical cavity the Hamiltonian is written as

$$H_c = \hbar\omega_c (a^\dagger a + 1/2). \quad (2.2)$$

The creation a^\dagger and annihilation a operators satisfy the following relations:

$$\begin{aligned} a^\dagger |n\rangle &= \sqrt{n+1} |n+1\rangle \\ a |n\rangle &= \sqrt{n} |n-1\rangle \end{aligned} \quad (2.3)$$

In the Fock-state basis the eigenvalues and eigenenergies amount to

$$\begin{aligned} (a^\dagger a)|n\rangle &= n|n\rangle \\ E_n &= \hbar\omega_c \left(n + \frac{1}{2} \right), \quad n = 0, 1, 2, \dots \end{aligned} \quad (2.4)$$

Here, n denotes the number of photons. Setting the ground state value to zero finally yields the Hamiltonian

$$H_c = \hbar\omega_c \cdot a^\dagger a \quad (2.5)$$

2.1.1.2. Single two-level atom

The single two-level atom can either be in its ground $|g\rangle$ or excited state $|e\rangle$ with the respective energy levels E_g and E_e . The resulting Hamiltonian then reads

$$H'_a = E_g |g\rangle\langle g| + E_e |e\rangle\langle e|. \quad (2.6)$$

With the corresponding lowering and raising operators

$$\begin{aligned} \sigma_- |e\rangle &= |g\rangle \\ \sigma_+ |g\rangle &= |e\rangle \end{aligned} \quad (2.7)$$

and by setting E_g to zero, the Hamiltonian can be written as

$$H_a = \hbar\omega_a \sigma_+ \sigma_- . \quad (2.8)$$

2.1.1.3. Coupling

The interaction of the atom and the cavity is described by an interaction Hamiltonian H_i in the dipole approximation¹ and by applying the rotating-wave approximation². It is then expressed by the creation of a photon and a lowering of the atomic excitation and vice versa:

$$H_i = \hbar g (a^\dagger \sigma_- + a \sigma_+) \quad (2.9)$$

This corresponds to an exchange of one quantum of excitation between the atom and the cavity mode. The exchange rate is determined by the coupling constant

¹ The dipole approximation assumes that the size of the single atom is small compared to the wavelength of the electromagnetic field. The amplitude of the field can thus be considered constant across the dimensions of the atom.

² The rotating wave approximation requires that the difference between the atomic resonance frequency and the frequency of the resonant field in the cavity is much smaller than the respective absolute values of the two frequencies, i.e. $|\omega_a - \omega_c| \ll (\omega_a, \omega_c)$. In this case rapid oscillation in the full dipole interaction Hamiltonian can be neglected, as they average out over the relevant timescales.

$$g = \sqrt{\frac{\omega_c}{2\hbar\epsilon_0 V}} d_{ge} . \quad (2.10)$$

It is proportional to the dipole matrix element of the atomic transition, d_{ge} and inversely proportional to the square root of the cavity mode volume, $V \approx \pi\omega_0^2 L/4$, where L is the cavity length and ω_0 is the beam waist, to be assumed constant over L . ϵ_0 describes the vacuum permittivity.

Combining Eqn. (2.5), (2.8) and (2.9) finally yields the total Jaynes-Cummings Hamiltonian

$$H_{jc} = \underbrace{\hbar\omega_a \sigma_+ \sigma_-}_{\text{bare atom}} + \underbrace{\hbar\omega_c a^\dagger a}_{\text{bare cavity}} + \underbrace{\hbar g (a^\dagger \sigma_- + a \sigma_+)}_{\substack{\text{dipole coupling} \\ \text{atom-cavity}}} . \quad (2.11)$$

2.1.2. The Dressed States

The eigenstates of the Jaynes-Cummings Hamiltonian (cf. Eqn. (2.11)) are arranged in doublets, which are called the n -th order dressed states $|n, \pm\rangle$. The only exception is the ground state $|0, g\rangle$. Each pair shares the same number of excitations n . Expressing the dressed states in terms of the cavity and atomic eigenstates yields

$$\begin{aligned} |n, +\rangle &= \cos\theta_n |n-1, e\rangle + \sin\theta_n |n, g\rangle \\ |n, -\rangle &= -\sin\theta_n |n-1, e\rangle + \cos\theta_n |n, g\rangle \end{aligned} \quad (2.12)$$

The transformation between the cavity-atomic basis and the dressed states basis is a rotation in the Hilbert-space of the system by the mixing angle θ_n .

$$\theta_n = \arctan \frac{2g\sqrt{n}}{(\omega_a - \omega_c) + \sqrt{4g^2 n + (\omega_a - \omega_c)^2}} \quad (2.13)$$

In case the cavity and the atom are almost on resonance $\sin\theta = \cos\theta = 1/\sqrt{2}$ can be assumed. The resulting eigenvalues amount to

$$E_{n,\pm} = \hbar n \omega_c + \frac{1}{2} \hbar (\omega_a + \omega_c) \pm \frac{1}{2} \hbar \sqrt{4ng^2 + (\omega_a - \omega_c)^2} \quad (2.14)$$

with a splitting of

$$E_{n,+} - E_{n,-} = \hbar \sqrt{4ng^2 + (\omega_a - \omega_c)^2} \quad (2.15)$$

between the doublets. This results in the well-known Jaynes-Cummings energy ladder which is depicted in Figure 2.2. The Jaynes-Cummings model can be extended to account for more than

one atom leading to the Tavis-Cummings model [89], [90]. This model will not be considered further in this thesis.

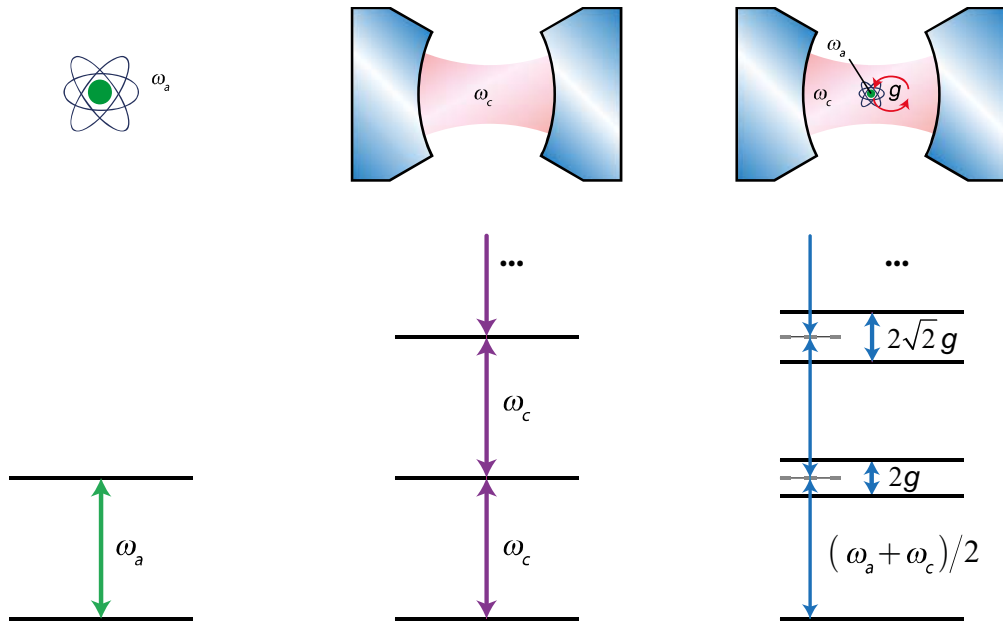


Figure 2.2: Jaynes-Cummings model of the strongly coupled atom-cavity system. The energy levels of the bare atom couple to the energy ladder of the resonant cavity mode. The coupled system features a new set of eigenstates, whose splitting is given by the coupling constant, g . The picture is valid for the case that atom and cavity are on resonance.

2.1.3. Hamiltonian for a Driven System

In the previous section the steady state eigenstates of the coupled atom-cavity system have been studied. In this section we will add a driving term. There are two ways to excite the system. The first one is to drive the cavity with a laser beam matching the mode of the resonator, while the second consists of directly exciting the atom with a side-ways laser beam. In the following we will only consider the first approach. Driving of the cavity with a near-resonant probe, as already sketched in Figure 2.1, is described by the following Hamiltonian [84]:

$$H_d = \hbar\eta \left(a e^{i\omega_p t} + a^\dagger e^{-i\omega_p t} \right) \quad (2.16)$$

The exchange of photons with the probe laser causes the energy of the system to be no longer conserved and is reflected by the time dependency of the Hamiltonian. It is hence useful to transfer the full Hamiltonian $H_{JC} + H_d$ to the rotating frame of the probe laser, permitting to eliminate the time dependency as described in [81], [88], [91], [92]. By doing so one obtains the transformed Hamiltonian

$$H_{d,JC} = -\hbar\Delta_{pa} \sigma_+ \sigma_- - \hbar\Delta_{pc} a^\dagger a + \hbar g (a^\dagger \sigma_- + a \sigma_+) + \hbar\eta (a + a^\dagger) \quad (2.17)$$

with the probe-atom detuning $\Delta_{pa} = \omega_p - \omega_a$ and the probe-cavity detuning $\Delta_{pc} = \omega_p - \omega_c$.

2.1.4. Dissipation and Master Equation

The influence of dissipation in the quantum system can be modelled by means of a master equation. The system Hamiltonian is given by $H_S = H_{d,JC}$ and is complemented by the additional Hamiltonian H_R , which models the environment as a reservoir of harmonic oscillators [86], [93]. The harmonic oscillators represent the continuum of modes of the quantized electromagnetic field to which the cavity mode or the atomic excitation can couple. The interaction of the reservoir and the quantum system is described by the coupling Hamiltonian H_{RS} , which is assumed to be linear in the system and bath operator [81], [84]. The system and the reservoir can be described by a density matrix $\rho_{RS}(t)$

$$\dot{\rho}_{RS} = -\frac{i}{\hbar}(H_S + H_R + H_{RS}, \rho_{RS}), \quad (2.18)$$

where the time evolution of the wave function Ψ is given by the Schrödinger equation

$$i\hbar \frac{\partial}{\partial t} \Psi = H\Psi. \quad (2.19)$$

In our system only the time evolution of the density matrix describing the system ρ_S is of interest, whereas the environment is simply a reservoir which provides a source of fluctuations and dissipates energy. The dynamics of the system alone are obtained by performing a partial trace over the eigenstates of the reservoir.

$$\rho_S(t) = Tr_R \{ \rho_{RS}(t) \}. \quad (2.20)$$

In huge reservoirs, correlations within the reservoir decay much faster than the timescale of the interaction with the system. Therefore, the state of the reservoir does not depend on the state of the system and hence has no memory of the system state at earlier times. Thus, the influence of the reservoir on the system only depends on the current state of the system and not its history. This is known as the Markov approximation. Additionally, the Born approximation is applied neglecting second and higher order terms of the system-reservoir interaction H_{RS} . Applying these approximations yields

$$\begin{aligned} \dot{\rho} = & -\frac{i}{\hbar} [H_{d,JC}, \rho] + \gamma(\bar{n}+1)(2\sigma_- \rho \sigma_+ - \sigma_+ \sigma_- \rho - \rho \sigma_+ \sigma_-) \\ & + \gamma\bar{n}(2\sigma_+ \rho \sigma_- - \sigma_- \sigma_+ \rho - \rho \sigma_- \sigma_+) \\ & + \kappa(\bar{n}+1)(2a\rho a^\dagger - a^\dagger a \rho - \rho a^\dagger a) \\ & + \kappa\bar{n}(2a^\dagger \rho a - a a^\dagger \rho - \rho a a^\dagger) \end{aligned} \quad (2.21)$$

The state of the reservoir only enters the time evolution in Eqn. (2.21) via the mean occupation number \bar{n} of its oscillatory states. The mean occupation number at temperature T is given by

$$\bar{n}(\omega_k, T) = \frac{e^{-\hbar\omega_k/k_B T}}{1 - e^{-\hbar\omega_k/k_B T}} \quad (2.22)$$

with the Boltzmann constant k_B . The terms in Eqn. (2.21) proportional to $(\bar{n} + 1)$ describe the transfer of excitation from the system to the reservoir, while the opposite direction, i.e. the transfer of excitation from the reservoir to the system, is described by the terms proportional to n . At room temperature and for optical frequencies of ω_k , the mean occupation of the oscillator states of the reservoir are very small $\bar{n} \ll 1$. Therefore, only terms describing the emission of an energy quantum from the system to the reservoir need to be accounted for. This finally yields the master equation

$$\dot{\rho} = -\frac{i}{\hbar}[H_{d,JC}, \rho] + \underbrace{\gamma(2\sigma_- \rho \sigma_+ - \sigma_+ \sigma_- \rho - \rho \sigma_+ \sigma_-)}_{\text{polarization decay}} + \underbrace{\kappa(2a\rho a^\dagger - a^\dagger a \rho - \rho a^\dagger a)}_{\text{cavity field decay}} \quad (2.23)$$

For an empty cavity, i.e. without atom present, Eqn. (2.23) can be solved analytically yielding the mean intracavity photon number

$$\langle a^\dagger a \rangle = \frac{\eta^2}{\kappa^2 + \Delta_{pc}^2} \quad (2.24)$$

2.1.5. Analytic Solution for Weak Excitation

The master equation derived in Eqn. (2.23) can be expressed formally in terms of a Lindblad operator \mathcal{L} :

$$\dot{\rho} = \mathcal{L}\rho \quad (2.25)$$

It can be solved numerically by truncating the Hilbert space of the cavity mode at some finite photon number and then utilizing the quantum optics toolbox for MATLAB [94]. In case of weak excitation, Eqn. (2.23) can also be solved analytically. Using Eqn. (2.20) the time evolution of a set of system operators $\langle \sigma_- \rangle$, $\langle \sigma_z \rangle$ and $\langle a \rangle$ can be written as:

$$\begin{aligned} \langle \dot{a} \rangle &= i\Delta_{pc} \langle a \rangle - \kappa \langle a \rangle - ig \langle \sigma_- \rangle + \eta \\ \langle \dot{\sigma}_- \rangle &= i\Delta_{pa} \langle \sigma_- \rangle - \gamma \langle \sigma_- \rangle + ig \langle \sigma_z a \rangle \\ \langle \dot{\sigma}_z \rangle &= ig \langle a^\dagger \sigma_- - \sigma_+ a \rangle - 2\gamma \langle \sigma_+ \sigma_- \rangle \end{aligned} \quad (2.26)$$

These are the Heisenberg equations of motion. The limit of weak excitation is realized by choosing an appropriate low pump intensity or by increasing the detuning of the pump beam in such a way that the overlap of the excited state with the bare atomic state is small. Mathematically, this limit is reached by setting $\langle \sigma_z a \rangle$ to $-\langle a \rangle$ and dropping the third equation in (2.26) [80]. This yields

$$\begin{aligned}\langle \dot{a} \rangle &= i\Delta_{pc} \langle a \rangle - \kappa \langle a \rangle - ig \langle \sigma_- \rangle + \eta \\ \langle \dot{\sigma}_- \rangle &= i\Delta_{pa} \langle \sigma_- \rangle - \gamma \langle \sigma_- \rangle - ig \langle a \rangle\end{aligned}\quad (2.27)$$

With the definitions

$$Y = \begin{pmatrix} a \\ \sigma_- \end{pmatrix}, \quad Z = \begin{pmatrix} i\Delta_{pc} - \kappa & -ig \\ -ig & i\Delta_{pa} - \gamma \end{pmatrix}, \quad I_\eta = \begin{pmatrix} \eta \\ 0 \end{pmatrix}\quad (2.28)$$

both equations in (2.27) can be rewritten as

$$\langle \dot{Y} \rangle = Z \langle Y \rangle + I_\eta. \quad (2.29)$$

The steady state solution of this system is then given by [77], [82]

$$\langle Y \rangle = -Z^{-1} I_\eta. \quad (2.30)$$

Transforming the result of Eqn. (2.30) back by employing Eqns. (2.28) finally yields:

$$\langle a \rangle = \frac{\eta(\Delta_{pa} + i\gamma)}{(\Delta_{pa} + i\gamma)(\Delta_{pc} + i\kappa) - g^2} \quad (2.31)$$

$$\langle \sigma_- \rangle = \frac{\eta g}{(\Delta_{pa} + i\gamma)(\Delta_{pc} + i\kappa) - g^2} \quad (2.32)$$

2.1.6. Intracavity Photon Number and Atomic Excitation

The steady state expectation value for the intracavity photon number, corresponding to the cavity excitation, $\langle a^\dagger a \rangle$ and the atomic excitation $\langle \sigma_+ \sigma_- \rangle$ can be calculated from Eqns. (2.31) and (2.32), yielding

$$\langle a^\dagger a \rangle = \eta^2 \frac{\Delta_a^2 + \gamma^2}{[(\Delta_{pa} + i\gamma)(\Delta_{pc} + i\kappa) - g^2]^2} \quad (2.33)$$

$$\langle \sigma_+ \sigma_- \rangle = \eta^2 \frac{g^2}{[(\Delta_{pa} + i\gamma)(\Delta_{pc} + i\kappa) - g^2]^2} \quad (2.34)$$

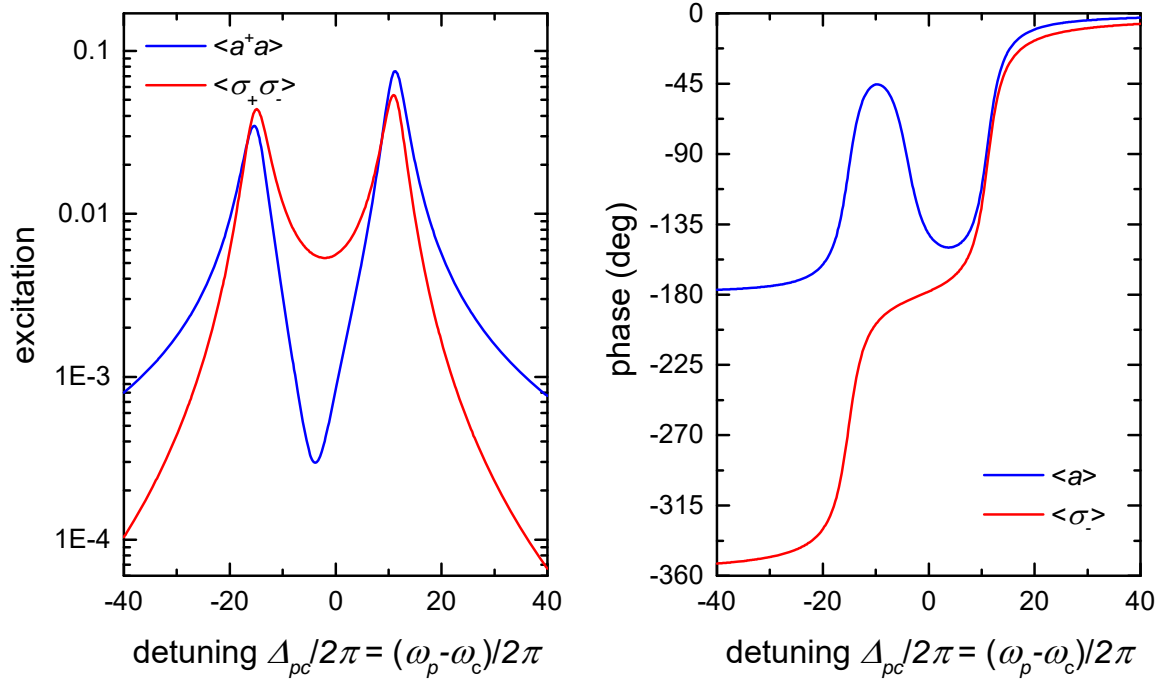


Figure 2.3: Excitation of cavity and atom as well as phase of the respective fields as a function of the probe-cavity detuning. a) shows the spectrum of the expectation value of the intracavity photon number (blue) and the atomic excitation (red). Here the two normal modes are clearly visible. b) illustrates the phase of the intracavity field (blue) as well as the atomic dipole polarization (red). The phase of the cavity field decreases by π between the two normal-mode resonances, whereas the phase of the atomic polarization does not show this behavior.

These equations correspond to the ones derived in [95]. They are sufficient to calculate the spectrum of the system, which shows the two resonances located at

$$\omega_{\pm} - \omega_p = -\frac{(\Delta_{pa} + i\gamma) + (\Delta_{pc} + i\kappa)}{2} \pm \frac{1}{2} \sqrt{4g^2 + [(\Delta_{pa} + i\gamma) - (\Delta_{pc} + i\kappa)]^2}. \quad (2.35)$$

As the frequencies in Eqn. (2.35) are complex-valued, the real part determines the position of the peaks, whereas the imaginary part describes their width.

A graphical representation of the intracavity photon number as well as the atomic excitation is plotted in Figure 2.3. Here, typical parameters of our system of $\Delta_{pa}/2\pi = -4$ MHz, $\Delta_{pc}/2\pi = 0$ MHz, $g/2\pi = 13$ MHz, $\gamma/2\pi = 3$ MHz and $\kappa/2\pi = 1.5$ MHz are chosen. In addition to the excitation also the phase of the intracavity field as well as the atomic dipole excitation is plotted. The phase ϕ is derived by writing Eqns. (2.31) and (2.32) in the form $Z = r \cdot e^{i\phi}$. The two resonances of the coupled system, the so called normal modes, are clearly visible in the atomic as well as the cavity excitation. Depending on which one of the two constituents holds the majority of the excitation these normal modes are also referred to as atom-like and cavity-like normal mode, respectively. The detailed shape of the excitation and also the phase behavior will be elaborated further throughout this thesis with a focus in Section 6.8. It will not be discussed at this point.

2.1.7. Saturation Intensity of a Single Atom

The saturation intensity of an atom is defined as [96], [97]

$$\frac{I}{I_{sat}} = 2 \frac{\Omega^2}{\Gamma^2}. \quad (2.36)$$

Where $\Gamma = 2\gamma = 1/\tau$ is the natural decay with a decay time of τ and $\Omega = -\vec{d}_{eg}\vec{E}/\hbar$ the resonant Rabi frequency. With $I = c\varepsilon_0 E^2/2$ the saturation intensity of a single atomic transition can be written as

$$I_{sat} = \frac{\hbar\gamma\omega_a^3}{6\pi c^2}. \quad (2.37)$$

Here, c represents the speed of light in vacuo. The ratio

$$\Gamma = \frac{|d_{ge}|^2}{4\pi\varepsilon_0} \frac{4\omega_a^3}{3\hbar c^3} \quad (2.38)$$

has been employed [98] to derive Eqn. (2.37). As we are working with an optical resonator we want to relate the saturation intensity to the intracavity intensity for n photons enclosed in the mode volume V

$$I_{cav} = \frac{n\hbar\omega_a c}{V}. \quad (2.39)$$

Setting $I_{sat} = I_{cav}$ in Eqns. (2.37) and (2.39) hence yields the number of intracavity photons n_0 required to saturate the atomic transition

$$n_0 = \frac{\gamma\omega_a^2 V}{6\pi c^3}. \quad (2.40)$$

Using the definition of the coupling constant g of Eqn. (2.10), Eqn. (2.40) can also be written as

$$n_0 = \frac{\gamma^2}{2g^2}. \quad (2.41)$$

From this equation we can see that a single intracavity photon is already sufficient to saturate the atom when $g > \gamma$ as it is the case for our experimental parameters.

2.2. Theory of Heterodyning

In this section, the theoretical framework for a heterodyne detection will be explained. Opposite to intensity measurements such as photon counting where only the expectation value of the cavity photon number $\langle a^\dagger a \rangle$ is experimentally accessible, heterodyning permits access to expectation value of the light field inside the cavity $\langle a \rangle$. It hence opens the way to experiments directly measuring non-classical light fields, such as the observation of squeezed light emitted by a single atom excited by two photons [71]. The spectrum of the phase of $\langle a \rangle$ has already been shown in Figure 2.3 b).

In principal, homodyning and heterodyning both consist in interfering two light fields. These are the so-called optical local oscillator and the signal light beam, which is to be measured. In case of homodyne these two beams have the same center frequency, while this frequency differs for the two beams, when a heterodyne measurement is carried out. The electric field operator for a mode of frequency ω inside the cavity can be written as

$$\hat{E}_{cav} = \sqrt{\frac{\hbar\omega}{2\varepsilon_0 V}} (\hat{a}e^{i\omega t} + \hat{a}^\dagger e^{-i\omega t}). \quad (2.42)$$

As the heterodyne detection is situated outside the cavity, a continuum of modes needs to be considered. In addition, the flux of photons rather than their number is measured. This leads to a slightly different operator describing the electric field in front of the detection

$$\hat{E}(t) = \int \sqrt{\frac{\hbar\omega}{2\varepsilon_0 S c}} (\hat{a}_\omega e^{i\omega t} + \hat{a}_\omega^\dagger e^{-i\omega t}) \frac{d\omega}{2\pi}. \quad (2.43)$$

Here, S is defined as the cross-section of the beam in front of the detector.

2.2.1. The Local Oscillator

The local oscillator is an essential component in the heterodyne detection process, since it is used to “amplify” the weak signal beam originating from the cavity, as it will be elaborated further throughout this section. This is the reason why local oscillator intensity levels on the high μW to mW scale will be used. The local oscillator is assumed to be monochromatic at the frequency ω_0 and will be described by $|\alpha\rangle_{\omega_0}$. As it is in a bright coherent state [99]

$$|\alpha\rangle_{\omega_0} = \sum_{k=0}^{\infty} \frac{(\alpha \hat{a}_{\omega_0}^\dagger)^k}{k!} |0\rangle = e^{\alpha \hat{a}_{\omega_0}^\dagger} |0\rangle \quad (2.44)$$

it can be treated classically. Using Eqn. (2.43) the field of the local oscillator can be written as

$$\begin{aligned}
E_{LO}(t) &= \langle \alpha | \hat{E}_{LO}(t) | \alpha \rangle_{\omega_0} \\
&= \sqrt{\frac{P_{LO}}{2\epsilon_0 S c}} \left(e^{i(\omega_0 t - \theta)} + e^{-i(\omega_0 t - \theta)} \right)
\end{aligned} \tag{2.45}$$

with $\alpha = |\alpha| e^{-i\theta}$. The term $|\alpha|^2$ hence represents the photon flux and θ the phase difference between the measured and LO quadrature. The power of the local oscillator beam is given by

$$P_{LO} = \epsilon_0 S \cdot c \langle E_{LO}^2 \rangle \tag{2.46}$$

As the local oscillator is classical, its power P_{LO} can simply be replaced in the following by $\eta_{LO} P_{LO}$ to account for the transmission efficiency $\eta_{opt,LO}$ and quantum efficiency of the photodiodes of the local oscillator beam η_q , together given by $\eta_{LO} = \eta_q \eta_{opt,LO}$.

2.2.2. Homodyne Detection Process

The probe and LO beam in the heterodyne detection are overlapped at a polarizing 50/50 beam splitter, adjusted in such a way that half the power of each beam is in each of the arms of the heterodyne detector.

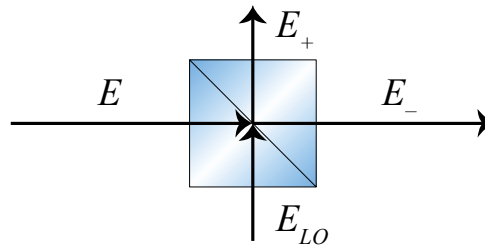


Figure 2.4: Overview of the overlapping of the signals at the beam splitter. The field of the probe beam E and the local oscillator beam E_{LO} are overlapped at the two input ports of a beam splitter. At the output ports the symmetric and antisymmetric combination of the overlapped fields is generated, which is subsequently termed E_+ and E_- .

The overlapping of the two beam is depicted Figure 2.4, while an overview of the detailed experimental setup is depicted in Figure 6.2. The output electric fields are

$$\hat{E}_{\pm} = \frac{E_{LO} \pm \hat{E}}{\sqrt{2}}. \tag{2.47}$$

Please note that the field of the local oscillator will be treated classically and is hence not indicated in the operator notation. As both beams are bright, they can directly be measured via standard PIN photodiodes (positive intrinsic negative) where they are converted into the electrical currents J_{\pm} with the ideal photon-electron conversion factor of $q_e/(\hbar\omega)$ with q_e being the electron elementary charge

$$J_{\pm} = q_e \varepsilon_0 S c \left(\frac{E_{LO}(t)}{\sqrt{\hbar \omega_0}} \pm \int \frac{\hat{E}_{\omega}(t)}{\sqrt{\hbar \omega}} \frac{d\omega}{2\pi} \right)^2. \quad (2.48)$$

The actual conversion factor for one photon amounts to $\tilde{\eta}_q = \eta_q q_e / (\hbar \omega)$ and is given by the manufacturer in units of A/W, where η_q is the dimensionless quantum detection efficiency. As mentioned by Ourjountsev [100], the quantum efficiency cannot directly be multiplied to the electrical currents J_{\pm} as this would only be correct if both beams were classical. Instead, η_q will be included in the overall detection efficiency of the ‘‘quantum beam’’

$$\eta = \eta_q \eta_m^2 \eta_{opt} \quad (2.49)$$

This efficiency also comprises the optical transmission efficiency η_{opt} as well as the mode-matching efficiency η_m^2 . The latter one corresponds to the square of the fringe contrast, also known as visibility, of the two beams. While η , which only applies to the probe beam, also depends on the detection efficiency of the diodes, it still varies from η_{LO} , which describes the overall efficiency of the local oscillator measurement.

As the photodiodes of the balanced detector are well-matched and are installed in a serial configuration, the difference of the two photocurrents J_{\pm} of the two arms can be tapped in between the two diodes. Afterwards, they are converted to a voltage V_{θ} by an amplifier with a transimpedance gain G

$$V_{\theta}(t) = G(J_+ - J_-). \quad (2.50)$$

If we further neglect rapidly oscillating terms and approximate $\hat{E}_{LO} \hat{E}$ by $\langle \hat{E}_{LO} \rangle \hat{E}$ as the light field of the local oscillator is classical, Eqn. (2.50) can be written for a single frequency component ω as

$$\begin{aligned} \hat{V}_{\theta, \omega}(t) &= 2 \frac{q_e}{\hbar \sqrt{\omega_0 \omega}} G \varepsilon_0 S \cdot c \cdot \hat{E}_{LO}(t) \hat{E}_{\omega}(t) \\ &= G \sqrt{\frac{\eta_{LO} P_{LO} q_e^2}{\hbar \omega_0}} \left(\hat{a}_{\omega} e^{i[(\omega - \omega_0)t - \theta]} + \hat{a}_{\omega}^{\dagger} e^{-i[(\omega - \omega_0)t - \theta]} \right). \end{aligned} \quad (2.51)$$

The measured voltage is obtained by integrating over all frequency components. As the frequency spectrum of a heterodyne detection usually only spans a few tens of MHz, frequency dependencies of η_{LO} can be neglected. However, for completeness G will be assumed to vary in frequency.

$$\widehat{V}_\theta(t) = \sqrt{\frac{\eta_{LO} P_{LO} q_e^2}{\hbar \omega_0}} \int G(\Omega) \left(\hat{a}_\Omega e^{i(\Omega t - \theta)} + \hat{a}_\Omega^\dagger e^{-i(\Omega t - \theta)} \right) \frac{d\Omega}{2\pi} \quad (2.52)$$

Here, Ω is defined as the frequency difference between frequency components of the signal and the local oscillator $\Omega = \omega - \omega_0$.

2.2.3. Shot Noise

The shot noise variance of the system, i.e. the measured voltage when no signal beam is present, is given by evaluating V_θ^2 in the vacuum state $|0\rangle = \int |0\rangle_\Omega d\Omega$

$$\begin{aligned} \sigma_{shot}^2 &= \langle 0 | \widehat{V}_\theta^2(t) | 0 \rangle \\ &= \frac{\eta_{LO} P_{LO} q_e^2}{\hbar \omega_0} \int_{-\infty}^{\infty} G^2(\Omega) \frac{d\Omega}{2\pi} \\ &= \frac{\eta_{LO} P_{LO} q_e^2}{\hbar \omega_0} 2G_0^2 \Delta\nu \end{aligned} \quad (2.53)$$

For simplicity a flat gain profile of the amplifier with gain G_0 was assumed over the frequency range $\Delta\nu$. Negative and positive frequencies are treated equally and zero gain was assumed for higher frequencies. Further including the electronic noise σ_e of the detection system yields

$$\sigma_0 = \sqrt{\frac{\eta_{LO} P_{LO} q_e^2}{\hbar \omega_0} 2G_0^2 \Delta\nu + \sigma_e^2} \quad (2.54)$$

An experimental measurement of the shot noise can be found in Section 6.3.

2.2.4. Heterodyne Detection of a Coherent State

The expected voltage level for a coherent state can easily be computed. Here, we assume such a state $|\alpha\rangle_{\Omega=0}$ at the same frequency as the local oscillator. Due to inherent losses in the system as summarized in Eqn. (2.49), it is transformed into $|\sqrt{\eta}\alpha\rangle_{\Omega=0}$. Writing its probe power as $P_c = \hbar\omega_0\alpha^2$ finally yields

$$\langle \alpha | \widehat{V}_\theta | \alpha \rangle_{\Omega=0} = \frac{\sqrt{\eta_{LO} P_{LO} \eta P_c}}{\hbar \omega_0} 2G_0 q_e \cos \theta. \quad (2.55)$$

The phase difference between the two beams is hence directly visible in the measured voltage level and permits to extract the amplitude of one quadrature of the light field. A slight detuning of the local oscillator frequency compared to the frequency of the coherent state Ω , changes Eqn. (2.55) to

$$\langle \alpha | \hat{V}_\theta | \alpha \rangle_\Omega = \frac{\sqrt{\eta_{LO} P_{LO} \eta_c P_c}}{\hbar \omega_0} 2G_0 q_e \cos(-\Omega t + \theta). \quad (2.56)$$

Instead of measuring one quadrature of the light field, we now periodically alternate between the two quadratures X and P . Furthermore, it should be noticed that the measured voltage level depends on the square root of the power of the coherent state as well as the one of the local oscillator. Thus, a strong local oscillator beam is important in order to increase the signal amplitude. On the other hand, high local oscillator powers also increase the optical shot noise described in Eqn. (2.53), but do not affect the electronic noise level.

3. Experimental Setup

In the course of this thesis an experimental system allowing the investigation of the interaction of a single photon with a single atom has been developed and built. A similar experimental setup was already present in the group. However, compared to this forerunner model [52], [77], [78], [80], [101], [102] the new design features a macroscopic control of the cavity length, improved side access to the cavity-axis, asymmetric mirrors and state-of-the-art data-acquisition and data-processing, including real-time heterodyne measurement and evaluation. This chapter will outline the major building blocks (see Figure 3.1) and will give a brief introduction of their working principle. It will start by introducing the main constituents of any cavity quantum electrodynamics system, i.e. the single atom (cf. Section 3.1) and the high-finesse optical resonator (cf. Section 3.2). It will then describe the laser-system (cf. Section 3.3) and vacuum chamber (cf. Section 3.5) needed to prepare the system. In the last part the actual excitation and detection scheme (cf. Section 3.6) along with the cavity stabilization (cf. Section 3.7) and experimental control (cf. Sections 3.8 and 3.9) are explained. The data-acquisition and real-time evaluation are addressed in a separate chapter (cf. Sections 4.4 and 4.5) since they mark an important improvement in the system's capabilities.

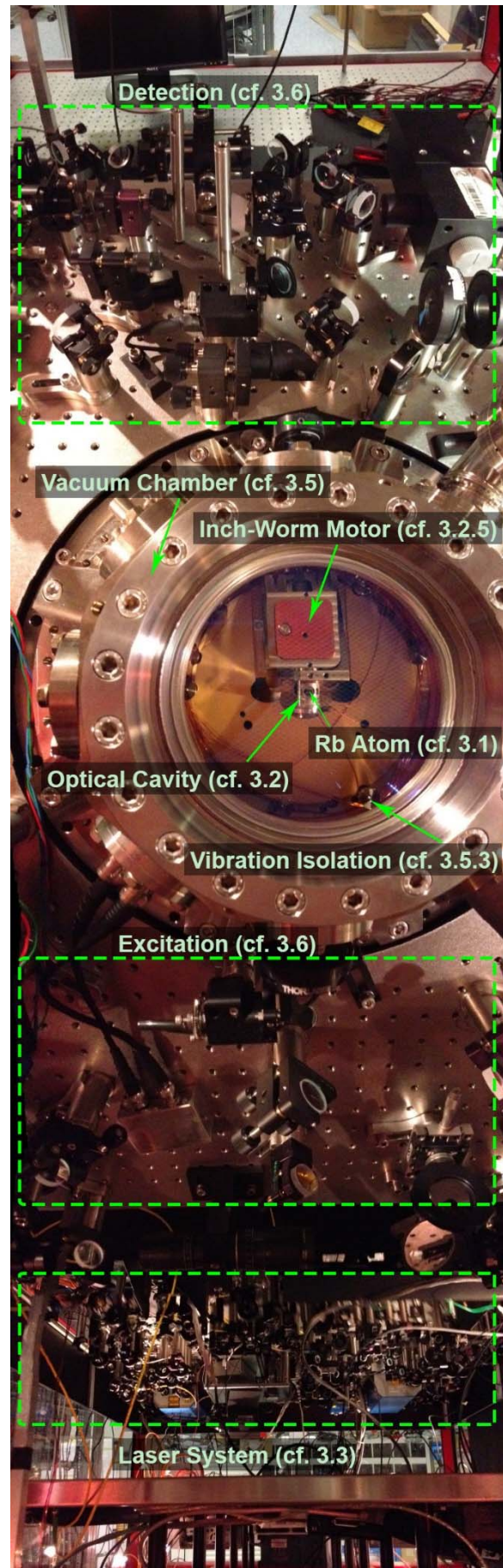


Figure 3.1: Photographic overview of the experimental setup (taken in a top-view perspective). The major experimental building blocks, which will be described in this chapter, can be seen and are labeled. The experimental control is not shown.

3.1. Single Rubidium Atom

In the experiment the interaction of a single atom with a weak light field on the single-photon level is investigated. Here, rubidium atoms are chosen which are hydrogen-like, belong to the group of alkali elements, and have one valence electron in the outer shell. The use of rubidium offers many advantages. It possesses a closed transition at a wavelength of 780.24 nm, meaning that an excited atom can only decay into one possible ground state. Furthermore, this wavelength can be easily accessed with commercially available diode and solid-state lasers. In addition, rubidium dispensers, evaporating rubidium atoms through an electric current, as well as vapor cells, which are used for laser stabilization, are widely available. Its two isotopes [103] ^{85}Rb (72.17%) and ^{87}Rb (27.83%) have different nuclear spins, leading to ground states with different quantum numbers, and hence easily permit to change important physical parameters linked to the level structure of the atom by swapping from one isotope to the other. We use ^{85}Rb at the $5S_{1/2}$ to $5P_{3/2}$ transition (D2 line).

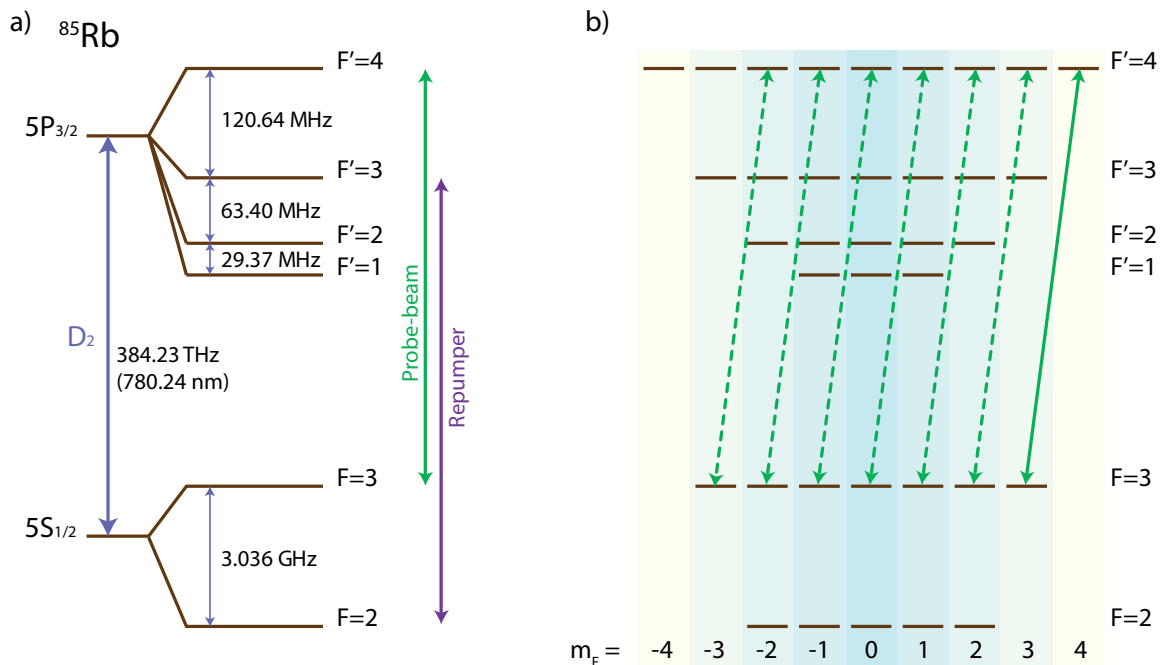


Figure 3.2: a) Hyperfine structure of the ^{85}Rb D2-line. Relevant transitions, which are used for probing (cf. 3.3.1) and repumping (cf. 3.3.2) the atom, are indicated by arrows on the side. b) Zeeman sublevels of hyperfine levels. Transitions mediated by σ^+ -polarized light are marked by green arrows. The solid green line shows the closed $F=3, m_F=3$ to $F=4, m_F=4$ transition, justifying the two-level approximation.

The hyperfine structure of the ^{85}Rb D2-line is drawn in Figure 3.2 a) [104]. In our system we probe the closed $F=3$ to $F'=4$ transition as indicated by the green arrow. Some atoms can be off-resonantly excited to the $5P_{3/2}, F'=3$ state, from where they can decay into the $5S_{1/2}, F=2$ state. In this state they cannot be detected by the probe light anymore and hence would be lost from the system. To recover the atoms, they are excited to the $5P_{3/2}, F'=3$ state (purple arrow), from where they can decay back to the $5S_{1/2}, F=3$ state. Figure 3.2 b) shows the hyperfine levels with their Zeeman sublevels labeled with their corresponding magnetic quantum numbers m_F . With the earth magnetic field compensated and no additional magnetic field applied, these

Zeeman sublevels are degenerate. The polarization of the used light determines the selection rules for the transition. We use σ^+ -polarized light which requires $\Delta m_F = +1$. The possible transitions are marked by the green arrows. Since the atom can decay with $\Delta m_F = 0, \pm 1$, the atomic population will end up cycling on the $m_F = 3$ to $m_{F'} = 4$ transition, as indicated by the solid green line, making this the closed transition. This permits to treat the rubidium atom as a textbook 2-level atom.

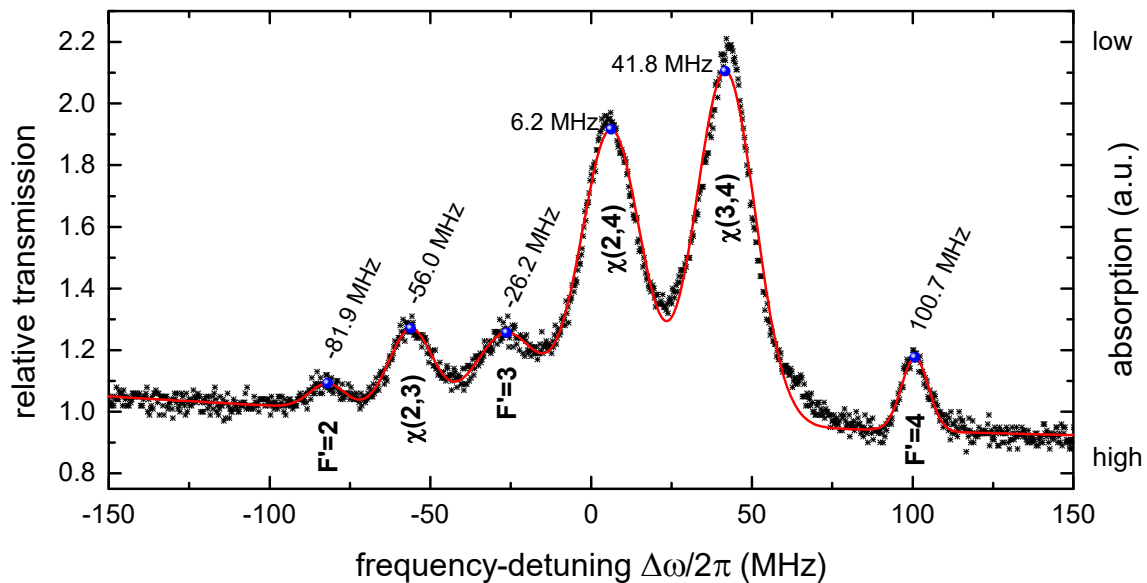


Figure 3.3: Doppler-free saturation spectrum of the ^{85}Rb D2-line starting from $F=3$. The spectrum was recorded with a laser set to $\omega_{\text{Laser,DF}} \approx 384$ THz. It shows the relative transmission of the laser light after passing through a rubidium vapor cell twice (in back reflection). The Doppler broadened transmission after the first passage through the cell is subtracted. A high transmission corresponds to a low absorption by the atomic vapor as indicated on the right scale. Six distinct peaks are visible, which can be attributed to hyperfine levels $F'=2$, $F'=3$ and $F'=4$ as well as to the corresponding cross-over resonances $\chi(2,3)$, $\chi(2,4)$ and $\chi(3,4)$. The red line shows a 6-fold Gaussian fit.

Figure 3.3 shows the spectrum of the different hyperfine levels recorded via Doppler-free saturation-spectroscopy [105] starting from the $5S_{1/2}$, $F=3$ manifold. The crossover resonances (marked with χ) are significantly enhanced. Their transition frequency is the mean value of the two participating levels. This technique will be used for stabilizing the probe and repump laser (cf. Section 3.3).

3.2. High-Finesse Optical Cavity

The heart of the experimental apparatus is a high-finesse optical resonator. It consists of two well aligned mirrors, which are distant an integer multiple of half the resonant light's wavelength, permitting this light to constructive interference on every round-trip. In our resonator a single photon makes – on average – a few ten thousand round-trips before it will leave the cavity. A single rubidium atom brought inside this high-quality resonator can interact with the photon on every round trip. The cavity hence significantly enhances the otherwise

weak interaction between the atom and the photon and thus enables a strong interaction revealing quantum features of the single atom. Described differently: A single photon sees a few ten thousand mirror images of the single rubidium atom.

3.2.1. Basic Definitions

Before the design of our cavity will be discussed, it is important to be familiar with the main parameters characterizing an optical resonator. In the following only the TEM₀₀ mode with a radial Gaussian mode profile will be considered. Its minimum radial spot size is the waist ω_0 . The most fundamental criterion for light to be resonant in the cavity is that the cavity length needs to be an integer multiple n of half the wavelength λ_n of the light.

$$l = n \cdot \frac{\lambda_n}{2} \quad (3.1)$$

Equation (3.1) defines a set of resonant longitudinal modes whose frequency spacing is defined as the free spectral range (FSR) and amounts to

$$\nu_{FSR} = \frac{c}{2l} . \quad (3.2)$$

The optical “quality” of a cavity depends on its free spectral range and its linewidth that is given by its amplitude field decay rate κ . One of the key figures of merit of an optical cavity is its finesse. The finesse \mathcal{F} is the free-spectral range over the linewidth of the cavity $\kappa/2\pi$ and can be expressed in terms of the transmission coefficients (T_1, T_2) and losses (L_1, L_2) of the two constituting mirrors. It is independent of its length and amounts to

$$\mathcal{F} = \frac{\pi c}{l \cdot \kappa} = \frac{2\pi}{T_1 + T_2 + L_1 + L_2} . \quad (3.3)$$

An atom which is caught at an antinode of the cavity-mode can interact with the light field. The strength of the interaction is given by the maximum coupling constant g_0 , which can be written as

$$g_0 = \sqrt{\frac{\mu^2 \omega_c}{2\hbar \epsilon_0 V}} = \frac{\mu}{\omega_0 \sqrt{l}} \sqrt{\frac{2\omega_c}{\hbar \epsilon_0 \pi}} \quad (3.4)$$

It depends on the transition dipole moment of the atom μ , the mode waist in the cavity ω_0 , the resonance frequency of the cavity ω_c , and the volume of the cavity mode $V = \frac{\pi l \omega_0^2}{4}$. Here, ϵ_0 is the vacuum permittivity.

3.2.2. Geometry

In our case the resonator is a Fabry-Perot interferometer with two spherical, concave mirrors. Its geometry can be characterized by the distance between the two mirrors³ l , also called cavity length, and the radii of curvature of the two constituting mirrors R_1 and R_2 [106]. The light inside the cavity bounces back and forth producing a standing wave pattern. The spatial period between the antinodes corresponds to half the wavelength of the light. In our case the cavity has a length of $l = 258 \mu\text{m}$ corresponding to 660 nodes of the probing mode $\lambda_p = 780.24\text{nm}$.

In order to set up an optical resonator it is mandatory that a stable cavity mode can build up. This poses boundary condition on the set of radii of curvature of the mirrors which can be used [107], since they need to constantly refocus the beam on each round-trip.

$$0 \leq \left(1 - \frac{l}{R_1}\right) \left(1 - \frac{l}{R_2}\right) \leq 1. \quad (3.5)$$

It is very intuitive to see that a cavity formed out of two convex mirrors ($R_1, R_2 < 0$) can never fulfill this requirement. The cavity that was built during this thesis consists of mirrors with $R_1 = 1 \text{ cm}$ and $R_2 = 20 \text{ cm}$. A schematic drawing is presented in Figure 3.4. It also shows an actual photograph of the cavity from the top-view. The radii of curvature were chosen very carefully and together with the cavity-length determine the waist ω_0 of the cavity mode [108] (cf. [107] Eqn. (10.2-19))

$$\omega_0 = \frac{\sqrt{\frac{\lambda}{\pi}} \sqrt{l(R_1 - l)(R_2 - l)(R_1 + R_2 - l)}}{\sqrt{R_1 + R_2 - 2l}}. \quad (3.6)$$

A small waist reduces the mode volume (cf. Eqn. (3.4)) and hence increases the maximum interaction strength g_{max} of the light field with an atom. The parameter g_{max} sets an upper limit on the coupling strength as it will be reached by an atom ideally located at an antinode of the cavity. High radii of curvature, on the other hand, tend to degrade the quality of the dielectric coating and increase the complexity required for mode-matching the cavity mode to the excitation and detection setup.

The coning of the mirrors is clearly visible in Figure 3.4. It reduces the full diameter of the highly reflective facet from 7.75 mm to 2 mm or 1.5 mm respectively. This value is still sufficiently large to support the cavity-mode without introducing further losses due to clipping and is now enabling side-ways access to the cavity [109]. This permits to introduce laser beams from the side yielding better cooling and confinement of the atom [110] as well as to observe

³ In reality one has to differentiate between the actual geometric distance between the two mirrors and the distance seen by the TEM₀₀ mode. The latter further includes the penetration of the light into the first layers of the dielectric mirror. However, for simplicity, these two terms will be used as synonyms in the further text.

the atom via a highly sensitive electron multiplying charge-coupled device (EMCCD) camera [111].

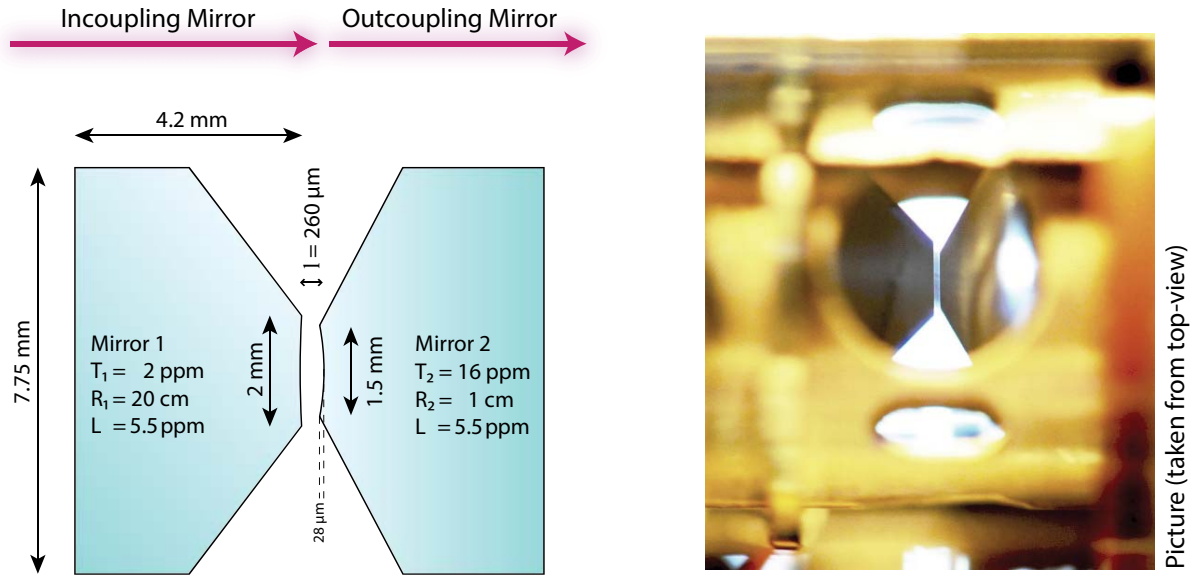


Figure 3.4: Schematic view and photographic impression of the mirror dimensions forming the optical resonator. All relative dimensions in the schematic view are up-to-scale, only the radius of curvature of mirror 1 is exaggerated. The average loss rate per mirror of the mirror pair is given by L . The picture taken at the actual setup shows the two mirrors. The view is partially obstructed by the piezo tube.

3.2.3. The Mirrors

The quality and uniformity of the high-precision dielectric coating of the mirrors is the bottle neck in building high-finesse optical resonators. The two mirrors which form our cavity were made by the company “Research Electro-Optics” (REO). A photograph of a similar mirror fabricated by REO is depicted in Figure 3.5. In order to select the mirrors which are best suited, multiple combinations of mirrors were tested and characterized. Previous experiments had the main focus to achieve the highest possible finesse \mathcal{F} , i.e. aimed for minimizing the transmissions (T_1 , T_2) along with the losses (L_1 , L_2) of the mirrors. However, this results in a very low detection efficiency as it can be seen in Eqn. (3.7). The photon flux leaving the cavity through the outcoupling mirror 2 corresponds to

$$\frac{I_2}{\hbar\omega} = 2\kappa \frac{T_2}{T_1 + L_1 + T_2 + L_2} \langle a^\dagger a \rangle = 2\kappa \cdot \eta_{out,2} \langle a^\dagger a \rangle = \frac{[photons]}{[sec]} \quad (3.7)$$

and vice-versa for mirror 1. Here, the outcoupling efficiency $\eta_{out,2}$ is introduced, which specifies the fraction of detectable photons. For a perfectly symmetric cavity with no losses, photons leave the resonator on both sides to equal amounts yielding $\eta_{out} = 0.5$. This value is further reduced if the losses and transmittances are on the same order of magnitude as it was the case in the forerunner experiment. In order to increase the outcoupling efficiency, an asymmetric

design was chosen. The weakly curved mirror is used to couple light into the cavity. It is specified to have a transmission of $T_1^s < 4$ ppm while the other mirror has a specified transmission of $T_2^s = 25$ ppm. The high-reflectivity is obtained by high-quality dielectric coating centered at 780.2 nm (4ppm: coating-run #L6-261; 25ppm: coating-run #L6-262). The back facet of the mirrors is anti-reflection coated (coating run #OX1618). The datasheets can be found in Appendix 10.1.

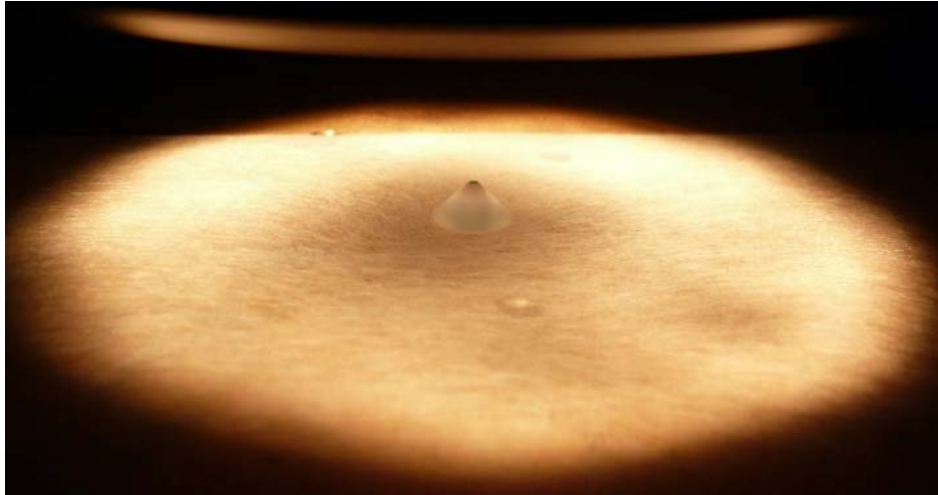


Figure 3.5: Picture of a single mirror from REO. Similar mirrors have been employed to build the resonator. The mirror is illuminated under a microscope, whose object is visible on the top. The coning of the mirror is clearly visible, leaving a remaining front facet of the mirror below 1 mm.

To avoid scattering losses e.g. due to dust particles, the mirrors were carefully cleaned with OptiClean and the result was verified under a dark field microscope. Both mirrors were initially coned with a 45° wedge resulting in an effective mirror diameter of 2 mm for the weakly curved mirror and more than 2 mm for the strongly curved one. In order to reduce the sag height of the latter one while preserving a minimum height at the back facet to clamp the mirror into the cavity holder, it was coned a second time with a 30° wedge by Hellma Optics down to an effective diameter of 1.5 mm. During the processing the mirror surface was covered by a special polymer provided by Hellma Optics.

3.2.4. Parameters

The field decay rate of the cavity can either be determined by a ring-down measurement [108] or by directly measuring the linewidth of the cavity. Both measurements were carried out with light at the probing wavelength of 780 nm and are presented in Figure 3.6.

The ring-down measurement yields an intensity field decay rate of $2\kappa / 2\pi = 2.999 \pm 0.015 \text{ MHz}$ which results in a finesse of our cavity of $\mathcal{F} = 194000 \pm 1000$. Figure 3.6 b) shows a heterodyne measurement of the cavity-resonance (details can be found in Chapter 5.6). From a Lorentz or arctangent fit, respectively (solid blue and red line), an amplitude field decay constant of $\kappa / 2\pi = 1.74 \pm 0.01 \text{ MHz}$ was obtained. This value is

considerably larger than the one obtained in the ring-down measurement. The discrepancy has two possible reasons: First, an additional broadening due to frequency fluctuations of the stabilized laser diode as well as of the cavity resonance due to mechanical vibrations. Both of these effects only have a minor impact on the ring-down measurement. Secondly, broadening due to birefringence splitting of the cavity. Stress induced by the mounts holding the cavity mirror as well as tiny asymmetries created during the production of the mirrors lift the otherwise perfect radial symmetry of the mirrors. Due to the high number of round-trips these small deviations add up to an optical path difference of the two main polarization axes. In the worst case the splitting equals or even surpasses the width of the cavity resonance. This deteriorates the circular polarization of the cavity mode needed to treat the atom as a simple two-level system. Assuming a value for the amplitude field decay of 1.5 MHz as measured by the ring-down measurements, we can assume an upper limit for the birefringence splitting of 27% of the cavity's linewidth [81].

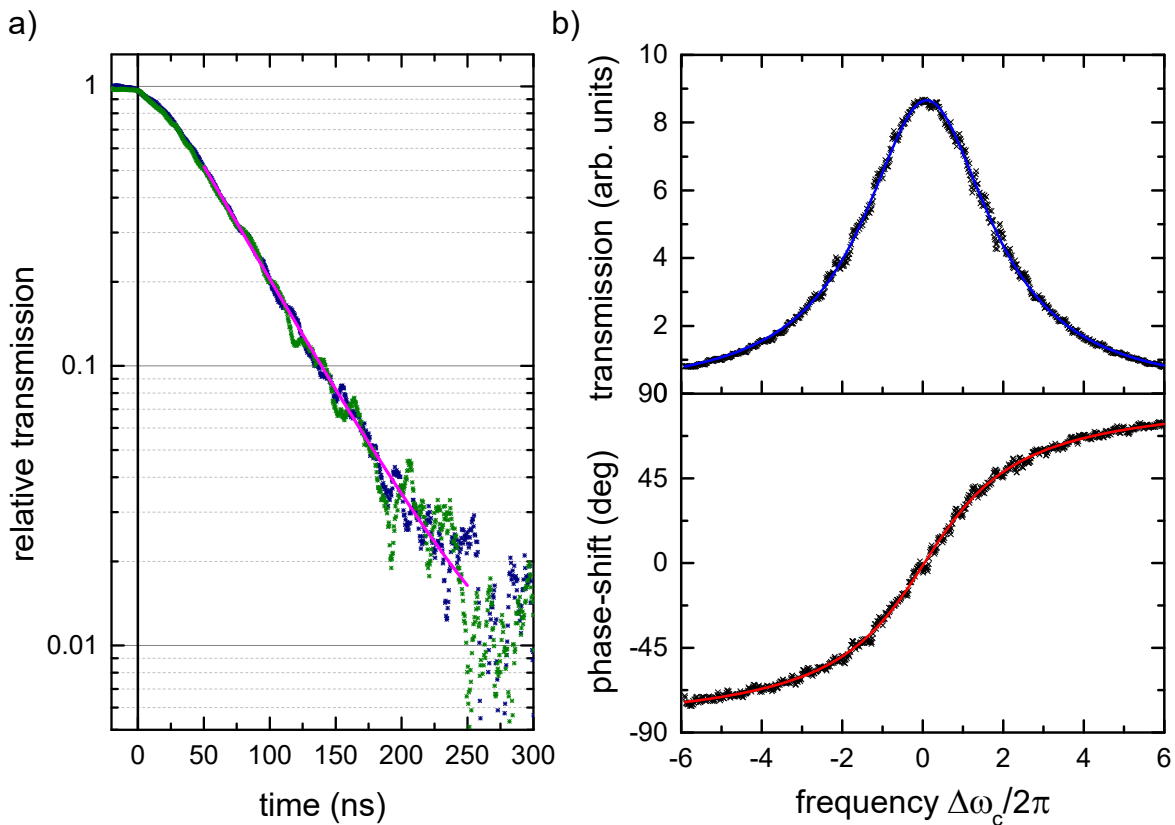


Figure 3.6: a) Ring-down measurement of the optical cavity. The cavity is brought on resonance with the light from the laser. Once the light is resonantly enhanced by the cavity, it is abruptly turned off at $t = 0$. The high reflectivity of the mirrors prevents the light-field inside the cavity to follow this abrupt change and causes a slow decay of the light-field through the mirrors. Two measurements are shown by the green and blue dots. An exponential decay fit (magenta line) then yields the FSR. b) Linewidth of the cavity in transmitted intensity and phase. A Lorentz (blue) and inverse tangent fit (red) are used to determine the linewidth of the cavity.

The losses and transmittances of the two mirrors cannot be extracted directly from the finesse. In order to estimate these values, the ratio of the impinging light compared to the transmitted and reflected light needs to be measured [106]. This results [81] in $T_1 = 2.5 \pm 0.5$ ppm and

$T_2 = 17.8 \pm 0.5$ ppm as well as in an average loss-rate of $L = (L_1 + L_2)/2 = 5.5 \pm 0.5$ ppm. The transmissions significantly depend on the wavelength and increase to $T_1 = 4 \pm 0.5$ ppm and $T_2 = 21 \pm 0.5$ ppm with $\mathcal{F} = 170000 \pm 5000$, if light of 772 nm wavelength is used. The overall outcoupling efficiency for a resonant mode at 780 nm amounts to $\eta_{out} = 0.57$, which is a significant increase compared to the forerunner experiment with $\eta_{out}^\dagger = 0.19$. The increased outcoupling efficiency is at the expense of a reduced incoupling efficiency which is as low as $\eta_{in} = 0.08$ and can be overcome by simply increasing the intensity of the incoupling laser beam.

3.2.5. Inch-Worm Motor

One of the most intriguing new features of the cavity is its macroscopically changeable length. Similar to comparable systems in the Rempé group, one of the cavity mirrors is mounted in a piezo tube (Ferroperm) responsible for fine-tuning the cavity length down to the sub-picometer level.

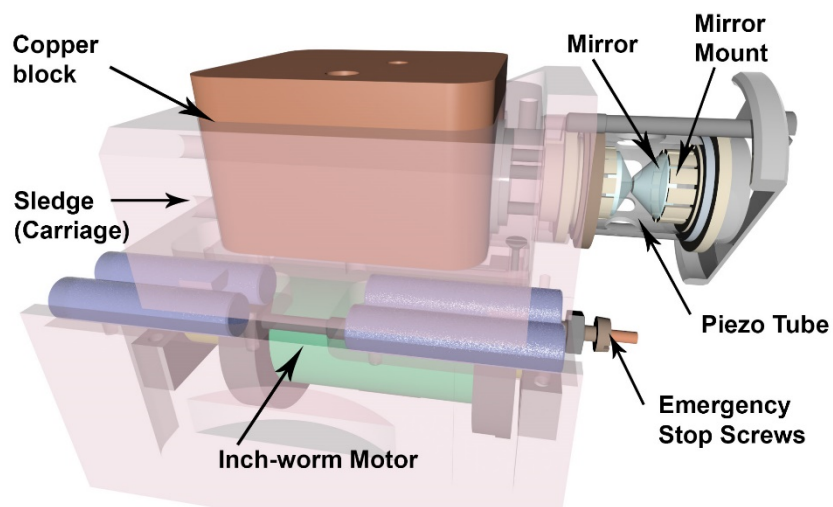


Figure 3.7: CAD drawing of the inch-worm motor. The sledge containing a copper block slides over four mated glass cylinders moving one of the mirrors macroscopically. The glass rods are made of ULE (ultra-low expansion) glass. The other mirror is fine-tuned with a piezo. Both mirrors are held by clamping into a mirror mount.

While this is very important to actively and accurately stabilize the cavity length, it only permits to scan its length on the order of two free spectral ranges (about $1 \mu\text{m}$). In addition, the other mirror is mounted on a sledge which can be moved macroscopically by what is called an inch-worm motor. A CAD (computer aided design) drawing is depicted in Figure 3.7. The inch-worm motor was manufactured by Burleigh and permits to alter the cavity length without the need to open the vacuum chamber or the requirement for major realignment [108]. It allows to change the cavity length l from $40 \mu\text{m}$, limited by the sag height of the mirrors taking into account an additional safety buffer, up to a maximum of ~ 5 mm. The traveling distance is mechanically and electrically safeguarded by two emergency stop screws on each side. A copper block increases the weight of the carriage resulting in a better vibration isolation. While those limits stem from the mechanical design, it has even been verified [81] that for lengths as large as 1.3 mm the quality, i.e. the finesse of the cavity, does not degrade ($\mathcal{F}(\lambda) > 190000$) as it would occur if the sledge did not travel exactly parallel to the cavity axis. This huge traveling distance permits to significantly alter the physical parameters of the cavity like C , g , κ , ω_0 once it is set up. Here

$C = g^2/2\kappa\gamma$ defines the cooperativity of our system. A graph with these parameters as a function of the cavity length can be found in Figure 3.8 a). The values used during the course of this thesis are marked by the vertical dashed line. In general, one can say that a shorter cavity increases the coupling rate of the atom and the cavity as well as the cavity decay rate, and shrinks the size of the waist. Beyond a length of around 5 mm this behavior changes to its opposite. The mode at the mirror surface now covers a large portion of it yielding a higher numerical aperture and thus a tight focusing of the diffraction limited mode inside the cavity. However, this regime cannot be reached with the current system since it would require mirrors with a larger area of the high-reflective surface and in the most extreme case, around ~ 10 mm, the mirrors even would need to form a perfect hollow half-sphere.

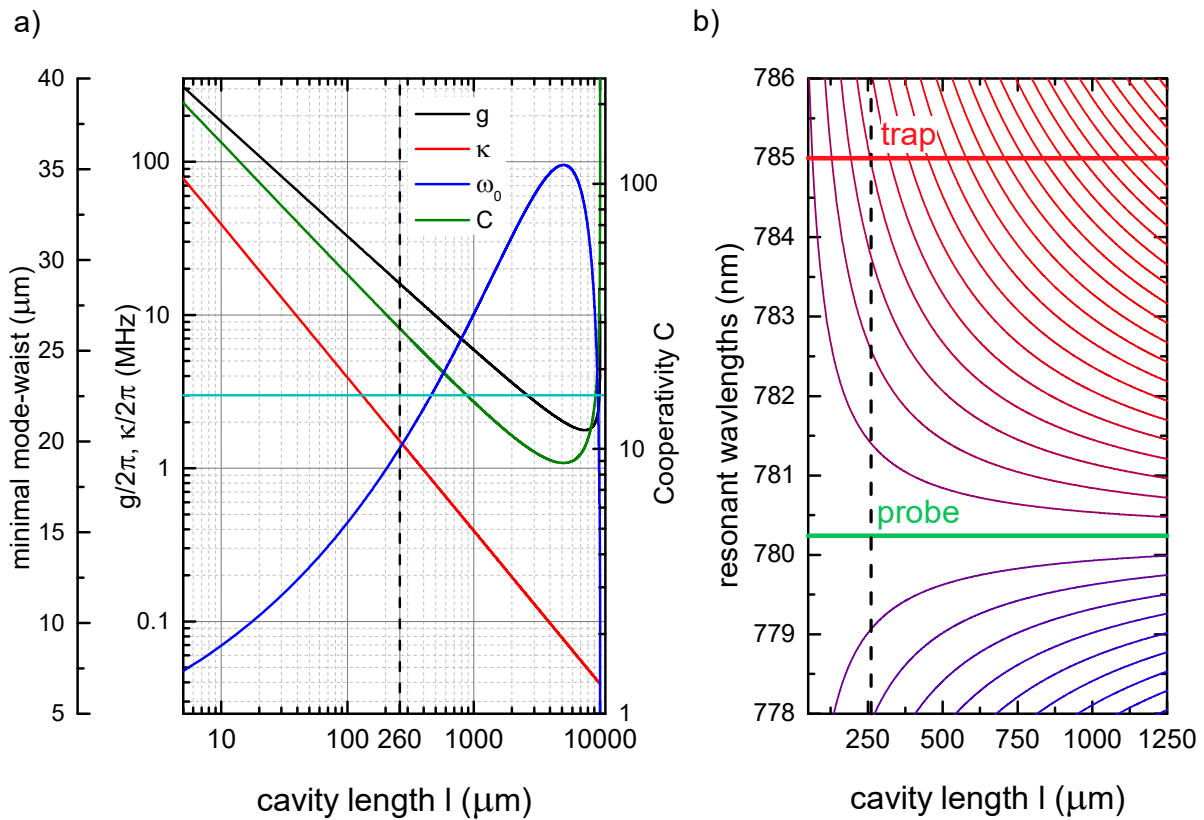


Figure 3.8: a) Parameters g , κ , ω_0 and C as a function of the cavity length. g , κ and C show a decreasing behavior with increasing cavity length while ω_0 is increasing. Around 5 mm the behavior of g , ω_0 and C changes to its opposite. The atomic polarization decay rate $\gamma/2\pi$ of 3 MHz is marked by a cyan horizontal line. b) Resonant wavelength for different cavity lengths. Typical trap and probe frequencies, as they are used throughout this thesis are marked by a red and green horizontal line. The resonance of the cavity with the ^{85}Rb D2-line (probe) is used as a prerequisite. The decreasing mode spacing with increasing cavity length is clearly visible. In this thesis the cavity is set to a length of $258 \mu\text{m}$ marked by the vertical black dashed line. Here, the trap beam with a wavelength around 785 nm is red-shifted 4 FSR from the probe beam.

The second main advantage of a length-variable cavity is the possibility to have control over the set of resonant wavelengths. One wavelength which needs to be resonant is already given by the D2-line of the rubidium atom (probe beam) at 780.24 nm, leaving no room for further adjustment in case of only microscopically movable mirrors. Figure 3.8 b) shows the resonant wavelength and nicely demonstrates the additional degree of freedom gained by a

macroscopically changeable length. As a reference, the wavelength of the probe beam (cf. Section 3.3.1) (horizontal green line) as well as the trap laser (cf. Section 3.3.3) (horizontal red line) is given. Albeit the great possibilities offered by the length adjustment, only a fixed length of 258 μm has been used for this thesis.

3.3. Laser System

The structure of the rubidium atom was already explained previously (cf. Section 3.1). Here, we will elaborate on the laser system used to prepare, cool and probe the rubidium atoms. For this purpose, three lasers are employed: A probe laser, driving the closed cycling transition of rubidium, a repumper, optically pumping the atoms back to the desired transition and a trapping laser, creating an attractive dipole potential holding the atom. The latter laser is additionally used to stabilize the cavity length as it will be explained in Section 3.7.

3.3.1. Probe Laser

The most crucial laser in this system is the probe laser. Photons from this laser are used to mediate the interaction of a single rubidium atom and the cavity. Furthermore, it is responsible to cool a cloud of rubidium atoms in a magneto-optical trap (MOT), as it will be described in Section 3.8.1. Its frequency needs to be stabilized to the ^{85}Rb D2 line with a linewidth below 500 kHz, which is below the cavity field decay rate $\kappa/2\pi = 3$ MHz, in order to avoid additional broadening effects in our experimental system. We use a commercially available diode laser fabricated by TOPTICA (TA 100). It consists of a grating stabilized diode laser in Littrow configuration [112]–[114] as a master laser which seeds a tapered amplifier. It delivers an output power of approximately 900 mW at 780 nm and is tunable over a range of a few nanometers. The mode hopping free tuning range, however, is significantly smaller and comprises only a few tens of GHz.

A schematic drawing of the full probe laser system can be found in Figure 3.9 a). A small portion of the light from the seeding laser is extracted at the auxiliary output of the laser and passes through an acousto-optic modulator (AOM5) in double pass configuration. This causes a frequency shift of the light by twice the AOM's resonance frequency. We employ a Doppler-free saturation spectroscopy setup [105] with a rubidium vapor cell to frequency-lock the laser to the $F = 3 \rightarrow F' = \chi(3,4)$ cross-over transition, which shows the biggest signal-to-noise ratio as it can also be seen in Figure 3.3. An electro-optic phase-modulator (EOPM) operating at 8 MHz generates sidebands on the laser light before it passes the vapor cell. By utilizing a Pound-Drever-Hall locking scheme [115] a dispersive error signal is demodulated, which is fed back to the laser via the FALC module available from TOPTICA. It acts as a proportional-integral-derivative controller (PID) altering both the laser's feedback grating and hence the parameters of the external, stabilizing cavity (slow lock) as well as the current of the laser diode (fast lock).

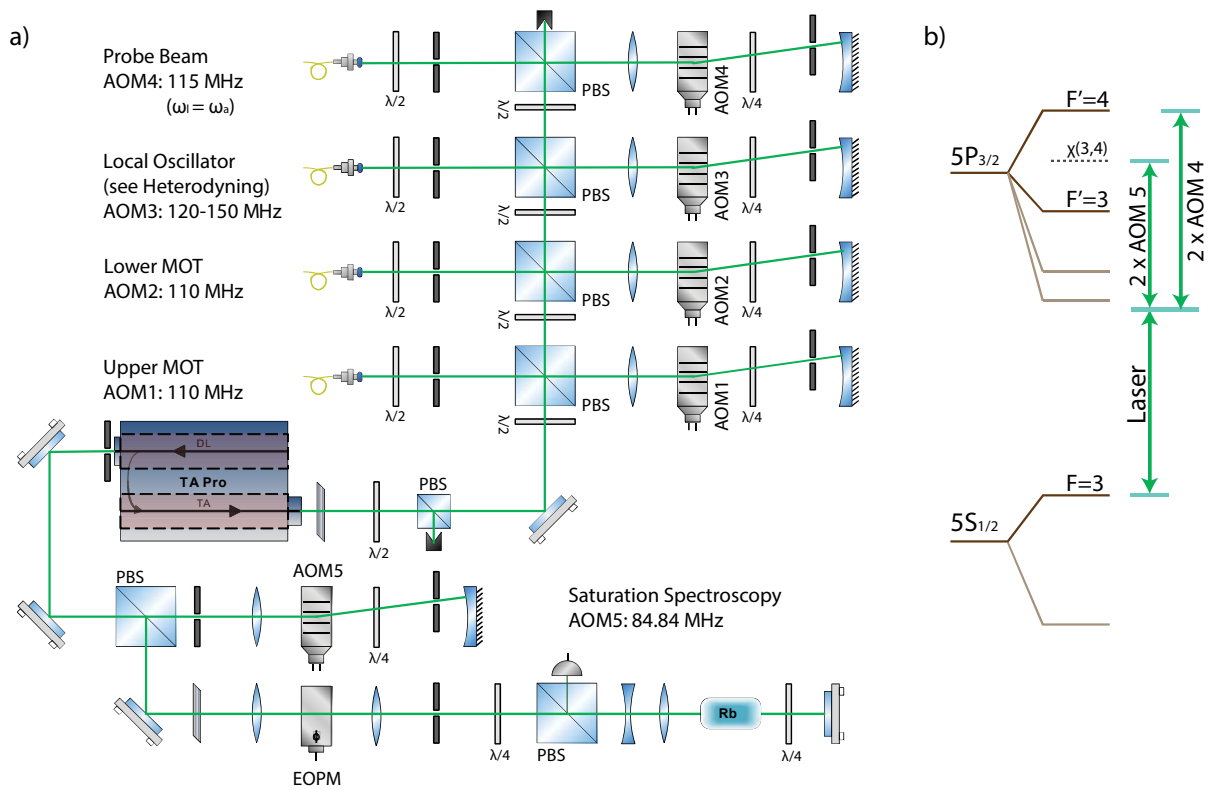


Figure 3.9: a) Optical breadboard setup of the probe and cooling laser. The auxiliary output of the laser (lower left side) passes AOM5 in double pass configuration. Afterwards, it is sent through an electro-optic phase modulator (EOPM) to modulate sidebands of 8 MHz used for the Doppler-free rubidium spectroscopy employed to lock the laser. The polarization of the amplified output beam of the laser is adjusted via a $\lambda/2$ waveplate and cleaned by a subsequent polarizing beam splitter (PBS). Afterwards, the beam is split and sent through a cascade of separate AOM lines. The input power entering the respective line is adjusted by a prior $\lambda/2$ waveplate. In each AOM line a lens focusses the beam on the AOM. A concave mirror retroreflects and refocuses the beam into the AOM a second time. The double passage through the $\lambda/4$ waveplate turns the linear polarization by 90° , making the PBS fully “transmissive”. Apertures block unwanted residual refraction orders of the beam, before an integrated lens in the fiber couplers focuses the beam into a fiber. The double passage through the AOM leads to a shift by twice the applied AOM frequency. b) Locking scheme of the laser to the $\chi(3,4)$ ^{85}Rb crossover resonance. The frequency of the laser as well as the frequency of the beam in the AOM lines four and five are depicted. The spectrum of the rubidium atom serves as a reference for showing the selected AOM frequencies. A legend of the symbols is found in Appendix 10.8.

The amplified laser output is split and sent through a cascade of separate AOM lines. Each AOM line comprises an AOM in double-pass configuration, a $\lambda/4$ waveplate, a concave mirror and a polarizing beam splitter (PBS) as main constituents. This setup allows to adjust the frequency and intensity of the light by controlling the frequency and power of a radio frequency (RF) applied on the AOM. An aperture system filters unwanted residual orders of the AOM while a lens system is employed to couple the light efficiently into a fiber. The AOM lines are installed in a sequential configuration. The power distribution of the laser light among the different lines is adjusted by $\lambda/2$ waveplates. Four different AOM lines are needed: Two for the magneto-optical trap as it will be described later (cf. Section 3.4), one for the local-oscillator (cf. Chapter 5.6) and one for the probe beam. An overview of the actual laser frequency as well as the frequency sent as probe beam and the one fed into the Pound-Drever-Hall lock is depicted in Figure 3.9 b).

3.3.2. Repumper

Atoms that are illuminated with light near-resonant to the $5S_{1/2}, F = 3 \rightarrow 5P_{3/2}, F' = 4$ transition can also be off-resonantly excited to the $5P_{3/2}, F' = 3$ state from where they can decay into the $5S_{1/2}, F = 2$ state. This state does not couple to light on the $F = 3 \rightarrow F' = 4$ transition and these atoms would hence be dark to the probe beam. In order to recover an atom and get it back to the cycling transition, it needs to be repumped back to the $5S_{1/2}, F = 3$ state. This is achieved by illuminating the atom with a laser resonant to the $5S_{1/2}, F = 2 \rightarrow 5P_{3/2}, F' = 3$. With a large probability they will then decay back to the $5S_{1/2}, F = 3$ state. By applying this laser beam continuously, it can be ensured to get the atoms back to the cycling transition. The repumping laser is responsible to accomplish this task. Similarly, to the probe beam, a grating stabilized diode laser from TOPTICA is employed (DL 100). Due to the low power requirements, however, a tapered amplifier is not necessary. A schematic drawing of the laser system is shown in Figure 3.10 a).

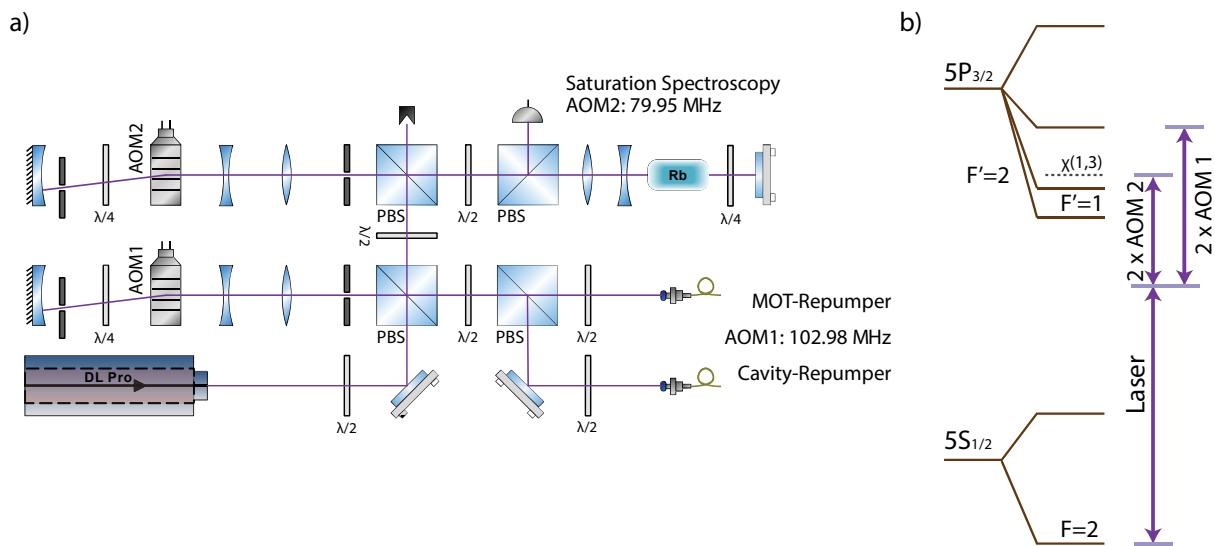


Figure 3.10: a) Optical breadboard setup of the repumping laser. The linear polarization of the laser light is adjusted by $\lambda/2$ waveplates. These waveplates permit to adjust the intensity distribution in the two arms into which the laser light is divided by the subsequent PBS. Each arm consists of an AOM in double pass configuration. The upper arm is used to stabilize the laser via Doppler-free rubidium spectroscopy. The lower arm is used to shift the light to the desired $F = 2$ to $F' = 3$ transition. This light is then coupled into two fibers guiding the light to the MOT and to the side access of the cavity (perpendicular to the resonator axis). b) Locking scheme of the laser to the $\chi(1,3)$ ^{85}Rb crossover resonance. The frequency of the laser as well as the frequency of the beams in both AOM arms are depicted. The spectrum of the rubidium atom serves as a reference for showing the selected AOM frequencies. A legend of the symbols is found in Appendix 10.8.

The beam is split into two arms each passing twice through an AOM. The spectroscopy arm, which is offset by twice the frequency of AOM2, is used to frequency-lock the laser to the $F = 2 \rightarrow F' = \chi(1,3)$ cross-over resonance. As for the probe laser, a Doppler-free rubidium spectroscopy is used. This time the side-bands, necessary to deduce the error signal, are generated directly by rapid modulation of the current of the laser-diode via the so-called “bias- t ” input of the laser. On the one hand, this different experimental realization considerably

simplifies the optical and electronic setup. On the other hand, it implies that also the beam sent to the atoms will have these sidebands imprinted as well. However, these sidebands neither affect the repumping capabilities nor do they lead to any unwanted disturbance of the system. The error signal from the spectroscopy is sent to a home build PID controller altering both the laser's feedback grating and hence the parameters of the external, stabilizing cavity (slow lock) as well as the current⁴ of the laser diode (fast lock). The light in the other arm, which is sent to the actual experiment, is shifted by AOM1, making it resonant to the $F = 2 \rightarrow F' = 3$ transition. Most of the light ($\sim 3\text{mW}$) is used for the MOT beams (cf. Section 3.4) while a small fraction ($\sim 2\text{-}3 \mu\text{W}$) is sent sideways through the cavity (cf. 3.6). An overview of the frequencies in the different arms along with the rubidium level scheme as reference is plotted in Figure 3.10 b).

3.3.3. Trapping Laser

A third laser is of great importance for our setup, this is the dipole trap laser. It is used to create a standing wave dipole pattern, acting as a potential valley for the atoms by exerting an external force on the atom and thus permitting to trap and localize single rubidium atoms [116], [117]. As for the probe laser, a commercially available laser from TOPTICA (TA pro) is employed. While also near-resonant light, which is used to probe the atom, has been used in the past to capture and store atoms [49], [50], independent, detuned light allows to achieve longer storage times [118]. Here, we employ light resonant with the cavity and centered at 785 nm. This yields a red-detuning by 4 FSR (5 nm) from the atomic resonance frequency, equivalent to a frequency detuning of $\Delta_{\text{dip}}/2\pi = (\omega_a - \omega_{\text{trap}})/2\pi = 2.5 \text{ THz}$. This wavelength is chosen for two reasons: First because its frequency is sufficiently far away from the atomic resonance and thus resulting in low scattering rates at a given trap-depth. This is due to a linearly decreasing force on the atom with increasing detuning $F \propto 1/\Delta_{\text{dip}}$ whereas the atomic excitation drops quadratically $\langle \sigma_+ \sigma_- \rangle \propto 1/\Delta_{\text{dip}}^2$ [77]. Secondly, the wavelength of the trap should be close to the probe light. This ensures a good axial overlap in certain regions inside the cavity. A red-detuning by an even number of FSRs furthermore guarantees that the overlap is best at the cavity center. The depth of the potential valley is proportional to the intracavity intensity of the beam with typical values around $k_B \cdot 1 \text{ mK}$ (with the Boltzmann constant k_B). The depth of the valley determines and even permits to control the atomic trajectory inside the cavity via feedback; a detailed discussion can be found in Chapter 5. A schematic overview of the trap laser setup is depicted in Figure 3.11.

Despite of having a tapered amplifier integrated into our laser only a part of the seeding beam is used at the moment. The amplified branch, however, permits to introduce a side-ways trap in

⁴ The current sent to the laser diode can be altered twofold. Once through the backplane of the laser control unit, as it is usually done if a PID is employed and second through the "bias-t" input, as it is necessary for high-frequency modulation. The latter uses an internal bias-t minicircuit component to modulate the signal directly onto the laser diode and permits modulations even above a few tens of MHz.

the future [110], which requires, due to the lack of amplification by the cavity, higher powers. Opposite to the previously described laser system this one is not locked to a rubidium vapor cell. The reason is the lack of available transitions around 785 nm. Instead, an ultra-stable optical frequency source is used as reference. In previous experimental realizations [52] a so-called transfer cavity has been utilized. This cavity is stabilized on the probe laser and hence can serve as a reference itself for a laser whose wavelength is an equal number of FSRs detuned.

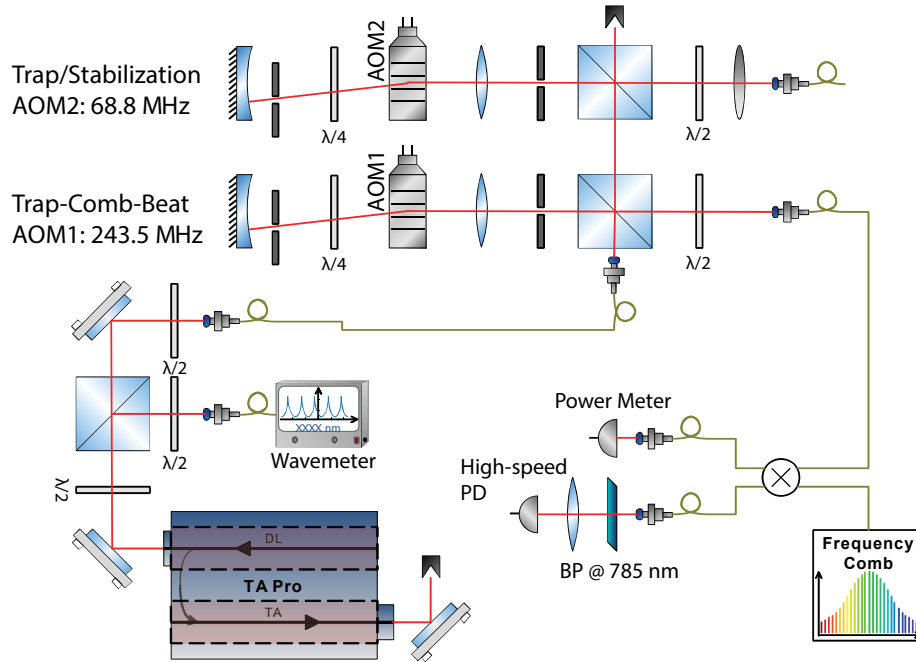


Figure 3.11: Optical setup of the trap laser. Currently only light from the auxiliary output of the laser is used. The amplified output is blocked with a beam dump. A small fraction of the light is coupled into a fiber which is connected to the wavemeter. The remaining light is coupled into a fiber before it is split into two arms. The smaller portion is sent to the stabilizing arm passing through AOM1 in double-pass configuration. The light is then coupled into one port of a fiber beam splitter. The other port is connected to the output of a frequency comb. The two outputs of the beam splitter feed a power meter and a high-speed photodiode. The second arm (on the top) consists of AOM2, controlling the trap beam's frequency and intensity and is then coupled into a fiber sending it to the actual experiment. A legend of the symbols is found in Appendix 10.8.

Here we decided to use the new technique of optical frequency combs [119] as optical frequency reference. An optical frequency comb is an optical spectrum which consists of equidistant lines in frequency space, called teeth, and thus can be used as an optical ruler. The optical frequency comb in our group generates teeth⁵ at

$$\nu_{comb,n} = 2 \cdot \nu_{comb,off} + n \cdot \nu_{comb,rep} = -40MHz + n \cdot 250MHz . \quad (3.8)$$

Here, $\nu_{comb,off}$ is the frequency-offset and $\nu_{comb,rep}$ the repetition rate of the comb, which is equivalent to the spacing of the teeth. The part of the light from the trap laser used for the locking passes through AOM1 in double pass configuration shifting the beam by $2 \cdot 243.5MHz$. Afterwards this beam is coupled into a fiber beam splitter. At the other end of the fiber beam splitter the optical frequency comb is connected, resulting in an overlap of the two beams. One

⁵ The sign of the offset beat $\nu_{comb,off}$ has been verified by an internal measurement in the Rempe group in 2009.

of the outputs of the beam splitter is connected to a power meter, which is used to balance the power of the two beams, while one beam is blocked at each time. The other output is connected to a high-speed, ac-coupled photodiode (MenloSystems FPD510). The detection process by the photodiode results in a mixing of the two beams yielding a spectrum of the difference frequencies of the two beams. A low-pass filtering at 80 MHz ensures that only one frequency component in the RF regime remains. This frequency is directly proportional to the frequency offset of the trap laser to the closest comb tooth and hence permits a stabilization of the laser [120]–[122]. A zero-crossing counter is implemented to create an error-signal, which is directly passed to a FALC (Fast Analog Linewidth Control) PID from Toptica in the laser-rack [81]. However, this basic locking scheme as well as the beat-frequency detection was significantly improved during the course of this thesis, as it will be described in Section 3.7 and 4.6. The coarse tuning of the laser frequency is achieved by a wavemeter from HighFinesse (model: WS/6), which features a resolution comparable to the spacing of the teeth and hence permits to select the correct frequency tooth. For this purpose, a fraction of the laser light is extracted by a PBS. The light that is used in the experiment passes through AOM2 in double pass configuration permitting to adjust its frequency and intensity before it is guided to the cavity in an optical fiber.

3.4. Magneto-optical Trap (MOT) with Atomic Fountain

In order to produce an ultra-cold cloud of rubidium atoms a magneto-optical trap is employed [123]–[127]. It combines laser cooling with magneto-optical trapping of atoms. It uses an arrangement of laser beams and magnetic fields to confine and slow down neutral atoms from a rubidium background vapor. The three-dimensional laser cooling is achieved by illuminating the cloud of atoms with three pairs of orthogonal laser beams. Each pair consists of two counter-propagating laser beams. The laser light is slightly red-detuned – in our case 16 MHz – to the $5S_{1/2}F = 3 \rightarrow 5P_{3/2}F' = 4$ transition. Atoms which are moving against the propagation direction of any of the laser beams (i.e. towards the source of the laser beams) will see a blue-shifted light field. This additional blue-shift moves the light closer to the atomic resonance frequency, the atom thus absorbs more likely a counter-propagating photon, resulting in a friction force, which is slowing down the atom. This mechanism so far only creates a velocity dependent force on the atoms which slows them down. In order to achieve an actual confinement of the atoms, a position dependent force needs to be exerted, in addition. This is achieved by adding a constant magnetic field gradient, which amount to zero in the center of the MOT, as it is realized by magnetic coils in Anti-Helmholtz configuration. The magnetic field now induces a Zeeman splitting of the atomic levels, which increases with the radial distance to the center of the MOT. This shifts the atomic resonance closer to the laser beam, increasing the probability to absorb a photon and pushing the atom towards the center. In order to only increase the probability of one of the two counter-propagating laser beams to be absorbed, the selection rules require the use of σ^+ , σ^- polarized light. The opposite k-vectors of the counter-propagating light beams in combination with the opposite sign of the magnetic

field due to the Anti-Helmholtz configuration require the correct and pairwise opposite choice of the σ^+, σ^- polarization for each pair of light beams. As discussed in [128], [129] temperatures below the Doppler limit T_{dl} , which is determined by the spontaneous emission rate of the excited atoms [130] and which is given by

$$T_{dl} = \hbar\gamma/k_B \quad (3.9)$$

can be reached. For ^{85}Rb this limit amounts to 146 μK for the employed transition.

In our system the MOT is located underneath the science chamber, which holds the high-finesse optical cavity as it will be described in the next section. The ‘‘transport’’ of the atoms is achieved by a ballistic flight of the atoms, called atomic fountain [45]. Compared to deterministic loading schemes, which feature a transverse optical dipole trap, this scheme does not require a transverse optical access and is hence also applicable to shorter cavity lengths. Our MOT is aligned in such a way that each of the three orthogonal pairs consist of an upper and lower MOT beam. In order to accelerate the atoms upwards, a net force needs to be exerted. This is achieved by detuning the upper to the lower MOT beams, which thus requires a separate control, as it will be described in Section 3.8.2. The three upper and lower MOT beams are derived from a single laser beam each. The distribution of the laser beams is achieved by two customized fiber port clusters from Schafter-Kirchhof [81]. Each one splits the incoming light equally among three polarization maintaining fibers. A built-in photodiode permits to stabilize the beams’ intensity. In addition, the fiber port cluster for the upper MOT beams features a second input which enables to overlap a weak repumper beam with the MOT beams. Besides a reduction in size and complexity the use of a fiber port cluster substantially enhances the robustness of the setup, as the risk of misalignment is minimized by employing fiber coupled MOT beams.

3.5. Vacuum Chamber

Experiments studying the properties of single atoms require an ultra-high vacuum on the order of a few 10^{-10} mbar in order to avoid scattering with the background gas. The vacuum chamber employed is based on a customized design and specifically tailored to the needs of our experiment setup. A sketch is depicted in Figure 3.12. In addition, a cut through the apparatus is provided in Figure 3.13. The vacuum chamber is divided into two main parts. In the lower part a cold cloud of rubidium atoms is formed which is then transferred via an atomic fountain to the upper chamber where they can interact with the field of the high-finesse cavity. Both chambers are connected via a small tube with a diameter of 15 mm and each one is evacuated by a separate ion-getter pump. The two pumps are oriented in a way that the magnetic-field gradients at the position of the atom are minimized. All vacuum components are made of non-magnetic VA4 steel (material number 1.4404). The viewports are broadband anti-reflection coated and have a non-magnetic seal.

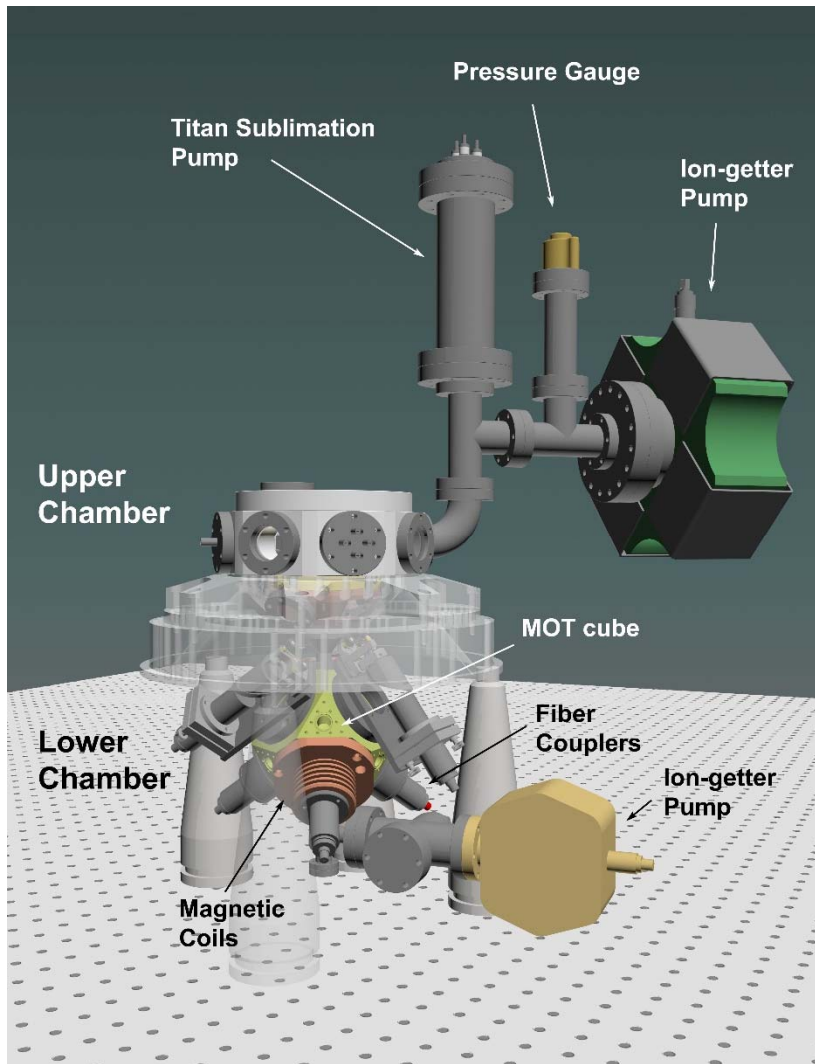


Figure 3.12: Sketch of the experimental apparatus. A complete view of the vacuum system, including the upper and lower chamber as well as pumps and gauges is depicted. The lower chamber features the MOT cube with fiber couplers visible (dark grey) on the outside as well as the magnetic coils (brown color).

The backing out of the vacuum chamber was accomplished in three steps. First, the bare chambers with blind-flanges installed were baked for a week at 350°C . This was done separately for the upper and lower chamber. After installing the actual viewports another baking run was performed for a week. As a last step the dispensers and the high-finesse cavity with its vibration isolation system was installed and the two chambers were connected. After two weeks of baking with 140°C a pressure of $1 \cdot 10^{-9} \text{ mbar}$ was achieved, which further decreased to $3 \cdot 10^{-10} \text{ mbar}$ after flashing the titan-sublimation pump connected to the upper chamber. In the following, we will have a closer look on each of the two chambers.

3.5.1. Lower Chamber

The lower chamber holds the MOT system and is used to prepare the atoms before they are launched to the upper chamber. It has the shape of a cube with the eight corners being cut away. All sides are equipped with CF-40 flanges which have viewports installed. They are used to focus the six pairwise counter-propagating, perpendicular laser beams through the center of the chamber by means of fiber couplers directly attached to the cube. The eight corners have CF-16 flanges installed. The corner facing upward is used to connect the chamber to the upper chamber. Another corner-flange is used to connect the pump, two flanges have rubidium dispensers installed and four are equipped with viewports. They are used to install an optical CCD camera to observe the formation of the MOT. Furthermore, two magnetic coils in Anti-Helmholtz configuration are mounted from the outside in such a way that they enclose one pair

of the fiber couplers. The pressure requirements are less strict than in the upper chamber, so that an 8 l/s ion-getter pump (Varian) is sufficient to keep the vacuum below $1 \cdot 10^{-9} \text{ mbar}$ even when the rubidium dispensers are turned on temporarily to generate a background gas of rubidium atoms needed for the MOT.

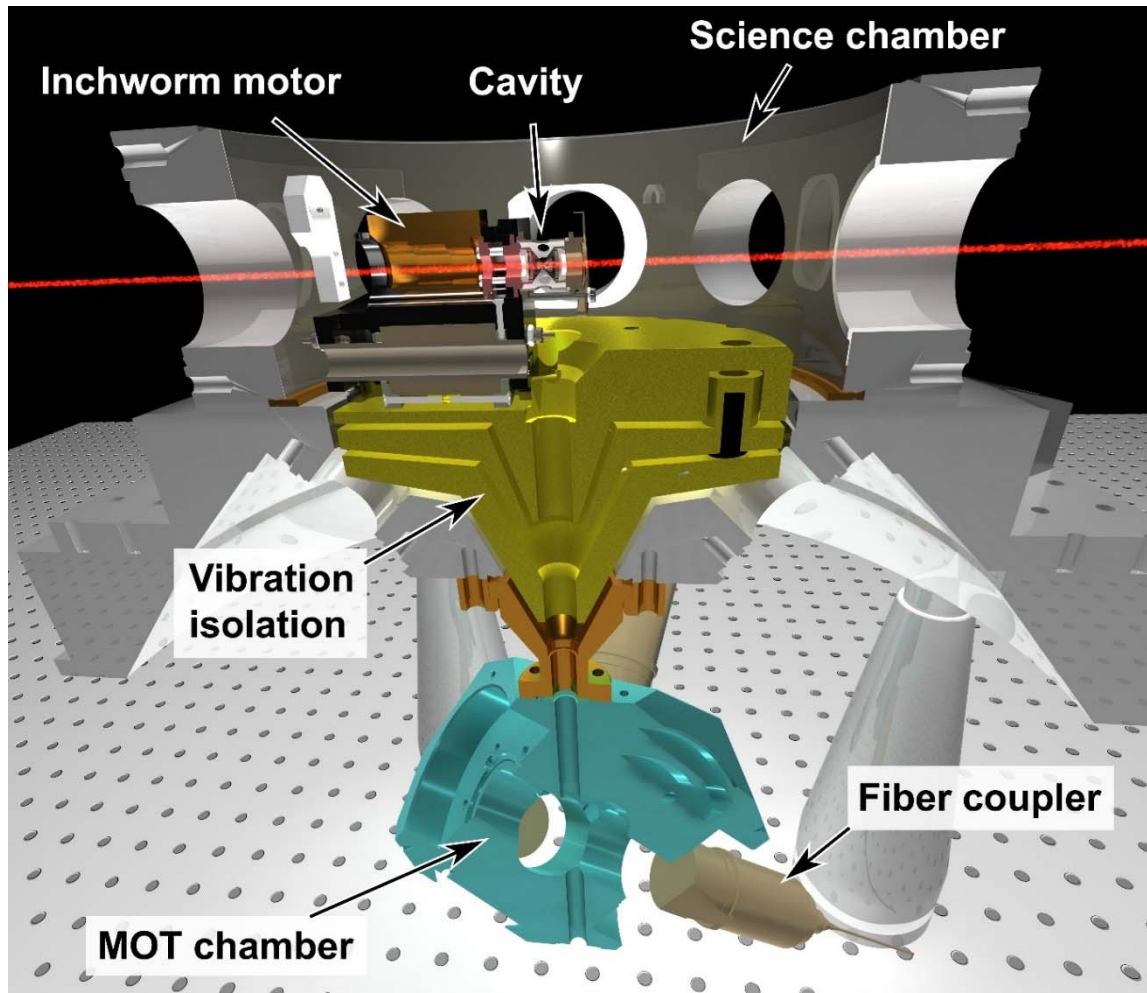


Figure 3.13: Cross-section of the vacuum chamber. Vacuum pumps, pressure sensors, viewports, flanges and screws are omitted for clarity. A cloud of cold atoms is prepared in the lower MOT chamber. The atoms are accelerated upwards through a hollow channel ranging to the science chamber, where they are captured inside the cavity. The cavity length is adjusted macroscopically by means of an inchworm motor. A three-stage system isolates the cavity from external vibrations.

3.5.2. Upper Chamber

The upper chamber holds the high-finesse cavity. Here, a 55 l/s ion-getter pump (Mecca) is used to maintain the ultra-high vacuum. The chamber has the form of an octagon. Four side-facets are equipped with viewports, two on the cavity axis and two perpendicular to the axis. Another one of the side-facets is used to maintain the vacuum. It holds the ion-getter pump as well as a pressure gauge. Furthermore, a titan sublimation pump is installed which can be temporarily flashed to further reduce the pressure. Another side facet has a valve installed

permitting the connection to an external pump as it was used during the initial setup. The two remaining facets have feed-throughs installed, used to connect the inch-worm motor and the piezo, respectively. The vacuum chamber is held by 4 feet. They are mechanically isolated to the optical table via rubber discs. Initially, it was planned to have an optical breadboard directly attached to the upper chamber, however this introduced significant vibrations, so that the breadboard used for the excitation and detection is now mounted fully independently to the vacuum chamber.

3.5.3. Vibration Isolation

The cavity in the present setup is very sensitive to any mechanical vibration or acoustic noise. Vibrations of the mirrors of less than one picometer are already sufficient to change the resonance frequency of the high-finesse cavity. Thus, this substantially disturbs the resonant light field as well as the result of the experimental measurement. Hence, it is mandatory to efficiently decouple the cavity from any noise source. Since the high-finesse optical resonator is embedded in vacuum, acoustic noise cannot be transferred directly to the cavity, causing a need for good mechanical noise isolation. Besides the usual, external damping provided by floating optical tables, our system features an additional three stage vibration isolation system, which is embedded directly in the vacuum chamber and is depicted in Figure 3.14. Each stage is fabricated as a massive copper cylinder with weights between one and two kilograms. The copper is galvanically gold plated to avoid oxidation, which would increase outgassing. The

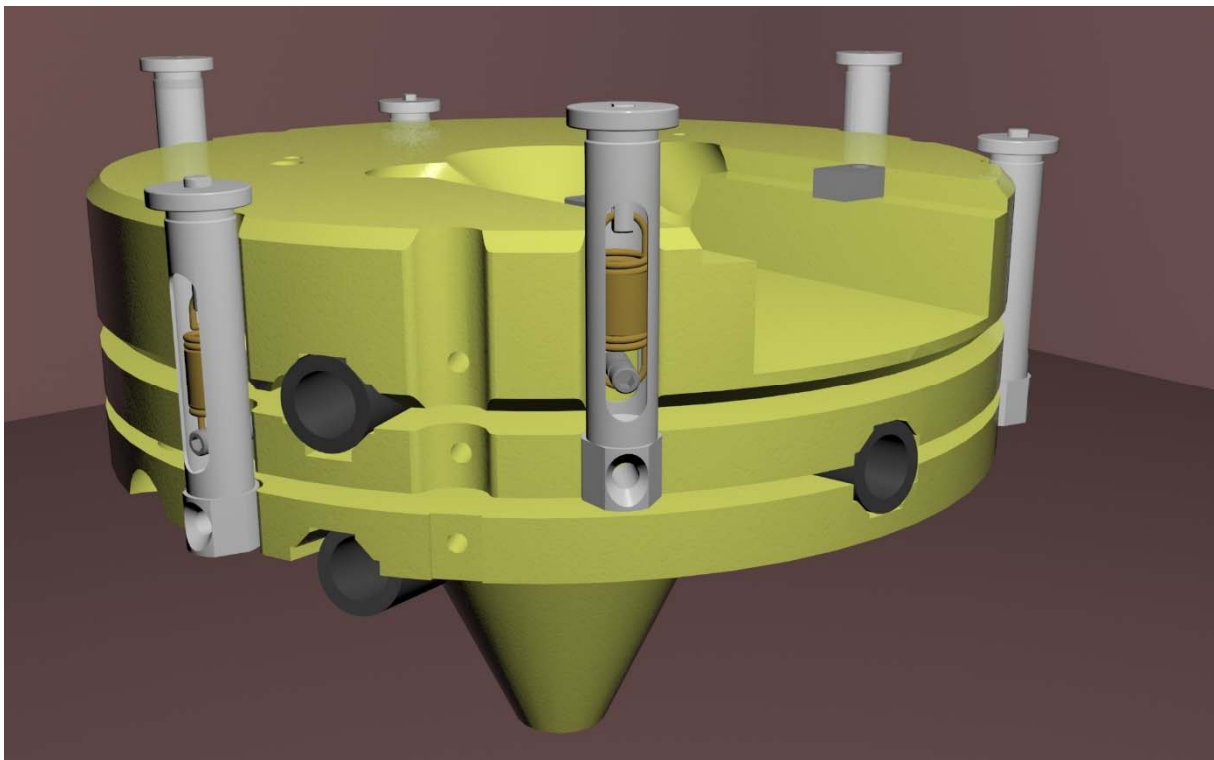


Figure 3.14: Schematic drawing of the vibration isolation system. The system consists of three layers of copper discs. The layers are connected to the respective adjacent ones via metal springs. Kalrez tubes are added in addition to damp the remanent oscillatory behavior. The lowest layer sits on the vacuum chamber and is solely connected by the Kalrez tubes. The cavity holder along with the inch worm motor is mounted in the open-space on the upper layer.

first stage sits directly on three elastic tubes made of Kalrez⁶ connecting it to the main vacuum chamber. The other two stages are supported by metal springs in addition to the elastic tubes. This reduces the mechanical vibration frequency of the cavity from 50-100 Hz in the elastic-tubes-only case to 10 Hz and provides damping due to the Kalrez. A detailed analysis can be found elsewhere [131].

3.6. Excitation and Detection

In the previous section the main building blocks of the setup were introduced. Here we will focus on how they are merged. It will be shown how the different laser beams are brought to the cavity and how the detection works. All the optical components needed are mounted on a breadboard surrounding the vacuum chamber at the level of the optical cavity. A detailed sketch of this excitation and detection system can be found in Figure 3.15. Both, the probe beam as well as the trap beam, need to be coupled into the cavity. Since the probe power required is very weak, a 99/1 beam-splitter is used to overlap the two beams leaving the intensity of the trap almost unchanged while the probe beam is substantially attenuated. Before they are overlapped each beam is intensity-stabilized separately by sending a small portion of the light to a photodiode. A PID controller then adjusts the RF amplitude of the respective AOM-driver to compensate for any drifts. After the stabilization, an additional set of neutral density filters⁷ (ND) is used to attenuate the probe beam, bringing it to the single-photon level. A quarter waveplate changes the polarization from linear to circular, which is needed to drive the closed cycling transition. Moreover, the dipole trap beam features an electro-optic phase-modulator (EOPM) generating sidebands at 15 MHz. These sidebands are necessary for the Pound-Drever-Hall lock of the cavity. The error-signal for the lock is derived from the light back-reflected by the high-finesse cavity. Because this back-reflected light passed the quarter waveplate twice, it can be easily extracted by a PBS and sent to an avalanche photo-detector. An electro-optic amplitude-modulator (EOAM) permits to keep the intensity level at the detector reasonably stable even when the initial dipole trap intensity varies significantly. The concept of the cavity-lock will be explained in Section 3.7 and 4.6. The actual incoupling into the cavity is very crucial and requires mode matching of the beams in direction, size and divergence with the cavity. Hence, an adjustable beam expander system with a $f = 50$ cm lens is used.

A small fraction of the repump light (typically a few μW) is coupled from the side through the cavity. It serves as repumper for the atoms in the intracavity dipole trap. The light is aligned perpendicular to the cavity axis and focused between the mirrors via a lens. A concave mirror retroreflects the beam on the other side of the cavity and sends it back to the fiber coupler. A quarter waveplate before the mirror rotates the linear polarization by 90 degree, forming a

⁶ Kalrez was chosen due to its better out-gassing properties than the most commonly used ultra-high-vacuum elastomer Viton.

⁷ Depending on the desired experiment a single or a combination of two ND filters is used. Via heterodyne detection their attenuation rates have been measured: OD4 intensity attenuation: $\sim 1/490$; OD2 intensity attenuation: $\sim 1/19.3$; combined intensity attenuation $\sim 1/9460$

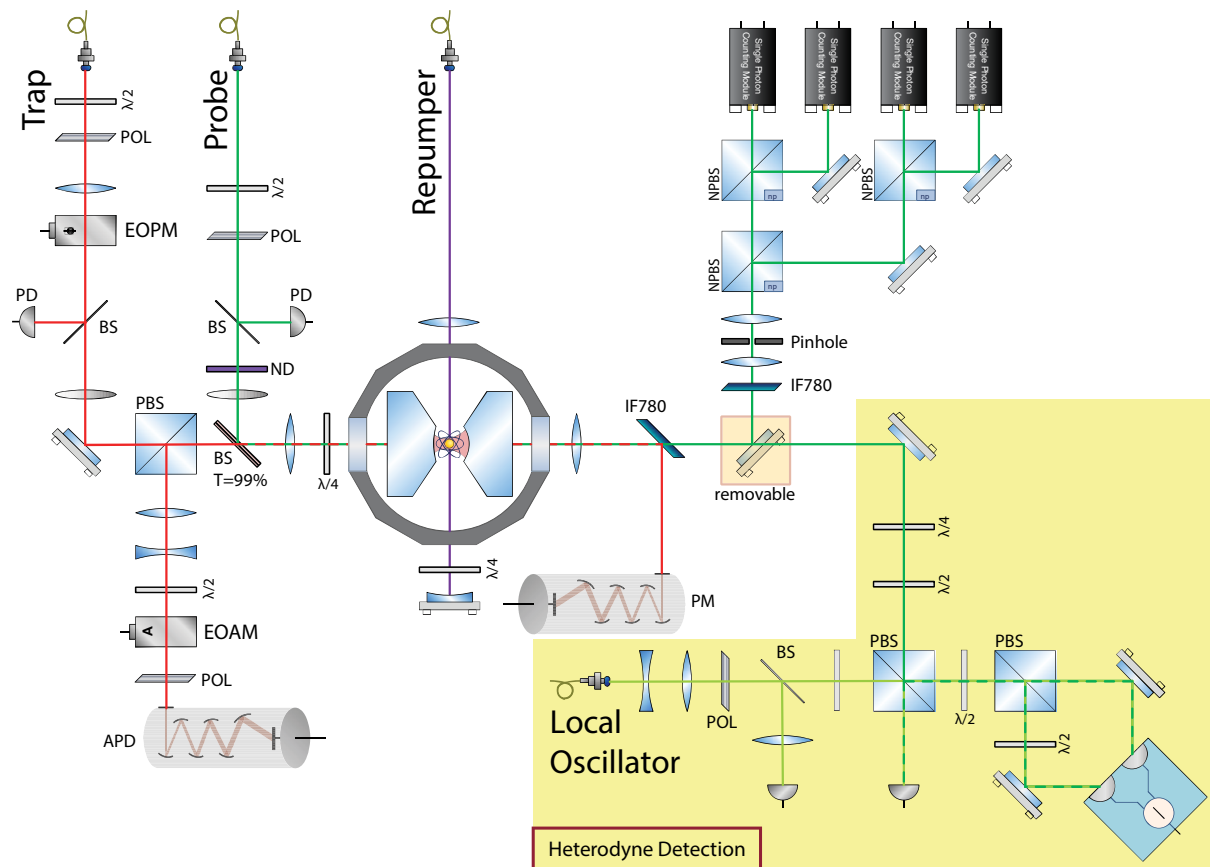


Figure 3.15: Optical setup used for excitation and detection around the high-finesse optical cavity. On the left side the two beams which are coupled into the cavity are depicted. These are the trap beam at 785 nm and the probe beam at 780 nm. The polarization of both beams is adjusted via a half waveplate and a polarizer. A part of the light of each beam is used to intensity-stabilize it and sent to a photodiode (PD) via a beam splitter (BS). Lenses along the beam path permit to match the modes of the beam to the mode of the cavity. Both beams are overlapped at a 99/1 beam splitter, which leaves the intensity of the trap beam almost unchanged. An additional set of neutral density filters (ND) are used to attenuate the probe beam, bringing it to the single-photon level. Afterwards, a quarter waveplate changes the polarization of both beams to circular. Before the beams are overlapped, sidebands at 15 MHz are modulated onto the trap beam via an electro-optic phase-modulator (EOPM). The sidebands are used to generate an error signal for monitoring the cavity length as the trap beam is reflected from the cavity. This signal is sent via a PBS to an avalanche photodiode (APD). An electro-optic amplitude-modulator (EOAM) permits to compensate for changes in the amplitude. The light which is transmitted through the cavity is spectrally separated by an interference filter at 780nm (IF780). It reflects everything but the probe beam. This way the trap beam is sent to a photomultiplier tube (PM). A removable mirror permits to choose whether the remaining probe beam is either sent to the heterodyne detection or to the single photon counting modules (SPCMs). The heterodyne detection (yellow background) will be explained later (cf. Chapter 5.6). To remove any residual light, the beam sent to the SPCMs is filtered by a second interference filter at 780nm (IF780). The beam is focused through a pinhole to clean the mode before the signal is equally distributed by passing through a pair of non-polarizing beam-cubes (NPBS) among the four SPCMs. Perpendicular to the cavity axis the repump beam is sent to the cavity. A lens focuses the beam to the cavity center and a concave mirror on the other side retroreflects the beam. A legend of the symbols is found in Appendix 10.8.

standing wave pattern in polarization not in intensity, called “lin-perp-lin” configuration. Clipping of the beam on the cavity mirrors needs to be avoided as it contributes to stray light on the sensitive photodiodes used in the detection. It is minimized by measuring the power of the repumper after its first and second passage through the cavity.

On the detection side, the probe and the trap beam are separated from each other by a narrow-band laser line filter by Semrock (LL01-780-12.5), which has a transmission rate for the probe

beam of $T_{\text{det,filter}} = 0.95$. A photo multiplier detects the intensity of the trap beam, which is only used as a reference. The detection of the probe beam is done either by an array of single-photon counting modules (SPCM) or by a heterodyne setup. The latter system requires an additional local oscillator and will be explained in detail in Chapter 5.6. Four SPCMs from PerkinElmer® (now Excelitas Technologies) AQR-14 are employed. They offer a detection efficiency of about $\eta_{\text{det}} = 0.55$ and have typical dark-count rates of below 100 counts per second. Reminiscent light from the trap beam is filtered by a second laser line filter (Semrock LL01-780-12.5) before it is directed to the SPCMs. In addition, a pinhole is employed to clean the mode. The light is distributed equally by passing through a set of non-polarizing beam-cubes onto the four detectors. In total the detection efficiency for the SPCM setup is given by $\eta_{\text{SPCM}} = \eta_{\text{det}} \cdot T_{\text{det,filter}}^2 = 0.5$. The four SPCMs permit to record correlations in the photon stream up to fourth order. The data is recorded and processed by a specially designed field-programmable gate array as it is described in detail in Section 4.4.

3.7. Cavity Lock

Building a stable cavity poses one of the key challenges in the current setup. Besides a good passive, mechanical vibration isolation, an active stabilization is needed. This permits to reduce fluctuations of the cavity length well below one picometre to around some hundred femtometers, which is equivalent to $1/500^{\text{th}}$ of the rubidium atom's diameter!

In a conventional locking scheme as it is employed in cavity QED systems, the high-finesse cavity is stabilized to the laser by employing the Pound-Drever-Hall technique [115]. The stabilization laser itself is then usually stabilized with respect to a narrow linewidth transfer cavity [101] as it has been done in the forerunner experiment. However, since this transfer cavity also needs to be stabilized, the complexity can grow substantially. This problem can be overcome by locking the laser to another high-precision, stable frequency reference. In our group frequency combs are now-a-days employed as a reference [120], [121]. In the beginning a locking scheme of this type, i.e. high-finesse cavity locked to the stabilization laser locked to the frequency comb, has also been used with this setup [81]. Despite of having a very stable reference, this locking scheme is not able to improve the quality of the cavity lock whose bottleneck is the finite bandwidth of the piezo tube, which is responsible to fine-tune the cavity length. Its maximum actuation frequency has been measured to be below 10kHz [132]. This bandwidth limitation prevents the piezo from compensating high frequency fluctuation of the stabilizing laser and thus leads to fluctuations of its intracavity power. In our case the stabilization laser is also used as dipole trap which in turn causes fluctuations of the ac-Stark shift as well as parametric heating of the captured atoms [133]. This can be solved by slightly modifying the locking chain as depicted in Figure 3.16. Now the stabilization laser is locked to the high-finesse cavity, which in turn is stabilized to the frequency-beat of the stabilization laser with the frequency comb.

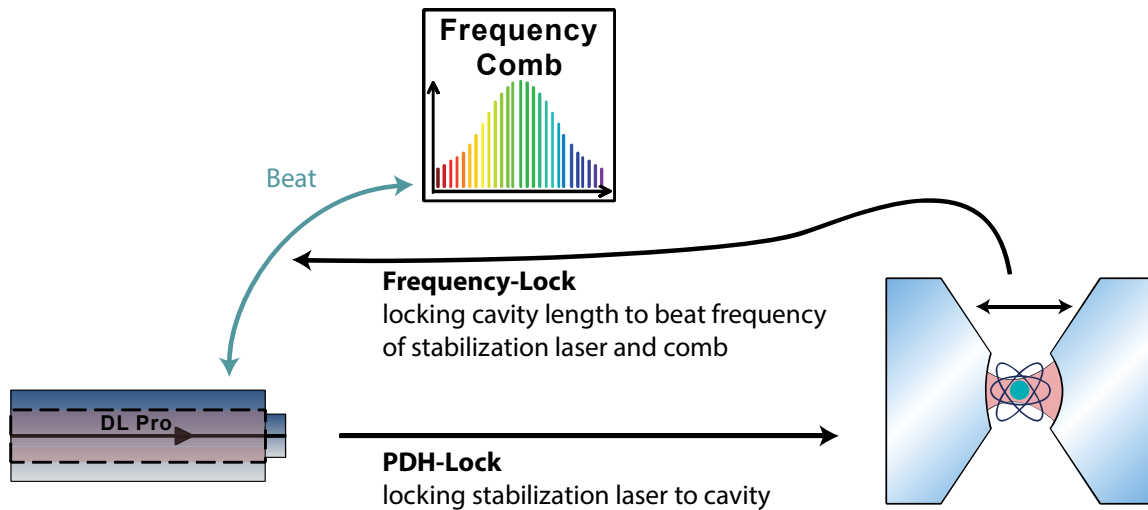


Figure 3.16: Overview of the locking scheme employed in the experimental setup. The stabilizing laser is frequency locked onto the cavity by employing the Pound-Drever-Hall technique. The length of the cavity itself is controlled by an error signal derived from the beat frequency of the stabilizing laser and the frequency comb, which serves as a reference.

Drifts in the cavity length are accurately detected by a PDH-locking scheme. The dipole trap light also serves as stabilization light. As it has been shown in Figure 3.15, an EOPM generates sidebands by means of a local oscillator at 15 MHz on the light which is sent to the cavity. An avalanche photodiode detects the back-reflected light from the cavity. The sidebands are demodulated by using the same local oscillator and are used to derive an error-signal [115]. This error-signal is directly passed to the FALC controller of the trap laser. The bandwidth of this lock is around 1 MHz enabling the laser to accurately follow the cavity length and hence guaranteeing low fluctuations of the intracavity dipole trap intensity. The length of the cavity on the other hand is stabilized by analyzing the beat frequency of the trap laser with the frequency comb. This beat-detection is done by an FPGA and will be described in detail in Section 4.6. Whereas the stability of the cavity significantly benefits from this locking scheme it also poses the disadvantage that the failing of one lock will necessarily unlatch the other.

3.8. Experimental Sequence

In this chapter the experimental sequence will be explained. The hardware aspects will be discussed subsequently in the following chapter. Every experimental run consists of five major steps and is consecutively repeated. Before a scan is started, a database entry is written containing all parameters and which is linked to the file recorded by the SPCMs or the heterodyne measurement.

3.8.1. Preparation & Magneto-Optical Trap (MOT)

In the beginning, a current of 3 A is sent for one to two seconds through the rubidium dispensers. They are aligned in such a way that atoms are predominantly emitted towards the center of the MOT, where it creates a well localized background pressure of rubidium atoms. At the same time, a current of 4A flows through the magnetic field coils at the lower vacuum

chamber, which creates a magnetic field gradient of 10 G/cm. The upper and lower MOT beams, which are both red-detuned by 16 MHz from the $5S_{1/2}F = 3 \rightarrow 5P_{3/2}F' = 4$ ^{85}Rb resonance are turned on. Each of the six MOT beams has a power of 10 mW. In addition, a weak repump beam of 3 mW, which is on resonance with the $5S_{1/2}F = 2 \rightarrow 5P_{3/2}F' = 3$ transition is switched on. Together this activates the MOT. In the meantime, the probe beam is brought on resonance with the high-finesse cavity and the trap beam is adjusted to a low light level, which only forms a weak intracavity potential valley for the atoms while still being sufficiently intense to provide a good signal for the laser-cavity lock.

3.8.2. Molasses & Atomic Fountain

After loading the MOT for 2 seconds, the detuning of the upper and lower MOT beams is increased to 42 MHz (red detuning) within 50 ms while also lowering their power to 1 mW per beam. The magnetic coils are turned off forming an optical molasses. After 3 ms of additional molasses cooling, a temperature of about 4 μK is achieved [81]. Afterwards, the cloud of cold atoms is accelerated upwards. This is accomplished by detuning only the upper MOT beams by 3 MHz⁸ (red detuning) from the lower ones within 5 ms. During this step the intensity of the MOT beams is increased to 3 mW. The cloud of atoms now performs a 23 cm long ballistic flight with the turning point at the center of the cavity. During the time of flight the MOT beams are turned off and the probe power is increased to be more sensitive to the passage of atoms.

3.8.3. Catching the Atom

As the probe beam is on resonance with the empty cavity resonance, a drop in its transmission heralds the presence of an atom inside the cavity. The intracavity dipole trap is immediately switched to a high value, confining the atom. The probe power is reduced in order to avoid excessive heating. A detailed description can be found elsewhere [77]. Some experiments are measured with passing atoms. In this case, this step as well as the following, will not be executed. In addition, frequencies of the probe beam away from the empty cavity resonance are chosen in some cases.

3.8.4. Experimental Data-Acquisition

Now the actual experiment starts. The data-acquisition is activated, which is either the photon counting measurement or the heterodyne detection. While the data-acquisition takes place, the frequency as well as the intensity of the probe beam – among others – can be altered as it is done e.g. for switching measurements (see Section 6.7). Additionally, the intensity of the trapping laser can either be controlled manually or by a feedback-routine (see Sections 4.4.2, 5.5 or 6.6). In general, this step is executed until the atom is lost.

⁸ The actual detuning depends on the experimental goal. A high detuning results in higher acceleration of the atoms, causing them to pass through the cavity.

3.8.5. Cleaning-Up

At the end of each scan, all parameters are restored to their initial values. Values which change from run to run are updated and the sequence starts all-over.

3.9. Experimental Control

To conclude the section on the experimental setup, a quick overview of the hardware system controlling the experiment will be given (see Figure 3.17). In principle, the whole system can be sub-divided into a control section and a data-acquisition section. The heart of the control section is a LabVIEW (short for Laboratory Virtual Instrumentation Engineering Workbench) program running our experimental sequence (cf. Section 3.8). It accesses an ADwin-Pro II box which is used to interface with the experiment via digital and analog outputs. In addition, radio frequencies are generated by a custom-made, FPGA-based Direct-Digital-Synthesis (DDS) box [134] as well as four Rohde&Schwarz signal generators. The set-points of all values are stored in a PostgreSQL (Structured Query Language) database. Synchronization of parameters as well as hand-shaking is achieved by an interface to a LabVIEW real-time system. The cavity-lock has been implemented to a FlexRIO FPGA (see Section 4.6), which is installed into a PXIexpress-rack (PCI eXtensions for Instrumentation). PXI systems are based on regular computer but offer improvements for laboratory usage. This computer also monitors the frequencies of a second, microcontroller-based DDS box. The generated frequencies are fixed and also written into the database. A second PXI-chassis holds the acquisition system. Its main component is a National Instruments controller (NI PXIe-8133). The data is recorded by two separate FPGAs (see Chapter 4). One is used for photon counting and features a four channel time digitizer with 1 ns resolution (see Section 4.4) while the other one is designed for heterodyne measurements (see Section 4.5). Furthermore, a third FPGA monitors the intensity level of the transmitted trap beam in time and frequency space (see Section 4.7). The actual data is stored on a 12 terabyte large RAID array (NI HDD-8265), which is indexed by the database. Hand-shaking and synchronization are assured by the real-time system. In order to evaluate the data, access to the raid-array as well as to the database is necessary.

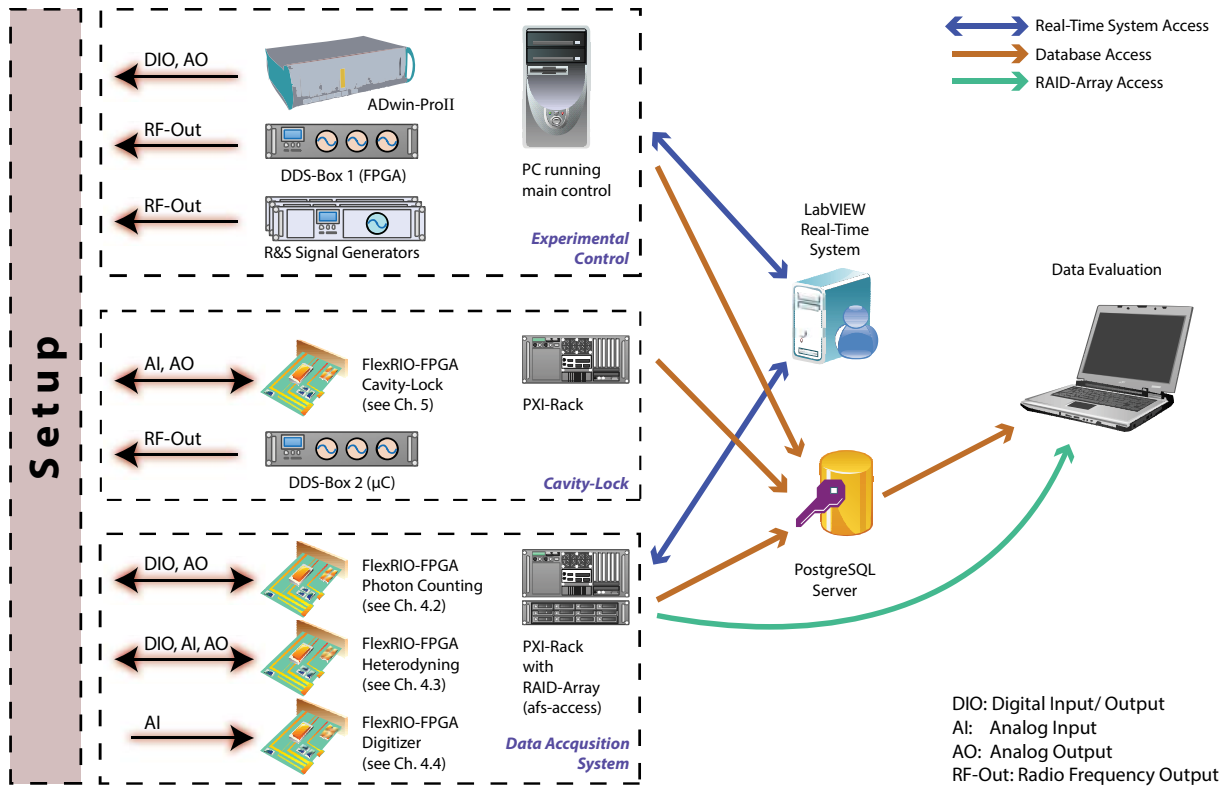


Figure 3.17: Overview of the experimental control system. Three main components are used to control and interface with the experiment: A standard PC, which is running the main control program, as well as two PXI-Racks, which both possess an internal controller. All of these components send their parameters in the beginning of each run to a PostgreSQL server, which in turn saves it into an SQL database. A LabVIEW Real-Time System is responsible to share data among the different components and to synchronize them. The PC running the main control program directly communicates with an ADwin-ProII box which is responsible for setting the major experimental parameters via digital and analog outputs. An FPGA based DDS-Box [134] as well as four Rohde & Schwarz signal generators are attached as well. They provide radio frequencies (RF) to the setup. The first PXIexpress rack with an internal controller running Microsoft Windows features a FlexRIO FPGA stabilizing the cavity length (see Section 4.6) via analog in- and outputs as well as a microcontroller-based (μC) DDS-Box providing additional radio frequency to the setup (RF). The experimental raw-data is stored by the data acquisition system which constitutes of the second PXIexpress rack. This system, in addition, has an external RAID-Array connected, permitting to quickly save large amounts of data in real-time. The data is gathered by three FlexRIO FPGAs. They are mainly responsible to collect and evaluate the data of the SPCMs (see Section 4.4), to save and interpret the heterodyne data (see Section 4.5) as well as to monitor different power levels and frequencies in the setup (see Section 4.7). The data evaluation is done by combining the data stored in the RAID-array with the respective parameters stored in the SQL database.

4. Field Programmable Gate Arrays (FPGAs)

The control of experiments dealing with single atoms requires fast electronics, which are able to react within typical timescales of a microsecond or even less. In the forerunner experiment specialized microprocessors running on a real-time operating system (OS) have been employed to fulfill these demands. However, in the past years a new generation of integrated circuits (ICs) gained more and more popularity. These devices are called Field Programmable Gate Arrays (FPGAs) and are designed to be (re)configured after manufacturing; once they are programmed with a custom hardware design they are highly specialized. This, in conjunction with their inherent parallelism – meaning that unlike, e.g. in a central processing unit (CPU), all instructions are executed in parallel – allows for fast and deterministic timing during execution and hence render them a universal and omni-potential tool in science and industry. Table 4.1 summarizes the main aspects when it comes to choosing a processing unit.

Aspect \ Device	CPU central processing unit (e.g. Intel Core i7)	GPU graphics processing unit (e.g. NVIDIA Tesla)	FPGA field programmable gate array (e.g. Xilinx Virtex-5)
Computational Performance	👎	👍👍	👍👍
Parallel Execution	👎👎	👍	👍👍
General Purpose	👍👍	👍	👎👎
Deterministic Timing	👎👎	👎👎	👍👍
Low Complexity of Code	👍👍	👍	👎
Turn-around-time	👍👍	👍	👎
Cost	👍👍	👍	👎
Best suited application	General purpose	Complex data evaluation	Fast and deterministic control

Table 4.1: Rating of different devices with respect to various aspects under consideration. The applicability is rated from favorable 👍👍 (green) over neutral (grey) to disadvantageous 👎👎 (red).

Three different categories of devices are listed. Besides FPGAs these include the well-known Central Processing Units (CPU). They are capable of executing very rapidly a fixed set of instructions as specified by the program which is currently executed. They are suited for all types of applications but lack both, the capability for parallel execution as well as deterministic timing. The high demands posed by computer graphics led to the development of Graphics Processing Units (GPUs). They are targeted to efficiently perform matrix and vector operations facilitated by their internal parallel architecture. In recent years also science discovered their

vast performance and today they are commonly used in scientific computation. The evaluation of the heterodyne-data (cf. Chapter 5.6) in this thesis was also entirely performed by GPUs as this reduces the computational time by more than a factor of 25. The high amount of tasks which are executed in parallel is accompanied by an increased complexity during the programming phase. As it is the case for CPUs, GPUs also do not offer deterministic timing during execution which remains the home turf of FPGAs.

In total FPGAs are ideally suited for the fast control of complex systems, which is mainly attributable to their deterministic timing and parallel execution of “code”, rendering them highly reliable. When programmed for a special task their computational performance can compete with GPUs and significantly surpasses the one of CPUs. However, these advantages are realized at the expense of a high complexity of the code and long compilation and debug times. The special architecture of FPGAs even sets an upper limit to the size of the “program-code” and thus prevents complex projects to be solely realized in FPGAs⁹.

4.1. Deployment of FPGAs in the Lab

Experimental setups similar to the one studied in this thesis are facing three major challenges when it comes to building the electronic control system. First of all, the very specific control environment, which is required by the setup, poses the need for highly specialized devices, which are tailored to the respective task. Secondly, most of the control algorithms are running in real-time and hence require fast processing of the signal. In order not to affect the experimental system, the delay between receiving an input signal and returning an output needs to be lower than the respective timescale, which is usually in microsecond range. Thirdly, the multitude of tasks which is usually solved by dedicated, specialized electronic devices along with their interdependency, significantly increases the complexity of cables and interconnects. A picture of some of the control electronics of the forerunner system are shown in Figure 4.1. Many of these controls are now integrated into a single FPGA as depicted in Figure 4.2. The complexity of cabling is a typical example for non-FPGA control electronics. FPGAs are an ideal tool to overcome the above-mentioned challenges. They can be tailored to a very specific application, their processing power is unparalleled and execution is fully deterministic in time. The customization in addition permits to integrate multiple devices into one chip and hence reduces the need for physical cabling.

⁹ To overcome the limitations of FPGAs, it is quite common to use a small fraction of the available FPGA area to include a RISC microprocessor (Reduced Instruction Set Computer) making them an omnipotent tool. Xilinx new Zynq family even possesses a fixed Cortex-A9-processor.

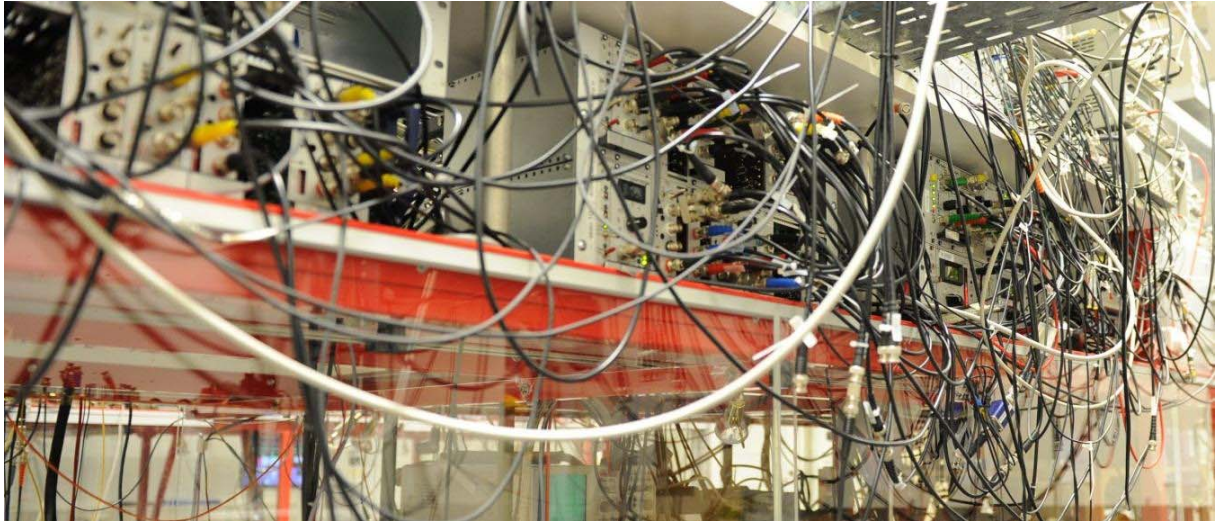


Figure 4.1: Typical cabling in experimental control systems. Cascaded specialized devices are employed to achieve the desired operation; this significantly increases the number of required cables.



Figure 4.2: Integration of FPGAs into experimental setup. The possibility to code hardware functions directly into an FPGA reduces number of devices and required interconnects. The FPGAs in the PXI-express rack are shown on the left side. Cables lead to breakout boxes where the individual signals are picked up.

4.2. FPGAs under the Hood

As already mentioned, FPGAs were introduced to fulfill the demand of time-critical operations in the setup. In this paragraph we will have a quick look in what these devices are made of. The basic architectural design of an FPGA is depicted in Figure 4.3 a). It can be divided into four basic building blocks. The communication with the “outside world” is accomplished by the input and output pads. They convert incoming signals to voltage requirements of the FPGA, so that they can be routed through the FPGA. In addition, by buffering the signal, they also safeguard the FPGA from external voltage peaks. These pads on the other hand can also be configured to buffer the outgoing signals to match the specific voltage and impedance. Programmable logic blocks are the key component and perform the actual computation. Routing channels connect the logic blocks among each other as well as with the surrounding I/O pads. Programmable interconnects act as a switching-matrix (cf. Figure 4.3 b)) and permit to steer the signal to desired part of the FPGA.

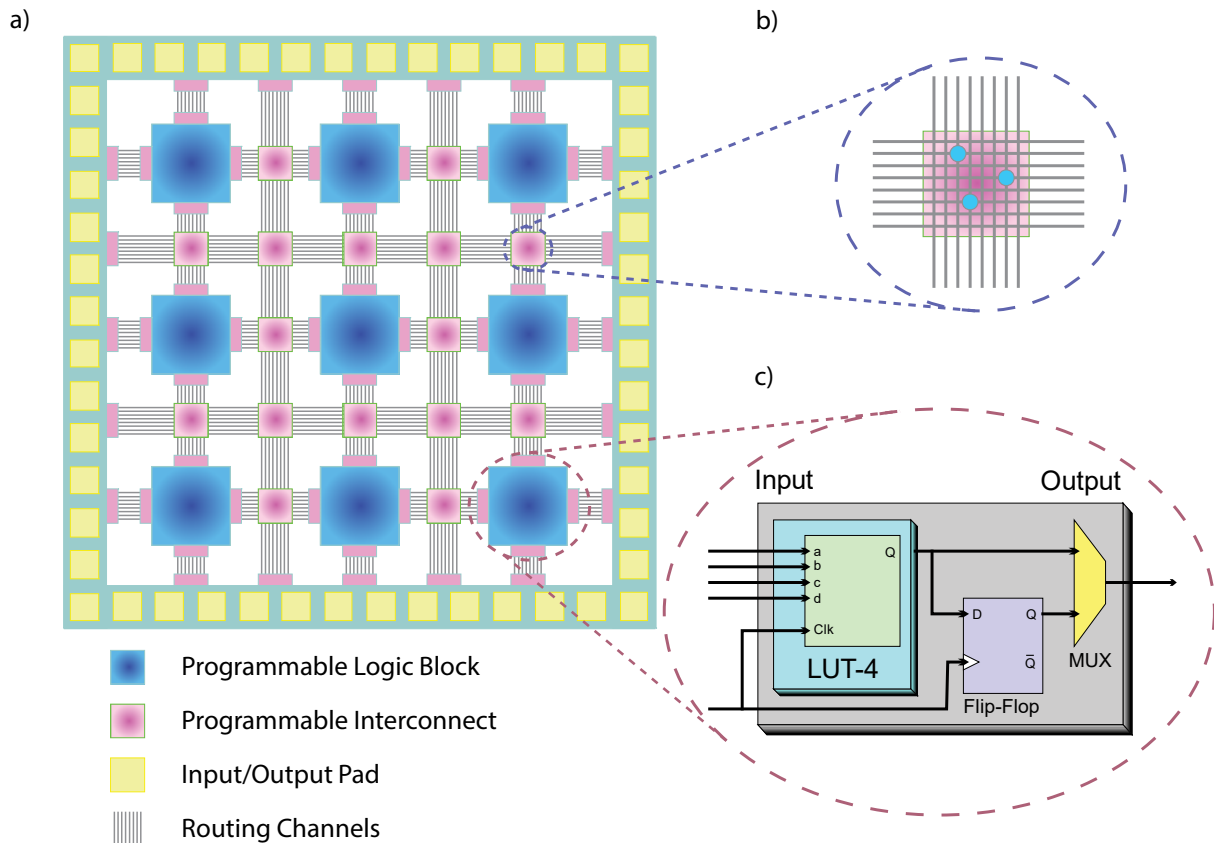


Figure 4.3: Overview of the architectural design of an FPGA. a) General, simplified overview of the most important structural elements of an FPGA. The actual logic is stored in the logic blocks. They are connected via routing channels, which are interconnected in the programmable interconnects. In- and output pads enable the communication of the FPGA with external signals. b) The programmable interconnects are responsible for distributing the signal by connecting different routing channels. c) Schematic, simple overview of a programmable logic block. The 4-bit LUT outputs a signal which is passed to a flip-flop, to make it stable during the clock cycle. A multiplexer (MUX) in the end determines whether the synchronous signal from the flip-flop or the asynchronous signal from the LUT is directly output.

The logic blocks themselves consist – in a very basic scheme – of a look-up table (LUT), a so-called gated D-latch¹⁰ (flip-flop) and a multiplexer (MUX) (cf. Figure 4.3 c)). Every clock-cycle the LUT outputs, based on its four input bits, a single bit which is passed to a flip-flop gated by the same clock. The flip-flop can be seen as a 1-bit memory element and produces a so-called registered output which is synchronous to the applied clock and can be used for further processing in the next cycle. A multiplexer at the end also permits to output the unregistered, asynchronous output directly from the LUT.

From the upper illustration the two main limitations of an FPGA become visible. As logic blocks are assigned to one dedicated operation in the “code”, the maximal complexity of a project is given by the number of available logic blocks in the FPGA. An increased number of logic blocks usually goes hand in hand with an increase in the physical dimensions of the chip. Within some limits the clock-rate of the FPGA can be chosen freely and can even vary across different sections of the FPGA. The maximum clock-rate for a specific section depends on the

¹⁰ The D-latch name refers to the fact that the flip-flop delays the data by one clock cycle. Besides the data input, it hence requires a synchronous clock signal.

required time for the signal to be routed through this part of the FPGA; here, the signal path with the longest delay sets the limit. The working principle of a logic block can be illustrated in an example which consists of a simple combination of three Boolean operators. Figure 4.4 a) shows the function to be embedded into the FPGA. In order to do so a LUT needs to be created which holds the values stated in part b). In principle, a LUT is comparable to a 16-bit memory element.

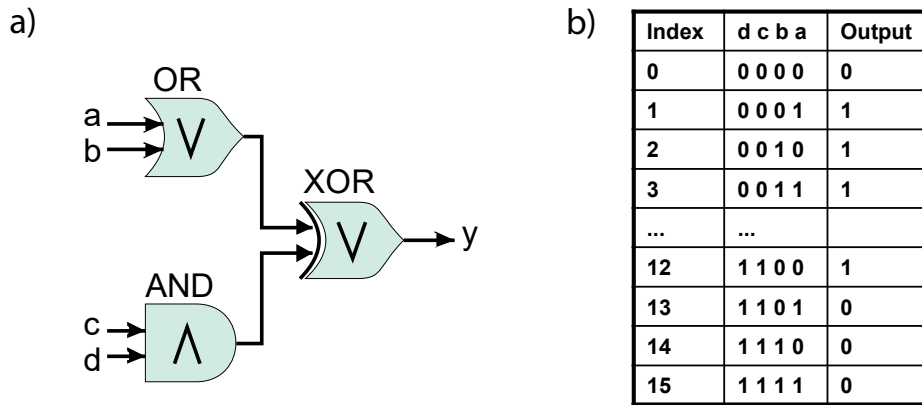


Figure 4.4: Transformation of a set of three Boolean operators to a 4-bit LUT. a) Representation of the three Boolean operators, which are acting on the four digital input signals to produce one digital output. b) Equivalent of the depicted Boolean operators in form of a look-up table (LUT). The 16 different input combinations all result in a specific output.

Modern FPGAs have a far more complex structure and also feature additional memory and digital signal processing blocks. More information can be found e.g. in [135], [136]. It shall be mentioned that the following chapters are based on Xilinx FPGAs, which are almost exclusively used in our experiment.

4.3. Intellectual Property (Programming/Coding)

The coding of an FPGA is essentially different to writing a program which runs on a regular CPU. A CPU already possesses a predefined design and features a fixed set of instructions. Programming thus does not involve altering its “*hardware*”. It only loads a code called “*Software*” into the execution stack of the processor which is then executed. FPGAs, however, neither have fixed set of instructions nor a predefined hardware design. Coding in that respect means to actually develop a piece of hardware. It can hence be seen as a way of “virtually soldering” multiple functional blocks. The code is now referred to as “intellectual property” or IP in short. Creating IP can be achieved in different ways. In this thesis two different “programming-languages” are employed.

4.3.1. Very High Speed Integrated Circuit Hardware Description Language

```

library ieee;
use ieee.std_logic_1164.all;
use ieee.numeric_std.all;

entity SimpleAdder is
  port (
    clk      : in std_logic;
    aReset   : in std_logic;
    cPortA   : in std_logic_vector(15 downto 0);
    cPortB   : in std_logic_vector(15 downto 0);
    cAddOut  : out std_logic_vector(15 downto 0) := x"0000"
  );
end SimpleAdder;

architecture rtl of SimpleAdder is
begin
  process(aReset, clk) begin
    if(aReset = '1') then
      cAddOut <= x"0000";
    elsif rising_edge(clk) then
      cAddOut <= signed(cPortA) + signed(cPortB);
    end if;
  end process;
end rtl;

```

Figure 4.5: Example of a simple VHDL code. The code simply adds two numbers, provided by the signal lines “*cPortA*” and “*cPortB*”. The clock signal is provided under the name “*clk*”.

They are provided through the signal lines “*cPortA*” and “*cPortB*”. In addition, a synchronous clocking signal (“*clk*”) and an asynchronous reset signal (“*aReset*”) are required. The clock signal determines the rate at which the addition-process is carried out while the reset is required during the initialization phase of the FPGA. The libraries which are loaded in the beginning hold the actual code in order to perform the addition itself. It is noteworthy to mention that all processes defined in the VHDL code will be executed at the same time. This necessitates special attention on the synchronization of processes and poses constraints on the data-exchange between them.

4.3.2. National Instruments: LabVIEW FPGA

A far more intuitive way of programming FPGAs is implemented by National Instruments. Their LabVIEW FPGA module provides an easy way of coding these devices. As an example the code of an edge-counter is presented in Figure 4.6. A loop, which is running at 100 MHz, compares the signal of a physical pin of the FPGA to its value in the previous iteration. If they differ, an integer-valued signal is incremented. It is noteworthy to mention that the clock rate of a so-called singled cycled timed loop (SCTL) is the rate at which the whole loop is executed – not just a single component in it. The code snippet visualizes that the dataflow programming structure of LabVIEW is to a certain extend analogous to the design of an FPGA and hence provides an easy way to build custom-made IP. Besides its intuitive layout, LabVIEW FPGA also handles the communication over the PCI-bus internally and ships with IP to address DDR (double data-rate) memory. This noticeably facilitates the communication and data-exchange with a host PC. Besides its high level of abstraction, LabVIEW FPGA still allows to seamlessly include custom-made VHDL code. This so-called component-level IP (CLIP) can be used to

Very High Speed Integrated Circuit Hardware Description Language (VHDL) is a low-level language to program FPGAs. It permits to generate fast code, however, requires complex programming. It furthermore offers access to built-in functions, called primitives, like they are used in Section 4.4.1. It is not the intention to give an introduction to VHDL, nonetheless it is instructive to present a short code-snippet. The code presented in Figure 4.5 adds two numbers. They are provided through the

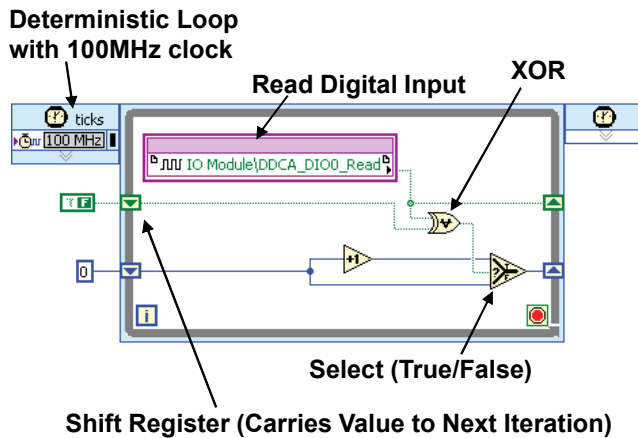


Figure 4.6: Overview of a LabVIEW FPGA code. The loop is deterministically executed at a clock-rate of 100MHz. A signal from one of the FPGA pins is read and compared to its value from the previous execution stored via the shift register (green path). In case the signal has changed (XOR) an integer counter is incremented (blue path)

implement functions coded in VHDL and in addition gives direct access to the pins of the FPGA (socketed CLIP). These features are mandatory for building an FPGA based photon counter, which is presented in the following section.

When the code is executed, LabVIEW FPGA internally transcodes the project into VHDL and then launches the Xilinx compiler. Compilation times vary from a few minutes up to 8 hours¹¹ depending on the complexity of the code. The long compilation times are an inherent disadvantage of programming FPGAs. They are caused by the hardware mapping process and cannot be overcome.

4.4. Deployment 1: Signal Processing in Photon Counters

Experiments with single atoms require working with extremely low light intensities. This necessitates the use of devices capable to detect single photons. These devices, called Single Photon Counting Modules (SPCM), are based on avalanche photodiodes and emit a digital electronic pulse (see Figure 4.7) whenever a single photon is detected. The high reverse-voltage applied to the photodiode is sufficiently high to enable a single photon to trigger the avalanche process making the diode conducting. Since this avalanche process does not stop automatically and would lead to the immediate destruction of the diode, a gating electronic needs to quickly interrupt this process. We use four AQR-14 fabricated by PerkinElmer®. The rising edge of the pulse reflects the arrival time of the photon with an accuracy of 500 ps¹² [137]. After a detection of a photon the respective detector is blind for about 30-40 ns.

Previous experiments used the FASTcomtec P7888 time-digitizer to record the arrival time of the digital pulses with 1 ns resolution. These devices, however, neither permit to perform real-time evaluation nor are they scalable and only feature 2 inputs at the given resolution. For our setup we set out to build a device which features real-time processing, at least 4 channels with 1 ns resolution, easy integration into our control system and an easy and useful visualization of the experimental data. We realized this ambitious goal by employing a National Instruments 7954R FlexRIO FPGA board. In addition, a NI 6581 digital adapter module was installed. Its main purpose is to buffer the digital channels and by doing so, to protect the FPGA pins against

¹¹ These values were achieved on an Intel Xeon W3565 with 6GB of memory running Windows 7 64bit.

¹² PerkinElmer initially stated an accuracy of < 350ps this value, however, is removed in current spec-sheets. Measurements [137] indicate a value of 500 ps.

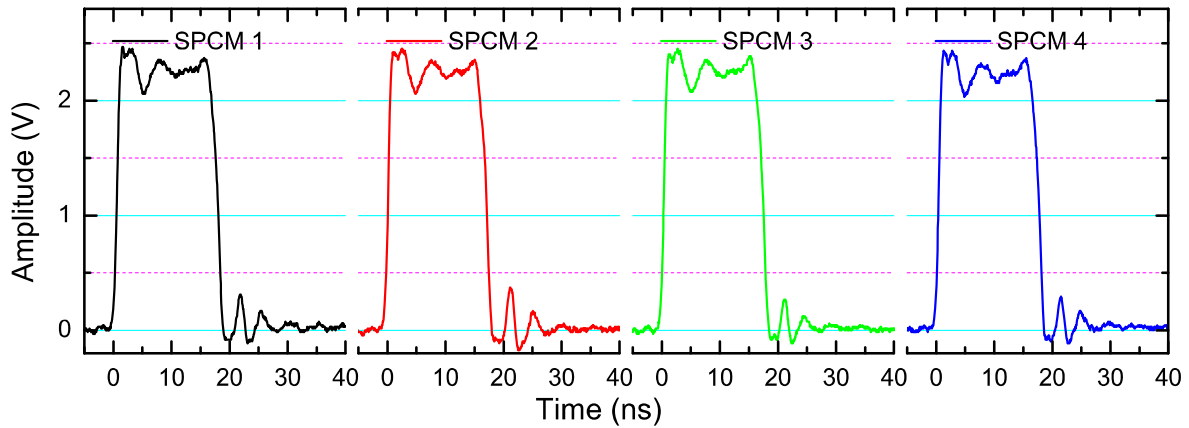


Figure 4.7. Pulses emitted by the utilized SPCMs upon detection of single photons. Each of the plots corresponds to the output signal of specific SPCM. The pulses are about 17 ns wide and feature a sharp rising edge. The output is measured into a $50\ \Omega$ load. Some residual overshoots are visible in the plots. They stem from a not fully impedance matched electronics of the SPCMs.

damage. Please note that despite using this adapter module, which is specified to handle data rates of up to 200 Mbit/s, it is still possible to detect rising edges with a resolution of one nanosecond as long as the count rate per channel will not exceed 100 MHz, which is assured in our system by the constraints imposed by the SPCMs¹³. In order to properly terminate the signal, a $50\ \Omega$ resistance to ground needs to be connected in parallel and as close as possible to the buffer chip inside the digital module. A simple and accurate way to achieve this goal is realized by outputting a 0V signal (equivalent to ground) to the same pin which serves as SPCM input. Since the output signal is equally matched to a $50\ \Omega$ impedance, this effectively serves as $50\ \Omega$ termination. The FlexRIO board is installed in a PXIe-Chassis (NI PXIe-1075) which also holds the integrated host controller NI PXIe-8133.

4.4.1. Deserialization

The demanded resolution of 1 ns requires the FPGA to sample each digital channel connected to an SPCM at 1 GHz. This is beyond the limit of LabVIEW FPGA, whose maximum clock rates go up to 350 MHz in the ideal case. This functionality is hence implemented by making use of a custom socketed CLIP (Component-Level Intellectual Property), allowing the integration of VHDL code, which is able to access the input/output pins of the FPGA. The high sampling rate is accomplished by utilizing the built-in data deserializer capabilities of the Xilinx Virtex-5 devices, i.e. the “iserdes” primitive [136], [138].

The iserdes primitive permit to convert a high-speed input data stream into 2 to 10 synchronous data streams each with a data-rate down-sampled by the number of streams. All of the streams hence represent a different part of the original data which is offset by 1 ns with respect to previous part. In our case we have chosen a 1:8 deserialization. This ratio can be represented as a power of two and thus permits easy data-handling. The resulting data-rate of 125 MHz is, in

¹³ The SPCMs have dead times around typically 32ns; this limits the maximum count-rate to ~ 30 MHz which is clearly below the 100 MHz limit of the digital buffer board. In addition, such high count rates would also lead to a rapid aging if not immediate damage of the SPCMs.

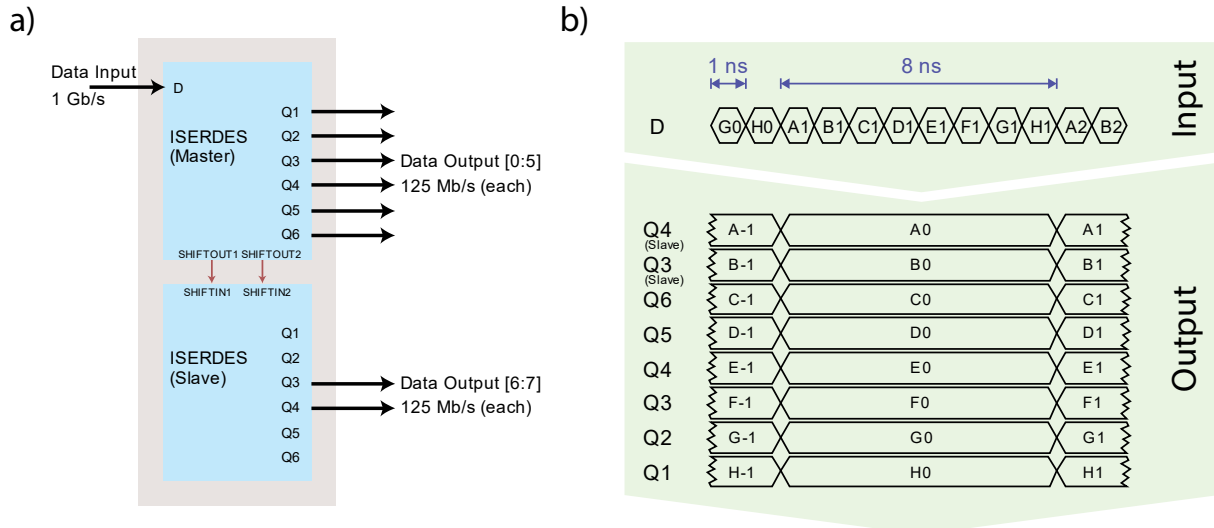


Figure 4.8: Serial-to-Parallel conversion of the input data. a) Inside the FPGA a pair of two “iserdes” primitives is connected to an input pin, where it receives data at 1 Gbit/s. It outputs 8 parallel streams at 125 Mbit/s each. In order to achieve this 1:8 deserialization, two iserdes primitives, one configured as master and the other as slave, have to be used; both are connected via the two shift-ports. b) Basic working principle of the iserdes primitive: The data stream “D” is split into 8 streams each holding data of different subsequent time intervals. Due to the synchronous nature of the 8 streams they are delayed by at least 8ns, so that the last serial data-bit can arrive before the parallel streams are output. Please note that there exists an additional timing offset [138].

addition, also convenient for further data-processing. Figure 4.8 a) shows a simplified version of the iserdes primitive in 1:8 configuration. The number of output streams per primitive is limited to six leading to the mandatory use of a second slave iserdes primitive. Figure 4.8 b) illustrates how the input data is interleaved among the output streams. The iserdes primitive operates in double-data rate mode. This means that the input data is sampled on every rising and falling edge. In this mode it requires a phase-locked clock at the output frequency of 125

```

PLL_500_gen : PLL_BASE
  generic map (
    CLKFBOUT_MULT => 25,
    DIVCLK_DIVIDE => 2,
    CLKIN_PERIOD => 25.000,
    CLKOUT0_DIVIDE => 1,
    CLKOUT1_DIVIDE => 4,
    CLKOUT2_DIVIDE => 1,
    CLKOUT0_PHASE => 0.0,
    CLKOUT1_PHASE => 0.0,
    CLKOUT2_PHASE => 180.0
  )
  port map (
    CLKFBOUT => clk_pll_fb,
    CLKOUT0 => clk_fast_pll,
    CLKOUT1 => clk_div_pll,
    CLKOUT2 => clk_fast_pll_n,
    LOCKED => pll_locked,
    CLKFBIN => clk_pll_fb,
    CLKIN => clk_lv_40,
    RST => aResets1
  );

```

Figure 4.9: Overview of the `pll_base` primitive. It is used to derive from a 40 MHz clock “*clk_{in}*” a 125 MHz clock “*clk_{out1}*”, a 500 MHz clock “*clk_{out0}*” as well as an inverted 500 MHz clock “*clk_{out2}*”. The respective multiplier and divisors are given in the upper configuration part.

MHz and at half the input frequency of 500 MHz (non-inverted and inverted). In order to permit the integration of the code into LabVIEW these clocks also need to run synchronously to the 40 MHz clock provided by LabVIEW. The `pll_base` primitive is used to internally generate clocks which are phase-locked to this 40 MHz reference. Its VHDL instance is shown in Figure 4.9.

Every rising edge of SPCM output corresponds to a photon click and has to be time stamped with a dynamic range of at least 36-bit; this is necessary to seamlessly record datasets of up to one minute while avoiding an overflow of the internal counter. The time-stamping is implemented by running an edge-detection unit which is scanning each of the 8-bit wide “deserialized” streams distributed by the “iserdes” primitive every 8ns. Whenever a rising

edge is detected, the event-flag of the respective channel is asserted. Furthermore, a 3-bit pattern is generated which represents where in this 8 ns interval the event occurred. This value is joined with a 61-bit counter running synchronously on the 125 MHz clock, yielding in total a 64-bit time stamp which is then – along with the event-flag – passed on to LabVIEW FPGA. Figure 4.10 shows how this data-transfer is implemented. It is important that the loop runs on the same 125 MHz clock as the VHDL code does. From that point on a LabVIEW “Virtual Instrument” (VI) is responsible for the remaining tasks. A more in-depth look in how the edge-detection works can be found in Appendix 10.2.

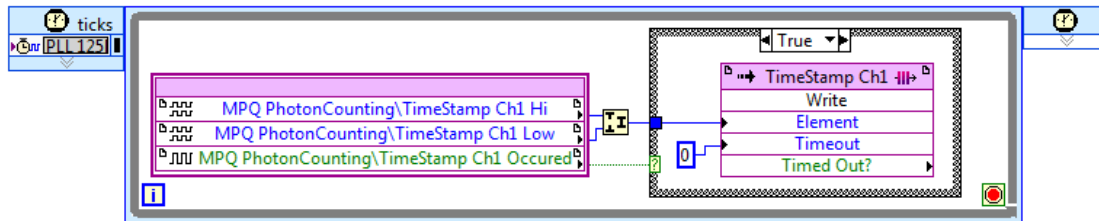


Figure 4.10: Transfer of data from the custom socketed CLIP to LabVIEW. The high and low part of the time stamp are joined to form an unsigned 64-bit integer which is written into a FIFO whenever the time stamp flag is asserted. The process is running on the phase-locked 125 MHz clock.

The time stamps of the photon clicks of each detector (in our case four) are buffered in FIFOs. Subsequently, they are sorted and then merged into one common data stream while preserving the information on which channel the event occurred. The data stream can also contain additional status information. A detail description of the protocol can be found in the Appendix 10.3. Before the stream is transferred via a direct memory access (DMA) channel to the host PC’s memory, it is again buffered locally in the DDR2 memory of the FlexRIO board.

4.4.2. Feedback

The major experimental task the FPGA has to fulfill is the control of the atomic trajectory in real-time. This task unveils the full performance concerning determinism and computational power of FPGAs. A detailed description of the underlying physical principle is given in Chapter 5 as well as in [56]–[58]. The two main features to keep in mind here are, first, that information about the motion of the atom is encoded in the detected photon flux, which is fed into the FPGA, and secondly, that the FPGA has the ability to exert a force onto the atom by means of altering the depth of the optical dipole trap.

The NI FlexRIO module sorts the arrival time of the photons transmitted through our atom-cavity system one-by-one into bins. Typical binning intervals consist of a few microseconds, referred to as exposure time, and are updated every 8 nanoseconds. The latter value is determined by phase-locking the feedback routine to the photon counting process. In a very simple case the variation of the scattered photon rate is evaluated by comparing the current bin to the preceding one, which are typically one exposure time apart in time; the delay is realized

by using FIFOs (first in first out)¹⁴. In our case, a decreasing flux of photons indicates that the atom is moving towards the center of the cavity, whereas an increase indicates that the atom is moving outwards. If this passes a certain threshold, it triggers a switching of the dipole trap between its high and low value. This very basic strategy already results in a significant increase in storage time [58] and permits further improvements by its extension to more complex algorithm. They will be described in Section 5.5.3 and unleash the full power of FPGA computing. They furthermore make use of an additional digital-to-analog converter, which permits to output analog signals at data-rates of up to 200MS/s.

4.4.3. Monitoring

Whenever it comes to adjusting the system and optimizing its performance, it is helpful to have good visual aids; this includes e.g. a graphical representation of the number of recorded photon clicks per channel or a visualization of the feedback algorithm. This is why the FPGA responsible for the photon counting features two 3-bit color VGA-outputs (video graphics array) as well as a digital-to-analog converter (DAC). The VGA screens permit to observe an arbitrary binning of the photon clicks and provides information about where an atom has been detected, which part of the data has been stored as well as feedback-information. The VGA-output requires 5 digital output channels from the FPGA¹⁵. The graphics engine has been coded in LabVIEW.

The digital-to-analog conversion is done by connecting an AD9744 chip (Analog Device) to the FPGA. It requires 15 digital outputs. The VHDL code controlling the device is interfaced with LabVIEW and permits to directly output the desired value. The DAC is either used to monitor the intensity of the transmitted light on an oscilloscope or to control the intensity of the dipole trap for specific feedback algorithms. More details about the hardware as well as the coding of the VGA IP are found in Appendix 10.4 and 10.5.

4.4.4. Overview and Specifications

Here, the final performance of the photon counter will be analyzed. An overview of the overall layout of the FPGA is depicted in Figure 4.11. Altogether, the presented architecture allows to record peak count rates of up to 125 million events per second and channel. This count rate can be sustained for a maximum of 2000 events per channel and is limited by the size of an internal buffer. Data from the internal buffer is continuously transferred to the internal DDR2 memory. This is done at a rate of 100 million events per second combined over all four channels. The size of the memory is sufficient to support 16 million events. Finally, photon clicks are transferred at a sustainable rate of 25 MHz from the DDR2 memory to the host PC where they are stored. The latter bandwidth is limited by the PXI bus. An upgrade to a PXI-express

¹⁴ These elements delay the information which is fed into them by a certain amount of iterations. The values are then output in the order as they arrived; hence the terminology first-in, first-out.

¹⁵ Two of the required signals comprise the horizontal and vertical sync for the VGA screen. The three colors are also represented digitally. Resistances are used to match a zero to no color and a one to full color.

FlexRIO board (NI PXIe-796x)¹⁶ did significantly improve the performance due to the increased PXI-express bus speed as well as the faster and larger DDR2 memory, respectively. The rising edge of the photon clicks are recorded with 1 ns resolution and a dynamic range of 58 bit¹⁷. This yields a maximum time per recorded dataset of $1 \text{ ns} \cdot 2^{58} = 9.13 \text{ years}$ before an overflow will occur. This is more than sufficient. In order to save disk space, the photon counting protocol is optimized to only record the lowest 29 bits of the time stamp if the highest 29 bits are identical to the ones of the previous value.

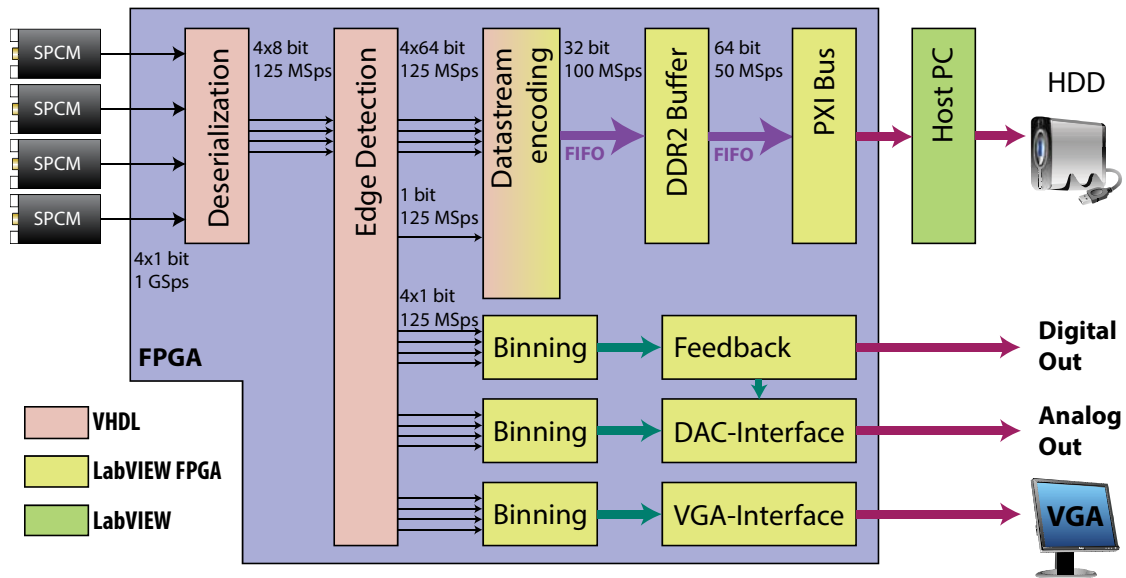


Figure 4.11: Overview of overall structure of the photon counting FPGA. Parts of the structure which are written in VHDL code (red), LabVIEW FPGA (yellow) and LabVIEW (green) are depicted. The part of the code which is executed on the FPGA is marked by the blue background. The four SPCMs deliver an input signal which is sent to the deserialization unit. The deserialized output is further processed by an edge detection unit before it is encoded in common data stream. The data stream is buffered in the internal DDR2 memory and transferred over the PXI bus to the host PC where it is finally stored on an HDD. The edge detection is furthermore providing a signal which serves as an input for different binning processes, each with its own set of parameters. They are used for the feedback routine, which acts on the setup via a digital output, to a DAC interface which provides an analog output as well as to the VGA interface, which is attached to a VGA screen. In some configuration the feedback routine requires an analog output; in that case the DAC interface is directly fed by the feedback routine.

The proper mode of operation has been verified by intensive testing with an Agilent 81150A pulse function generator. As an example, a long-term scan recording emulated clicks at a rate of 10 mHz for almost eight consecutive days is plotted in Figure 4.12. A systematic offset of 10 ppm (parts per million) is visible in the data. Furthermore, slight fluctuations on the order of 0.1 ppm are detected. Both features stem from a finite accuracy of the two independent, internal quartz oscillators. In order to achieve the highest possible level of accuracy all clocks in the lab are thus phase-locked to a common accurate 10 MHz clock. In this configuration deviations are below our measurement resolution of 1 ns.

¹⁶ It is very important to keep the maximum global clock rate per FPGA in mind. Some physically large FPGAs like the Virtex-5-SX95T require at least speed grade (-2) in order for the photon counting routine to work (see table 71 in [138]).

¹⁷ Six bits are sacrificed for an efficient implementation of the data-stream encoding. This, however, does not influence the overall performance of the system.

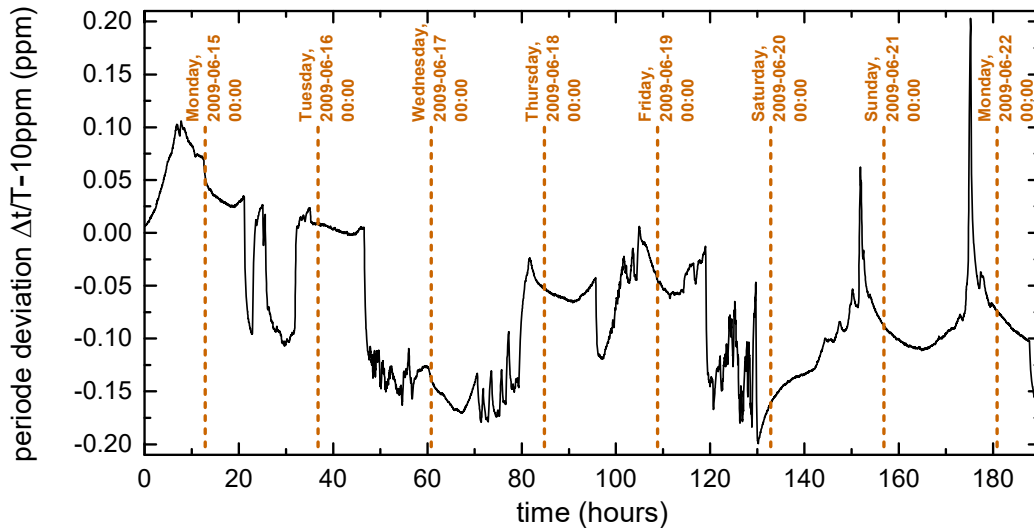


Figure 4.12: Long-term scan verifying the proper mode of operation of the FPGA photon counting module. Deviations from the set value are caused by a mismatch of the two quartz oscillators in the FPGA as well as the arbitrary function generator and demonstrate the importance of using a common and accurate 10 MHz clock.

4.5. Deployment 2: Signal Processing in Heterodyne Systems

The processing of heterodyne data in real-time poses a far more demanding challenge than in the photon counting case before. So far, real-time evaluation of the data was only possible by the help of analog components. The physical principle of the heterodyne detection itself will be explained in Chapter 5.6. For now, it is sufficient to keep in mind that the heterodyne signal is the down-mixed optical field transmitted through the cavity. The optical frequency is down-converted by an optical local oscillator from 384 THz to a radio-frequency of around 25 MHz.

A separate FPGA is dedicated to process the data coming from the heterodyne detection. Due to the more complex data treatment and higher requirements concerning the data-transfer to the host PC, a NI FlexRIO PXIe-7966R board equipped with the more advanced Xilinx Virtex-5 SXT95 (-2) is employed. In this device the computation is facilitated by the large number of embedded DSP-slices (digital signal processing), while the 4x lane PCI-express interface guarantees transfer-rate close to 1 GB/sec. To maintain high through-put rates even while storing files, a NI HDD-8265 raid array (configured in raid-mode 6) is used.

4.5.1. Direct Digital Synthesis of Radio Frequencies

The generation of RF-signals by means of DDS (direct digital synthesis) is very prominent¹⁸ in this thesis. Hence, it is worth to quickly describe the underlying principle. The frequency is adjusted by an integer value called frequency tuning word (FTW). We will assume the case where it is N-bit wide, as it is depicted in an overview in Figure 4.13 a). On every clock cycle

¹⁸ Besides the commercially available DDS-chips which are used to provide a frequency for the AOM drivers, this frequency synthesis is also used to demodulate the heterodyne signal, to compute the beat frequency of the cavity as well as to compute the parametric feedback.

an integer counter is increased by the FTW. In case its maximum value of $2^N - 1$ is surpassed, an arithmetic overflow occurs, which is disregarded and the accumulation is carried on as shown in Figure 4.13 b). This is identical to taking the current value modulo 2^N . The integer range of the counter hence can be mapped to the interval from 0 to 2π . This signal of the counter thus corresponds to the phase of the generated frequency. As shown in part a) a sine-LUT, which is simply a sine curve stored in the memory, achieves the fast angle-to-amplitude conversion.

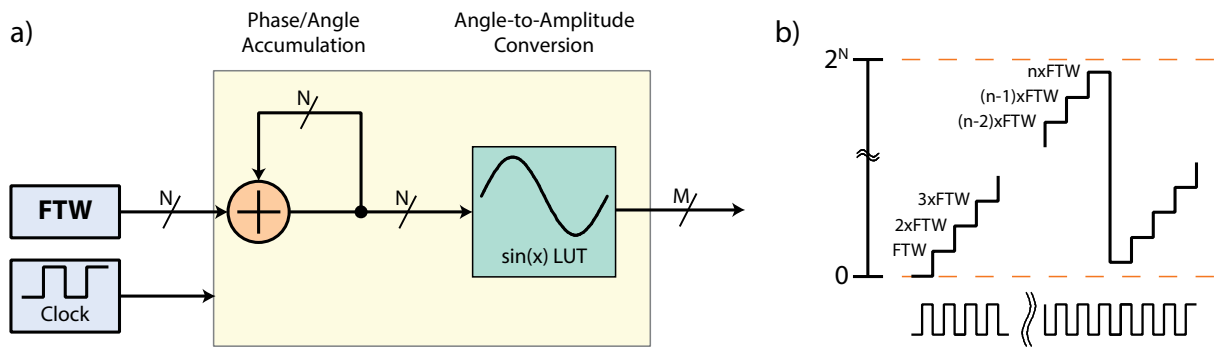


Figure 4.13: Working principle of a direct digital synthesis (DDS). a) Every clock cycle an internal counter is raised by the value of the FTW. The value of the counter corresponds to the phase of the generated frequency and is fed into a sine LUT. This outputs an M-bit wide sine wave. b) Visualization of an overflow occurring while iteratively adding the FTW to the counter. The vertical axis shows the maximal value range of the counter and the horizontal axis depicts the clock signal.

Assuming that the clock is running at the sampling rate f_s , the frequency output by the DDS routine f_{DDS} is given by the FTW. Its desired value can be determined by

$$FTW = \text{round} \left(2^N \cdot \frac{f_{DDS}}{f_s} \right) \quad (4.1)$$

Employing this DDS routine, all local oscillator frequencies inside the FPGA are generated, supporting frequencies from as low as $f_s/2^N$ up to the Nyquist frequency $f_s/2$.

4.5.2. Real-time Processing of the Heterodyne Carrier

The heterodyne signal, which is centered around 25 MHz, is sent to the FPGA system. There it is sampled by the NI-5781 adapter module. The sampling rate of this module is set to $f_s = 100 \text{ MHz}$ with a resolution of 14-bit. Additional Bessel filters at the input, bandwidth-limit the data to 40 MHz. The now digitalized signal is passed to the pins of the FPGA for an actual processing of the data stream.

An overview of the processing is depicted in Figure 4.14. In the beginning, the data stream is multiplied with a local oscillator, which converts it to the complex baseband¹⁹. The local

¹⁹ The term complex baseband refers to a signal comprising an in-phase and a quadrature phase component. It is the same as working with a complex number, where one component is the real part and the other the imaginary one.

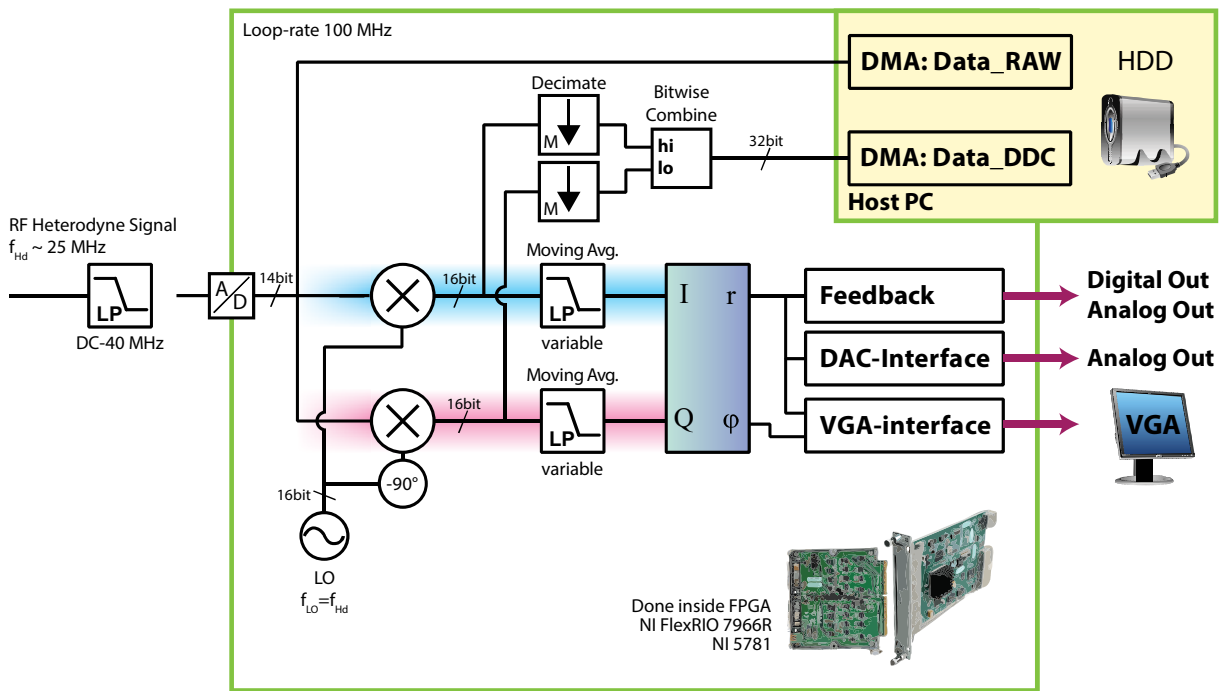


Figure 4.14: Overview of the processing of the heterodyne signal. Before the signal is digitized by an analog-to-digital converter (ADC), it passes a 40 MHz low-pass filter (LP). The digital signal is multiplied with a local oscillator (LO) and its -90-degree phase-shifted facsimile. This down-mixes the signal and shifts the heterodyne carrier to DC frequency. The two components (I/Q) subsequently pass a set of variable low-pass filters before they are converted to an amplitude (r) and phase (ϕ) information. The amplitude information is used by the feedback routine and is also output as an analog output. The VGA screen in addition also displays the phase information of the carrier. Data is transferred in two ways to the host PC, either as raw data or as digitally down-converted data (DDC). The latter one is derived by sending the two components of the down-mixed signal through a pair of decimators and combining these two signals bitwise to have one common data stream.

oscillator is produced by an internal DDS generator. The FTW is 32-bit wide. A frequency of 25 MHz hence corresponds to an $FTW = 2^{30}$. The multiplication is performed twice in parallel, once with the unshifted local oscillator (in-phase; I component), and once with a 90-degree delayed local oscillator (quadrature-phase; Q component). These two components pass a variable moving average low-pass filter, whose frequency response can be controlled via the LabVIEW front-panel. Afterwards, they are converted to an amplitude and phase information, which is subsequently used for the feedback-logic as well as output by a DAC and displayed on a VGA screen.

The transfer of data to the host PC is achieved by a direct-memory-access (DMA). Two DMA channels are used. One is responsible to directly transfer the 14-bit RAW data generated during the digitization²⁰. The other one takes the digitally down-converted (DDC) data, decimates²¹ it by a variable factor M and then bitwise joins the 16-bit wide I/Q component into a single 32-bit wide signal. The selected data stream is then saved onto a RAID-array which guarantees a sustainable write rate of more than 600MB/sec. The RAW data permits to reconstruct the full bandwidth of the signal and has the heterodyne carrier at its original frequency. The data after

²⁰ The transfer uses a 16-bit wide data channel. The remaining two bits are hence free to be used for additional control information. This is e.g. done during the switching measurement (c.f. 6.7).

²¹ Decimation means to reduce the data rate of data stream by a certain factor M . Adjacent M samples of the original stream are averaged and output as one sample.

the DDC and decimation has the heterodyne signal centered at 0 MHz and a bandwidth of $\Delta f_{3dB,FWHM} = \frac{f_s}{M} \cdot 0.44$ (see Appendix 10.6.3.1). The latter data stream helps to significantly reduce the size of the stored files, while preserving the necessary information.

4.6. Deployment 3: Locking of a Cavity

The cavity in our system needs to be stabilized down to a few hundred femtometers. Sophisticated mechanical vibration isolation is used as a passive means to approach this objective. However, a good active stabilization is indispensable to achieve the high stabilization needed. The basic locking scheme is described in Section 3.7. A stabilization laser is locked to the cavity via a Pound-Drever-Hall technique and follows the resonance frequency of the cavity closely. The beat of this laser with a frequency comb hence holds information of fluctuations in the cavity length. Here we will focus on how this beat-frequency between the comb and the dipole trap is very accurately and quickly determined and how this information is used to control the piezo voltage. In order to precisely fulfill the requirements, we decided to use a NI FlexRIO 7962R FPGA with the baseband transceiver module NI-5781.

4.6.1. Introduction

A schematic overview of the lock is depicted in Figure 4.15. The laser beam as well as the frequency comb are overlapped in a fiber beam splitter. One of the outputs is connected to a fast photodiode by MenloSystems (FPD 310-FV), which converts the optical beat signal into an electric frequency in the RF range. The other output is used to monitor the power of both beams. In order to filter out the beat signal with other teeth, which have a 250 MHz spacing, two low-pass filters, which are connected in series, are employed. The signal is then amplified and sent through a combination of high- and low-pass filter, to clean the signal again and remove any DC offset induced by the amplification. Typical beat-frequencies of the stabilization laser on resonance with the cavity and the comb are about 40 MHz. To better suit the frequency range of the FPGA, this signal is down-converted by an external analog RF-mixer to around 15 MHz before it is digitized by the FPGA and can be analyzed. It is important to remember that any frequency fluctuation in the optical beat is transferred unscaled to the down-mixed signal. It is hence sufficient to accurately compute the fluctuations residual in this signal. It is done by what will be called a “phase-drift-lock” and is described in the following section. The generated error-signal is proportional to the deviation in frequency and is then sent to a PID controller. The output of this controller is low-passed by a SR560 low noise amplifier. Frequencies around the mechanical resonance frequency of the piezo are filtered by a notch filter [132]. The shielding of the coaxial cable is connected to ground and the inner lead is connected via a 2 k Ω potentiometer to the inner side of the piezo tube. The outer side of the tube is connected to an additional offset voltage, which is needed for the coarse tuning of the cavity length. It is provided by a differential power supply, whose other end is connected to the same ground.

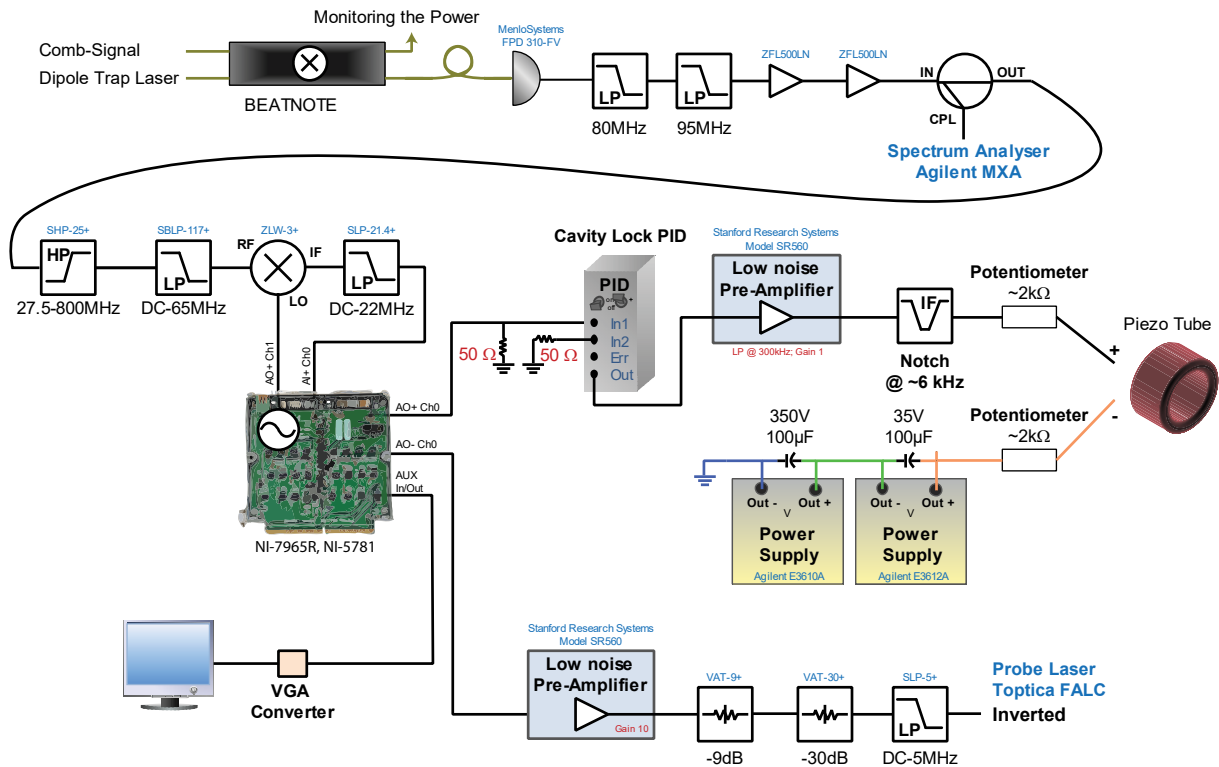


Figure 4.15: Overview of the electronic setup keeping the cavity locked. The beat note from the comb and the stabilizing dipole trap laser is recorded via a fast photodiode (PD). The signal passes two low-pass filters at 80MHz and 90MHz before it is amplified by two amplifiers (ZFL500LN). A small part of the signal is coupled to a spectrum analyzer. The remaining part is filtered again by set of high-pass (27.5-800MHz) and low-pass filter (65MHz). The signal is sent together with a local oscillator provided by the FPGA board to a mixer (ZLW-3+). The resulting output passes a 22MHz low-pass filter and is sent to the FPGA. The FPGA analyses the signal and provides a control signal to a PID controller. The output of the PID then passes a low noise pre-amplifier and a notch filter. The shielding of the cable is connected to ground and the inner lead of the coaxial cable via a 2kW potentiometer to the inner side of the piezo tube (shielding not shown). The outer side of the tube is connected to an array of differential power supplies which have one of their poles connected to the same ground. An identical control output of the FPGA is sent to a second low noise amplifier. After passing through an array of attenuators and a 5 MHz low-pass filter it is connected to the input of the FALC controller of the probe laser. The visualization is done by connecting a VGA screen via small converter to the digital outputs of the FPGA.

Information about the stability of the cavity is displayed in real-time on a VGA screen, directly attached to the FPGA. Additionally, a second analog output permits to adjust the frequency of the probe laser according to length fluctuation of the cavity. This is achieved by passing the error-signal derived from the beat detection to a second low noise amplifier used to clean the signal and acting as variable amplifier and low-pass filter. Successively this signal is attenuated and passes a second low-pass filter before it is connected to the “inverted” input of the FALC PID controller of the probe laser. Although this feature reduces intensity fluctuation in the transmitted probe-light, it did not lead to measurable improvements in the storage time of the atom and is thus currently not in use.

4.6.2. Under the Hood

One of the key challenges in building a reliable cavity lock consists in the fast and accurate determination of the beat frequency. In a previous work [81], a technique based on the steep increase of the transfer function of a low-pass filter was employed [139]. This technique, however, does not permit to fully decouple intensity and frequency fluctuations of the trap laser and hence causes significant long-term frequency drifts. In addition, it features a non-trivial dependency between the derived error-signal and the frequency deviation, which is proportional only in a very narrow range. Another possibility to determine deviations in the beat frequency is to count zero-crossings of the beat signal. This method leads to very accurate results, yet drastically suffers from a noisy signal [140]. Thus, it requires an extension to improve its robustness [141]. A digitization of the data by the FPGA would in principle enable to perform a fast Fourier transform (FFT) and to determine the peak value in the spectrum. However, the relatively long computational time and its complexity render it difficult to build a fast and accurate lock with this method.

We decided to implement a method which is based on a phase lock, but only considers the evolution of the phase. A pure phase lock is not possible here, since it lacks a fast reaction time of the piezo tube ($\sim 100\mu\text{s}$) as it would be required to compensate for typical fluctuations. The locking scheme employed here is hence called phase-drift lock. The way how it works and how it is implemented can be found in Figure 4.16. The RF beat-frequency of the laser with the comb is around 38 MHz. This is fairly close to the 40 MHz input bandwidth of the NI-5781 adapter module. In a first step, it is hence necessary to down-mix the signal to about 15 MHz before it is digitized. The difference frequency is synthesized by a DDS logic integrated into the FPGA (local oscillator LO1). The actual frequencies in the signal path are indicated in the upper blue ribbon of Figure 4.16. Similar to the heterodyne detection, the digital signal is down-converted by a second local oscillator (LO2) as well as its -90-degree phase-shifted replica. The resulting I- and Q-components are in the complex baseband and permit to differentiate between positive and negative frequency deviations. A low-pass filter applied separately to both components eliminates higher frequencies. A Cartesian-to-polar converter generates an amplitude and phase information. The phase corresponds to the phase-difference between the input beat signal and the second local oscillator and its temporal evolution determines its frequency mismatch. As an example: If the beat signal has exactly the same frequency as the local oscillator, the phase difference will stay the same. A change in this difference hints on a change in the beat frequency. The whole loop is executed every 10 ns. The change in the phase difference from one iteration to the next is computed and decimated by a factor of 8. Before the signal is output to the PID controller controlling the cavity length, it is low-pass filtered with a 3dB-bandwidth of 550 kHz. A down-mixed frequency of 40 kHz is chosen as this proved better results in combination with the PID controller employed.

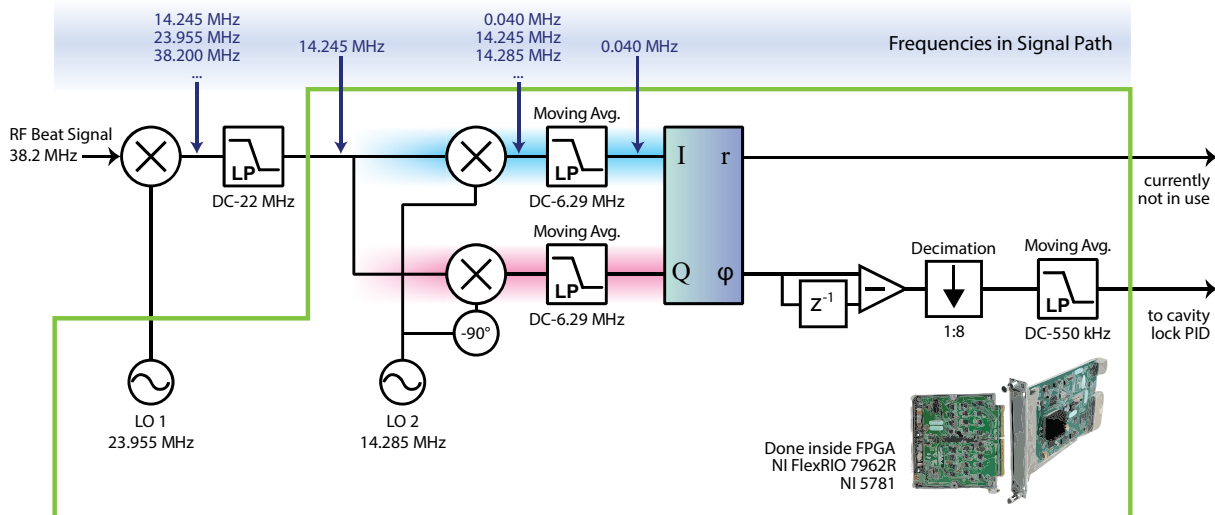


Figure 4.16: Overview of the signal path of the RF beat signal. The 38.2 MHz beat signal is sent to an analog multiplexer together with a 23.955 MHz local oscillator (LO1). The mixer produces sum and difference frequencies as they are indicated in the blue upper ribbon. A 22 MHz low-pass filter along with the built-in 40 MHz low-pass filter of the FPGA module only let the 14.245 MHz component pass. A second local oscillator (LO2) at 14.285 MHz along with its -90-degree phase-shifted copy are multiplexed digitally. This generates the I/Q component of the signal. After passage through a set of digital, moving average low-pass filters only a down-mixed, low-frequency component around 40kHz survives. The I/Q component is converted to amplitude (r) and phase (ϕ) information. The difference of the phase information with its value from the previous iteration (Z^{-1}) is computed. It passes a 1:8 decimator before it is filtered by a second 550 kHz moving average low-pass filter. This signal is then output to stabilize the cavity length and displayed on a VGA screen along with the amplitude information.

4.6.3. Performance

In order to verify the proper operation of the FPGA-based cavity lock, its performance needs to be tested. This is done by simply recording the raw input data which is digitized by the FPGA. It has a frequency around 14.2 MHz as shown in Figure 4.16. The spectrum of the recorded data is computed. The frequency deviation $\Delta\nu$ can be translated to a deviation of the cavity length Δl by the following expression

$$\Delta l = \frac{n}{2c} \lambda^2 \Delta\nu . \quad (4.2)$$

In this equation, n is the number of nodes in the cavity. For the trap beam at $\lambda = 785\text{nm}$, which also serves as stabilizing beam, n amounts to 656 nodes.

The resulting spectrum is depicted in Figure 4.17. This spectrum shows a FWHM of the amplitude of the beat signal of 667 MHz corresponding to a length variation of the cavity of 450 fm. This shows that the lock is capable of stabilizing the cavity length to the sub-picometer level as initially stated as requirement.

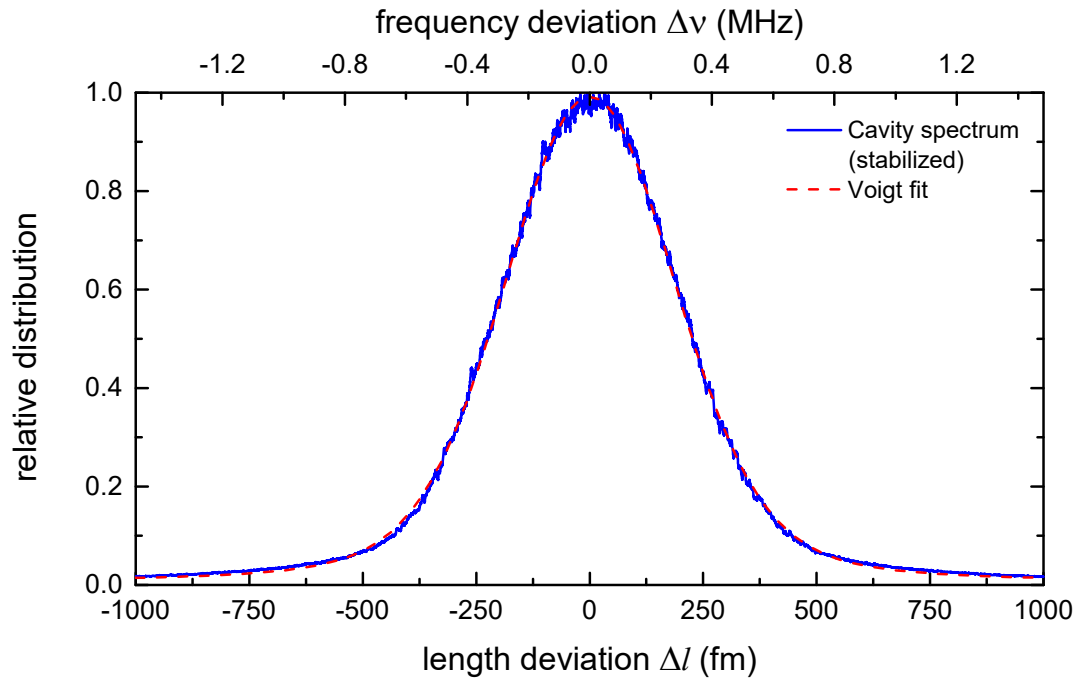


Figure 4.17: Spectrum of the beat signal of the stabilizing laser with the frequency comb. The spectrum is derived by performing an FFT of the amplitude of the recorded beat signal. The x-axis is scaled with respect to the corresponding length deviation, which is derived from the frequency deviation. A Voigt curve is fitted to the experimental data and serves as a guide to the eye. The spectrum shows a FWHM of the amplitude of 450 fm.

4.6.4. Increased Storage Time

A second way of checking the performance of the new cavity lock in the system is to perform a storage time measurement, as variations of the cavity length will directly translate into increased motion, i.e. heating of the atom mediated by the dipole trap field. We execute a standard experimental run as described in Section 3.8 and capture a single atom. While the atom is held in our optical cavity, the laser fields inside the resonator will heat the atom. The laser fields are the near-resonant probing field as well as the far-off resonant trapping light. The heating caused by the probe beam can be attributed to momentum diffusion. In general, this frequency is chosen such that it mediates additional, axial cavity cooling as studied by Maunz [77]. However, it does not provide any radial cooling forces. The trap beam on the other hand confines the atom, but intensity fluctuations, mainly caused by cavity length variations, along with frequency fluctuations of the laser will lead to parametric heating of the atom. This effect is especially prominent in the axial direction, where the dipole field gradient is two orders of magnitude larger. A more detailed analysis of the atomic motion in the dipole trap is found in the following Chapter 5. The stability of the cavity length hence directly relates to the average storage time of the atom. In order to diminish heating effects caused by the near-resonant probe, its intensity is gradually decreased while the average storage time is measured (see Figure 4.18).

The plot shows two different data-sets. One was recorded with the previous [81] analog cavity-lock (red), while the other was taken with the FPGA-based lock in-place (blue). The analog

lock detects frequency deviations of the beat based on the steep rise of the transfer function of a low-pass filter at this frequency. The probe power is given in terms of intracavity photons for an empty resonator. Above probe intensities of 0.05 intracavity photons, both measurements show similar results. In this regime the heating is almost entirely dominated by the near-resonant probe. This behavior changes if the probe power is further reduced. Particularly the data recorded with the analog cavity lock shows a saturating or even decreasing behavior of the storage time for small probe powers. Even lower values of the probe beam show a similar decreasing behavior; they are not shown, since not enough traces have been recorded. In this case, the dipole trap is the main heating source. In addition, as the probe is further reduced, the axial cavity cooling becomes smaller and hence yields this decrease in storage time. For the FPGA-based cavity lock, the saturation of the storage time starts at substantially lower probe powers as it can be seen by a comparison to the green reciprocal fit, depicting the assumed evolution if the storage were mainly limited by radial momentum diffusion. This shows that the parametric heating due to the trapping laser is drastically reduced, which can be accredited to the improved performance of the cavity lock.

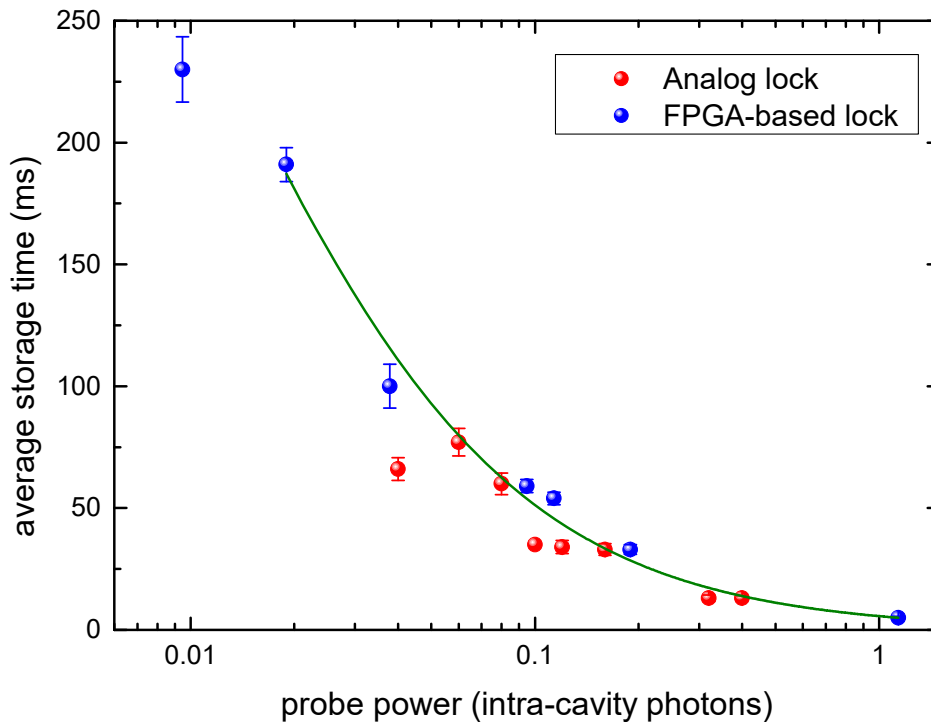


Figure 4.18: Average storage time as a function of the probe power. The average storage time of atoms is measured at different probe powers. The remaining other parameters like the ones for the trap beam are kept constant. The measurement is carried out twice. Once with the previous analog cavity lock as described in [81] (red dots) and once with the improved FPGA-based locking scheme. The green line is fit to a reciprocal function, estimating how the storage time evolves if it is only limited by radial momentum diffusion, caused by the intensity of the probe beam. At low values, all the way on the left side of the graph, a clear decrease in the storage time of the analog lock (red) becomes visible while the FPGA lock (blue) almost continues to follow its previous behavior.

4.7. Deployment 4: Digitizing and Monitoring of Signals

The real-time monitoring and visualization of experimental parameters are essential for adjusting the setup. The possibility to perform certain real-time evaluation of the data, furthermore enables to ensure the proper operation of the experimental setup while it is running. The digitization and processing of the data by an FPGA is an efficient means to implement this functionality. In our system an NI FlexRIO 7965R FPGA in combination with the high-density digitizer adapter module NI-5751 is used for this purpose. It features a large number of 16 analog inputs which are 14-bit wide and sampled with 50 MHz. As for the other FPGAs, a VGA screen connected to the digital outputs enables the visualization. One of the analog input channels is connected to the photo multiplier tube, which measures the transmitted dipole trap power. The FPGA provides sufficient computation power to determine the full spectrum of this signal by what is called a streaming FFT with 1024 points. The word “streaming” means that no dead-time occurs between different FFT evaluation windows. The resulting values are displayed with a log scaling. This enables to properly adjust the setting of the PID controller of the trap laser and cavity lock as well as to adjust the incoupling of the trap laser. For this purpose, the transmitted trap power is maximized in the time-domain while spectral features in Fourier-domain (around 200 kHz) are minimized. During the MOT-phase (cf. Section 3.8.1) the FPGA also computes the mean value of the transmitted trap power over one second and sends it to the host PC where it is saved into the database. This value also permits to perform a post-selection of the recorded data. Part of the remaining analog inputs is used to monitor – in a similar manner – the error of crucial PID controllers, regulating the intensity level of the trap and repump beam.

4.8. Conclusion

In this chapter FPGAs have been introduced as a versatile and omnipotent tool to solve even complex experimental tasks. In the beginning a quick overview of the architecture of FPGAs was given. Unlike other processing units like CPUs or GPUs, FPGAs feature an inherent parallel execution of tasks along with a deterministic timing. Programming of the FPGA microchips is done by generating a hardware layout of the chip. This permits the creation of devices tailored to the experimental needs as well as the integration of multiple “devices” on a single chip. By doing so, the complexity as well as the cabling of the experimental setup can be drastically reduced. What is more, the vast computational power offered by FPGAs also enables to solve complex tasks such as counting and processing of single photon clicks, evaluating heterodyne data, feedbacking onto the atomic motion, detecting frequency and phase deviations in beat-signals or computing the full FFT spectrum of an input signal all in real-time. Further tasks can be easily integrated into existing system. This makes FPGAs a very powerful tool facilitating the integration of more complex control algorithm and hence enabling the studies described during the course of this thesis.

5. Control of Atomic Motion

Single atoms are loaded into our optical trap by means of an atomic fountain. The probe laser is on resonance with the empty cavity. A drop in the cavity transmission hence heralds an arrival of a single atom. This results in a rapid increase of the trapping potential which confines the atom in the optical resonator (cf. Sections 3.4 and 3.8). The storage time of the single atom is limited by heating mechanism caused by momentum diffusion due to the near-resonant probe beam as well as by parametric heating due to intensity fluctuations of the dipole trap. The latter one is either caused by small fluctuations in the cavity length (cf. Sections 3.7 and 4.6.4) or frequency fluctuations of the dipole trap beam. This results in an increase of kinetic energy. If it surpasses the depth of the trapping potential, the atom can escape from the trap and is lost. In this chapter we will give insight into this atomic motion in the trap and show how it can be damped by fast feedback cooling.

5.1. Introduction

The red-detuned dipole trap inside the cavity forms a standing wave pattern inside the cavity and creates an attractive potential for our atoms. The higher the intensity of the trap is the lower the resulting potential valley for the atom, which is formed. An overview of the shape of this pattern around the center of the cavity is presented in Figure 5.1.

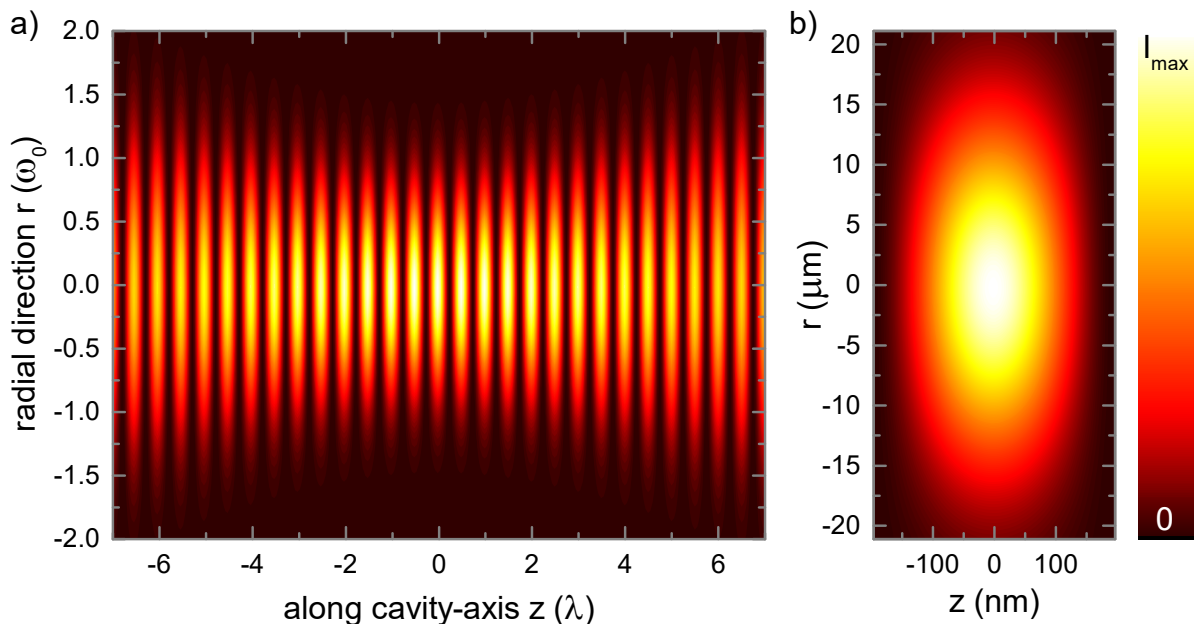


Figure 5.1: Visualization from the side of the intracavity dipole trap field. The color is coded from white, high intensity level, to black, low intensity level. a) Standing wave pattern which forms around the center of the cavity. The x-axis is scaled in units of the wavelength λ while the y-axis is expressed in terms of the waist of mode in the cavity center ω . The Rayleigh length, i.e. the distance along the cavity axis from where the mode waist increases by a factor of $\sqrt{2}$, amounts to 6 wavelengths λ . b) Single node with an absolute scaling on both axes.

The axis in part a) are scaled in terms of the wavelength of the dipole trap (785 nm) and the waist of the beam-mode (19 μm). The axis of abscissas covers 11 μm while the axis of ordinates corresponds to 76 μm . The asymmetry of a node of the mode in axial and radial direction becomes evident in part b). The difference in slope in the two directions amounts to two orders of magnitude. This causes a significantly steeper dipole-trap intensity gradient along the cavity-axis, i.e. in axial direction than in radial direction. An atom moving in one of the antinodes hence possesses two distinct oscillation frequencies as it will be shown in the next section.

5.2. Harmonic Approximation

The oscillation frequencies of the atom in radial and axial direction can be determined analytically by assuming a harmonic dipole potential. This approximation is valid until the excursions of the atom are small. Deviations from the harmonic frequency will be discussed in Section 5.4.

The intensity-distribution as plotted in Figure 5.1 is given by

$$I(r, z) = I_0 \cdot e^{-\frac{2r^2}{\omega_0^2(z)}} \cdot \cos^2\left(2\pi \cdot \frac{z}{\lambda}\right). \quad (5.1)$$

Here, z is the distance in axial direction measured from the position of the minimal beam-waist. The variable r is the radial displacement from the cavity axis. As it is shown in [142], the optical dipole potential is proportional to the intensity:

$$U(r, z) \propto I(r, z) \quad (5.2)$$

Equation (5.1) can be factorized in terms containing only r and z . Because of the significantly larger modulation caused by the standing wave character, an axial confinement due to focusing of the trap can be neglected. This yields a second order Taylor approximation for the optical potential of

$$U(r, z) = -\hat{U} \left[1 - 4 \left(\frac{r}{\omega_0} \right)^2 - 2 \left(\frac{2\pi z}{\lambda} \right)^2 \right] \quad (5.3)$$

with $\hat{U} = U(r=0, z=0)$ being the trap depth in the center of the mode. This harmonic approximation in radial as well as in axial direction is depicted in Figure 5.2. The black solid line shows the actual trap depth, whereas the red dotted line corresponds to its harmonic approximation according to Eqn. (5.3). The two plots already show up to which oscillation amplitude this approximation stays valid. For the radial oscillation this range extends to excursion of $r \leq \pm 7 \mu\text{m}$ and for the axial excursions of $z \leq \pm 70 \text{ nm}$, respectively.

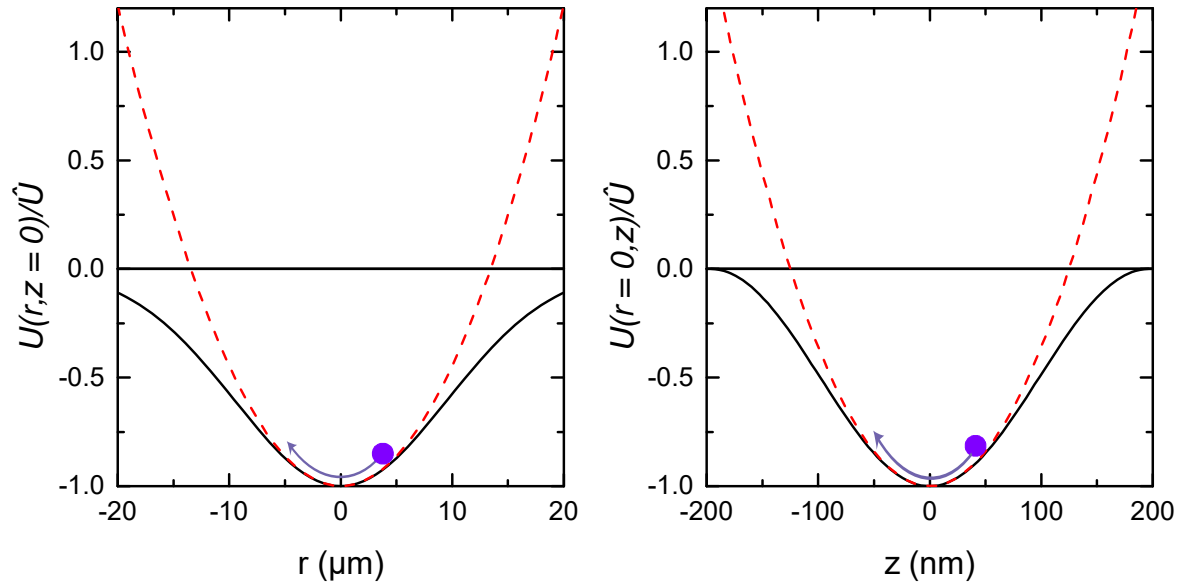


Figure 5.2: Visualization of the harmonic approximation of the dipole trap potential. A plot in radial as well as in axial direction is shown. The actual potential is plotted as black solid line. The minimal potential is found at the center of the cavity, i.e. at $r = 0$ and $z = 0$. The force acting on the atom is given by the gradient in the respective plot. Its harmonic approximation is shown by the red dotted line. As it can be seen, the approximation holds only for small excursions of the atom.

Atoms moving away from the cavity in radial direction feel a restoring force $F_{rad} = \partial U / \partial r = 8\hat{U}r / \omega_0^2$, whereas axial confinement is provided by a restoring force $F_{axial} = \partial U / \partial z = 4\hat{U}z \cdot (2\pi/\lambda)^2$. This yields a harmonic radial oscillation frequency of

$$\omega_{rad} = \sqrt{\frac{4\hat{U}}{m\omega_0^2}}. \quad (5.4)$$

The tighter axial confinement results in roughly 2 order of magnitude larger axial oscillation frequency:

$$\omega_{axial} = \frac{2\pi}{\lambda} \sqrt{\frac{2\hat{U}}{m}} \quad (5.5)$$

It is important to point out that these harmonic oscillation frequencies are only valid for small excursions for which the approximation still holds, as it can be seen in Figure 5.2. In Section 5.4 deviations from these harmonic oscillation frequencies will be introduced. A typical trap depth of $\hat{U} = k_B \cdot 850\mu K$ is employed during many experimental runs in this thesis. Here, k_B is the Boltzmann constant. This yields a radial oscillation frequency of $f_{rad} = \omega_{rad} / 2\pi = 4.8kHz$ and an axial one of $f_{axial} = \omega_{axial} / 2\pi = 520kHz$.

5.3. Measuring Atomic Motion

The motion of an atom in the dipole trap is governed by its radial and axial oscillations. In addition, the atom also orbits around the cavity axis in an azimuthal path. However, due to the radial symmetry of the intracavity trapping and probing field, one can neither observe nor control this motion. We will hence focus on the two independent and detectable oscillations in radial and axial direction. As it has been shown previously, the harmonic oscillation frequency of the atom along these directions is determined mainly by the dipole trap potential, i.e. the trap depth of the dipole field inside the cavity. In this section two methods of measuring the harmonic oscillation frequency will be explained. The standard approach is to analyze the spectrum or the correlations, respectively, of the transmitted probe beam [77] (see Sections 5.3.1 and 5.3.2). The second method employs the fact that the atom can be resonantly excited at the harmonic oscillation frequency. This can be achieved e.g. by parametric heating with the dipole trap (see Section 5.3.3). While the first method allows an easy implementation, it suffers from a nonlinear response of the transmitted probe beam with respect to the amplitude of the atomic oscillation. As it will be described in detail in Section 5.4, this will increase the weight of anharmonic oscillations in the recorded spectrum and hence cause deviations in the measurement.

5.3.1. Correlation Measurement

The position of the atom determines its overlap with the probe-field, which in turn leads to a change in the effective coupling and hence alters the normal-mode spectrum. Since the frequency of the probe beam is fixed, variations in the normal-mode spectrum also cause a change in the transmitted probe beam.

The intracavity intensity of the probe-field (similar to Eqn. (5.1)) is given by:

$$I_p(r, z) = \hat{I}_p \cdot e^{-\frac{2r^2}{\omega_0^2(z)}} \cdot \cos^2 \left(2\pi \cdot \frac{z - z_0}{\lambda_p} \right) \propto g_{\text{eff}}(r, z) \quad (5.6)$$

We introduce z_0 as the axial displacement between the antinode of the probe- and trap-field. The effective coupling g_{eff} is proportional to the intensity of the probe-field at the position of the atom. Its behavior in axial and radial direction is plotted as dark blue line in Figure 5.3. For simplicity, $z_0 = 0$. We assume a probe-cavity detuning of $(\omega_p - \omega_c)/2\pi = 0\text{MHz}$ and an effective atom-cavity detuning of $(\omega_a - \omega_c)/2\pi = -4.6\text{MHz}$. The effective detuning includes a position dependent ac-Stark shift as it is caused by the trap depth of $k_B \cdot 850\mu\text{K}$. In general, this configuration leads to a suppression of transmission, when the atom is well coupled, while the transmission through the cavity increases as the coupling of the atom decreases. Using Eqn. (2.33), the exact relative transmission of the probe beam compared to the empty-cavity case can be computed and is shown in the same graph as red line. Typical length scales, i.e. the waist

ω_0 and $\lambda/8$ are indicated by vertical dashed lines. The position $r = 0, z = 0$ corresponds to the center of the antinode in the middle of the cavity.

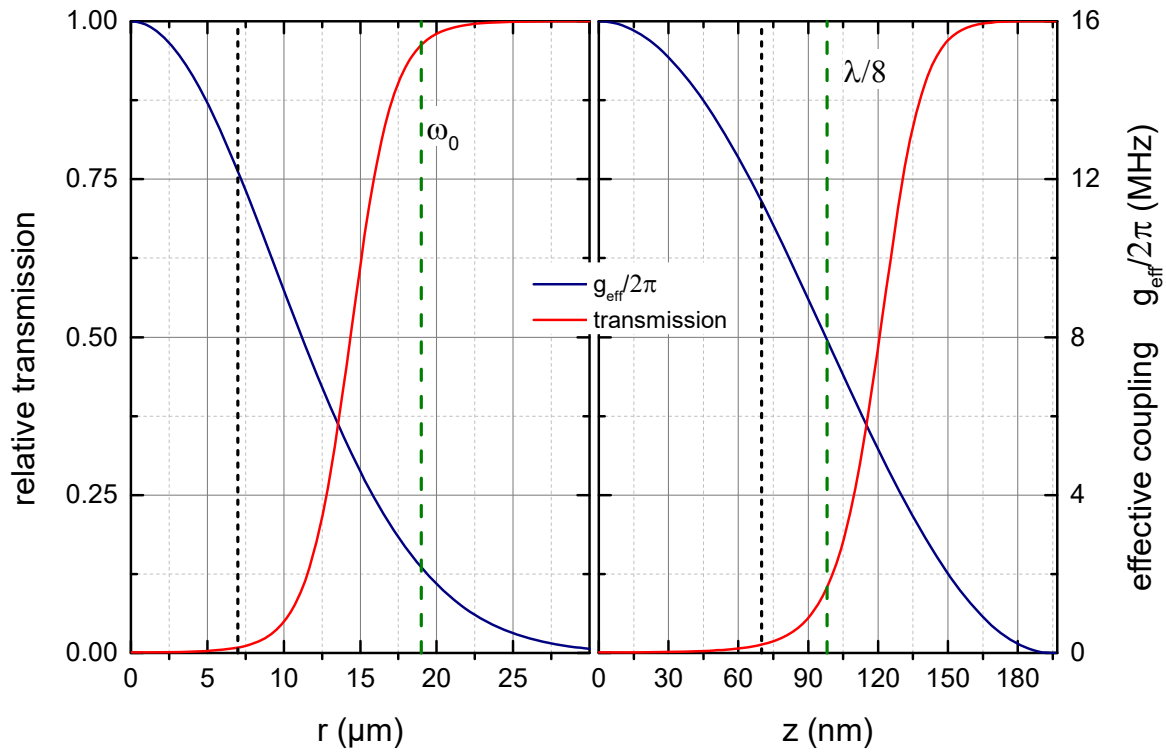


Figure 5.3: Effective coupling g_{eff} (blue) and relative transmission of the probe beam (red) as a function of the radial (r) and axial (z) distance from an antinode of the intracavity probe field. Typical length scales, as the waist ω_0 and the wavelength λ , are marked by vertical dashed lines in the respective plots. The breakdown of the harmonic approximation is marked by vertical dotted lines.

Information about the dynamics of the atomic motion can be derived from a periodic pattern of the transmitted probe beam. One way of detecting this pattern consists in measuring correlation functions. Here, the second order correlation function $g^{(2)}(\tau)$ from data recorded by the SPCM is employed. The second order correlation function is a measure of how many photons arrive in pairs with a detection time difference of τ . As it can be seen from Figure 5.3, the probability to detect a photon passing through the cavity becomes larger as the atom has a larger excursion from the center of the antinode, due to the decreasing coupling and thus increasing transmission. An atom which is oscillating in the trap produces a transmission signal with peaks at its turning points. This subsequently leads to a modulation of the photon-stream at twice the atom's oscillation frequency and hence, a high probability to detect both photons at the turning point or the second after half an oscillation period of the atom at the other turning point. The correlations have been measured for atoms stored in the cavity. The feedback, which will be described in Section 5.5, was switched off and the probe-laser was on resonance with the cavity as described before.

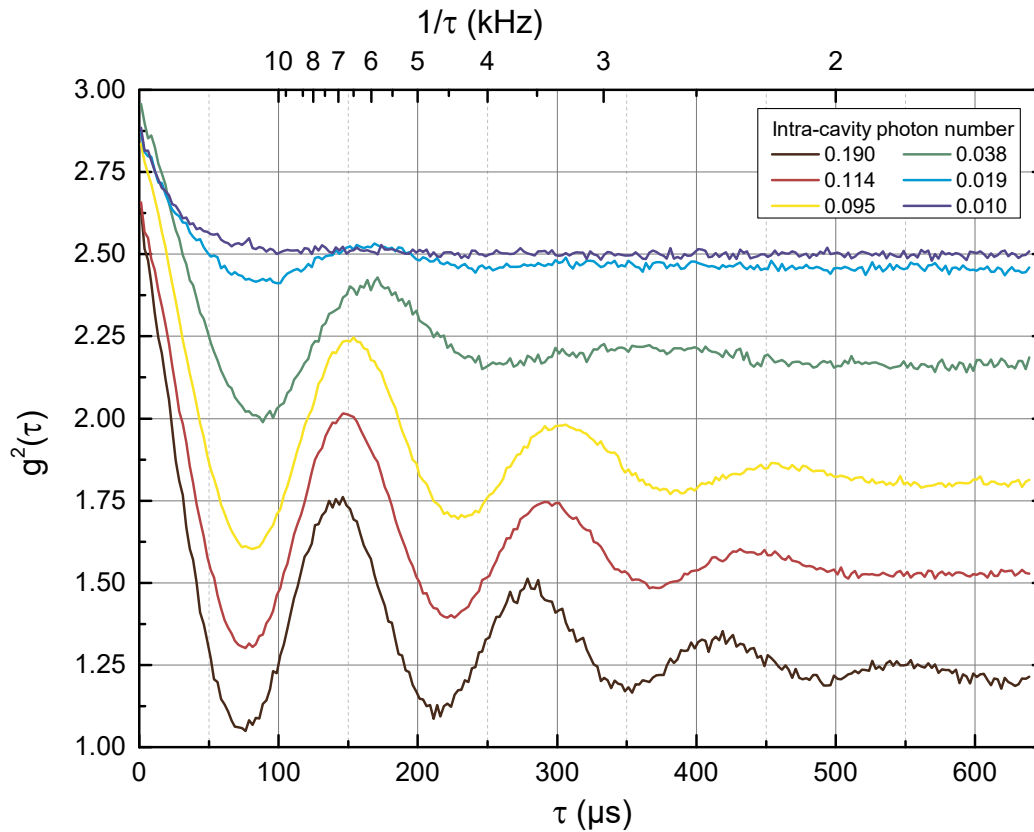


Figure 5.4: Second order correlation function recorded for different probe powers. The graphs for different probe powers are stacked by a vertical offset of 0.25. The correlation time is plotted on the lower x-axis. The frequency corresponding to an oscillation with a period as indicated by the time on the lower axis, is given on the upper axis. This directly reflects the modulation frequency of the transmitted probe beam at the respective peak.

The correlation measurements obtained for different probe-powers are depicted in Figure 5.4. A clear peak around $150 \mu\text{s}$ is visible, corresponding to a modulation between 6 and 7 kHz. The modulation is strongest for high intracavity photon numbers and becomes hardly visible if the number is reduced to as low as 0.01 intracavity photons on the empty cavity resonance. This dependency shows that high probe-power causes momentum diffusion which leads to an increase of the oscillation amplitude. As expected, the position of the peak, which is mainly determined by the depth of the dipole trap, remains almost unchanged. Typical probe-powers corresponding to 0.1 intracavity photons for an empty cavity (yellow) are employed during an experimental scan. In this regime two oscillation bumps are observed. The number of bumps portends to the coherence of the atomic oscillation. A low value thus indicates a low quality-factor of this oscillation. The detected modulation corresponds to twice the radial oscillation frequency of the atom, which hence amounts to $f_{rad} = 3.4 \text{ kHz}$. This value is clearly below the theoretically expected value of 4.8 kHz for the harmonic oscillation frequency computed in Section 5.2. A discussion of the discrepancy is given in Section 5.4.

Correlation measurements can also be used to detect the fast, axial component of the atomic oscillation. The two orders of magnitude smaller oscillation period in combination with their small modulation of the probe beam make them more difficult to observe. To counteract this,

the duty-cycle of our system, i.e. the time an atom is captured in the cavity vs. the time it takes to load the atom, is increased by performing feedback cooling in the radial-direction. This so-called bang-bang feedback will be described in detail in Section 5.5.2 and shall here only be seen as a tool to increase the storage time. By doing so, the average storage time is increased by almost a factor of 50. The recorded correlation is plotted in Figure 5.5.

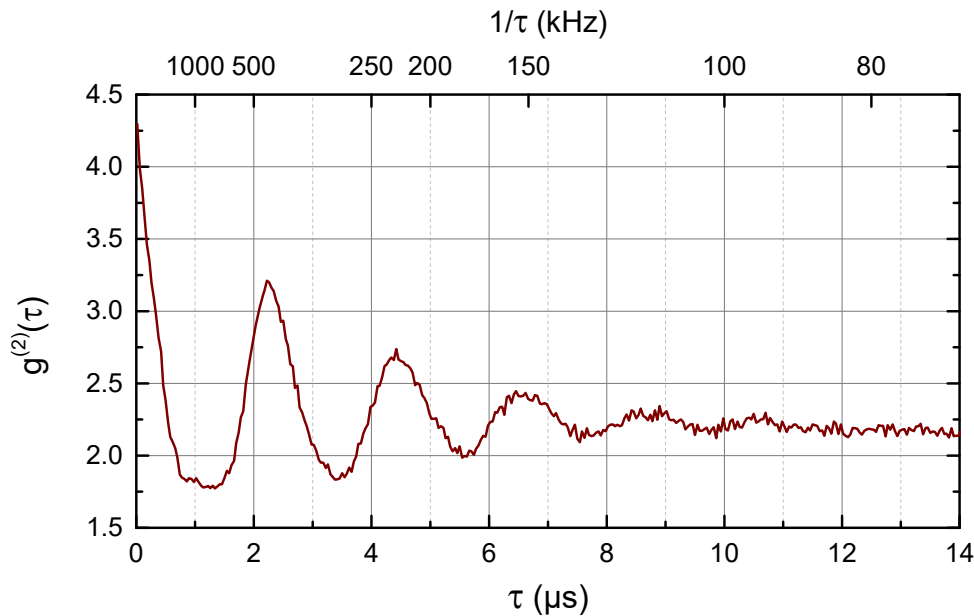


Figure 5.5: Second order correlation function recorded for the transmitted probe beam. As before, the correlation time is plotted on the lower x-axis with the corresponding frequency upper axis. Multiple peaks are visible with the first one being slightly below 500 kHz.

In this measurement the probe power was set to 0.11 intracavity photons on the empty cavity resonance. The trap power was set to 950 nW and only lowered to 400 nW for very short time intervals, if required by the outcome of the feedback. A clear modulation at 450 kHz is visible. This corresponds to an axial atomic oscillation of $f_{axial} = 225$ kHz. This value is more than a factor of two away from the expected value of 520 kHz. The radial feedback causes a slight decrease in the average trap depth, which only lowers the expected value slightly. A different method to measure the oscillation, this time without radial feedback, is presented in the next section. However, the discrepancy between the detected and expected frequency has already been observed in previous works [77] and will be further elucidated in Section 5.4.

5.3.2. Fourier Analysis

A Fourier analysis is a very powerful method of identifying and analyzing periodic signals. Here it will be used as another method for examining the transmitted probe-field conveying information about the atomic oscillation frequency. In order to see the dependency of this motion on the trapping potential, scans for different trap depths were recorded (see Figure 5.6). The plots show the Fast Fourier Transform (FFT) of the transmitted probe-field. Unlike the previous measurement, the data was recorded employing the heterodyne technique, which will

be explained in Chapter 5.6. The data was sampled with 100 MHz and sub-divided in time into intervals of 4096 samples, corresponding to 41 μ s. The Fourier transform was performed separately on each of these intervals and its resulting absolute values of the spectrum were accumulated. The data obtained while the atom was captured in the cavity is normalized to the Fourier spectrum of an empty cavity. Figure 5.6 shows the ratio of the spectrum of the transmitted field for the coupled system over the empty cavity case. The frequencies are shifted so that the heterodyne carrier is at DC (direct current). As for the correlation measurement, $\omega_p - \omega_c = 0$ MHz.

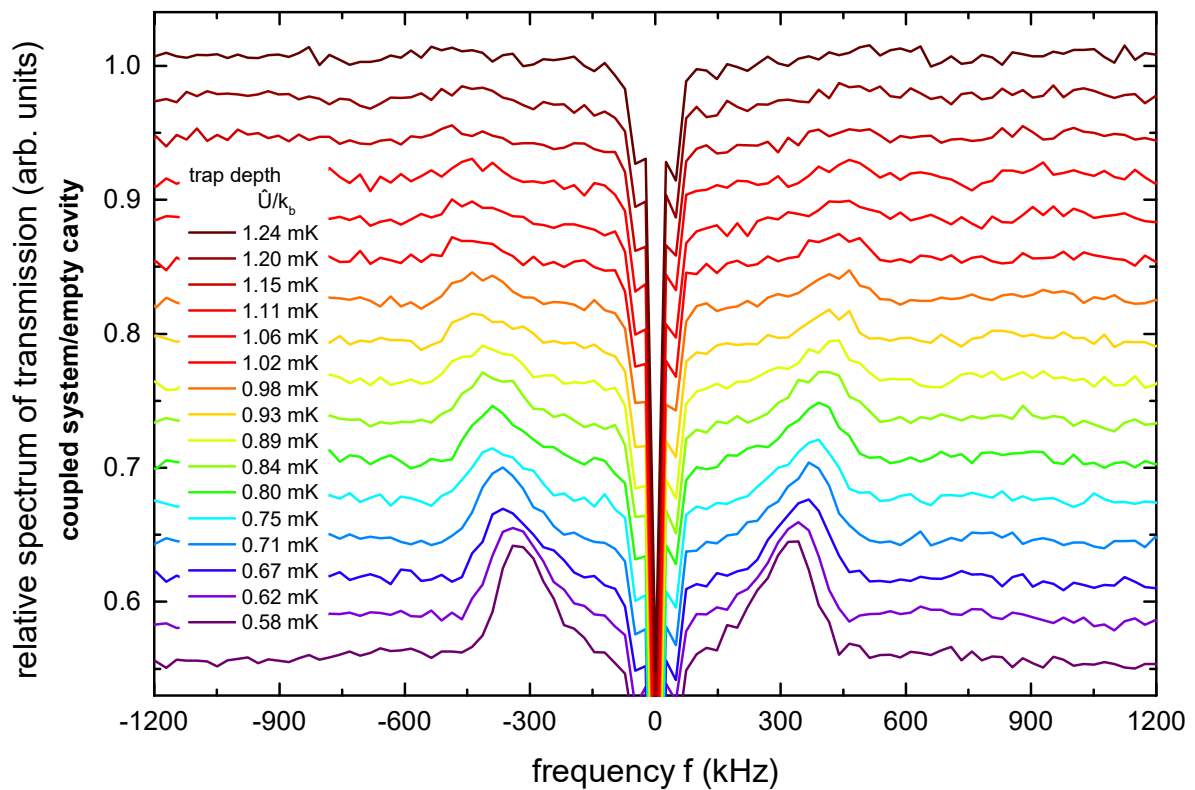


Figure 5.6: Fourier spectrum of the transmitted probe light. Experimental runs were carried out at different trap depth. The different plots are offset by 0.03 (arb. units) and color coded as indicated in the legend. A clear peak for low trap depth is visible around 300kHz which is shifting to higher frequencies and diminishing in amplitude for larger trap depths.

At 0 kHz a huge drop in the data can be observed. It is caused by the suppression of the DC transmission when an atom is coupled to the cavity-mode. Especially for low trap depth around 600 μ K a clear peak around 300 kHz is visible. This peak can be attributed to the axial motion of the atom. When the trap power is increased, the trap potential increases correspondingly. This leads first to a better confinement of the atom, resulting in a smaller amplitude of the oscillation and secondly to higher oscillation frequencies due to the increased steepness of the traps. Both features are clearly visible when going to plots recorded for larger trap depth. The modulation frequency can be extracted by means of peak fitting. This frequency corresponds to twice the atom's axial oscillation frequency. The obtained frequencies are plotted as a function of the trap depth in Figure 5.7.

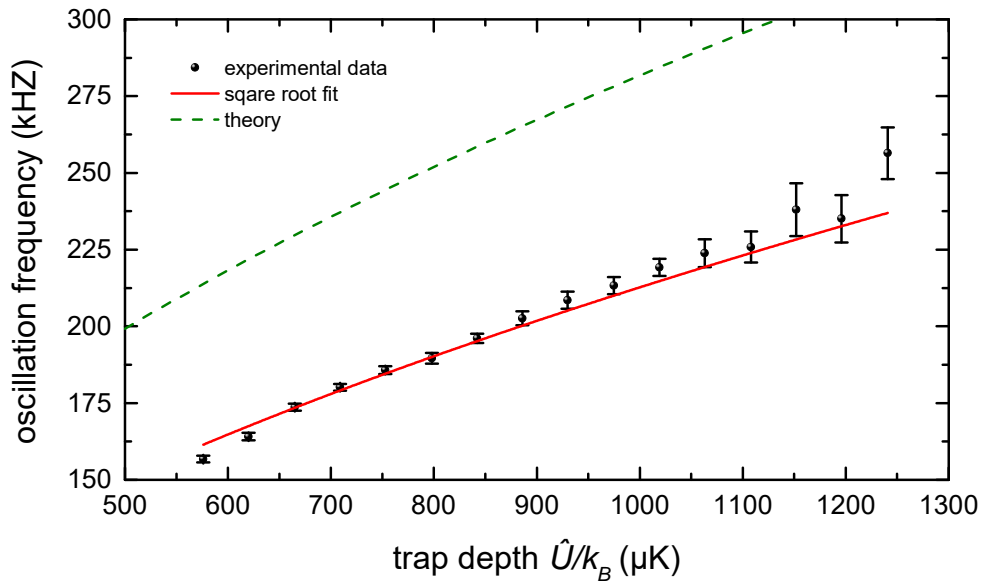


Figure 5.7: Detected oscillation frequency as a function of the trap depth. The data is recorded by means of a Fourier transform of the transmitted light. The experimental data points are indicated by black dots. The error bars are obtained from peak fitting. A square-root fit has been evaluated and is shown as red line. The theoretically expected values for the axial oscillation frequency are given by the dashed green line.

The experimentally obtained data-points show good agreement with the expected square-root behavior, as it is indicated by the fitted red line. Conversely the overall value is – as it was the case in the previous measurement – off by more than a factor of two. This deviation has already been observed in previous studies [77]. As both measurement methods, which have been presented, show the same deviation to the theoretical value, one has to consider using a completely different technique to determine the actual atomic oscillation frequency. A method based on parametric heating, overcoming this restriction, is described in the following section.

5.3.3. Parametric Heating

In this chapter a new technique for measuring the atomic oscillation frequency, essentially different to the previously mentioned ones, will be shown. Instead of measuring the transmitted photon flux, the atom is purposely being heated, i.e. forced to an oscillatory motion. If the induced motion coincides with one of the oscillation frequencies, the atom can quickly gain energy and will be lost from the trap immediately. The main advantage of this measurement technique is the direct actuation on the atom. It is put into practice by a RF modulation of the dipole-trap intensity. Due to the low bandwidth of the PID controller which is stabilizing the intensity (typically below 100 kHz), this modulation needs to be applied behind the PID's output. A mixer from mini-circuits accomplishes this task. A modulation depth of 45 μK was chosen. This is sufficiently small compared to the trap depth but still has a significant influence on the atom. The actual, measured trap intensity is plotted in Figure 5.8 d). The experimental run is performed with the same parameters as mentioned before (cf. Section 5.3.1), i.e. the cavity being on resonance with the atom. Atoms are launched from underneath and as soon as

the atom is detected, the trap is switched to its high value and the modulation is activated. In case of the plot, the modulation frequency was set to 700 kHz and is clearly visible. Atoms are captured in the cavity for three different trap depths. For each trap depth a scan of different modulation frequency is performed one after the other and the average storage time is measured. The result is plotted in Figure 5.8 a)-c).

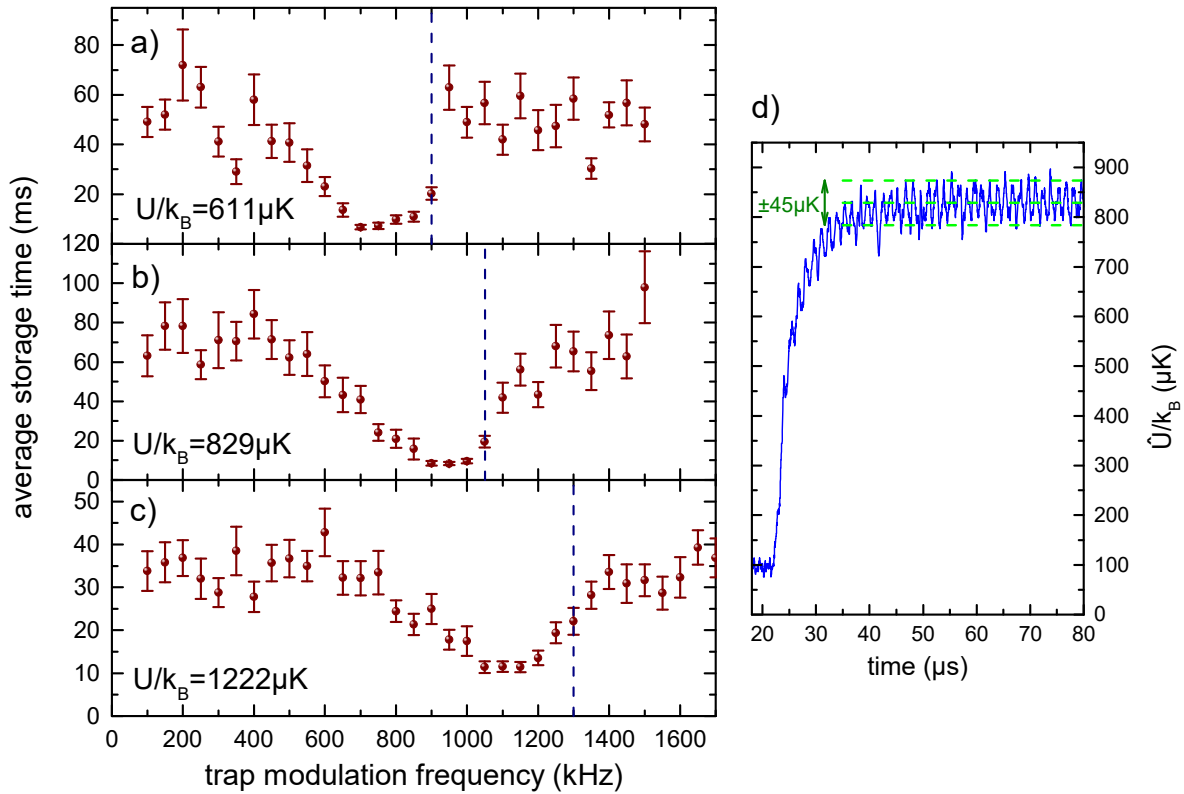


Figure 5.8: a)-c) Parametric heating of atoms. The average storage time is plotted as a function of the applied modulation frequency of the dipole trap. Different trap depths are shown in each of the sub-figures a)-c). The frequency above which atoms are not heated anymore is depicted by a dashed line in each sub-figure. This frequency is evident by an increase in storage time. d) Modulation of the trap beam. The temporal evolution of the dipole trap depth is recorded. An atom is caught at $\sim 22 \mu\text{s}$ as it can be seen by the steep increase in the trap depth. The dashed light green lines indicate the modulation amplitude in positive and negative direction.

Each graph shows a clear reduction of the average storage time for a certain range of modulation frequencies. On the low-frequency side, this drop is shallow while a steeper drop is observable on the high-frequency side. Coming from high frequencies, we attribute the drop to the onset of parametric driving of the atom at its harmonic oscillation frequency. At this frequency kinetic energy can add up coherently and cause the atom to escape. For lower frequencies a similar but not so drastic effect is visible. Here, the atom needs to acquire a certain amount of kinetic energy to shift its resonance frequency down, before parametric heating occurs: The accumulation of kinetic energy leads to larger excursions, which in turn causes a break-down of the harmonic approximation (see following Section 5.4). In this case, the atom's – now anharmonic – oscillation frequency is reduced. Parametric heating now occurs at lower frequencies as it can be seen by the soft shoulder in the reduction of the storage time. Since the parametric driving

frequency corresponds to twice the atom's oscillation frequency, we can extract the atom's harmonic oscillation frequency from the sharp onset of the parametric driving on the high-frequency side, as it is shown in Figure 5.9.

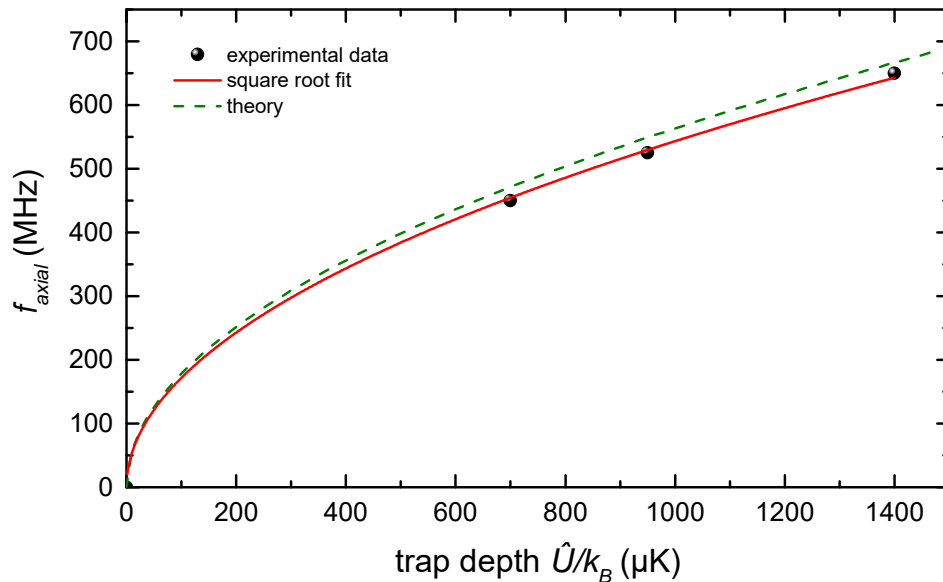


Figure 5.9: Onset of parametric heating as function of the trap depth. The experimental data points are marked by black dots. A red line shows a fitted square-root curve. The theoretically expected behavior is plotted as dashed green line.

The obtained data points follow nicely the expected square-root behavior, cf. Eqn. (5.5). The obtained fit is indicated by the red line. In contrast to the previous measurements, the theoretically calculated values, indicated by the dashed green line, agree now well with the measured data points. The small remaining discrepancy can be explained due to small deviations associated in gauging the trap depth. This gauging was performed by a heterodyne measurement as it will be described later in Section 7.6. The parametric heating technique hence is a useful and simple method to gain information about the harmonic oscillation frequency of an atom. On the other hand, providing that this frequency is known, it can also serve for gauging the trap depth. In the next section an explanation will be developed showing where the discrepancy between the parametric heating method and methods relying on a frequency analysis of the transmitted photon stream stems from.

5.4. Anharmonic Oscillator

The break-down of the harmonic approximation for increasing atomic excursions is the key driver for deviations of the observed atomic oscillation frequency, obtained by analyzing the transmitted photon stream, from its expected value. These values on the other hand are successfully confirmed by a parametric heating measurement. The harmonic approximation was already described in Section 5.2. As it can be seen in Figure 5.2, the actual trapping potential yields substantially shallower trapping potentials than the harmonic approximation starting from atomic excursion beyond $7 \mu\text{m}$ for the radial and 70 nm for the axial direction,

respectively. These excursion levels are reached once the atom possesses a kinetic energy around $300 \mu\text{K}$, assuming typical depth of the dipole trap potential of $850 \mu\text{K}$. When this level is reached, the deviations from the harmonic approximation cause an actual oscillation frequency which is below the corresponding harmonic value. This anharmonic oscillation frequency is computed for different maximum excursion levels of the atom with a numerical simulation. The result is plotted as a function of the axial and radial excursion separately and is depicted in Figure 5.10. The harmonic boundary values $f_{rad, hm}$ and $f_{axial, hm}$ are indicated by the solid red lines.

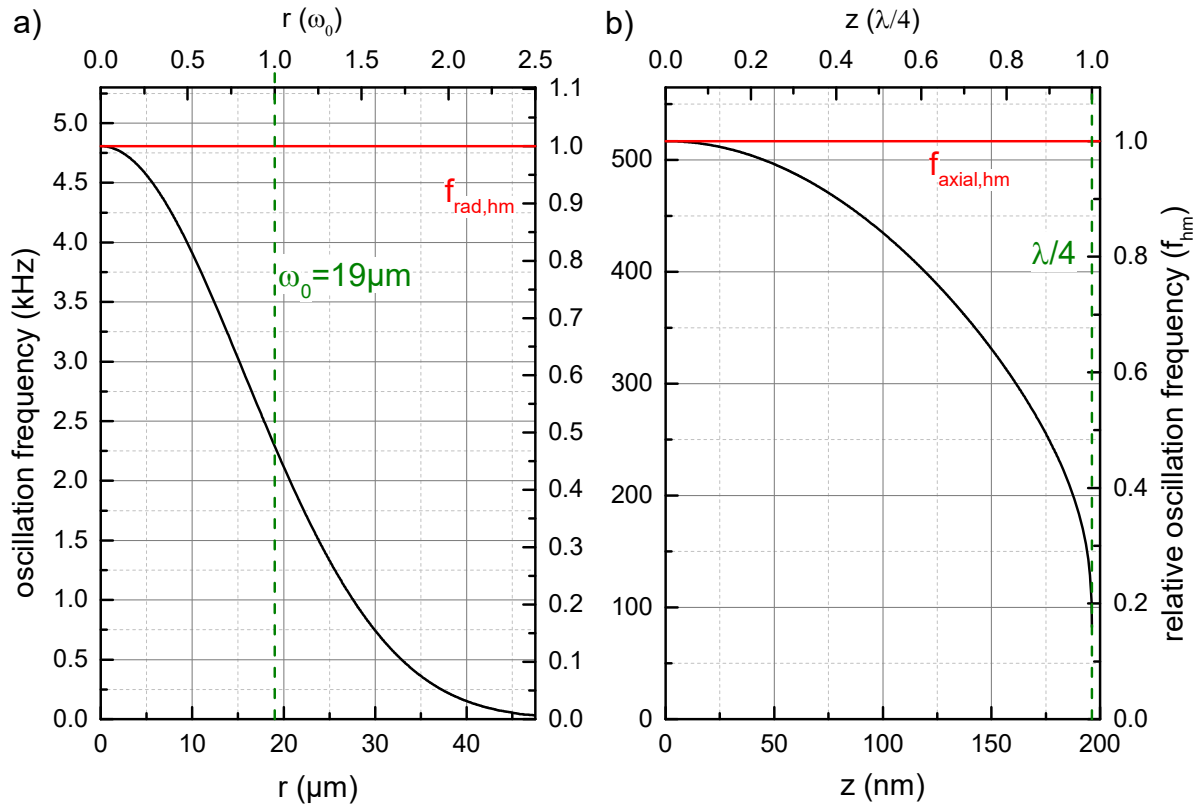


Figure 5.10: Deviation of the oscillation frequency from its harmonic value, once the harmonic approximation breaks down. The behavior of the oscillation frequency is shown for excursions of the atom in the radial direction r a) and in the axial direction z b). Each left vertical axis shows the frequency in kHz while the right axis features its relative value compared to the respective harmonic boundary value. The excursion is given once in absolute values for our cavity parameters (lower axis) and once with respect to the respective typical length scales (upper axis), as they are also indicated by the dashed, vertical, green lines. A decrease of the oscillation frequency down to 0 Hz is visible in both cases.

As expected, a significant drop in the actual oscillation frequency is visible as the excursion of the atom increases. This occurs when the atom is heated up and hence increases its oscillation amplitude. When interpreting the measurements of the oscillation of the atom by means of a spectral analysis of the transmitted probe power (cf. 5.3.1, 5.3.2), it is important to examine the modulation strength of the probe beam corresponding to different excursion amplitude of the atom. In order to determine the modulation strength, one has to consider the probe-light transmitted through the cavity. This light depends on the position-dependent coupling constant $g_{eff}(r, z)$ as given by Eqn. (5.6) and shown in Figure 5.3. The motion of the atom hence leads to

a modulation in the transmission. The strength of this modulation is given by the difference of the minimal and maximal transmission per oscillation period. Since the oscillation amplitude corresponds to its maximum excursion depicted in Figure 5.10, one can assign a relative modulation strength of the transmitted probe beam for every anharmonic oscillation frequency. These values are depicted in Figure 5.11 and indicate how well each frequency component will be visible in the transmitted probe beam spectrum. As visible from Eqn. (5.6), a mismatch of the center of the trapping and probing mode will result in a different effective coupling strength. This is why the behavior is evaluated for two different scenarios. In the first both modes overlap perfectly, causing $z_0 = 0\text{nm}$ and in the second both modes are offset by $z_0 = 76\text{nm}$. This has been proven to be a typical average value for our system, cf. [81].

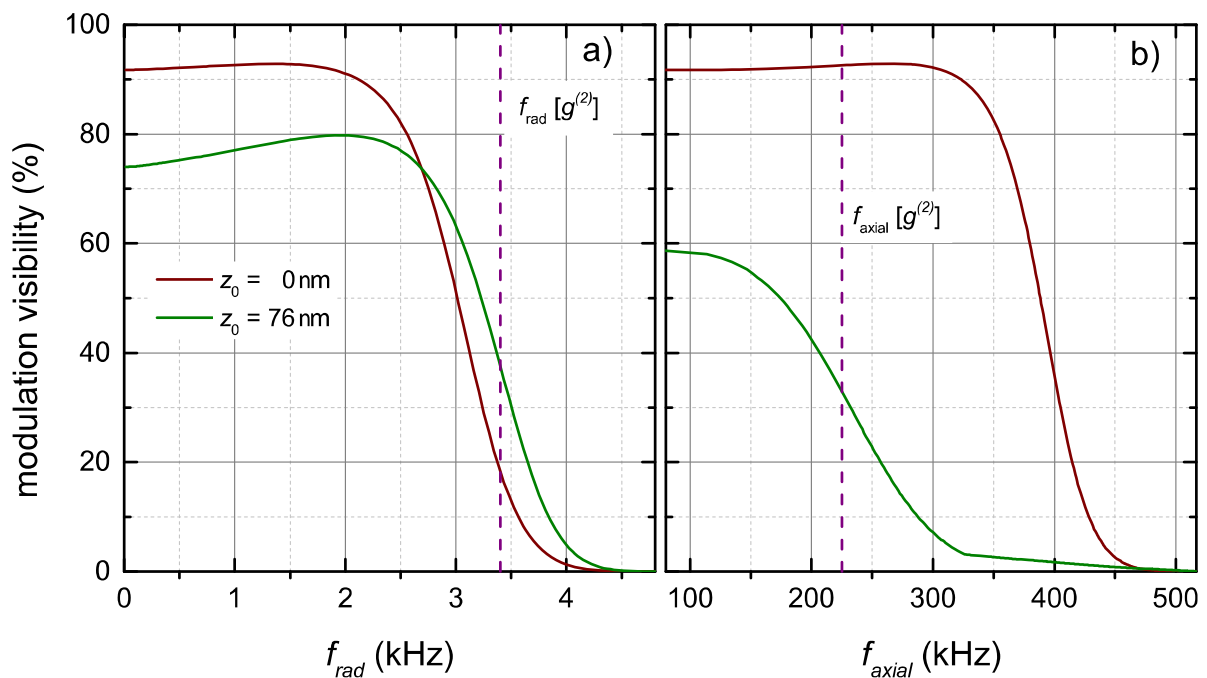


Figure 5.11: Visibility of the modulation of the transmitted probe signal for different oscillation frequencies of the atom in the cavity mode. The anharmonicity of the trapping potential causes the oscillation frequencies of the atom to depend on its oscillation amplitude. The relationship is plotted separately for the radial oscillations a) and for the axial oscillations b). Two scenarios are depicted, once for the case that the dipole trap and probing mode exactly overlap $z_0=0\text{ nm}$ (brown curve) and once for the case that both modes are offset by a typical value of $z_0=76\text{ nm}$ (green curve). The dashed vertical line indicates the measured atomic oscillation frequencies from the correlation measurements.

The plots show that hardly any information about an atom oscillating at its harmonic oscillation frequency is encoded in the transmitted probe light. Only when the atom has acquired a certain kinetic energy, which results in a larger oscillation amplitude and reduced frequency, its motion becomes “visible”. This is also the reason why any measurement of the transmitted probe beam will output drastically smaller oscillation frequencies. The frequencies measured via the second order correlation function are also indicated by the vertical dashed lines in Figure 5.11. These frequencies exactly mark the border of the region above which the visibility of the frequency components is significantly reduced. Thus, this confirms our initial hypothesis, that when measuring the spectral properties of the transmitted probe beam we will mainly detect the

spectrum of anharmonic oscillation frequencies, while with the parametric heating measurement we do not rely on the visibility of the motion, and can hence address the real harmonic oscillation frequency. In the following section we will show how we can use the information encoded in the transmitted probe beam nevertheless to cool the motion of the atom.

5.5. Feedback on a Single Atom

As described in the previous section, information about the atomic motion is conveyed by photons which are transmitted through the cavity. Even though the amount of information is limited due to the quantumness of our system, we can still extract sufficient evidence to feedback on the motion of the atom. In this section the basic concept of a feedback loop will be introduced (see Sub-section 5.5.1). Afterwards, two different feedback strategies will be explained and their performance will be measured. The first one aims to detect when the atom is moving towards and away from the cavity center (see Sub-section 5.5.2), whereas the second one uses pre-knowledge about the atomic oscillation to predict the atoms future trajectory (see Sub-section 5.5.3). While both yield excellent results for oscillations in the radial direction, only the latter one allows an extension to the fast axial oscillation of the atom (see Sub-section 5.5.4).

Part of the results presented in this section have been published in:

“Continuous parametric feedback cooling of a single atom in an optical cavity”

C. Sames, C. Hamsen, H. Chibani, P. A. Altin, T. Wilk, and G. Rempe; Phys. Rev. A **112**, 053404 (2018)

5.5.1. Basic Idea

Every feedback loop can be broken down into 4 stages. These are a change in the parameter under control, the observation of this parameter, the interpretation of the gathered data and last the actuation back on the parameter. In the concrete case of our system, they are the actual motion of the atom, i.e. the change of the atomic position with respect to the cavity, the observation of that motion, the real-time processing of the acquired data by the feedback algorithm and finally the actuation back on the atomic motion, as they are depicted in an illustrative way in Figure 5.12. The efficiency of the feedback depends crucially on two parameters, which are the accuracy of the actual measurement and the reaction time of the feedback circuit. The latter one is the time necessary to go through one iteration of the loop and was mainly limited in previous experiments by the real-time processing capabilities of the computing device. The employment of FPGAs, as they were described in Chapter 4, permits to lift the computational limitations into a regime where only the physical availability of information sets the limit.

For the experiments carried out in this section, we assume a probe-cavity detuning of $\omega_p - \omega_c = 0$ MHz and an effective atom-cavity detuning of $(\omega_a - \omega_c)/2\pi \approx -5$ MHz. In this case a low transmission yields a good overlap of the atom with an antinode of the probe-field.

As this overlap decreases, the transmission increases until the atom is lost and the transmission reaches its maximum value, which will be referred to as the empty cavity transmission. The actuation is achieved by changing the depth of the dipole trap inside the cavity. Since the intensity and frequency of the trap laser is controlled by an AOM, this is accomplished by changing the amplitude of the RF frequency driving this AOM (cf. Section 3.3.3).

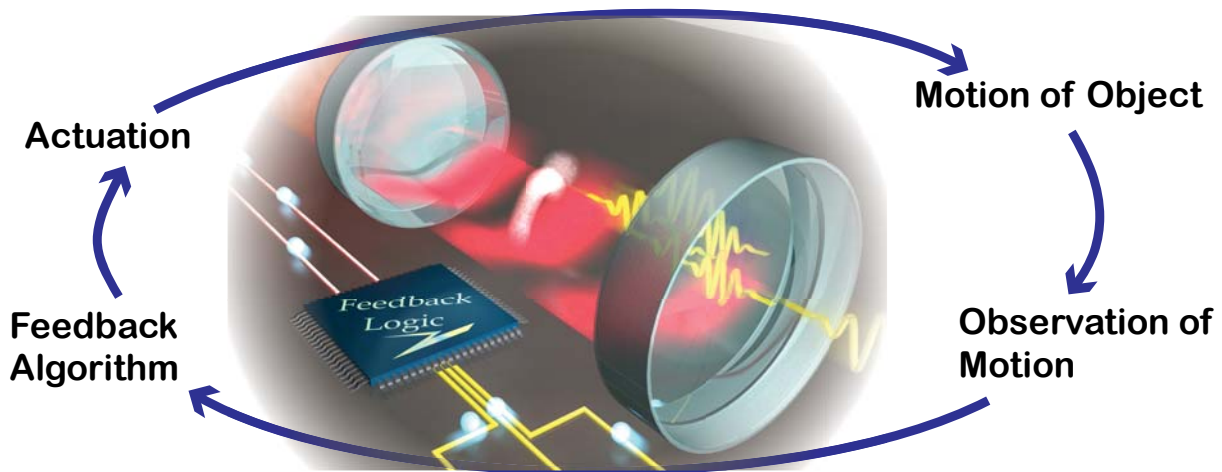


Figure 5.12: Illustration of the basic idea of the feedback loop. The motion of the atom, i.e. the atomic position with respect to the cavity, is the key parameter which shall be influenced. This motion is observed and the information gathered is transferred to the feedback algorithm. The algorithm interprets the data and sends a command to the actuation mechanism, which in turn alters the motion of the atom. Now the whole loop restarts.

5.5.2. Bang-Bang Feedback

A very intuitive approach to implement a feedback strategy consists in simply considering whether the atom is moving away or towards the cavity center. This is achieved by determining the slope of the transmitted probe intensity. As an example, an increase in the photon-flux corresponds to a decreasing overlap between the probe-field mode and the atomic position. This corresponds to an atom which is moving away from the center of the antinode and hence away from the cavity center. In order to damp the motion of the atom, the depth of the potential valley, created by the dipole trap, is altered. When the atom is moving outward, the potential valley is switched to a high value and vice-versa, when it is moving inward. Since this feedback routine only assumes two discrete values for the dipole trap, it is thus termed “bang-bang” feedback. Due to the fact that the bang-bang feedback only reacts on changes in the photon flux, its integration time needs to be smaller than a typical oscillation period. The advantage of this “naïve” behavior is that no previous knowledge about the system is needed. However, the low probe power with the associated limited photon flux renders this mechanism impossible for feedback cooling of the axial motion, since the required probe-powers would heat and eventually also saturate the atom. As it was shown in Section 5.2, the timescales for the radial and axial oscillation periods differ by two orders of magnitude and hence permit to treat both directions separately. This ensures that this feedback method is applicable for the radial motion. A detailed description of this feedback strategy can be found elsewhere [56]–[58]. Here, the

objective is to give a short introduction which allows for a better comparison with the new feedback algorithm to be introduced in Section 5.5.3.

A systematic overview of the bang-bang feedback routine is depicted in Figure 5.13. The 4 photon counters are connected to an FPGA, which records the single clicks (cf. Section 4.4). For further processing, all clicks are handled equally irrespective from which SPCM they stem from. It is hence equivalent to having a single SPCM. An edge-counter outputs the number of detected photon clicks every 32 ns. This signal passes a moving average filter, whose 3dB bandwidth depends inversely on the exposure time T_{exp} and amounts to $0.44 \cdot T_{\text{exp}}^{-1}$. The exposure time defines the length of the moving average filter and is typically set to 16 μs , so that the filter corresponds to a 28 kHz low-pass filter. Afterwards, the signal is compared to its delayed duplicate. The delay time amounts to $m \cdot 32\text{ns}$ and is usually chosen to be equivalent to the exposure time. Depending on whether the difference falls below a threshold value (normally two photon clicks), a digital channel signals whether the low or high trap power is output, respectively.

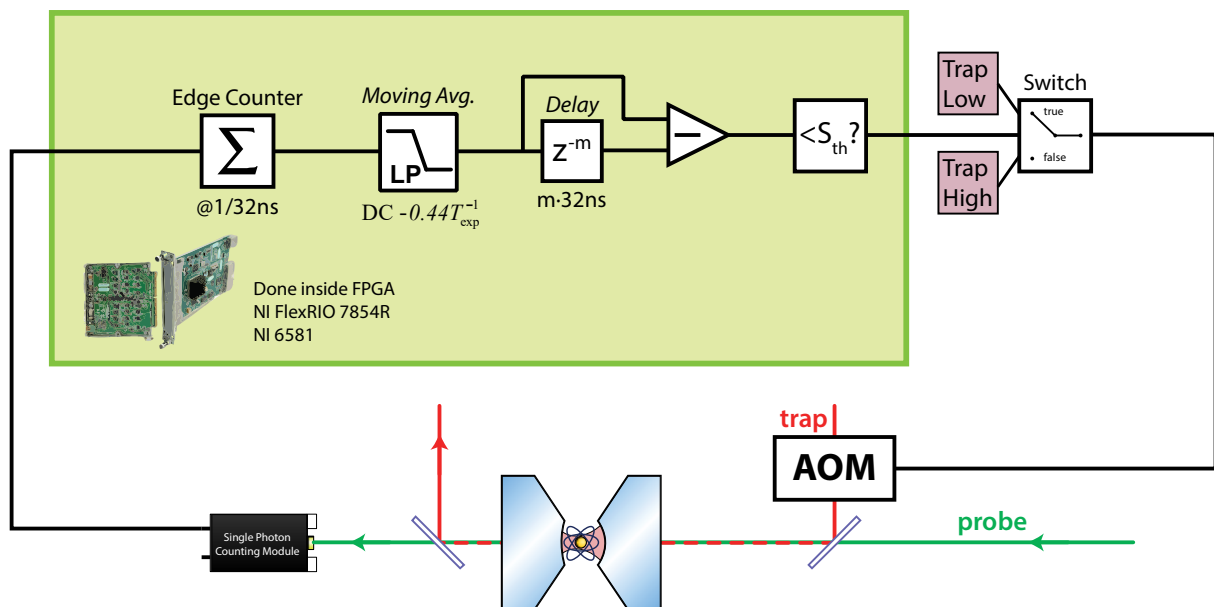


Figure 5.13: Schematic overview of the bang-bang feedback routine. The light of the probe beam is transmitted through the atom-cavity system. Its amplitude is recorded by an SPCM (for simplicity the array of SPCMs is shown as a single SPCM), which emits a digital pulse upon detection of a photon. The pulses are fed into an FPGA and counted by an edge counting unit. A signal representing the number of clicks per time interval is low-passed by a moving average filter. The temporal evolution of this signal is detected by comparing the current signal to its delayed facsimile. Depending on whether this evolution is below or above a certain threshold value, a digital channel is asserted. This controls a switch, sending the high or low dipole trap set-point to the AOM unit, which in turn alters the power of the intracavity dipole trap.

The entire processing described before is done inside the FPGA. This ensures that the speed and effectiveness of the feedback is not limited by the computational unit. The switching of the dipole trap to the desired value is achieved by an external switching chip. Its output signal is passed to the set-point input of the stabilizing PID of the dipole trap. It is crucial to have the parameters of the PID controller adjusted correctly, so that the actual switching of the dipole trap is achieved fast enough but no overshooting occurs. The bang-bang feedback measurement

has been carried out in a collaborative effort together with Koch. In his thesis “*Classical and Quantum Dynamics of a Strongly Coupled Atom-Cavity System*” [81] a detailed description and analysis of the results sketched briefly in this sub-section can be found. Here we will only summarize – for reasons of completeness – the two major results, which are also plotted in Figure 5.14.

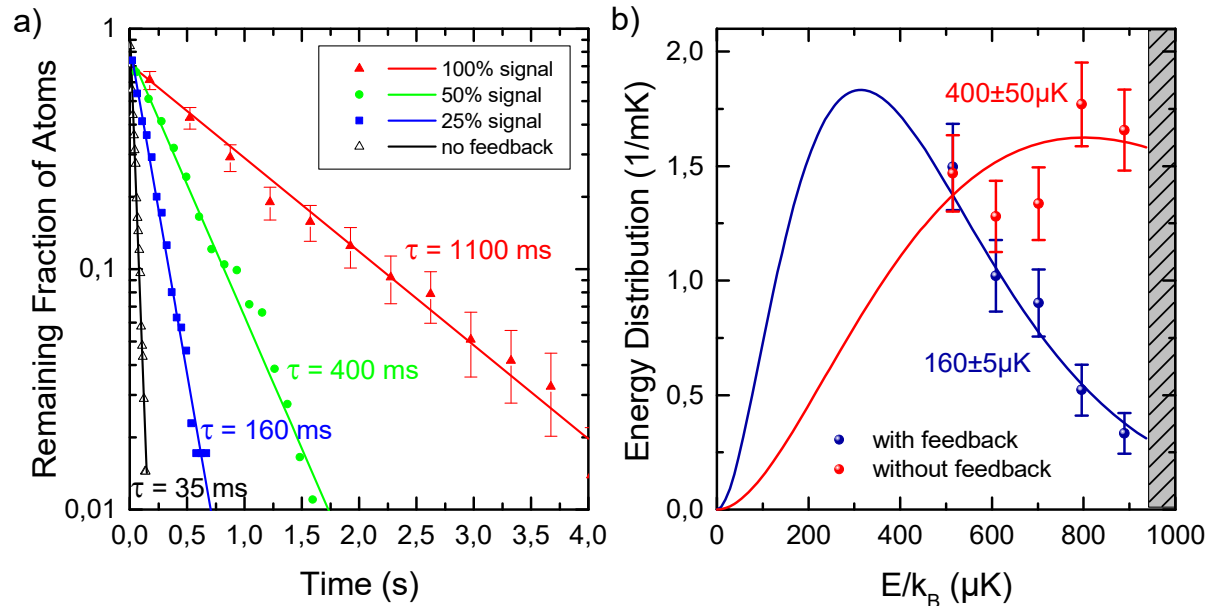


Figure 5.14: Performance of the bang-bang feedback routine. Graphs taken from Koch [81]. a) Increase of storage time of captured atoms. The remaining fraction of atoms after a certain storage time is plotted. The data is recorded for an ensemble of sequentially captured single atoms. The data-points are indicated by symbols and an exponential fit is shown as solid line in the respective color. The colors represent which percentage of the recorded photon clicks is processed by the feedback routine. In case of the black line, the feedback was fully turned off. As more atoms are lost during the first few μs the lines do not necessarily cross the ordinate axis at zero. b) Cooling of atoms by means of fast electronic feedback. The energy distribution is deduced for an ensemble of captured atoms. A three-dimensional Boltzmann fit permits to extract a temperature. Plots for feedback activated (blue) and deactivated (red) are presented.

The most obvious effect becomes evident in a storage time measurement, which is depicted in part a) of the figure. In this plot the remaining fraction of atoms after they were trapped for a certain amount of time is shown. The numbers are evaluated from an ensemble of single atoms which have been trapped in the cavity one after the other. An exponential fit yields the decay time, which corresponds to the average storage time. For the black curve the feedback was turned off and the atoms stay on average for 35 ms in our cavity. This time gets significantly increased as soon as the feedback is turned on. If 100% of the detected signal is fed into our feedback algorithm, average storage times of more than 1 second are achieved. This corresponds to an impressive increase by more than a factor of 30. The performance is limited by the amount of information which can be extracted from the data. It can be seen that a reduction²² of the signal fed into the feedback-routine considerably degrades its performance.

²² The reduction is accomplished by simply disconnecting some of the SPCMs. Since the incoming photon clicks are truly randomly distributed among the 4 SPCMs, this equals a reduction in the detection efficiency.

General parameters	
Probe-cavity frequency detuning	$\Delta_{pc}/2\pi = 0$ MHz
Atom-cavity frequency detuning	$\Delta_{ac}/2\pi = -5$ MHz
Probe power	$P_{probe} = 0.5 \text{ MHz}/(\eta_{SPCM} \cdot \eta_{out}) \cdot \hbar\omega_p = 450 \text{ fW}$
Dipole trap power	$P_{trap,low} = 400 \text{ nW}$ $P_{trap,high} = 950 \text{ nW}$
Feedback parameters (bang-bang feedback)	
Integration time	$T_{exp} = 16 \mu\text{s}$
Delay between two intervals	$T_{delay} = 16 \mu\text{s}$
Threshold value	$S_{th} = 2$

Table 5.1: Overview of the optimal settings of the radial bang-bang feedback. The settings have been determined in various scans and are employed for majority of the depicted graphs.

Since a better confinement of the atom, as it could in principle also be achieved by simply increasing the dipole trap depth, would also lead to an extension of the storage time, it is important to show explicitly that the feedback is indeed a cooling technique for the atomic motion. In order to do so, the temperature of an ensemble of sequentially trapped single atoms is measured. Atoms are stored for 10 ms with or without feedback, respectively. Afterwards, the trap is ramped down slowly and the time at which the atom escapes is determined. This enables to reconstruct the energy distribution. The result is plotted in Figure 5.14 b). A three-dimensional Boltzmann fit yields a temperature reduction from $400 \pm 50 \mu\text{K}$ to $160 \pm 5 \mu\text{K}$. This shows that fast electronic feedback is indeed capable to cool the motion of single trapped atoms down to temperatures slightly above $150 \mu\text{K}$.

The positive results of the feedback cooling scheme led to employing this as a standard means to increase the storage time of single atoms in order to perform additional experiments. This hence leads to a significant increase in the duty cycle of the experimental setup, which requires around 2 seconds for loading and capturing the atoms. Some typical traces where a single atom was captured for more than 10 seconds are depicted in Figure 5.15. While plots b) and c) are recorded with the optimal parameters, which have also been used for the previous measurement, plot a) was recorded with higher probe power, corresponding to 0.2 intracavity photons on the empty cavity resonance. The optimal parameters are also given in Table 5.1. In all plots the effect of the feedback cooling is clearly visible. Spikes in the traces appear, indicating where the atom acquired a certain amount of kinetic energy. In case no feedback is applied, this would normally lead to an abrupt loss of the atom. Nevertheless, the feedback is able to cool this motion and keep the atom in the cavity. A second interesting effect becomes evident, especially in Figure 5.15 b), the region between 4.5 seconds and 8 seconds shows an increased offset of the transmitted probe beam. We assume this to be caused by “hops” of the atom along the cavity axis from one antinode of the dipole trap to the next. As the overlap of the probe beam and the dipole trap varies over the length of the cavity, axial hopping over multiple antinodes could well explain this behavior. This behavior is, however, not the scope of this thesis and can be verified by observing the atom with a high sensitive EMCCD camera [111].

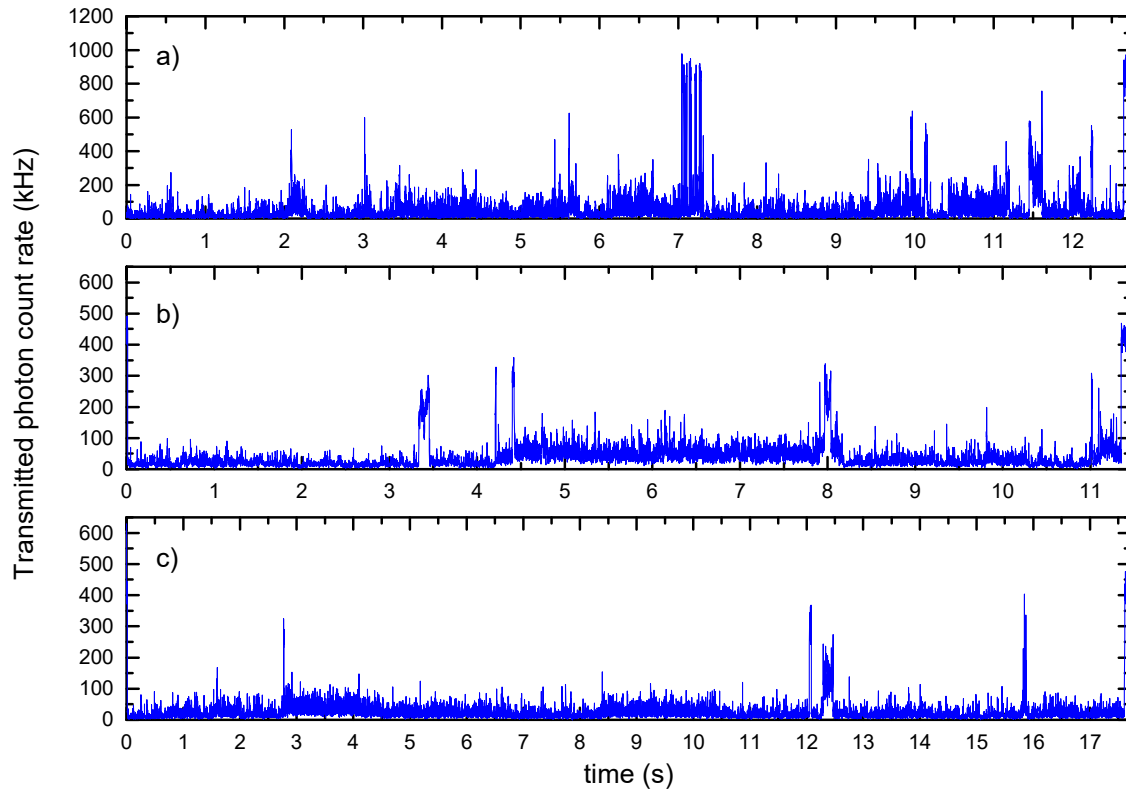


Figure 5.15: Typical traces of the transmitted probe power for the bang-bang feedback at work. The photon count rate of the transmitted probe power is plotted as a function of the capturing time. While part a) was recorded for a probe power of 0.2 intracavity photons for the empty cavity, part b) and c) are recorded for values of 0.1 intracavity photons. The loss of the atom is visible by the increased transmission towards the end of each trace.

5.5.3. Radial Parametric Phase Feedback

The pre-knowledge we have about the atomic motion can be used to enhance the performance of our feedback [60]. This is essentially different to the previous strategy where no *ab initio* knowledge about the system was needed and the “decision” was based on the history of photon clicks over a period shorter than the period of the oscillation itself. Usage of the pre-knowledge enables to consider the history of the system on a timescale solely determined by the coherence time of the oscillation, i.e. the time during which the phase of the mechanical oscillation of the atom stays predictable. This time can be deduced from the number of peaks visible in the second order correlation function (see Section 5.3.1) and is further verified by a derivation of the q -factor of the atomic oscillation (see Section 5.5.3.2). In our case, the timeframe considered for the feedback decision is typically around two oscillations of the atom. This feedback algorithm hence considers substantially longer time intervals than the previously explained bang-bang feedback. Thus, it reduces the signal-to-noise ratio of the input signal and hence enhances the quality of the prediction itself. The technical implementation on the other hand of this so-called “parametric feedback” strategy is significantly more complex.

5.5.3.1. Implementation/Working Principle

Our system can be described as a parametric oscillator, which is a harmonic oscillator whose parameters alter in time. An intuitive example of such an oscillator is a child pumping while standing on a swing [143]. By bending its knees, the oscillation frequency alters. Assuming that the child performs a sinusoidal movement of its center of gravity, the equation of motion can be written as:

$$\ddot{x}(t) + \gamma \cdot \dot{x}(t) + \omega_0^2 \cdot (1 + A_d \cos(\omega_d t)) \cdot x(t) = 0 \quad (5.7)$$

Here, ω_d is the driving frequency with magnitude A_d . The damping of the oscillation is given by γ . The underlying physics corresponds to our case. However, instead of bending the knees, the depth of the potential valley where the atom is trapped is changed, which in turn also leads to a variation in the oscillation frequency as described in Section 5.3.2 and shown in Figure 5.6. The knowledge about this motion will be employed for refining the feedback strategy.

The idea of the parametric feedback strategy is somewhat similar to the parametric heating described earlier (cf. Section 5.3.3). For the parametric heating the mechanical oscillation of the atom was driven by applying a steady sinusoidal modulation close to the mechanical resonance frequency of the atom. While for parametric heating the phase of the applied modulation was stable and did not change, this phase is continuously updated in case of the parametric feedback, based on the detected pattern in the recorded photon stream. As oscillations with increasing amplitude will show up in the transmitted photon stream, it is possible to phase-lock the applied modulation to the detected oscillation in the photon stream. If the phase difference is now set in such a way that the applied modulation of the trap is phase-shifted by $+\pi/2$ to the detected oscillation, the alternating trap depth will counteract the motion of the atom, damping it and hence lead to cooling. In this case the feedback predicts the future evolution of the system and the applied modulation is advanced by $+\pi/2$ to the excursion of the atom. This parameter will hence be termed phase advance $\phi_{pfb} = \phi_{Mod-out} - \phi_{atomic\ motion}$ in the following. Based on its origin of parametric heating and cooling, this feedback strategy is hence called “parametric feedback”. A schematic overview of its implementation into the FPGA also responsible for the photon counting is found in Figure 5.16. In order to ensure that no phase drift between the detected and applied modulation occurs, it is important to note that the phase of the output modulation needs to be locked to the clock of the FPGA, which also clocks the detection of the oscillation.

Two crucial parameters need to be set in advance before the feedback starts to work. These are the frequency f_{pfb} , at which the feedback will operate, and the phase advance ϕ_{pfb} , which gives the phase relationship between the output modulation and the detected oscillation. The feedback starts by summing the number of photon clicks it received during the past 8 ns. This signal is sent through a moving average low-pass filter with a 3dB bandwidth of 3.2 MHz. The oscillation strength and phase position at f_{pfb} is determined by performing a discrete Fourier

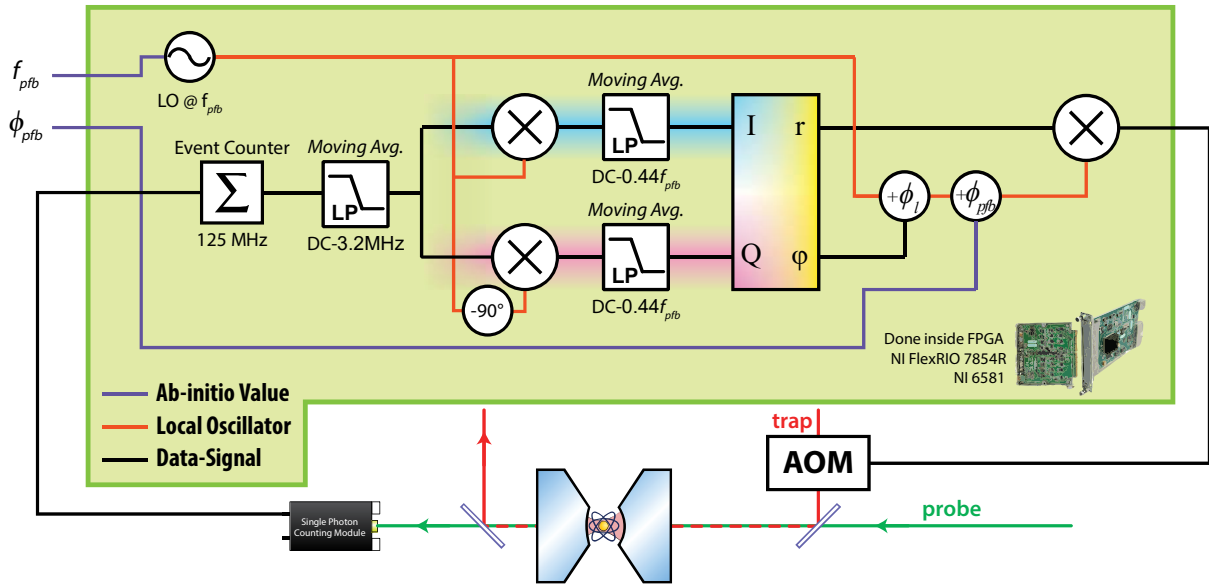


Figure 5.16: Scheme of the implementation of the parametric feedback routine in the FPGA. Clicks from the photon counters (here depicted as a single one) are sent to an FPGA. An event counter running on a 125 MHz clock adds up all recorded photon clicks per 8ns interval. This number passes a moving average low-pass filter and is multiplied with a local oscillator, which is generated inside the FPGA at the frequency f_{pfb} as well as its -90° phase-shifted facsimile. Subsequently moving average low-pass filters are applied. A complex-to-polar converter (I , Q to r , ϕ) in the end yields the magnitude and phase of the detected oscillation at f_{pfb} . This information is used to phase-lock the local oscillator to the detected oscillation. The phase of the local oscillator is additionally shifted by f_{pfb} before the magnitude information is employed to adjust the amplitude of the output oscillation.

transform at this frequency. In order to do so, the signal is multiplied by a local oscillator and its 90-degree phase-delayed facsimile. The two channels represent the complex oscillation amplitudes at f_{pfb} . They each pass a moving average filter, whose length is adjusted to match an integer multiple of the oscillation period. Non-integer multiples can lead to significant artefacts, especially whenever the integration length is on the order of only a few oscillation periods. In our case we have chosen an averaging length equal to only one oscillation periods. In this case, the filter acts as a low-pass with a 3dB bandwidth of $0.44 \cdot f_{pfb}$. A subsequent complex-to-polar converter extracts the magnitude and phase information. The phase information is used to phase-lock the local oscillator generated by the FPGA to the detected oscillation. The phase of the oscillator is additionally shifted by the phase advance ϕ_{pfb} parameter, which is set ab initio. The amplitude of the output oscillation can either be set to a fixed value or is varied depending on the magnitude of the detected oscillation.

The actual output of the feedback algorithm based on a real trace is shown in Figure 5.17. Part a) shows a full trace where the atom was captured for 25 ms in the cavity. During this time no feedback was applied. The black curve shows the signal recorded by our photon counting modules. The simulated response of the feedback circuit is depicted bellow. The red curve indicates the strength of the oscillation S_l found at a frequency of $f_{pfb} = 6.6$ kHz. The blue curve shows the detected phase ϕ_l at this frequency. S_l and ϕ_l correspond to the output of the complex-to-polar converter in Figure 5.16. As it can be seen nicely by looking at the phase

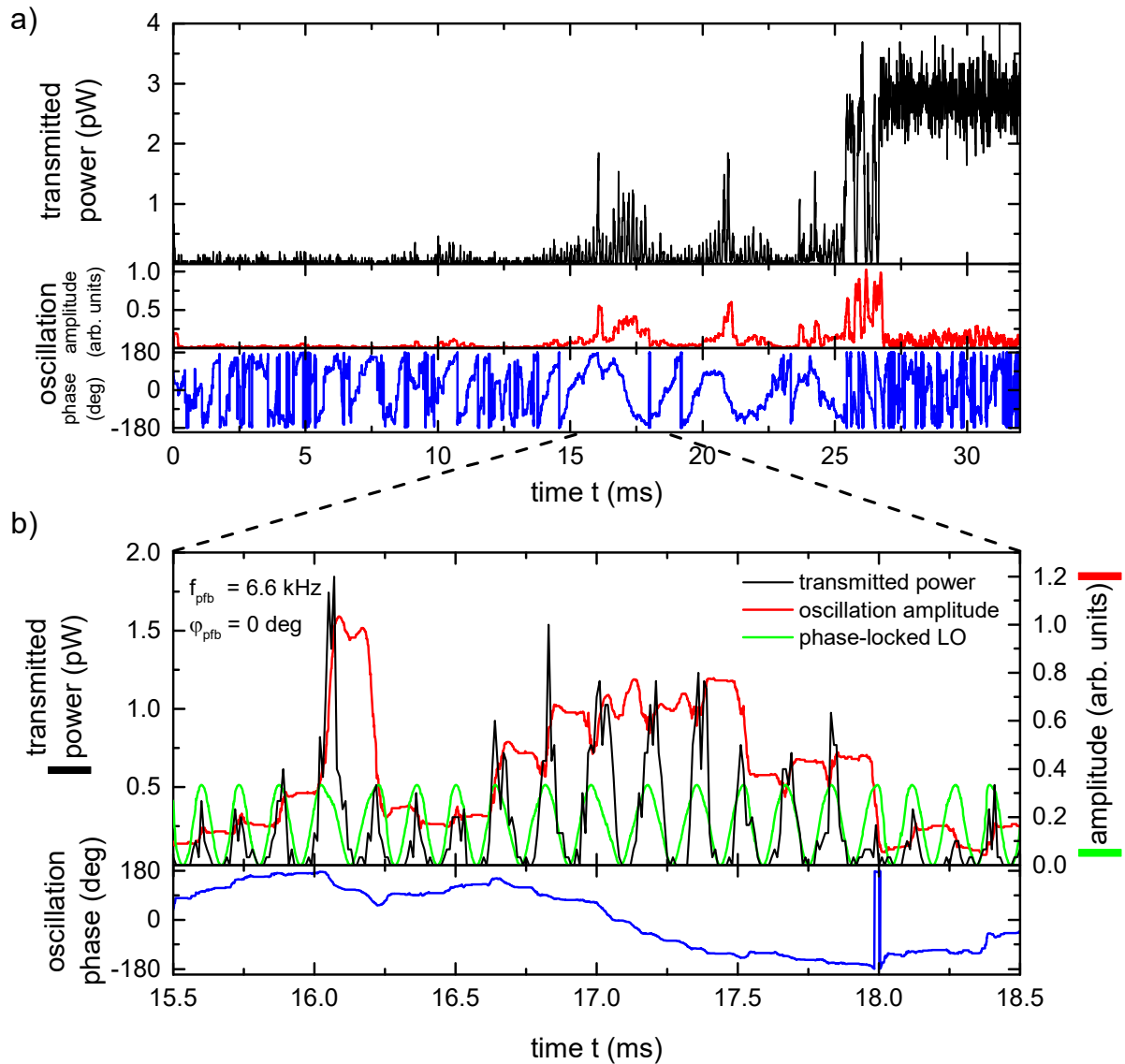


Figure 5.17: Working principle of the parametric feedback. a) Full trace of an atom which has been captured for 25 ms without feedback applied. The black line shows the transmitted power as recorded by the SPCMs. The red and blue line show the simulated values, which the parametric feedback would derive for the magnitude and phase of the detected oscillation respectively. b) Zoom into the region around 17ms. The depicted graphs are identical to part a). In addition, a green curve shows the local oscillator, which is phase-locked to the detected oscillation.

information, a clear oscillation is evident between 14 ms and 25 ms. During this time a clear and quite stable phase at the input frequency is found. This indicates that the atom is oscillating at a very stable frequency. Furthermore, an increase in the detected magnitude is also partially visible. Once the atom is lost, the transmitted power significantly increases, however, as expected, no oscillation at the feedback-frequency is detected. This is visible by a vanishing magnitude signal and a randomly fluctuating phase signal.

Part b) of Figure 5.17 shows a zoom into the region around 17 ms. Here, the oscillation is clearly visible. The detected magnitude of the oscillation is directly overlapped with the transmitted power, showing excellent agreement. In addition, the phase-locked local oscillator for a phase-advance of $\phi_{pfb} = 0^\circ$ is plotted as green line. One can nicely see that despite the anharmonicity

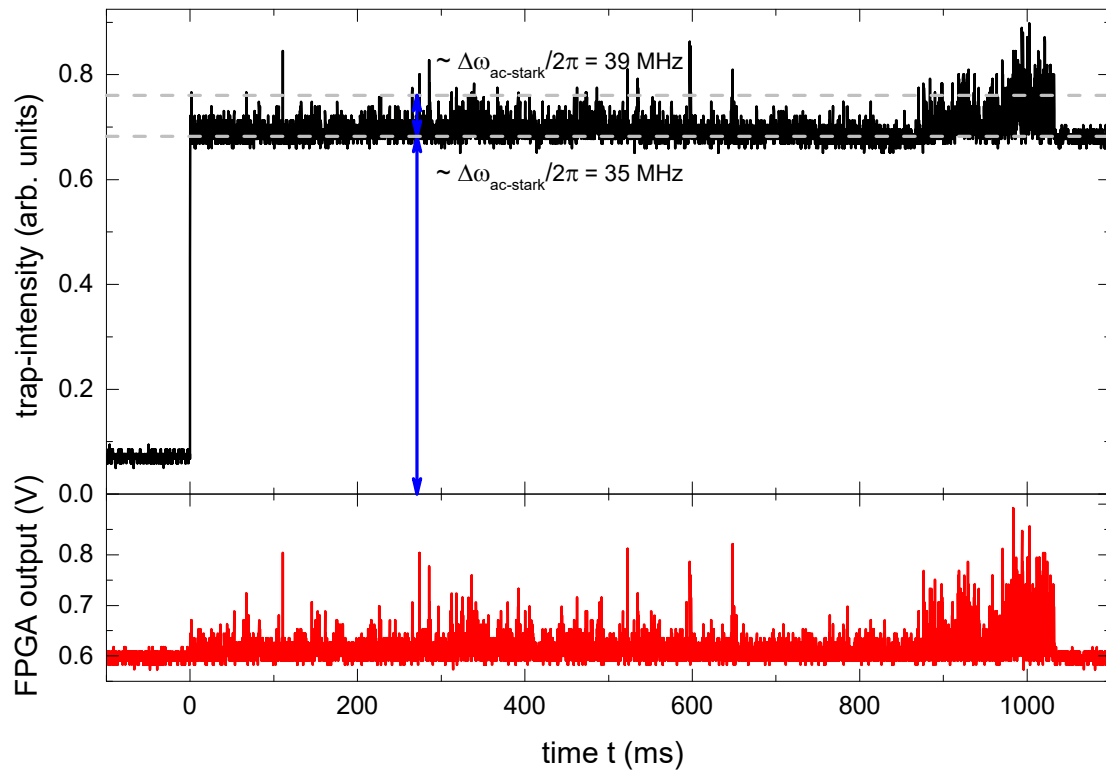


Figure 5.18: Output voltage level of the FPGA (red curve) and the corresponding measured modulation of the intracavity dipole trap power (black curve). As a reference, two dipole trap levels corresponding to an ac-Stark shift of 35 MHz and 39 MHz are marked by horizontal grey lines.

of the mechanical oscillation of the atom, the phase-locked local oscillator accurately follows the atom's motion. The continuously updated phase ϕ_l , necessary to lock the phase of the local oscillator to the atomic oscillation, is plotted as a blue line below. During the depicted timespan the phase stays quite stable on a timescale of 0.5 to 1 ms, indicating a very steady oscillation of the atom, which is typically once the atom picked up a certain momentum and is close to getting lost out of the cavity.

The routine described and visualized above is implemented into the photon counting FPGA. The resulting analog output is directly fed as set-point to the PID controller stabilizing the intensity of the trapping laser. The output voltage level is given by the following formula.

$$S_{out}(t) = S_0 + G \cdot \left[\sin(2\pi \cdot f_{pfb} + \phi_l(t) + \phi_{pfb}) + 1 \right] \quad (5.8)$$

Here, S_0 is an offset voltage output when no oscillation is detected and G is the gain of the feedback circuit. The voltage offset S_0 ensures that the dipole trap intensity is kept above a certain threshold value which is especially important since the trap beam is also used to stabilize the cavity length. Values below the threshold will make the lock unstable and eventually cause the cavity to fall out of lock. Furthermore, the absence of this field would reduce the ac-Stark

shift and hence alter the detuning of the atom and the cavity. An example of a typical FPGA output and the resulting dipole trap intensity is depicted in Figure 5.18.

At time zero the atom is trapped, the dipole trap power is increased and the control over the intensity is handed over to the FPGA. In the upper plot the lower dashed horizontal line shows the dipole trap power as it would be applied if the feedback is deactivated. For this dipole trap power level the ac-Stark shift amounts to $\Delta\omega_{ac-stark} = 35$ MHz resulting in an atom-cavity detuning of $\Delta_{ac}/2\pi = (\omega_a - \omega_c)/2\pi = -5$ MHz. The gain parameter in Eqn. (5.8) is adjusted in such a way that it only slightly changes the value of the ac-Stark shift. The dipole trap power which would correspond to an increase of the ac-Stark shift to $\Delta\omega_{ac-stark} = 39$ MHz and hence $\Delta_{ac}/2\pi = -1$ MHz, is depicted by the upper dashed horizontal line. However, as it is visible in Figure 5.18, this value is hardly ever reached. Usually the influence of the parametric radial feedback leads to an increase of the ac-Stark shift $\Delta\omega_{ac-stark}$ of less than 1 MHz and can hence be disregarded. Furthermore, small deviations caused by a change in the ac-Stark shift are compensated due to the fact that the feedback only switches to higher dipole trap powers once a large and clear oscillation of the atom is determined. In this case the dipole trap field at the position of the atom is reduced anyway, which in turn leads to a decreasing ac-Stark shift.

5.5.3.2. Quality Factor of Atomic Oscillation

Besides the small number of photons transmitted by our atom-cavity, the key challenge for any feedback circuit lies the low-Q regime where the measurement backaction decoheres the atomic motion after only a few oscillations. The quality factor of the atomic motion in the resonator can be deduced from the FFT recorded for many trapped atoms in the resonator while the feedback is turned off. Traces of 200 atoms have been evaluated and a 1024-point FFT was computed for every 10.24 ms interval. The magnitude of these individual FFT spectra have then been added together; the result is shown in Figure 5.19. In the resulting spectrum the Q-factor is represented nicely on the lower frequency side while the higher frequency side is sharper and governed by the reduced visibility $V(f)$ of higher frequency atomic oscillations in the transmission of our system as described in Section 5.4 and depicted in Figure 5.11²³. In addition, the spectral data shows a constant offset T_0 and a frequency dependent one best described by T_{back}/f . Taking these considerations into account the recorded data is represented by

$$T = T_0 + \frac{T_{back}}{f} + \left[\frac{A}{\pi\gamma \left[1 + \left(\frac{f - f_0}{\gamma} \right)^2 \right]} \right]^2 \cdot V(f). \quad (5.9)$$

²³ Please note that frequencies here are twice the value shown in Figure 5.11. This is due to the fact that here the actual frequency in the transmitted signal is considered while in Figure 5.11 the oscillation frequency of the atom is plotted.

Here A represents the magnitude of the peak in the transmitted data, γ the half-width at half-maximum (HWHM) and f_0 the center-frequency of the oscillation. Taking the theoretically expected value of $f_0 = 9.6$ kHz, a non-linear square fit yields a Q-factor of

$$Q = \frac{f_0}{2\gamma} = 2.4. \quad (5.10)$$

Our feedback loop therefore operates in the regime of poor quality factor, where a measurement can only be used to predict the future motion of the atom for a short time.

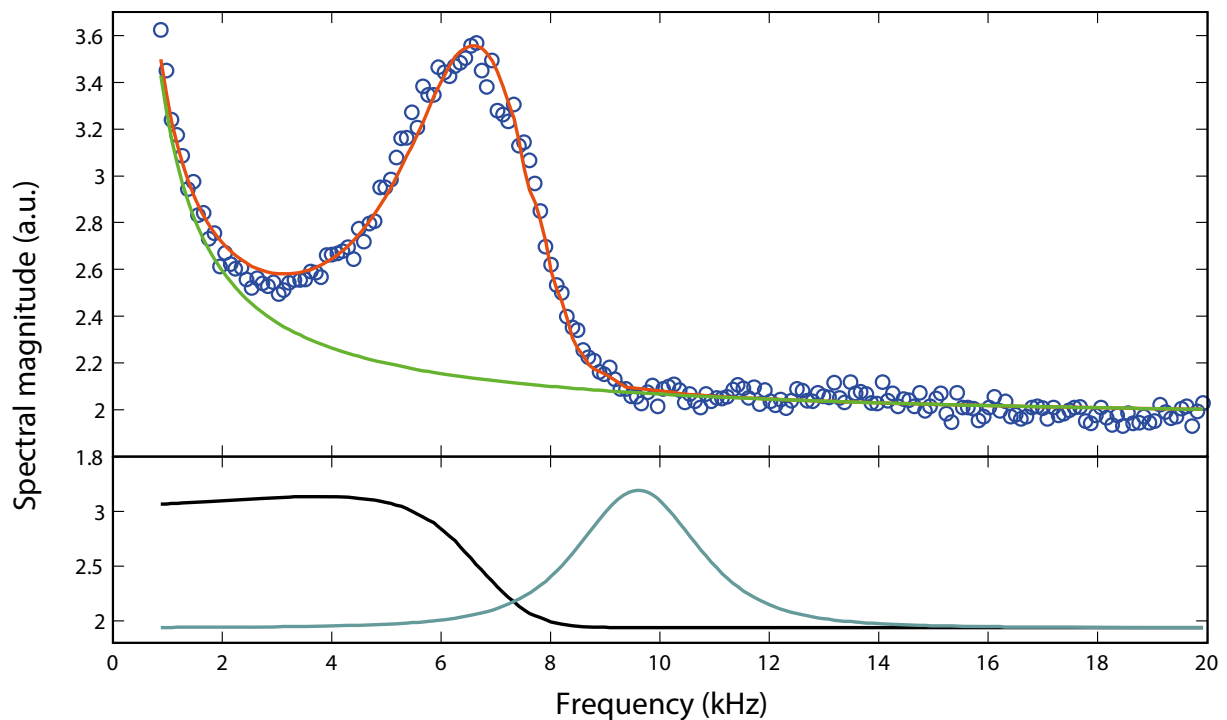


Figure 5.19: Frequency spectrum of measured transmission. The recorded spectrum is shown by the blue circles. The background $T_0 + f/T_{back}$ is given by the green line. The resulting peak appears below the expected frequency of $f_0 = 2\omega/2\pi$ (cyan line in lower plot) due to the non-linear dependence of cavity transmission on radial position (black line in the lower plot). It is broadened due to the measurement backaction, reflecting the decoherence of the atomic oscillation by the probing laser beam. A fit incorporating the nonlinear transmission function, which connects the atomic position to the transmitted intensity, yields a Q-factor of 2.4 (red line).

5.5.3.3. Phase Dependency

The phase advance ϕ_{pb} is a crucial parameter for the correct operation of the parametric feedback. It determines the phase relationship between the applied modulation of the dipole trap and the detected excursion of the atom. Thus, it permits to adjust the feedback loop to amplify or decrease the motion of the atom in the dipole trap, which leads to heating or cooling of the atom. The average storage time of the atom is a good means to determine the position of heating and cooling regions. The drastic change in the storage time associated with the value of

the phase advance is plotted in Figure 5.20. The phase advance is scanned over 2π . The average storage time is determined by measuring the time the atom remained strongly captured inside the cavity. Per each data-point, i.e. per frequency and phase setting, around 20 individual atomic traces are recorded. During all scans the probe-power was set to 0.11 intracavity photons on the empty-cavity. The dipole trap was adjusted in such a way that its value without feedback results in an 840 μK deep potential valley. As mentioned previously, the feedback operates at an integration time, which corresponds to its oscillation period, which is the inverse of the parametric feedback frequency $1/f_{\text{pfb}}$. This optimum integration time was found empirically and is expected due to the low Q-factor: the measurement backaction renders the atomic motion incoherent over timescales longer than the oscillation period, so integrating for longer than this degrades our estimates of the atom's amplitude and phase. Scans for three different oscillation frequencies are plotted. The dashed black line indicates the storage time with the same parameters, however, without any feedback applied. At a phase value of 90 degrees two data points per set are shown. These data points were derived with two different settings of the feedback routine which correspond to the internal $-\pi$ and $+\pi$ phase settings. The overlap of these data points confirms the correct working principle of our routine.

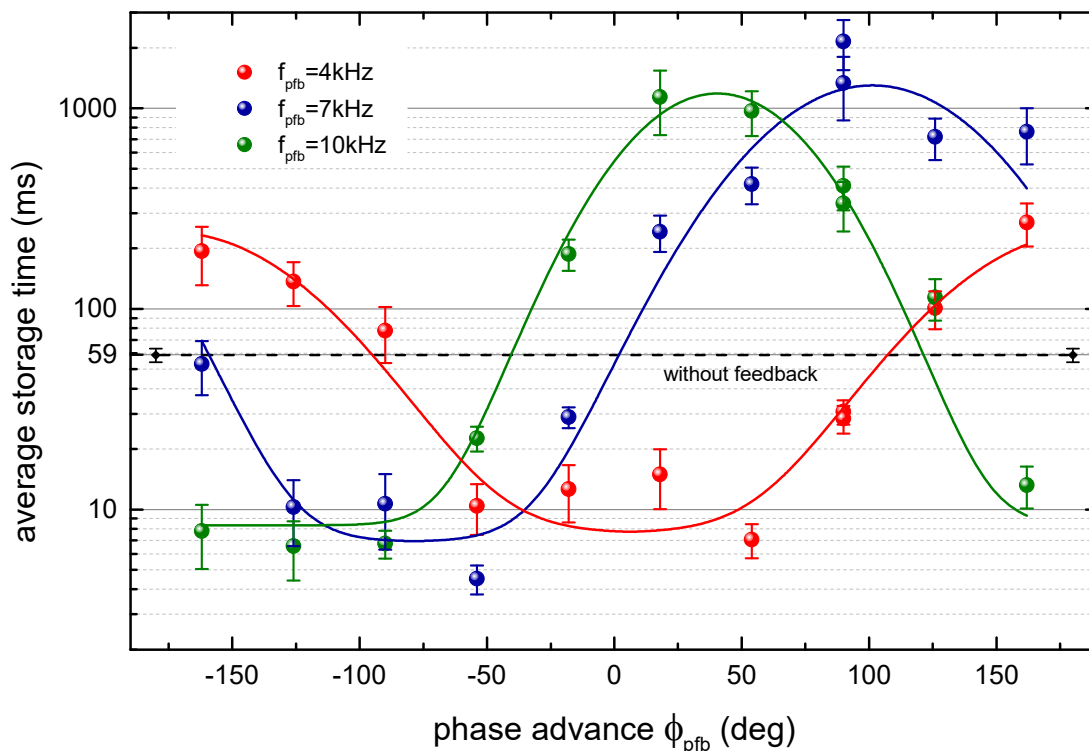


Figure 5.20: Influence of the phase advance on the storage time of atoms captured in the dipole trap. The phase advanced is scanned from $-\pi$ to $+\pi$ and the average storage time of multiple individual traces is determined. Three different plots for different settings of the feedback frequencies are recorded. Sine curves are fitted to the single curves which serve as guide to the eye. The average storage time in case no feedback is applied is plotted as vertical black line.

The graph recorded for $f_{pfb} = 7$ kHz (blue curve) shows a clear increase in storage time around 90 degrees. At this point its average value is close to 2 seconds. At the opposite phase setting, i.e. at a 180-degree phase offset, the contrary behavior takes place. Here, strong heating occurs, pushing the storage time well below 10 ms. The actual value at this setting is even lower, since many atoms were captured for such short times, typically below 4 ms, that they have not been considered as being captured at all. The phase dependency changes if the oscillation frequency of the feedback is altered. In this case the main peak is either moved to higher or lower values of the phase advance. This frequency dependency will be studied closely in the next section.

5.5.3.4. Frequency Dependency

Besides the phase advance of the parametric feedback, which has been discussed in the previous section, the frequency setting of the feedback plays a key role. As already mentioned above, this frequency value is used as reference to detect the atomic oscillation as well as to generate the phase-shifted local oscillator which is modulating the dipole trap. The value is derived from previous knowledge about the system. As feedback is supposed to anticipate the motion of the atom and counteract it with a modulation of the dipole trap, its frequency setting should be close to the atom's oscillation frequency. In order to show this dependency, scans at various frequency settings have been carried out. They are depicted in Figure 5.21. At each feedback frequency value traces for phase advance parameters spanning across the full 2π region are recorded yielding a 2D matrix of data-sets. For each data-set the average storage time is evaluated. The values determined for the same frequency setting at the different phase settings are fitted to a Gaussian distribution which is periodic in 2π . This permits to extract the phase advance at which the feedback works best $\hat{\phi}_{pfb}$ as well as the average storage time at this optimal phase setting. These two values are plotted in Figure 5.21 as black and red line. As reference, a second order intensity correlation plot measured for the same setting with no feedback applied is added in the same plot (blue line). As described in the previous chapter, this correlation function hints on the atomic oscillation.

The average storage time at the optimal phase setting shows a clear peak around a feedback frequency of 7 kHz. At this setting the average storage times reaches a value around 1.7 seconds in the Gaussian fit. However, the actually measured value at the optimal phase and frequency setting amounts to 2 seconds. Going to higher frequency settings, the average storage time drops to values which are even below the value without any feedback of 60 ms. In this case the switching of the dipole trap occurs with a random pattern and hence leads to heating of the atom independent of the selected phase advance. At lower frequency a clear drop in the average storage time is visible as well. However, in this case a second structure around 3 kHz appears. We attribute this structure to a positive effect of the feedback operating at half the oscillation frequency of the atomic excursion and hence only interacting every other oscillation cycle. Besides the clear influence of the feedback frequency on the storage time, a dependency of the optimal setting of the phase advance parameter is evident as well. For the maximum storage time, which occurs around 7 kHz, an optimal setting of the phase advance of 90 degrees is used.

Going to higher feedback frequencies where the storage time reduces the optimal phase advance changes to values lower than 90 degrees. In this case the oscillation is faster than the intrinsic oscillation of the atom and hence a smaller phase advance compensates for this effect and yields the best results. The behavior is similar for feedback frequencies below 7 kHz with the difference that the phase advance changes to larger values. Here, the local oscillator of the feedback routine is too slow to follow the oscillation of the atom. Thus, a larger phase advance is required in order to achieve the best possible cooling of the atom, which is possible at this respective setting.

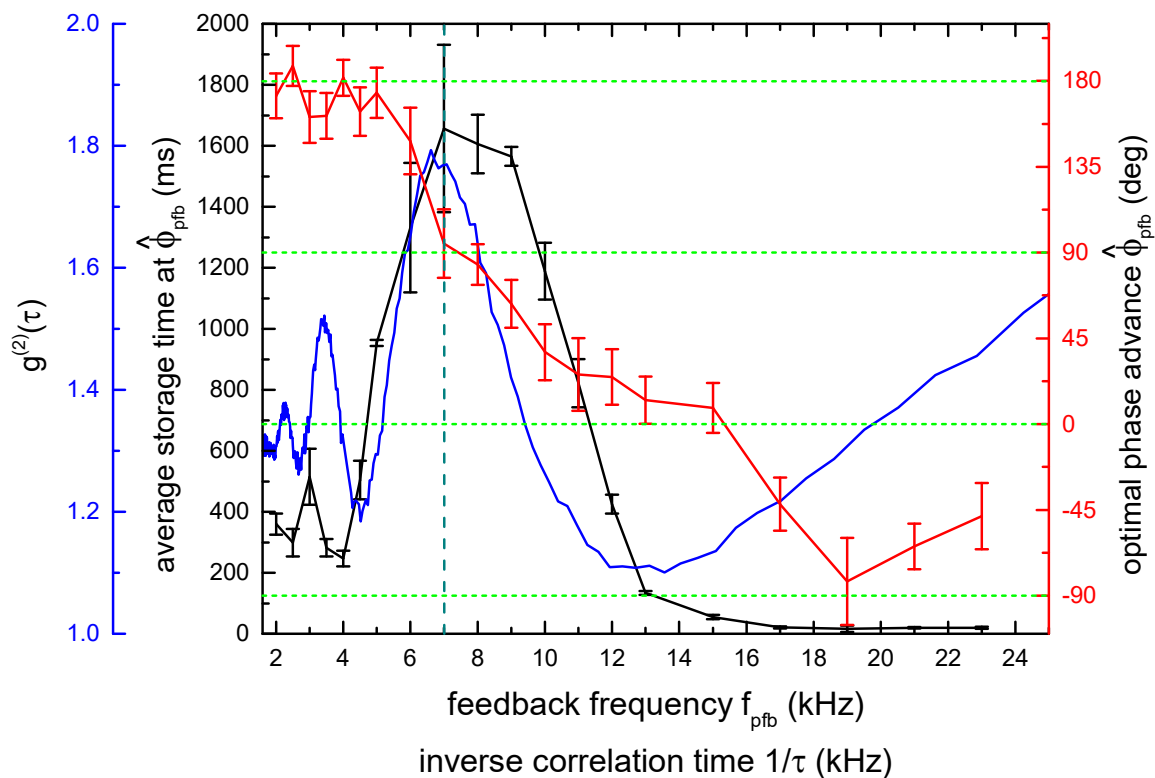


Figure 5.21: Average storage time of the atom as a function of the feedback frequency. The black curve shows the storage time as it was measured for the best phase advance setting at a given feedback frequency. This optimal setting of the phase advance parameter is also depicted by the red curve. The error bars of the storage time indicate the standard deviation, i.e. one σ confidence level, of the periodic gauss fit carried out to determine the average storage time for each feedback frequency. In order to derive the error bars for the optimal phase, a sine curve has been fitted to the same storage time/ phase data at each feedback frequency. From this value also the optimal phase advance has been determined. Here as well the standard deviation level is shown. As a reference, a second order correlation measurement of traces recorded with the same parameters but without feedback is depicted as blue curve.

5.5.3.5. Maximum storage time

Unlike the previously used bang-bang feedback, the parametric feedback described in this section requires more knowledge about the system and hence more significantly relies on the input settings. Their choice has already been described in the two previous paragraphs. Here, the best parameters are employed and the actual application as an efficient means to increase the storage time will be shown. A detailed overview of the settings of the parameters can be found in Table 5.2.

General parameters	
Probe-cavity frequency detuning	$\Delta_{pc}/2\pi = 0$ MHz
Atom-cavity frequency detuning	$\Delta_{ac}/2\pi = -5$ MHz
Probe power	$P_{probe} = 0.6$ MHz/ $(\eta_{SPCM} \cdot \eta_{out}) \cdot \hbar\omega_p = 540$ fW
Dipole trap power (base-value)	$P_{trap} = 950$ nW
Dipole trap modulation depth	ΔP_{trap} varies; depending on confidence of detected oscillation
Feedback parameters (parametric feedback)	
Frequency of parametric feedback oscillator	$f_{pfb} = 7$ kHz
Integration time of feedback	$T_{int} = 1/f_{pfb} = 142.86$ μ s
Phase advance	$\phi_{pfb} = 90^\circ$
Internal FPGA parameters	
DDS increment for local oscillator	<code>feedback_phase_ddsinc = 300647</code>
Cycles between feedback iteration	<code>feedback_phase_fiforate = 9</code>
Integration steps of feedback	<code>feedback_phase_fifoshift = 1428</code>
Internal phase setting of feedback	<code>feedback_phase_phase = -1.0</code>
Feedback output modulation strength	<code>pfb_multiply = 16</code> <code>pfb_offset = 78000</code> <code>pfb_dac_scaling = -4</code> <code>pfb_mag_scaling = true</code>

Table 5.2: Overview of the settings determined to offer the best mode of operation of the radial parametric feedback. These settings are also employed to record the traces depicted in this paragraph. The FPGA internal parameters are also given as reference.

Multiple experimental runs with these settings have been carried out. A semi-logarithmic plot of the obtained storage times for each captured atom is shown in Figure 5.23. Here, the fraction of the remaining number of atoms remaining captured in the cavity is plotted as a function of the storage time. The fraction is reduced every time an atom is lost. Hence, every data point represents a single captured atom, which has been recorded one after the other. The average value of the storage time of the atoms computed as arithmetic mean amounts to $t_{avg} = 2.15$ seconds. The $1/e$ storage time determined by an exponential fit of first order results in $\tau_{d1} = 2.3$ seconds (purple dotted line). The strong presence of atoms which only stay for a short time in the cavity (less than 250ms) significantly lowers this value. An exponential decay fit of second order permits to overcome this limitation. This yields decay times of $\tau_l = 213$ ms (blue dashed

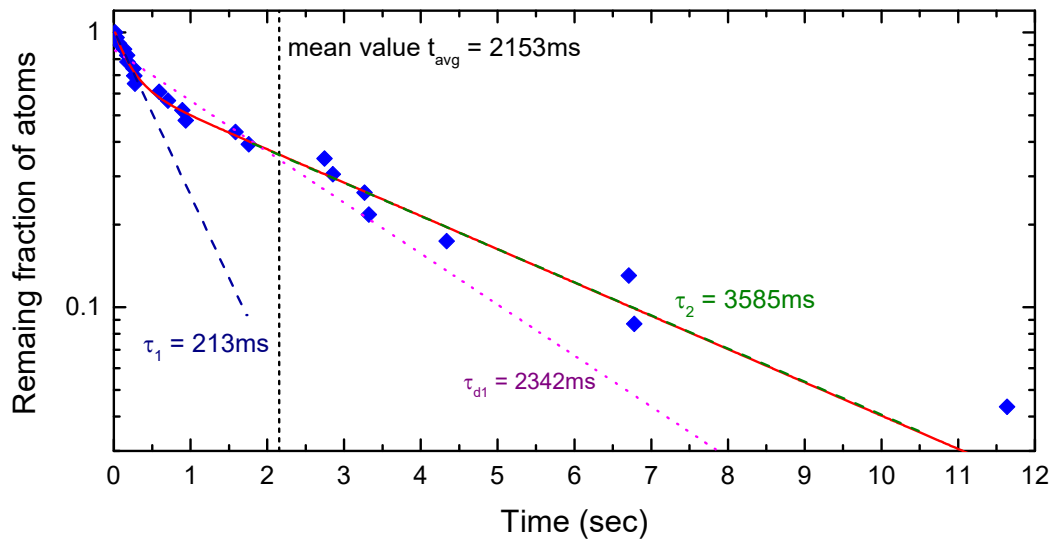


Figure 5.23: Fraction of atoms remaining in the cavity after a certain time has passed. The actual data points are depicted by blue rhombs. 23 captured atoms are considered. An exponential decay of first and second order is fitted to the data-points. The first order fit is depicted as purple dotted line with the decay constant τ_{d1} . The second order one is plotted as red line with the two decay constants τ_1 and τ_2 , which are also shown by the dashed blue and green line. The vertical black dotted line represents the average storage time.

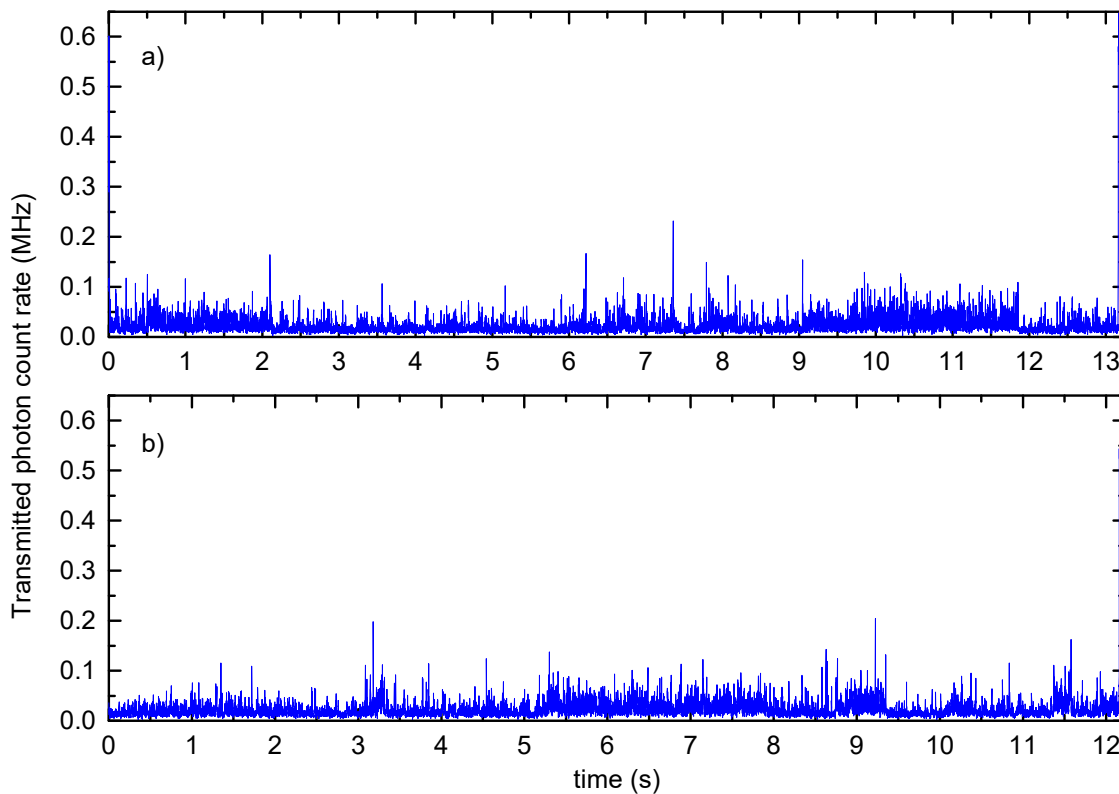


Figure 5.22: Two sample traces of the radial parametric feedback at work. The traces are recorded with the settings listed in Table 5.2. Part a) is recorded with the probe level set to 0.13 intracavity photons and 0.11 intracavity photons in part b).

line) and $\tau_2 = 3585$ ms (green dashed line), respectively and is plotted as red line in Figure 5.23. The faster decay in the beginning can e.g. be caused by an improper operation of the feedback routine for atoms which are caught not directly in the center of an antinode of the probe beam.

If we compare the acquired data to the bang-bang feedback measurement an increase by a factor of 3 can be observed, see Figure 5.14 a) (red curve). In this Figure each data points represent a binning of individual captured atoms on the x-axis. This hence shifts the weight to larger time, and thus yields reasonable values for the single exponential decay. Evaluating both data-sets in the same way results in decay times of the parametric feedback data of 3.2 seconds, compared to 1.1 seconds obtained in case of the bang-bang feedback.

In order to show the parametric feedback at work, two sample traces are depicted in Figure 5.22. Here, storage times of more than 13 seconds in a) or 12 seconds in b), respectively, are found. The overall low transmission of the probe beam through the cavity demonstrates the well working principle of the parametric feedback.

5.5.4. Axial Parametric Feedback

Up to now, all feedback routines are only applied on the radial direction of the atomic motion away from the cavity axis. Here we will extend our scope and show a first implementation of axial feedback. Since the axial motion occurs on much faster timescales, i.e. two order of magnitude, only the parametric feedback routine offers the possibility to tackle this ambitious challenge. The low count-rates caused by the low transmission of the probe beam through our atom-cavity system in combination with the necessary fast response time require that the feedback decision is based on the timing of a single photon click. An overview of the settings employed to demonstrate the axial feedback is given in Table 5.3.

General parameters	
Probe-cavity frequency detuning	$\Delta_{pc}/2\pi = 0$ MHz
Atom-cavity frequency detuning	$\Delta_{ac}/2\pi = -5$ MHz
Probe power	$P_{probe} = 6 \text{ MHz}/(\eta_{SPCM} \cdot \eta_{out}) \cdot \hbar\omega_p$
Dipole trap power (base-value)	$P_{trap} = 950$ nW
Dipole trap modulation depth	$\Delta P_{trap} = 0.36 \cdot P_{trap}$
Feedback parameters (parametric feedback)	
Frequency of parametric feedback oscillator	$f_{pfb} = 500$ kHz
Integration time of feedback	$T_{int} = 2/f_{pfb} = 4$ μ s
Phase advance scanned	$\phi_{pfb} = 0 - 360^\circ$
Internal FPGA parameters	
DDS increment for local oscillator	feedback_phase_ddsinc = 21474836
Cycles between feedback iteration	feedback_phase_fiforate = 0
Integration steps of feedback	feedback_phase_fifoshift = 400

Table 5.3: Overview of the settings used for the axial parametric feedback scan. The probe power is significantly increased compared to the previous radial scans.

5.5.4.1. Implementation

The high frequency of the axial oscillation in the few hundred kHz regime also requires a modulation of the same frequency which will be output by the parametric feedback routine. This frequency value is way beyond the bandwidth of the PID controller, which lies well below 100kHz. Hence it is not possible to use the feedback output as set-point of the PID loop as it has been done for the radial feedback routine. In Figure 5.24 the required changes on the dipole trap AOM driver, when going from radial to axial feedback, are depicted. If high modulation frequencies are used as for axial feedback, the set-point for the dipole-trap stabilization PID is a fixed value output by the main program controlling the experimental run. The output of the PID is then multiplied with the oscillator generating the fixed AOM frequency via a mixer (Mini Circuits ZLW-3+). Now a second mixer of the same kind is used to modulate this signal with the frequency of the feedback routine output by an analog channel of the FPGA module. In total this results in a fast modulation of the radio frequency driving the AOM and with that also of the dipole trap beam. The limited bandwidth of the PID, which is below the high modulation frequency, ensures that the PID controller itself does not get “distracted” by the modulation and consequently tries to compensate for it. Instead, it only “sees” a time-averaged value of the signal, which makes the modulation invisible.

5.5.4.2. Phase Dependency

The fast timescale of the axial motion in combination with its low quality factor, as it can be seen in the number of peaks showing up in correlation measurements, necessitates to increase the information rate emitted from the cavity. In order to do so, the probe power impinging on the cavity is increased by a factor of 10 compared to the measurements of the radial oscillation, resulting in an empty cavity photon number of 1.1. It is important to keep in mind that this value is determined for the case where the cavity is on resonance with no atom inside. The presence of an atom significantly reduces the actual number of intracavity photons once the atom is

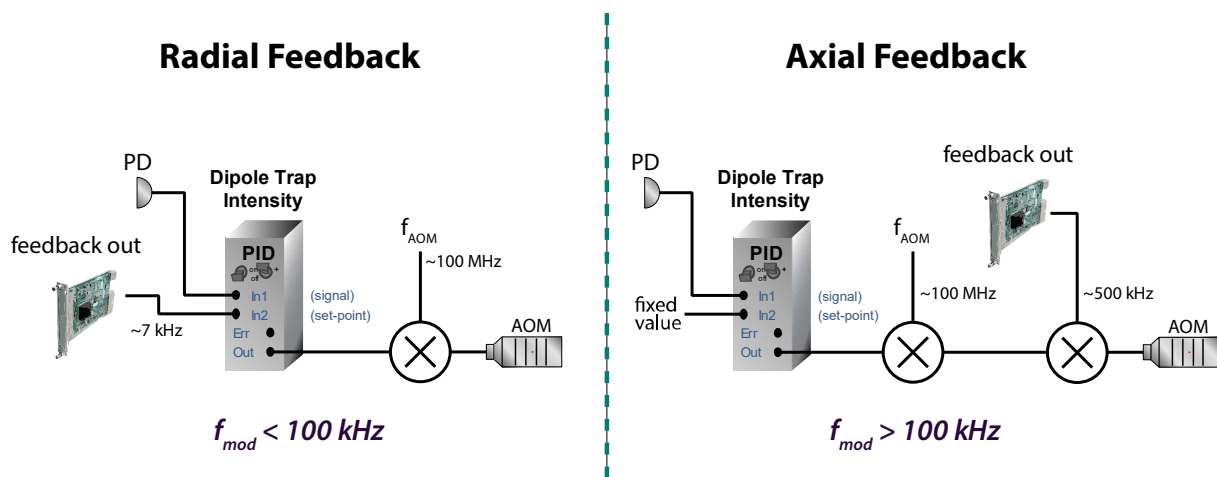


Figure 5.24: Setup of the PID and AOM mixer for slow and fast modulations as they are used in the radial and axial feedback, respectively. A PID is used to stabilize the intensity of the dipole trap laser via a photodiode (PD). In case of the radial feedback, the signal of the FPGA is directly fed into the PID controller. The output of the PID subsequently controls the amplitude of the modulation by passing through a mixer. In case of axial feedback, a fixed value controls the set-point of the PID. The output of the PID controls the amplitude of the modulation while passing through a first mixer. A second mixer is used to create an amplitude modulated signal controlled by the output of the FPGA.

strongly coupled; this way we are close to saturating the atom but still not in the saturation regime. However, the high probe powers cause significant heating and hence reduce the average storage time when no feedback is applied to a value as low as 7.1 ms. The exposure time is set to two oscillation periods of the expected modulation, i.e. 4 μ s. This increase reduces the bandwidth of the feedback algorithm on one hand, but, on the other hand permits to increase the signal-to-noise ratio by a factor of two. The trap depth without modulation is set to a value of 840 μ K. In order to increase the effect of the feedback on the atom, the modulation depth of the dipole trap is set to a value of 36% of its mean value. The modulation is applied continuously with a fixed amplitude. The modulation is neither turned off nor reduced in times where no or only a weak oscillation is detected as it would be possible by the feedback routine. This permits to exclude additional effects stemming from pure changes in the amplitude of the modulation and hence permits to attribute the emerging pattern as being caused by a change in the phase. For the scan a feedback frequency of 500 kHz was chosen, as this is on the high-frequency side of the peak in the correlation plot (cf. Figure 5.5) and hence closer to the harmonic oscillation frequency. An overview of the parameters is given in Table 5.3.

Applying feedback at the calculated harmonic oscillation frequency of the atom around 1 MHz, with which the atom oscillates for small excursions, would in principle enhance the efficiency of the feedback algorithm. However, only a very little modulation is visible at this harmonic oscillation frequency in the transmitted signal due to the little change in the coupling constant for small excursions, rendering this frequency choice impractical. As for the radial oscillation, the phase advance is scanned and the average storage time is measured. For each data point more than 100 individual atoms have been captured. The result is plotted in Figure 5.25. The

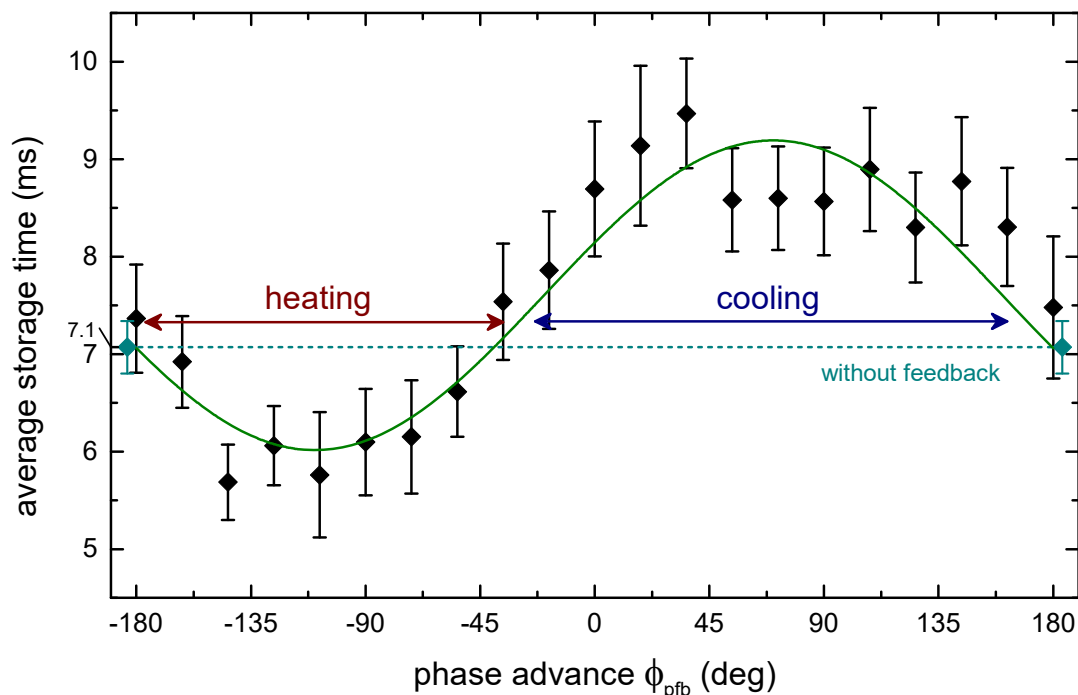


Figure 5.25: Influence of the phase advance on the average storage time for axial feedback. The average storage times for different phase advance settings is plotted. As a reference the average storage time with the same setting, however, with feedback disabled, is plotted as dotted dark cyan line. A dark green line shows a sinusoidal fit and serves as guide to the eye.

average storage time varies around the value measured without any feedback and with no modulation applied. Around a phase advance of 45 to 90 degrees the storage time increases which indicates cooling of the atom. At opposite phase values the inverse behavior occurs, which clearly indicates heating of the atom. A sine curve is fitted and plotted as a guide to the eye. The values for the phase advance in this plot can only be seen as relative values since small delays in the signal path already lead to an additional phase offset. The overall increase in storage time is not as pronounced as for the radial case. This is caused by the very weak detection efficiency of the axial oscillation, due to the very limited amount of photons. Here the decision is solely based on the absence or the presence of a single photon at a certain point in time. Yet, this measurement shows that parametric feedback in principle permits an extension even to the axial oscillation.

5.6. Conclusion

In this chapter the motion of an atom trapped inside a high-finesse optical oscillator is studied in detail. Besides correlation methods, parametric heating is employed to determine the harmonic oscillation frequency. Unlike the first method the latter one yields values which agree well with the computed ones. In addition to the detection of the atomic motion, fast electronic feedback has been introduced as a method to effectively cool this motion. The very low number of photons emitted by our atom-cavity system poses a limit to the information, which can be gained about the atomic motion. Different strategies have been employed for the radial oscillation. While the so-called bang-bang method does not require any pre-knowledge about the system and relies on the evaluation of a change in the emitted photon flux, the radial parametric feedback relies on the input of the frequency at which the atom moves and outputs a modulation. This pre-knowledge about the system permits to have integration times which are on the same order or larger than one oscillation period. This significantly improves the quality of prediction and thus leads to an increase of the storage time by almost a factor three. The possibility to have longer integration times with respect to the atomic oscillation additionally enables an extension of the parametric feedback strategy to the axial direction. This feedback, however, requires higher probe powers substantially increasing the heating rate of the atom in order to have a visible effect. While this renders it impractical for day-to-day use in our experiment, it is a powerful demonstration of the possibilities of fast electronic feedback.

Compared to experiments relying on transverse beams to trap and cool atoms, the feedback cooling strategy demonstrated in this thesis substantially benefits from its easy and flexible way to be implemented. As it only depends on information derived from the transmitted photons and does not require any transverse optical access, it is thus applicable also for systems incorporating short cavities or systems with limited optical access, consisting e.g. of optical fibers [144] or microtoroids [145]. Further advances in the processing algorithm of the feedback strategy to incorporate real-time estimation of the quantum state can even permit to extend this method into the quantum domain, rendering it possible to stabilize the quantum state of a trapped particle.

6. Heterodyning

Photodiodes provide an easy way to measure the intensity of a light field. The rapid oscillation of the light field – with its few hundred THz – is significantly faster than the highest frequencies, of a few tens of GHz, state-of-the-art photodiodes or electronic circuits are able to detect and handle. All photon detectors are hence only capable to detect the energy of the impinging field, but not the field itself. However, in order to be able to fully reconstruct the optical field transmitted through the cavity, more information except the overall intensity is needed. To gain actual information about amplitude and phase of the light field, one can use a method, which is well known from RF telecommunication and based on a down-conversion process [63], [146]. Its extension into the optical domain is also referred to as optical homo- or heterodyning; the difference between them shall be explained later.

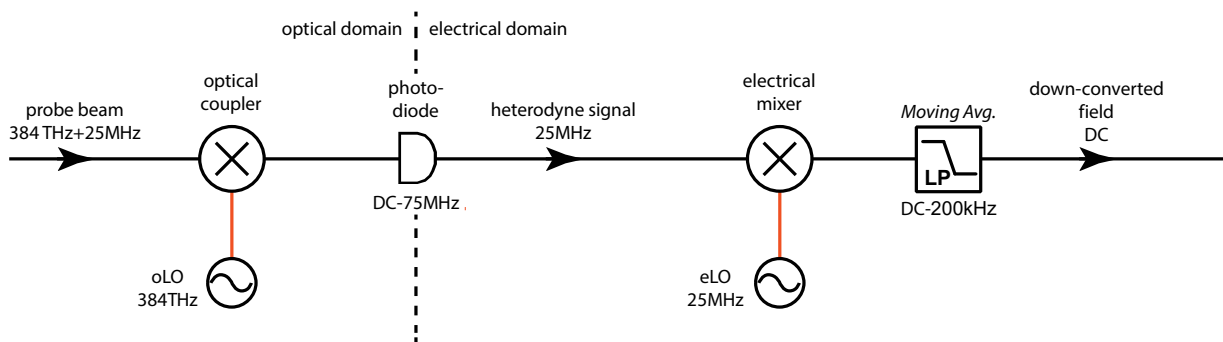


Figure 6.1: Schematic overview of the down-conversion. The probe beam is overlapped with an optical local oscillator (oLO), centered only a few MHz away from the probe beam. The resulting optical signal is measured by a photodiode. The photodiode mediates the mixing of the two constituting light-fields in the beam, generates an electrical signal and passes this heterodyne signal onto a second mixer, which down-converts the RF-signal to DC frequency by means of an electrical local oscillator (eLO). A moving average low-pass filter in the end ensures that high frequency components are filtered out and hence blocks any residual signal from the eLO.

With heterodyning it becomes possible to shift the frequency-spectrum of the light impinging on the photodiode to frequencies in the MHz range which are easily detectable by standard photodiodes and can be handled by the electronic circuitry. Despite being shifted to a different frequency-range, the signal recorded by the photodiode still possesses all the information, within a certain bandwidth, which is given by the diode, carried by the original light field, but now references to the local oscillator field used for the down-mixing. Knowing the field of the local oscillator, this permits to accurately determine amplitude and phase information of the impinging light field at a certain optical frequency (called carrier). By employing multiple electrical or optical local oscillators or by processing the full signal recorded by the photodiode, it furthermore becomes possible to independently measure this amplitude and phase information for adjacent, optical carriers which may be separated by only a few MHz in frequency. This is far below any limit which can be achieved by conventional spectral separation mechanisms, like prisms, grating or DBR-filters. It hence also paves the road to simultaneously analyze multiple spectral components individually with the same setup. A theoretical description of heterodyning has already been given in Section 2.2. The main

difference between photon counting and heterodyning is that the first one relies on the detection of single photons, while the second one is a measure of the optical field. Photon counting is a discrete measure of the statistical probability $\langle a^\dagger a \rangle$ to annihilate a single photon, which is proportional to the intensity of the field. Heterodyning on the other hand is a continuous measurement of the superposition of the electromagnetic field $\langle a \rangle$ and the electromagnetic field of the local oscillator. As the latter one is well known, $\langle a \rangle$ can be extracted. As already derived in Section 2.2.2, the mixing of the two beams permits to use the local oscillator as an amplifier for the probe beam. This hence permits to even detect the smallest light quantities with regular photodiodes.

A schematic overview of the heterodyne technique, as it will be elucidated in this chapter, is depicted in Figure 5.25. In Section 6.1 the optical down-conversion as it occurs at the optical coupler is explained. Section 6.2 then describes the subsequent electronic down-conversion. Sections 6.3 and 6.4 give further details on how the heterodyne detection setup is designed and presents its physical performance. Sections 6.5 and 6.6 present actual measurements of the phase and amplitude information of our coupled atom-cavity system. Section 6.7 gives an introduction to a measurement technique, where subsequent cooling and probe intervals permit to record spectral features of the coupled system. At the end of the chapter, i.e. in Section 6.8 nonlinear effects caused by high driving of the atom-cavity system are examined. These effects can only be revealed spectrally by a heterodyne detection.

6.1. Setup of the Optical Down-Conversion

The down-conversion step is the essential part of any heterodyne detection. It utilizes the principles of optical interference together with sum and difference frequency generation as it is known from nonlinear optics [147]. Since light in free-space only interferes but does not interact, the probe beam along with the optical local oscillator have to be mixed by some means. Here, the actual mixing is not obtained by employing a nonlinear crystal but rather by detecting the superimposed fields with a simple square-law photodetector, which in our case is a regular photodiode [148]. This however requires, that at the position of the detection the two beams have to perfectly overlap.

A schematic overview of the setup is depicted in Figure 6.2. A laser close to the cycling transition of the ^{85}Rb D₂ line serves as the probe beam. It passes a $\lambda/4$ waveplate making it circularly polarized and is sent to the cavity. After its passage through the atom-cavity system, the transmitted beam is rotated back to linear polarization by a second $\lambda/4$ waveplate before it is superimposed with the optical local oscillator (oLO²⁴) on a polarizing beam splitter (PBS1).

²⁴ In this chapter an optical and electronic local oscillator will be introduced. In order to be able to differentiate between them, the optical one will be abbreviated by oLO, the electronic one by eLO.

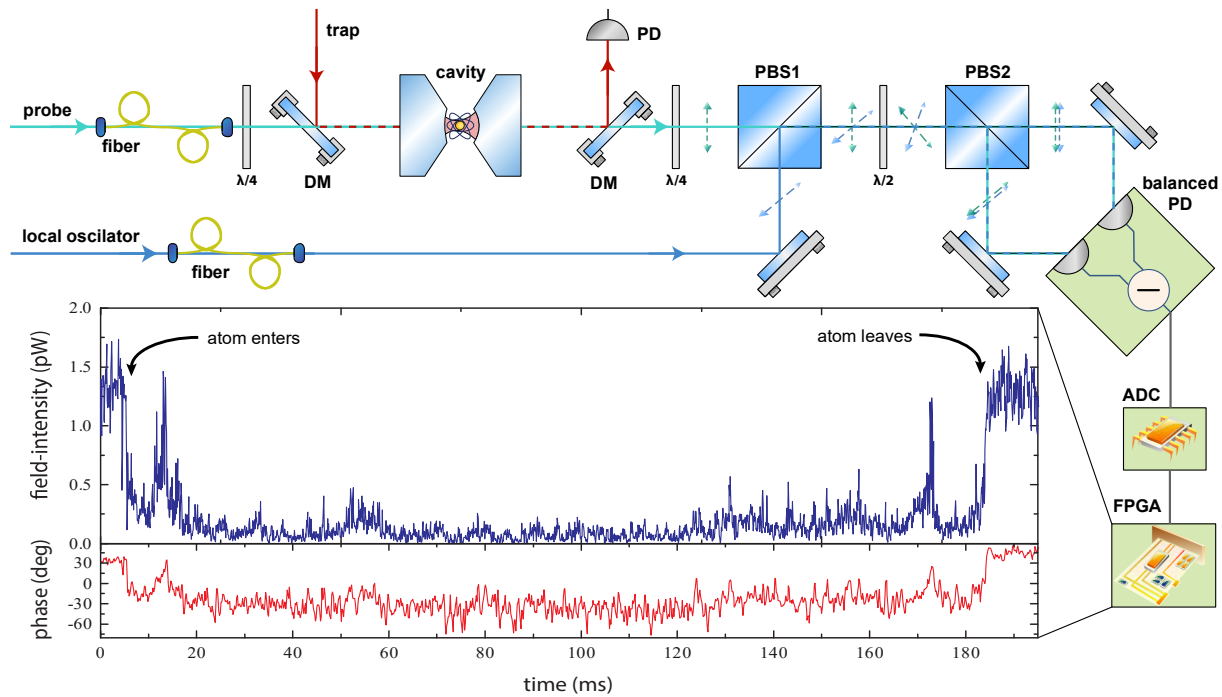


Figure 6.2: Overview of the heterodyne detection setup. The probe beam is sent via an optical fiber to the cavity. Before it is coupled in, it passes a $\lambda/4$ waveplate and is superimposed with the dipole trap beam on a dichroic mirror (DM). After its passage through the atom-cavity system, the trap beam is extracted by using a second dichroic mirror. The remaining probe beam then passes a $\lambda/4$ waveplate. A polarizing beam splitter (PBS1) is employed to overlap it with the local oscillator. A set consisting of a $\lambda/2$ waveplate and of a second polarizing beam splitter (PBS2) splits the combined probe-LO beam into two equal parts with equal distribution but orthogonal polarization. These two parts are individually detected by the diodes of a balanced photodetector. The resulting electrical current is sampled by an analog-to-digital converter and sent to an FPGA for further processing. The so obtained magnitude (blue) and phase (red) information when an atom is captured for ~ 180 ms is depicted as well.

Probe and oLO originate from the same laser source and are typically separated in frequency by about 25 MHz. They are both brought to the setup via optical fibers which induce slight drifts in their relative phase difference. The fluctuations are mainly caused by temperature drifts in the laboratory and are depicted in Section 6.2.2. After PBS1, the polarizations of probe and oLO are mutually perpendicular. The two beams pass a $\lambda/2$ waveplate which rotates their polarizations by 45° before being sent onto another polarizing beam splitter (PBS2), which directs equal portions of probe and oLO onto each photodiode of a balanced Si photo-detector (Thorlabs PDB120A²⁵). The balancing is achieved by slightly adjusting the $\lambda/2$ waveplate between the two PBS. The difference of the photocurrents is amplified and passed via a 100 MS/s digitizer to a field-programmable gate array (FPGA), which extracts the magnitude and phase information encoded in the heterodyne signal. The internal data path in the FPGA will be explained in detail in the following section. The clock of the FPGA is locked to a common 10 MHz reference, which also feeds the signal generators producing the frequency difference between the probe and oLO. This permits the phase stable extraction of the magnitude and

²⁵ Thorlabs Balanced Amplified Photodetector, Si, 75 MHz, 320-1000 nm

phase information encoded in the heterodyne signal. A typical trace for an atom trapped inside the cavity for 180 ms is also shown in the lower part of Figure 6.2.

6.2. Technical Implementation and Electric Down-Conversion

The data acquisition and processing in a heterodyne detection significantly differ from the one employed for photon counting measurements. The amount of data which needs to be handled as well as the processing complexity are substantially higher. All of the data-processing is done on a Xilinx Virtex-5 (SX95T) FPGA. This chapter will elaborate on the internal processes which are embedded into this FPGA. Further information is given in Appendix 10.6.

6.2.1. Schematics of the Heterodyne Detection Signal Paths

The digitized RF data which is fed into the FPGA corresponds to the down-converted optical field, typically around 25-30 MHz. In case of optical homodyning, probe and oLO beam are exactly at the same frequency. This causes a down-conversion of the optical carrier to a DC frequency. This can be especially useful if only one quadrature of the optical field is of interest as it is the case in squeezing measurements [71]. However, this does not permit to determine the amplitude and phase of the transmitted field, since for this purpose both quadratures would need to be known. In a heterodyne detection the frequency difference between probe and oLO yields a continuous, periodic transition between the two quadratures of the light field at a rate equal to the frequency difference. This permits to reconstruct the full electric field transmitted through the cavity. In all measurements we decided to use a heterodyne detection. In this case the probe- and oLO-beam are phase-locked to each other and are offset in frequency by a

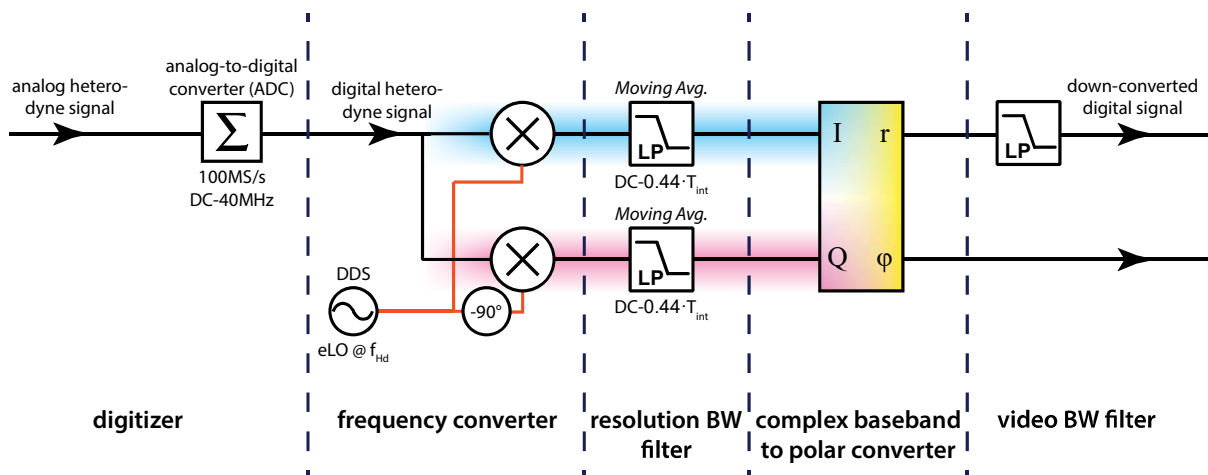


Figure 6.3: Overview of the digital extraction of the heterodyne signal. The analog heterodyne signal from the balanced photodiode is sampled by a 100MS/s, 40 MHz bandwidth-limited analog-to-digital converter. This digitized signal is mixed in the FPGA with an internally generated phase-locked local oscillator (eLO) as well as with its -90-degree phase-shifted facsimile. The resulting I/Q amplitudes pass a low-pass filter before they are converted to magnitude and phase information. The magnitude subsequently passes a second low-pass filter. The name of the basic processing step is indicated below the respective section in the diagram. The difference and reasoning of the resolution and video bandwidth filtering is described in Appendix 10.6.2.

typically 25-30 MHz (cf. Section 6.4.1). Their frequency difference will be referred to as heterodyne frequency $f_{Hd} = f_{oLO} - f_{pr}$ in the following.

A diagram of the computation carried out by the FPGA is shown in Figure 6.3 and corresponds to an extraction of magnitude and phase information of the heterodyne carrier at f_{Hd} with a certain bandwidth. The signal is digitized by an analog-to-digital converter (ADC) integrated into the NI 5781 adapter module (cf. Section 4.5). It features a sampling rate of 100 MS/s at 14-bit and possesses an elliptical filter²⁶ with a bandwidth (-3dB) of 40 MHz. A quadrature DDS (direct digital synthesis) embedded on the FPGA generates an electronic local oscillator (eLO) as well as its -90° phase-shifted counterpart. The frequency of the eLO is adjusted via a 32-bit wide frequency tuning word (FTW) permitting a frequency resolution of $100 \text{ MHz}/2^{32} = 23 \text{ mHz}$. The two quadratures of the eLO are multiplied with the input signal producing sum and difference frequencies. Since the eLO frequency corresponds to the frequency difference of the oLO and probe beam, the signal is converted to DC $f_{oLO} - f_{pr} - f_{eLO} = 0 \text{ Hz}$. The two quadratures of the down-converted electric field I and Q correspond to the X and P quadratures of the optical field of the probe beam. Similarity to the real and imaginary part of complex valued numbers, these two components are also termed the complex baseband. Small drifts in the experimental setup mainly caused by temperature fluctuations in the optical fiber induce a tiny optical path difference between the oLO and probe beam (cf. Section 6.2.2); this difference in the optical path causes a drift of the detected phase and hence a mismatch between the electronic I/Q and the optical X/P quadratures. This is the reason why in the following we will rather speak of the I/Q components than the X/P components. The I/Q components each pass a separate low-pass filter before they are converted to polar coordinates. These filters determine the spectral bandwidth of the extracted signal, which is hence termed resolution bandwidth (RBW). The low-pass filtering is implemented by a moving average filter, its width corresponds to roughly twice its inverse integration time. The characteristics of such a moving average filter are described in Appendix 10.6.3.1. After being converted to magnitude and phase information, the earlier one passes an additional, optional low-pass filter which smoothens the data before it is displayed. Since this filter only determines the smoothness on a “video device”, its bandwidth is termed video bandwidth (VBW). The different influence of the resolution and video bandwidth is described in the Appendix 10.6.2.

6.2.2. Phase drifts

The heterodyne detection as it is implemented in this setup, does not possess an active stabilization of the optical local oscillator branch with respect to the probe beam. An active stabilization would require an additional laser beam to pass through the cavity, which could lead to unwanted, disturbing effects on the single atom, such as heating. In our case, a phase

²⁶ Elliptical filters are also known as Cauer or Zolotarev filter, named after Wilhelm Cauer or Yegor Zolotarev, respectively. They feature equalized ripple behavior in the pass- and stopband and have the steepest gain between pass- and stopband at a equal order. Here a 7th order elliptical filter is integrated. A detailed discussion is outside the scope of this thesis. More information can be found in Appendix 10.6.3.

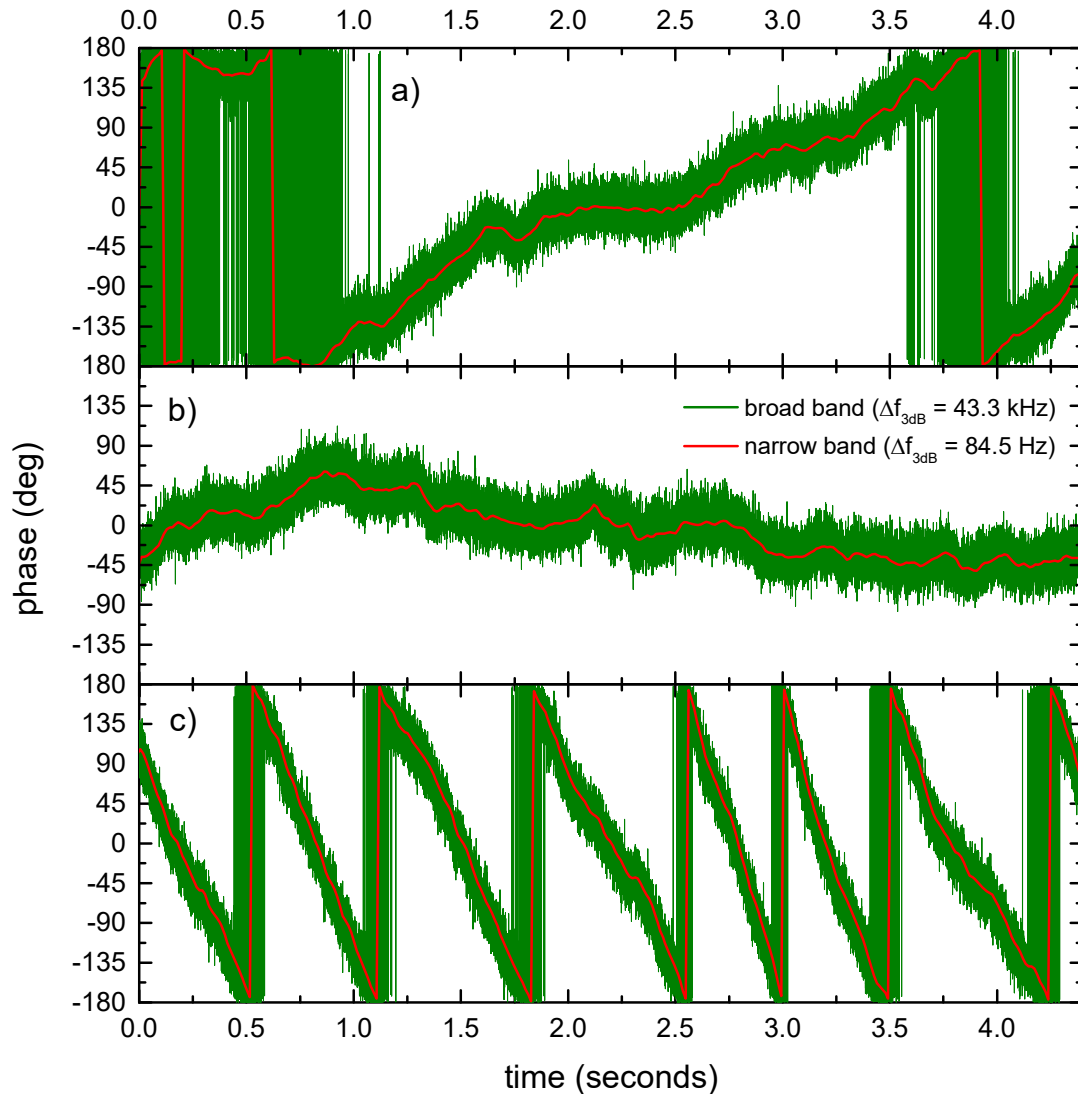


Figure 6.4: Drifts in the phase of the heterodyne signal. All three plots a) to c) show the extracted phase of the transmitted probe beam through the empty cavity. The green curve shows the data if a low-pass filter with 43.3 kHz is applied. The red curve was filtered with 84.5 Hz. a) represents a typical phase drift, while b) depicts a quite stable condition of the setup. c) was recorded under very harsh conditions and can be seen as worst case of the phase drift.

referencing by interleaved check intervals as it will be described later is performed. In order for this technique to work properly, it is necessary that the timescale of typical phase drifts is long compared to the timespan between reference intervals, which are typically separated by less than 10 ms. In Figure 6.4 three typical evolutions of the phase are depicted. The data of each subplot shows two curves. One which is filtered with an RBW of 43.3 kHz (green) and one with 84.5 Hz (red). Part a) shows an average phase drift as it occurs in either direction for normal operation and stable temperature conditions. A 2π phase shift occurs within a 4 second interval. For very stable environmental conditions this value further decreases as it is depicted in part b). Part c) shows the case of higher temperature fluctuations caused e.g. by people walking past the setup or long opening times of the laboratory doors. Here, the phase drifts by as much as 3π per second; this will be considered as the worst case for the phase drift. Assuming

reference times during the experimental run of 5 ms before and after each probe interval of 0.5 ms length, the worst case yields inaccuracies caused by phase drifts of less than 2.4 mrad. This means that the phase relationship can be seen as constant throughout the scan.

6.3. Vacuum Noise

The heterodyne signal is subject to various noise sources. A lower limit of the noise floor is set by the shot noise caused by vacuum fluctuations of the light field. However, this fundamental limit can also be overcome by amplitude-squeezed light [87], [149]. For a similar atom-cavity system this was studied in a previous publication [71] and will not be elaborated further in this thesis. In addition, classical noise sources as they are added by the photodetector, e.g. due to dark current or by the electronic circuit, e.g. stemming from the amplification process, contribute to the final signal. The amplification of the vacuum noise depends on the power setting of the optical local oscillator used for the heterodyne detection, while the classical noise sources remain almost constant. Because of this, the power of the local oscillator permits to adjust the ratio of the shot noise to the classical noise sources. In our system the power of the local oscillator was chosen such that power spectral density of the shot noise exceeds the other classical noise sources. The signal-to-noise ratio is then at its fundamental limit [150], [151].

The shot noise variance is given by evaluating the voltage level of the balanced photo detector U_θ^2 in the vacuum state, i.e. with the probe beam blocked $|0\rangle = \int |0\rangle_\Omega d\Omega$ [100]. In this equation Ω denotes the beat node frequency of the heterodyne signal. Hence, the integration has to be carried out over the full spectral range limited by the digitizer. Utilizing Eqn. (2.52) results in:

$$\begin{aligned}\sigma_{shot}^2 &= \langle 0 | U_\theta^2(t) | 0 \rangle \\ &= \frac{\eta_0 P_{oLO} q_e^2}{\hbar \omega_0} 2G_0^2 \Delta\nu\end{aligned}\quad (6.1)$$

Here, η_0 is the effective detection efficiency of the local oscillator beam, P_{oLO} its power, ω_0 its angular frequency, q_e the elementary charge, G_0 the DC gain of the electric amplifier in the balanced detector and $\Delta\nu$ the electronic detection bandwidth. Including electronic noise of the detection system σ_e into Eqn. (6.1) results in the overall measured shot noise standard deviation.

$$\sigma_0 = \sqrt{\frac{\eta_0 P_{oLO} q_e^2}{\hbar \omega_0} 2G_0^2 \Delta\nu + \sigma_e^2}\quad (6.2)$$

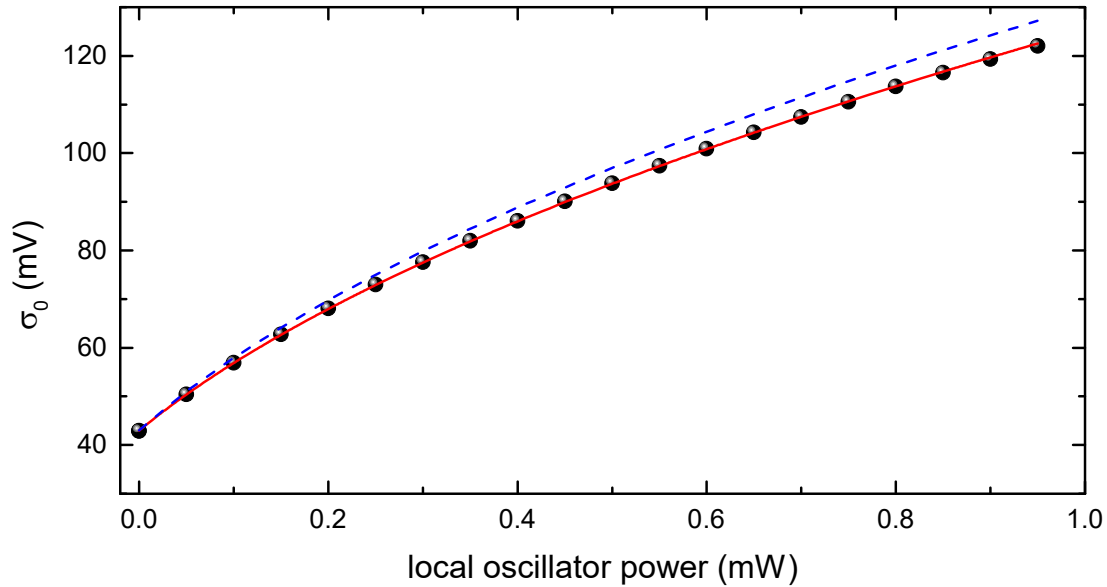


Figure 6.5: Measurement of the shot noise and electronic noise in the heterodyne detection system. The power of the optical local oscillator is scanned while the standard deviation of the noise of the photodetector current is determined. The black dots represent the actual data points, while the red line shows the corresponding square root fit. The blue line shows the expected value based on the Eqn. (6.3)

The dependency of the standard deviation on the power of the local oscillator, as it can be seen in Eqn. (6.2), enables an independent measurement of both noise terms and hence permits to check whether the measurement is shot-noise limited. In order to do so, the noise in the photocurrent as a function of the power of the optical local oscillator is determined. The result of this measurement is shown in Figure 6.5.

The actual data points are depicted as black dots. The red line shows a fit to a square root profile of the following form.

$$\sigma_0 = \sqrt{R_{vm} \cdot P_{OLO} + \sigma_e^2} \quad (6.3)$$

Here, R_{vm} includes all fixed parameters given by the detection system in Eqn. (6.2). There are two aspects which are noteworthy. First, one can see that for a blocked optical local oscillator, i.e. a power level of 0 mW, the measured noise corresponds to $\sigma_e = 43$ mV, which can be contributed solely to electronic noise. Secondly, the detected noise increases with the square root of the local oscillator power. This shows that the detection scheme is mainly limited by the shot noise for local oscillator powers above 0.5 mW. The power levels indicated are measured for the entire beam and hence comprehend the power of the local oscillator in both arms. Apart from this very basic check, the actual magnitude of the measured noise can be verified as well. The parameters of Eqn. (6.2) which are present in our setup amount to:

- The effective detection efficiency of the local oscillator at 780 nm is $\eta_0 = 0.8$. This value is derived from the responsivity of the photodiode of 0.53 A/W including the

overall optical transmission of 95% for our system, which is mainly limited by the interference filter also present in the SPCM setup, cf. Section 3.6

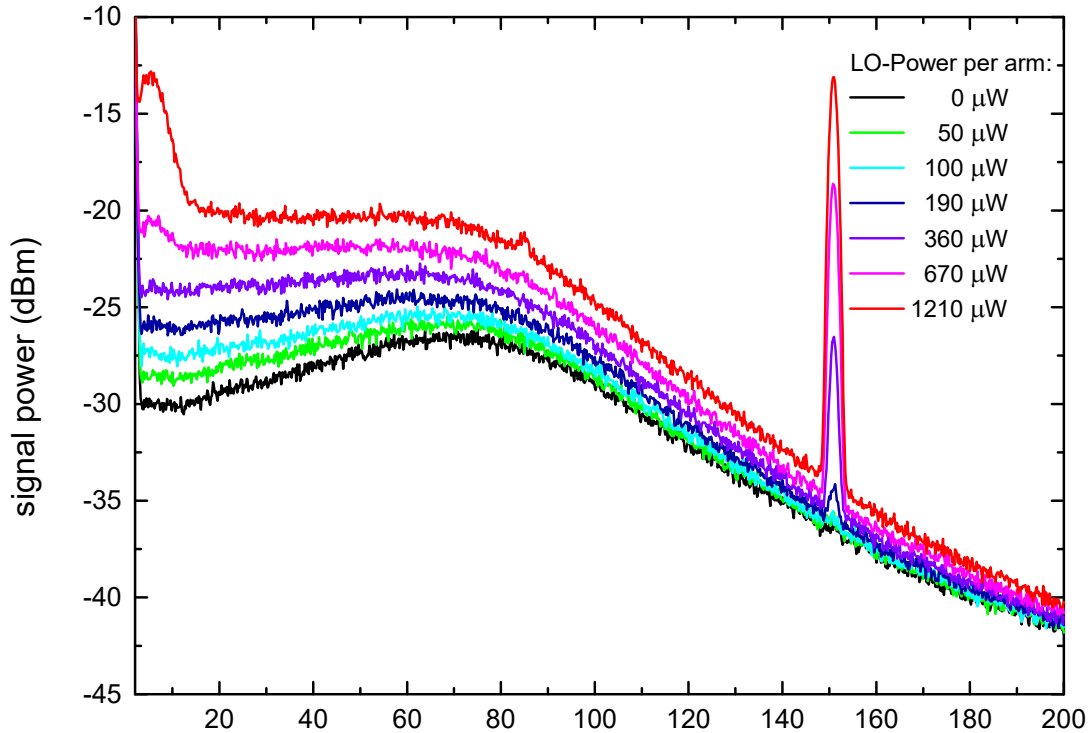


Figure 6.6: Spectral noise power for different power levels of the local oscillator. The spectral noise power of the photo current is plotted from 0 to 200 MHz. A spectrum is recorded for various power levels of the local oscillator. The power level is measured in one arm of the balanced detection and thus represents half the total power of the local oscillator, which is indicated in Figure 6.5.

- The DC gain of the amplifier $G_0 = 90 \text{ kV/A}$ is measured with $50 \text{ } \Omega$ termination.
- The detection bandwidth $\Delta\nu = 40 \text{ MHz}$, which is given by the 40 MHz anti-aliasing filter on the adapter module.

Furthermore, an overall factor of 17 needs to be multiplied to all voltage levels. This factor is caused by an additionally implemented amplifier ZFL-500²⁷ by mini-circuits. This hence also applies to the standard deviation of the noise given in Eqn. (6.2). An electrical noise power of 43 mV is extracted from the above measurement. This permits to compute the total noise of the detection system. At a local oscillator power of 0.9 mW , the computed value of 124 mV corresponds very well to the measured one of 119 mV . The fitting of Eqn. (6.3) to the data yields $R_{vn} = 13.9 \text{ } \Omega$ which matches the computed value of $R_{vn} = \frac{\eta_0 q_e^2}{\hbar \omega_0} 2G_0^2 \Delta\nu = 15.1 \text{ } \Omega$. The

values measured in the range which is depicted in Figure 6.5 correspond nicely to the expected values. The deviation to the theoretically computed line can be attributed to small additional losses caused by optical elements in the beam path. The agreement with the theoretically expected value, however, changes significantly as the local oscillator power is further increased.

²⁷ The ZFL is operated at 15.2 V . The measured gain is $\sim 24.64 \text{ dB}$, which corresponds to an increase by a factor of 17.

In order to understand this discrepancy, the spectral noise density is plotted for different power levels of the local oscillator. This is depicted in Figure 6.6.

The scans are recorded by connecting the voltage output of the balanced photodiode to a spectrum analyzer with a $50\ \Omega$ termination (Agilent MXA). The spectra are directly transferred from the analyzer with no further processing. The power levels are measured in one arm of the heterodyne detection and thus only present half the power of the local oscillator. At a frequency of 150.5 MHz a sharp feature starts to appear from around $100\ \mu\text{W}$ onwards. This is caused by residual light of zeroth order which can pass through our AOM bench. Normally this light is suppressed during the adjustment of the AOM bench. However, the high amplification in the heterodyne detection permits to even detect tiny residual components. Due to its high frequency offset, this signal is completely filtered before the digitization and thus does not disturb the measurement. On the other hand, a second feature is visible at measured power levels of 1.2 mW in one arm at a frequency range between DC and 10 MHz. The origin of this signal can be traced back to the AOM in the local oscillator path. If no AOM is in the path, this feature disappears. Moreover, does the spectral shape depend on the specific AOM and its manufacturer. We assume that nonlinear effects inside the crystal of the AOM due to the radio frequency driving it, which reaches power levels as high as 1 W, cause this feature. Whereas this feature can have a significant impact when considering the total noise of our system, its impact is diminished by choosing a heterodyne carrier above 15 MHz and using frequency filtering techniques to discard this feature. The choice of the heterodyne carrier frequency will be elaborated in Section 6.4.1. In the following, a local oscillator power of 1 mW, i.e. a power of 0.5 mW in each arm, will be employed. At this power level a good amplification of the transmitted probe signal and thus a good signal-to-noise ratio is achieved. However, it is still sufficiently low to suppress the features stemming from the AOM.

6.4. Beat Node

The full information about the transmitted probe beam is encoded in the beat node of the heterodyne signal. Its frequency is given by the frequency difference of the local oscillator and the probe beam. Figure 6.7 shows the transmission of a probe beam with a typical intensity of a few pW, which is on resonance with the empty cavity.

Part a) shows the full spectrum of the signal recorded by the digitizer at 100 MS/s. It is computed by performing a fast Fourier transform (FFT) with a length of 0.2 seconds of the recorded data. To reduce the amount of data, 50 adjacent samples of the spectrum are averaged to one sample. A sharp drop occurring after 40 MHz is visible. It is stemming from the bandwidth filter of the digitizer. The heterodyne carrier at 27 MHz is clearly visible. It is overlain by a spectrally uniformly distributed noise background. The height of the peak compared to the noise background is reduced by the previously described averaging. A closer look at the carrier is shown in Figure 6.7 b). Here an FFT is applied to 0.5 seconds of the data. This time, no averaging was carried out. The sharp width of the peak is evident. In case of an

empty cavity the width is mainly limited by phase fluctuations as they are shown in Section 6.2.2.

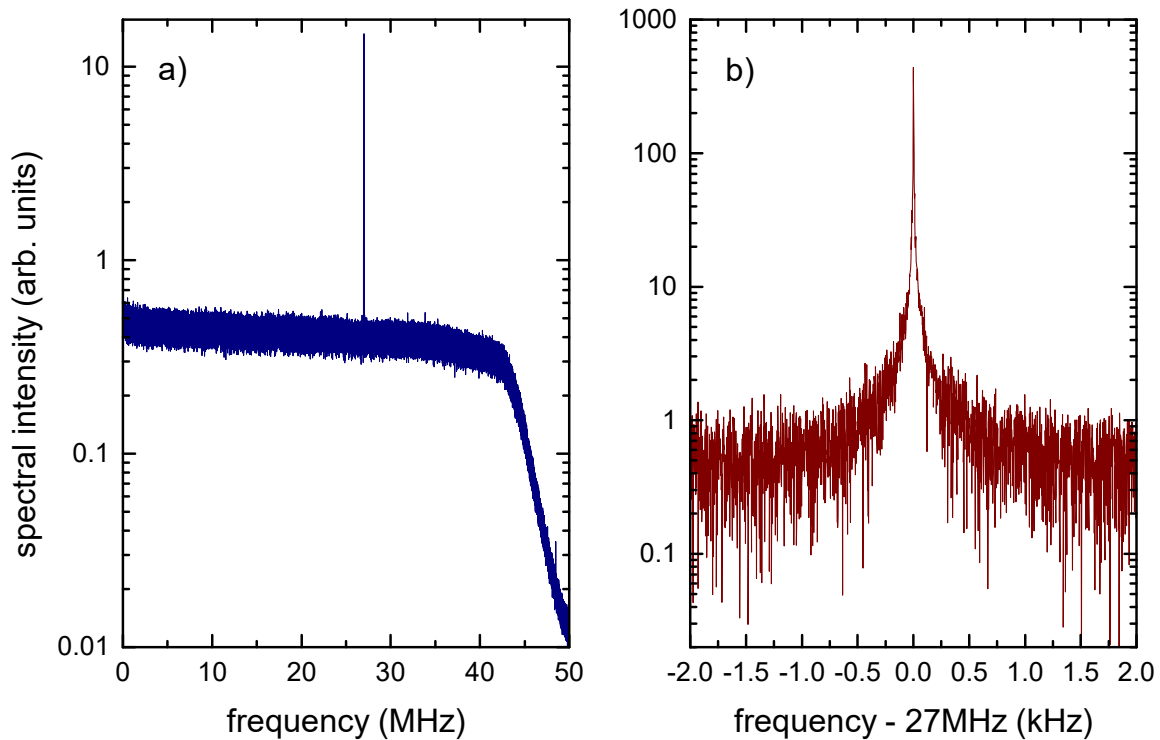


Figure 6.7: Beat signal of the probe and local oscillator beam. a) shows the full spectral width of the 100 MS/s digitizer. The heterodyne carrier appears as sharp peak in the spectrum. b) shows a zoom-in into the region where the heterodyne carrier is placed.

The beat is characterized by two main parameters. One is its magnitude, which also significantly depends on the efficiency of the detection system. This in turn is to a large extent determined by the overlap of the probe beam with the local oscillator at the position of the photodiode. For this setup a visibility of the heterodyne system of $\eta_{vis} = 0.82$ is measured, see Appendix 10.6.4. The parameters for the photo detection itself have already been given in Section 6.3. The second parameter characterizing the beat is its frequency, the choice of this parameter will be elaborated in the following paragraph.

6.4.1. Choice of Local Oscillator (LO) Frequency

The local oscillator in the heterodyne detection fulfills the main task of down-converting the probe beam into the radio frequency range, which can be recorded by standard electronic equipment. Furthermore, the detectable intensity of the down-mixed signal is proportional to the product of the probe and local oscillator amplitude, which hence permits to amplify the weak probe beam to a range so that it can be detected by a standard pin-photodiode²⁸. In order

²⁸ pin-diode: positive intrinsic negative diode

to accomplish these tasks, the choice of the best operating frequency is crucial and needs to obey certain boundary conditions. This will be eluded in this sub-section.

6.4.1.1. Scattered Light of LO

The heterodyne detection comprises a weak probe beam as well as a bright local oscillator. While the probe beam is on the order of only a few pW, the intensity of the LO is significantly higher by a factor of about a billion. The optical setup which is required to overlap these two beams also causes a weak back-reflection of the local oscillator that impinges on the cavity. This back-reflection cannot be attributed to a single component, but is rather due to very little reflections at each component in the optical path of the overlapped beams. Due to the grossly unbalanced intensity levels, part of the back-reflected local oscillator can enter the optical cavity and heat the atom. One way to quantify this effect is to store the atom inside the cavity and measure the probability of losing the atom by tuning the local oscillator to the frequency under study for a short time, which is on the order of a few hundred μs . Before and after each interval the local oscillator is tuned to its original frequency, which is detuned by $(\omega_{LO} - \omega_c)/2\pi = 27\text{MHz}$ to the probe beam. During this time the transmission is measured to check if the atom is well captured. This is determined by a suppression of the transmission probe beam, which is on resonance with the cavity, to 4% of its empty cavity value. This switching technique is exactly identical to the one which will be described in detail in Section 6.7 with a qualification factor of 4%. Scanning the frequency of the local oscillator during the probe intervals yields Figure 6.8.

Here, a significant drop at a local oscillator frequency around the resonance frequency of the atom can be observed whereas for higher and also lower frequencies a steady value of slightly

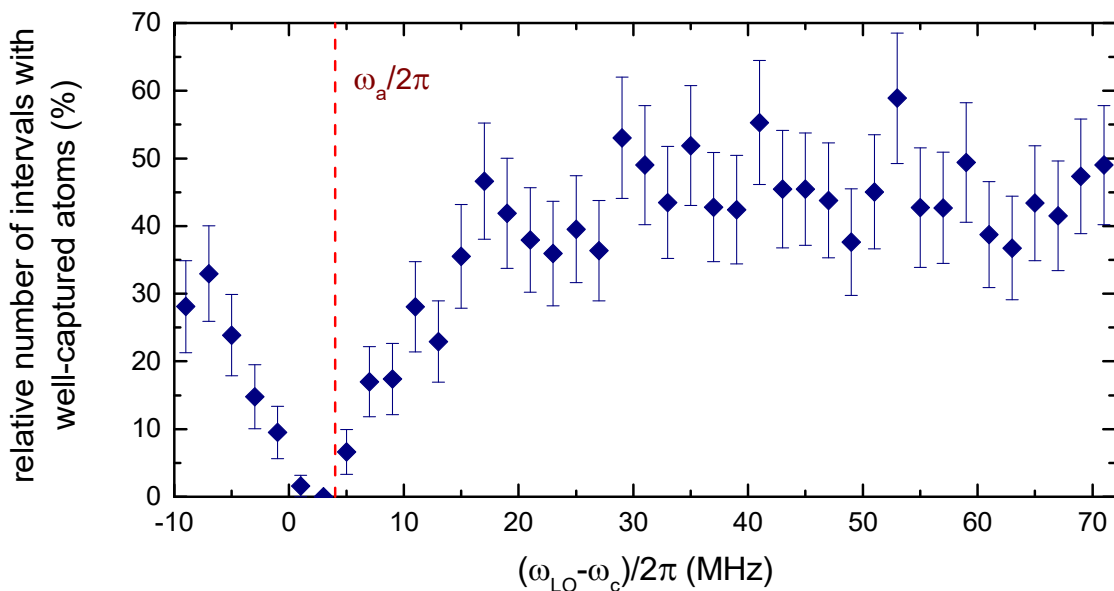


Figure 6.8: Heating of the atom by residual local oscillator power. The remaining number of atoms after intervals where the local oscillator is tuned to the value indicated on the x-axis is measured. The position of the atomic resonance is marked by the vertical dashed red line. The probe beam is set to be on resonance with the empty cavity, which is blue-detuned by 4 MHz to the atomic resonance. The error bars represent the 2 sigma confidence level.

below 50% is attained. The drop is explained by remnant light of the local oscillator impinging on the cavity and heating the atom. It is important to note that this light mainly enters the cavity by diffuse scattering on the coned facet of the mirrors. Coupling to the cavity mode would possess a strong dependency on any small misalignments of the local oscillator beam, which is not visible. The negative effects of back-reflection could be reduced by employing an optical faraday isolator at the detection port of the cavity. This, however, would be on the expense of probe beam intensity and would further require complex compensation of the generated magnetic field gradient. We decided to circumvent this effect by choosing local oscillator frequencies sufficiently far away from the atomic resonance so that heating effects are reduced to a minimum.

6.4.1.2. Frequency Response of Heterodyne Detection

Besides limitation in the choice of the heterodyne frequency imposed by the atomic resonance frequency, effects related to the heterodyne detection itself also need to be considered. As already mentioned in Section 6.3, noise in the LO beam in a frequency range of up to 15 MHz requires beat frequencies above this range. This way also higher LO powers can be used. For large frequency differences on the other hand, it needs to be ensured that bandwidth limitations of the digitizer do not minimize the frequency response. In order to measure the response curve, we scan the frequency difference between probe and LO, corresponding to the heterodyne frequency, while the probe is on resonance with the empty cavity. The detected probe heterodyne carrier is extracted and its magnitude is plotted as a function of the frequency difference as it is shown in Figure 6.9.

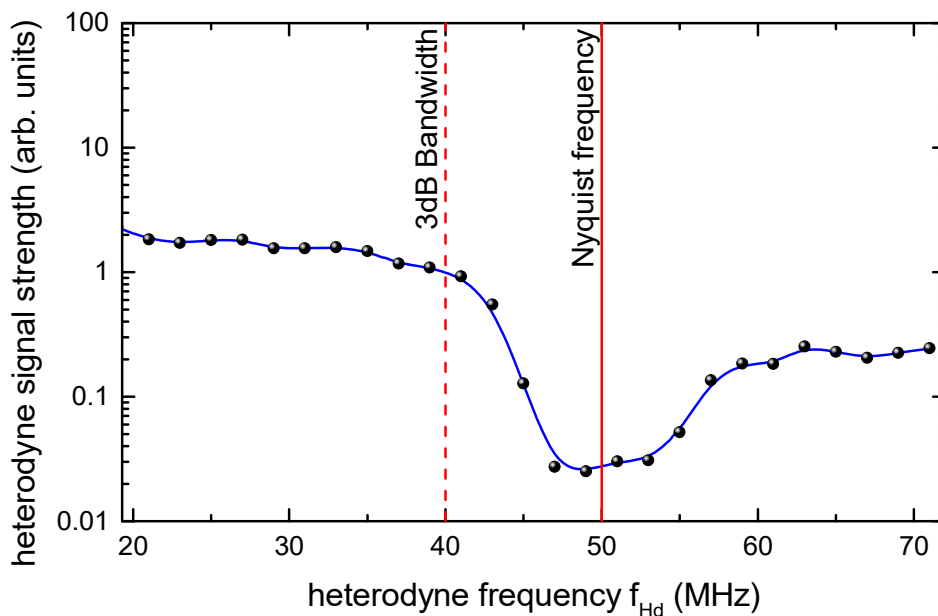


Figure 6.9: Frequency response of the heterodyne detection system. The heterodyne signal strength detected by the system is plotted as a function of its frequency. The Nyquist frequency (solid) of the digitizer as well as the -3dB bandwidth (dashed) of the low-pass filter in front of the digitizer are plotted by vertical red lines.

It can be seen that at 40 MHz the signal strength starts to drop. This is caused by the -3dB bandwidth filter at the analog input of the digitizer module as well as the bandwidth limitation of the digitizer. The latter one is given by the Nyquist frequency which corresponds to half the sampling frequency of the digitizer. From this we can deduce that the heterodyne frequency, i.e. the frequency of the beat between probe beam and local oscillator, needs to stay below 40 MHz, which sets another limitation to the frequency choice.

6.4.1.3. Variable Beat-Frequency

The various boundary conditions described above require using a variable heterodyne frequency which depends on the frequency of the probe beam. The best choice for the respective heterodyne frequency considering these effects is depicted in Figure 6.10. The AOM frequency of the probe beam (red) is indicated as a reference. The AOM frequency of the local oscillator (blue) is chosen such that it avoids the typical atomic resonance frequency as indicated by the horizontal, dashed line. The resulting absolute heterodyne frequency is always kept in the range between 18 MHz and 40 MHz where the heterodyne detection has a flat frequency response. Only at probe-cavity detunings of $(\omega_p - \omega_c)/2\pi < -30\text{MHz}$ this condition is weakened due to the missing tuning flexibility of the AOM which is centered at 150 MHz. The following scans unless otherwise noted are recorded with these frequency settings.

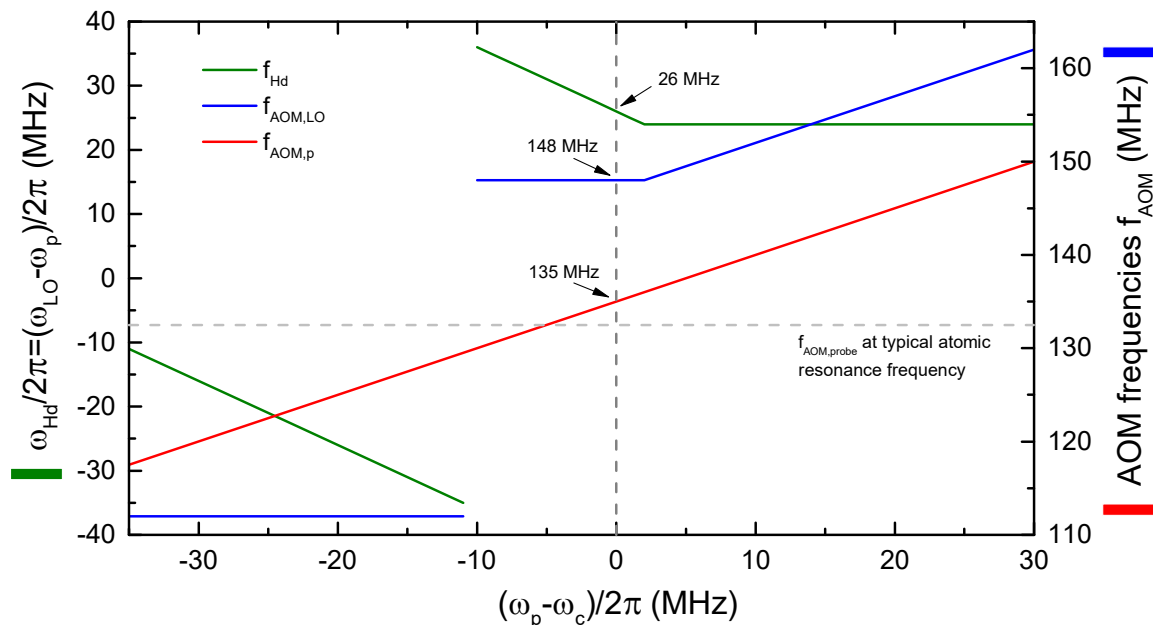


Figure 6.10: Choice of the heterodyne frequency as a function of the probe beam frequency. The frequency of the local oscillator (blue) as well as the probe beam (red) is plotted as a function of the probe-cavity detuning. The resulting heterodyne frequency (green) is also plotted. The dashed horizontal line depicts the frequency where the local oscillator (and also the probe) is on resonance with the atom resonance. It is noteworthy to remember that the actual frequency difference is twice as high due to the double pass configuration of the AOM.

6.4.2. Comb-beat vs. Heterodyne Phase

Compared to photon counting, heterodyning due to its phase sensitivity is more sensitive to fluctuations in the cavity length. Especially the phase of the probe beam is a good measure for the stability of the setup. At the empty cavity resonance this phase to first approximation changes linearly with the length of the cavity and undergoes a π phase shift within the bandwidth of the cavity. Various noise sources contribute to fluctuations of the cavity length. Here we will exemplarily demonstrate the influence of acoustic noise. A tone at a fixed frequency is generated and its artefact in the heterodyne signal is observed. The result is plotted in red in Figure 6.11. As a reference, the length deviation of the cavity, as it can be derived from the error-signal of the cavity-lock described in Section 4.6, is plotted in blue.

The phase of the beat node while driven by an 82.41 Hz acoustic oscillation is plotted in the frequency as well as in the time domain in part a) or b), respectively. The driving frequency is clearly visible in both signals. In addition, the linearity between the cavity-length and the phase of the heterodyne signal is also evident. In part c) and d) the “artificial” noise source was turned off, leaving only the active cavity-stabilization as actuator on the cavity. In this case, the full-width linewidth of the cavity lock corresponds to ~ 667 MHz (see section 4.6.3). The correlation between the phase of the heterodyne signal and the length fluctuations are again visible. This time, the magnitude is smaller and the main frequency component is now slightly above 1kHz.

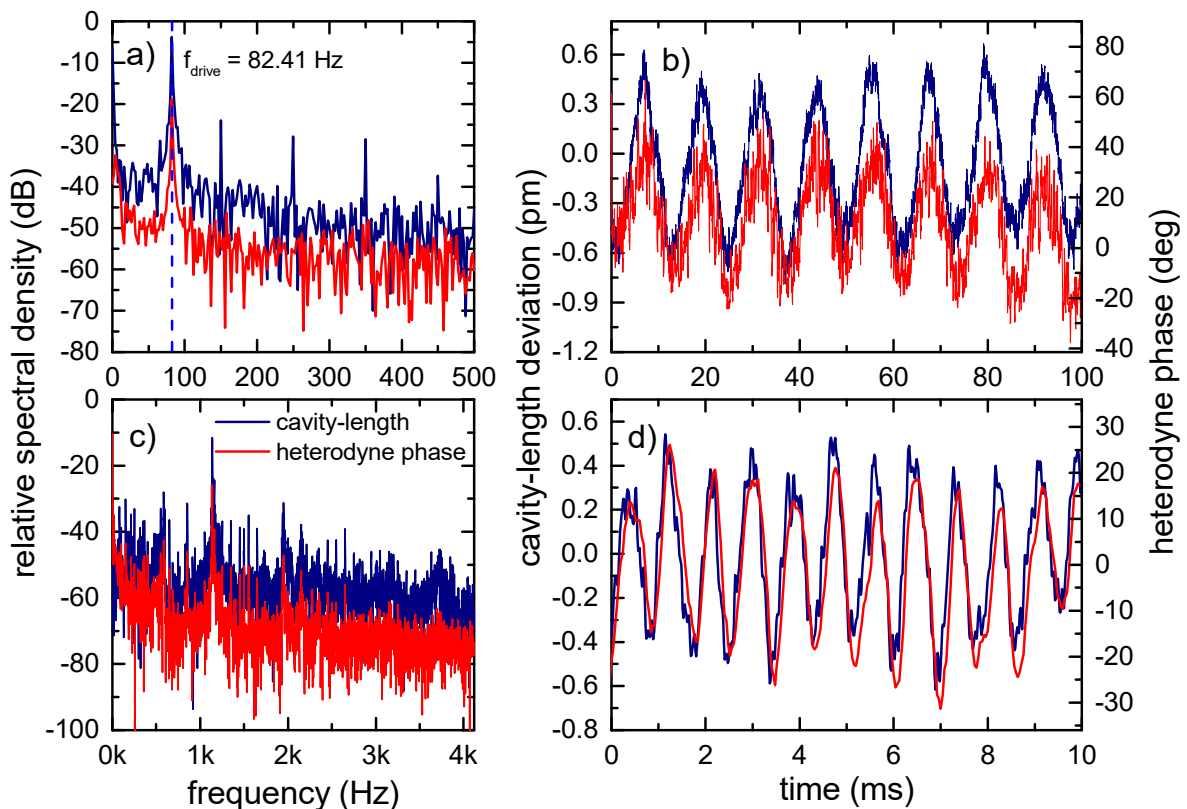


Figure 6.11: Influence of fluctuations of the cavity length on the heterodyne phase. The red plots show the measured phase of the heterodyne signal of the probe beam while the blue plots depict length deviations of the cavity measured by the PDH-lock of the dipole trap beam. a) and b) show measurements in the frequency and time domain while an 82.41 Hz acoustic noise was applied. c) and d) show a similar measurement but without any external noise signal.

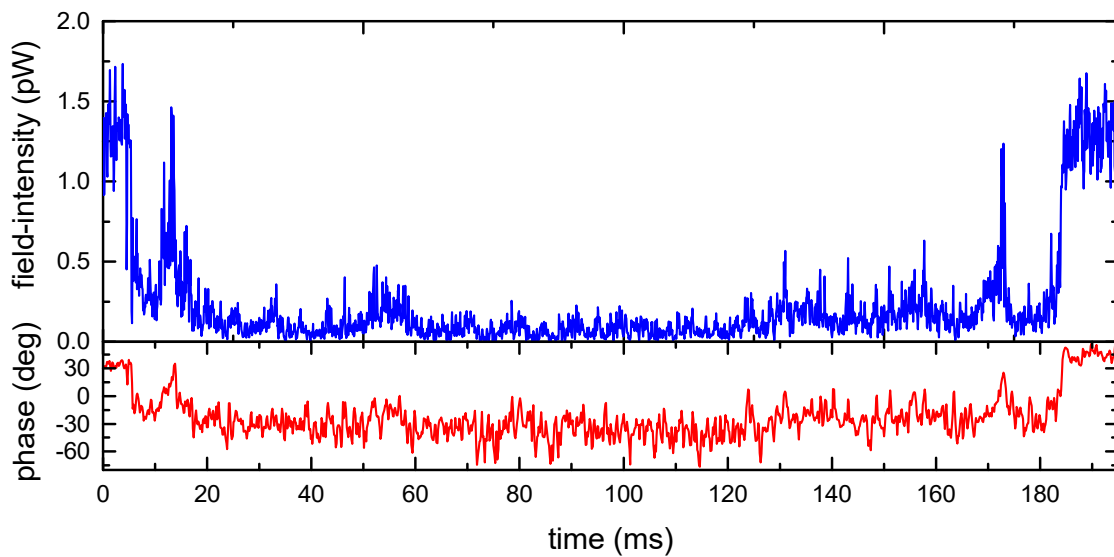


Figure 6.12: Typical heterodyne trace without feedback. The extracted intensity (blue) and phase (red) information is depicted. The atom is captured after 5ms and stays for around 180 ms.

This frequency could be attributed to the mechanical resonance frequency of the titan sublimation pump [132]. The linear dependency between the two signals would in principle also permit to use the probe beam for additional cavity stabilization. The interdependency, however, if an atom is present in the cavity, becomes more complex. First tests of employing the trap and probe beam for stabilization did not show any significant improvement, but would in principle permit to decouple the cavity from noise sources of one single laser.

6.5. Sample Heterodyne Trace

The loading procedure to get an atom inside the cavity as well as the experimental sequence in case of a heterodyne detection is the same as it was used for photon counting. Figure 6.12 shows a typical trace for an atom which was stored in the cavity for 180 ms without applying feedback. The probe laser was on resonance with the cavity so that a drop in the transmission signals a coupled atom. The field intensity is derived by squaring the respective field-amplitude and hence looks similar to the signal recorded by photon counting. Heterodyning, however, also permits to observe the phase of the transmitted probe beam. This parameter also depends on the effective coupling constant which is altered by the atomic motion as it was described in Section 5.3. At first glance, the behavior of the phase resembles the one recorded for the amplitude. This becomes very clear when the atom leaves the cavity and causes a jump in the phase of around 60 degrees. In order to gain a more quantitative view of this behavior, the amplitude and phase dependency as a function of the radial atomic position is plotted in Figure 6.13. This theory curve includes, besides the direct influence due to the reduced coupling in case of a decreasing probe beam field at the atomic position, also the change of the atomic resonance due to the radial dependency of the ac-Stark shift. It was further assumed that the node of the probe

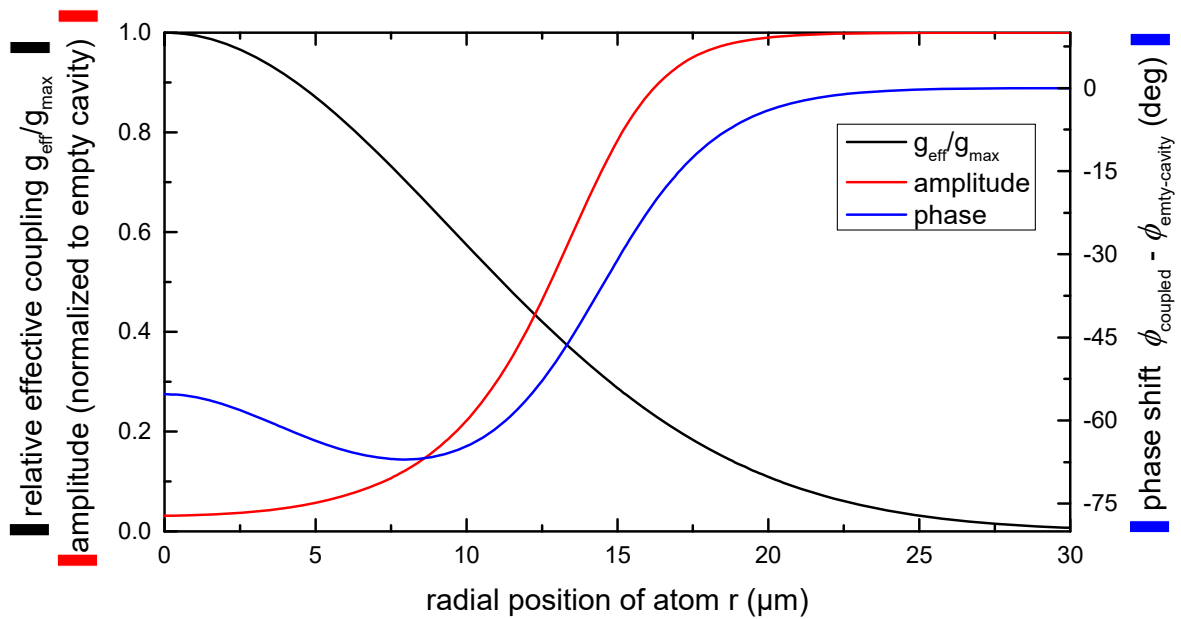


Figure 6.13: Amplitude and phase for different coupling strengths. The effective coupling strength (black) is plotted as a function of the radial position of the atom away from the cavity axis. The resulting transmitted amplitude (red) and phase shift (blue) as recorded by a heterodyne measurement are depicted as well.

beam and the trapping beam overlap perfectly at the position $r = 0\mu\text{m}$. As the atom moves further away from the center of the cavity, the effective coupling constant g_{eff} continuously decreases from its maximum value g_{max} until it reaches 0 MHz. Since the probe beam is on resonance with the empty cavity, the amplitude of the transmitted beam increases for weakly coupled atoms. The change in the phase of the transmitted probe beam is depicted by the blue curve in Figure 6.13. A phase shift of around 60 degrees can be observed, which agrees nicely with the measured trace depicted in Figure 6.12. The richer structure of the phase signal originates from a phase change that is on one hand due to the ac-Stark shift and on the other hand due to the actual position of the atom in the mode of the probe beam. The two effects are partly counteracting each other yielding the first decreasing and then increasing phase for increasing radial distance.

6.6. Feedback Implementation

In the previous section, a sample trace without feedback was depicted. In this section, a feedback algorithm similar to the one employed for photon counting is introduced. As done previously, a differentiation between the radial or axial direction has to be done. The Fourier transform of the heterodyne signal of the transmitted probe beam for typical parameters is depicted in Figure 6.14. A strong radial oscillation around 7.5 kHz and a weaker axial oscillation around 450 kHz are visible.

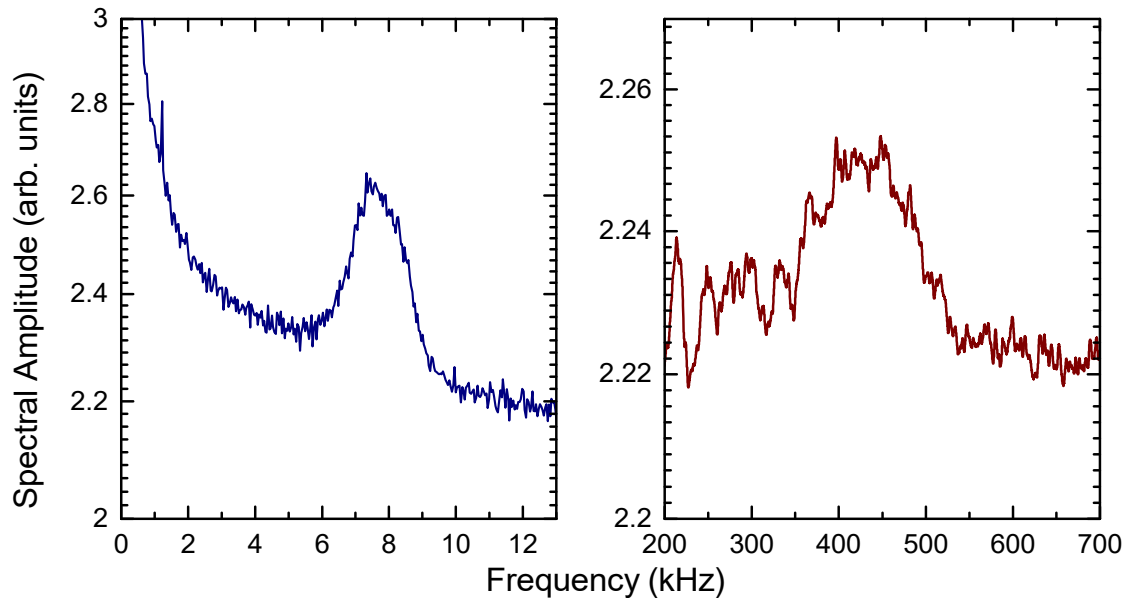


Figure 6.14: Radial and axial oscillation observed by heterodyne detection. The blue graph on the left shows the FFT in the kHz range where the radial oscillation becomes visible. The brown plot on the right side shows the FFT for higher frequency values. Here the fast axial oscillation becomes visible.

6.6.1. Radial Oscillation

The feedback algorithm employed for the radial feedback corresponds to the bang-bang method as it was implemented for photon counting (cf. Section 5.5.2). The implementation of the algorithm, however, is substantially different. The simple way of comparing the number of clicks in one interval to the preceding one is not applicable for heterodyne detection. Instead, the radio frequency heterodyne carrier data is down-converted by the electronic local oscillator, as described in Section 6.2.1. Afterwards, the data is filtered by an RBW filter (cf. Appendix 10.6.2) and subsequently converted to an amplitude and phase information. The amplitude part is then solely used for the feedback algorithm, which computes the slope of the signal over a fixed period of time. Depending on the result of the feedback algorithm, a digital output channel then switches the dipole trap from high to low value. A typical trace for an atom which is captured with the feedback routine as just described is depicted in Figure 6.15.

In the upper window the blue curve shows the squared amplitude of the transmitted probe beam. The arrival of the atom is visible by the sharp drop in the transmission. The atom stays in the cavity for more than 3 seconds before it leaves the cavity giving a steep rise in the amplitude. The measured relative phase of the transmitted probe beam is depicted in the brown graph underneath. The overall drift is caused by changes in the relative path length of the local oscillator compared to the probe beam, as it was described in Section 6.2.2. When the atom exits the cavity, a jump in the phase by roughly 60 degrees is visible as it was the case for the trace recorded without feedback. The feedback itself will not be described in this section, since it was already described in detail earlier. Here, the feedback will only be used as tool to cool the atom and increase the storage time.

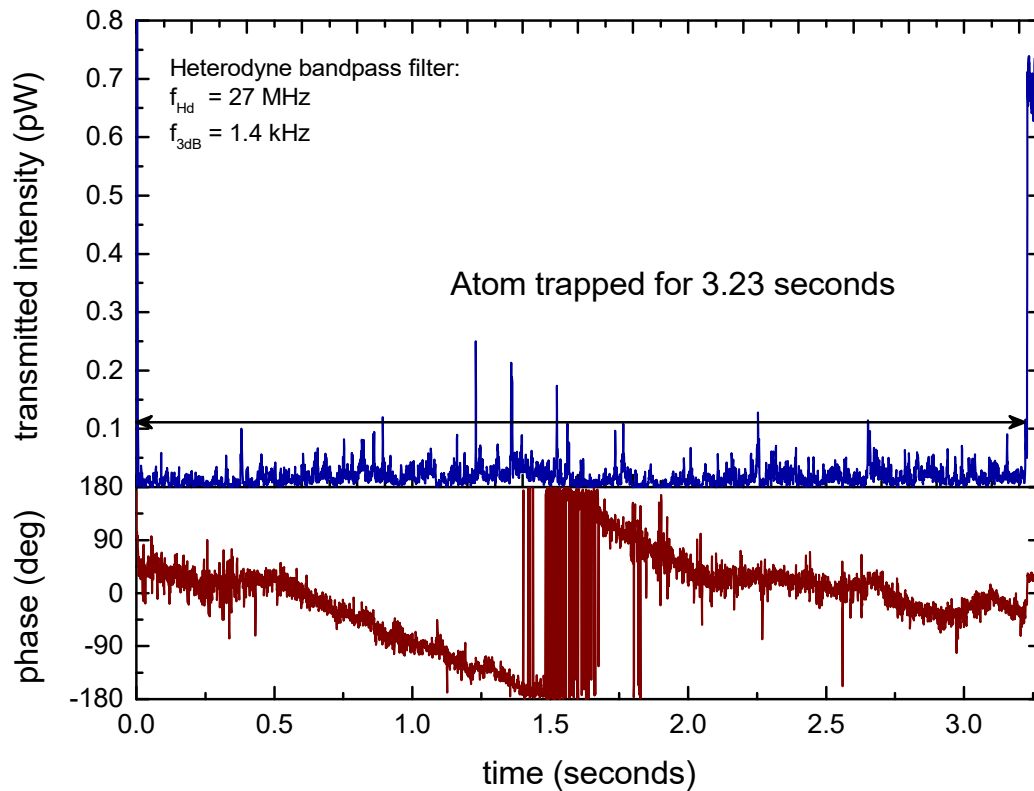


Figure 6.15: Typical heterodyne trace with feedback. The blue trace shows the measured intensity, i.e. amplitude squared signal. The brown trace below shows the measured phase. The heterodyne frequency was set to 27 MHz and a 1.4 kHz 3db RBW was applied during the extraction of the data for the plot. The atom stayed for 3.23 seconds.

6.6.2. Axial Oscillation

Similar as it was done for the radial bang-bang feedback routine, the axial parametric feedback, which has been described in Section 5.5.4, is also transferred to the heterodyne detection FPGA. The proper mode of operation has been extensively examined by generating artificial traces with an arbitrary function generator and observing the reaction of the feedback routine. Unfortunately, the actual implementation of the feedback algorithm into the experimental setup did not offer any improvements concerning the storage time of the atom. Nor did the adjustment of the parameters inside the feedback routine show any deterministic or reproducible effect. We attribute this to be caused by the only weak axial oscillation, whose correlation measurement is plotted in Figure 6.16. The increased bandwidth setting of the RBW-filter in the heterodyne data processing path, as it is required for the fast oscillations to pass the filter, also increases the noise-floor and hence significantly reduces the signal-to-noise level. Thus, the quality of the prediction of the atomic position done by the feedback algorithm is also significantly degraded. Here, multiple values for the RBW filter between 500 kHz and 1 MHz have been tested. Similar to how it was done for photon counting, the amplitude correlations of the axial oscillation can be evaluated. The result is depicted in Figure 6.16.

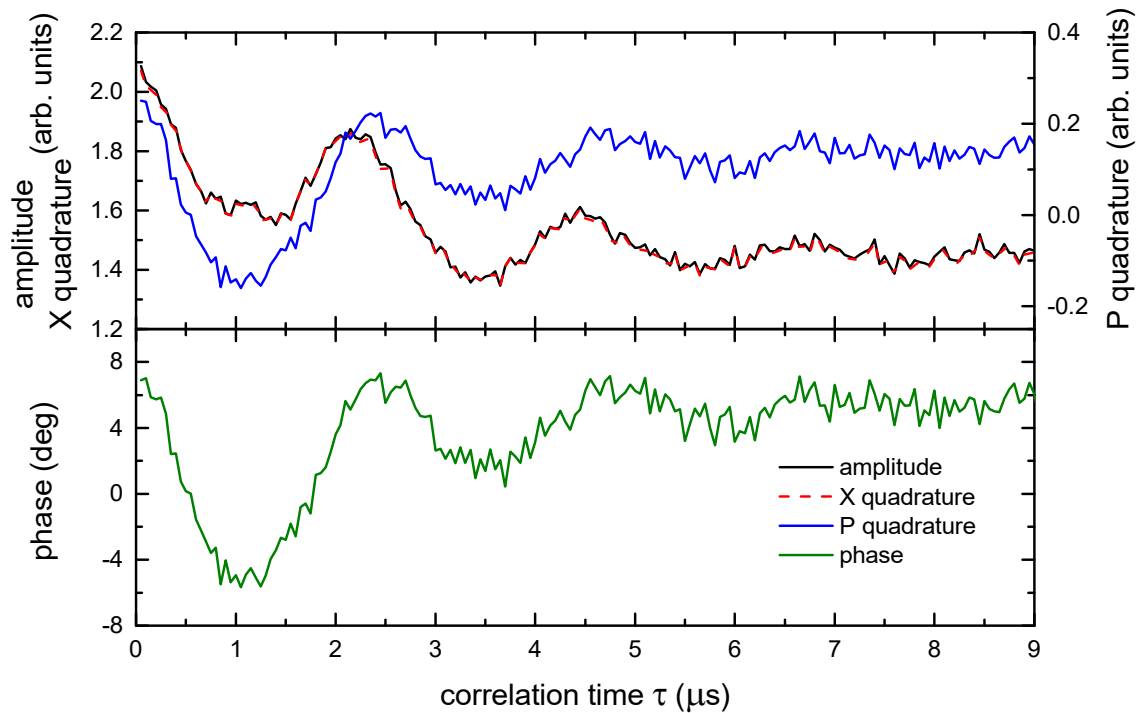


Figure 6.16: Correlation measurement of the heterodyne data. The I and the Q component of the heterodyne data, corresponding to the X and P quadrature of the light field, are correlated independently. From this the amplitude and phase signal are derived.

The data is derived by correlating the I and the Q part of the complex field amplitudes, which correspond to the X and P quadrature of the light field. Long-term phase drifts are compensated by referencing the data to the low-passed phase value while the atom is captured. The curves are plotted in arbitrary units and show a distinct signature of the atomic oscillation in the dipole trap. As expected, the oscillation is detectable in the amplitude and phase signal.

6.7. Switching Measurements

In this section an omnipotent technique which is referred to as switching measurement will be employed. It permits to examine the atom e.g. at various detunings of the probe light, also at values where heating effects become dominant, while still ensuring a good overlap to the mode of the probe field inside the cavity. This technique has been applied earlier for photon counting measurements to determine e.g. the normal-mode spectrum of the coupled system. Here, its application to heterodyning including the phase-measurement will be explained. The basic idea of a switching measurement is to probe the atom only during short intervals and to prepare the atom by cooling and confining it during the remaining time.

6.7.1. Implementation

The experimental sequence is identical until the atom is trapped to the one employed to trap and store a single atom inside the cavity (cf. Section 3.8). Once the atom is trapped inside the cavity, subsequent probe and cool intervals are employed to study and cool the atom alternately. A sample trace of the implementation is depicted in Figure 6.17. As in previous graphs, the intensity corresponding to the field amplitude squared as well as the phase of the heterodyne signal are plotted. The respective levels during cooling intervals are indicated by the blue lines whereas the levels during probe intervals are plotted in red. It is important to note that the length of the probe intervals in this exemplary measurement is increased by roughly one order of magnitude compared to typical values in order to ensure a better visualization. In this sample trace the atom is trapped for slightly above 60 ms, as it can be seen by the suppression of intensity in the cooling intervals. During these intervals, the probe laser is on resonance with the empty cavity $\Delta_{pc}/2\pi = (\omega_p - \omega_c)/2\pi = 0\text{MHz}$ and the effective atom-cavity detuning is set to $\Delta_{ac}/2\pi = (\omega_a - \omega_c)/2\pi = -4\text{MHz}$. The atom-cavity detuning

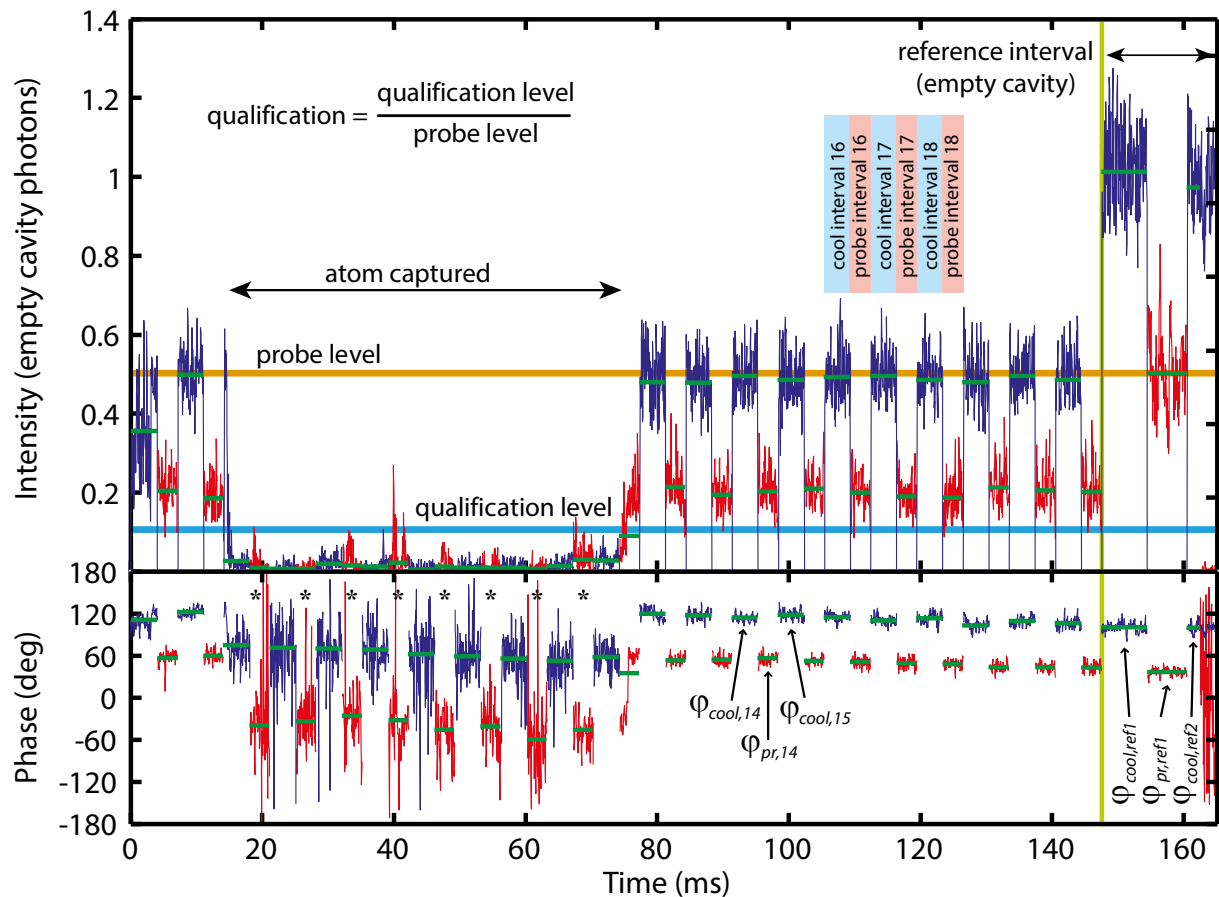


Figure 6.17: Implementation of the switching measurement. The intensity (amplitude squared) as well as the phase of the heterodyne measurement are shown. The experimental run is divided into cool and probe intervals. During these intervals some parameters of the system especially the frequency of the probe laser are changed. These intervals are indicated by the blue or red graphs. The expected transmission through the cavity if no atom is present is indicated by the dark orange solid line. If an atom is captured the transmitted probe power during the cool intervals drops. A qualification level marked by the blue horizontal line selects the intervals during which the atom was well coupled. After a certain number of probe-cool intervals the intensity of the probe laser is increased and a reference measurement of the empty cavity is carried out.

includes the ac-Stark shift due to the dipole trap, and is set to the ideal value to allow for cavity cooling of the atom along the cavity axis [76]. Cooling in the radial directions is achieved by fast electronic feedback switching of the dipole-trap depth as it was described earlier (cf. Section 6.6.1). As in previous experiments, a weak repumping laser is employed to counteract for off-resonant light scattering, which can transfer the trapped atom to another hyperfine ground state that is not coupled to the cavity [57]. The intensity of the transmitted probe laser during cooling intervals reflects the strength of the coupling between atom and cavity; the lower the amplitude, the higher the coupling. By setting an upper limit for the amplitude in the cooling intervals preceding and following a given probe interval, we are able to post-select only those intervals in which the atom was known to be well coupled. This process will be described in more detail in Section 6.7.3. During the probe and cool intervals, the frequency of the probe beam will be switched. This switching might also require a change in the necessary local oscillator frequency, as it has been elaborated on in Section 6.4.1.3. In order to avoid unwanted effects caused by the switching, one needs to ensure a fast switching speed as well as a stable phase of the generated RF frequency, as it will be explained in the next section. Due to those requirements, two pairs of Rohde & Schwarz analog signal generators are employed to drive the AOM controlling the probe as well as the local oscillator beam during the probe and cool intervals, respectively. A high-speed minicircuit RF-switch is employed to synchronously switch between the two frequency sets.

6.7.2. Phase Sensitive Switching Measurement

While relative changes in the phase are directly evident in the recorded traces (see Figure 6.15), inferring information about the absolute phase of the transmitted light poses a more challenging task. In case an atom is trapped while a switching measurement is performed, the typical duration of the probe-cool sequence amounts to 250 ms. This sequence consists of about 40 probe intervals with a duration of 0.5 ms, which are interleaved by 5.5 ms long cool intervals. After the sequence the trap intensity is decreased and the probe laser power increased. This ensures that atoms that are still captured will be heated out of the trap within a few ms. Hence, a reference measurement of the now empty cavity is performed. In the exemplary trace of a switching measurement in Figure 6.17, this reference measurement is carried out starting at a time indicated by the vertical green line at 148 ms. During the reference interval two measurements of the phase of the probe laser at the cool interval setting $\varphi_{cool,ref1}, \varphi_{cool,ref2}$ interleaved by a measurement at the probe interval setting $\varphi_{pr,ref1}$ are carried out. This compensates for any linear drifts in the phase during the reference measurement, which typically takes around 20 ms.

The relative phase difference of the probe and cool intervals for the coupled atom-cavity system is determined by comparing the phase of each probe interval $\varphi_{pr,n}$ to the phase of its neighboring cool intervals $\varphi_{cool,n}, \varphi_{cool,n+1}$. These values are referenced to the phase of the empty

cavity measured during the reference interval at the end of the scan. In total this yields a phase value $\varphi'_{pr,n}$ for each probe interval, which is computed as

$$\varphi'_{pr,n} = \underbrace{\left(\varphi_{pr,n} - \frac{\varphi_{cool,n} + \varphi_{cool,n+1}}{2} \right)}_{\text{coupled system reference}} - \underbrace{\left(\varphi_{pr,ref1} - \frac{\varphi_{cool,ref1} + \varphi_{cool,ref2}}{2} \right)}_{\text{empty cavity resonance}}. \quad (6.4)$$

The extraction of $\varphi'_{pr,n}$ is a measure for $\phi_{\text{coupled}} - \phi_{\text{cavity}}$, which does not provide an absolute phase measurement of the phase shift induced by the coupled atom-cavity system on the driving probe laser $\phi_{\text{coupled}} - \phi_{\text{drive}}$, but delivers all necessary information to infer this information. Since the probe laser has a constant detuning of $\Delta_{pc}/2\pi = 0$ MHz during the cool intervals, it can be used as a reference throughout the different scans. The phase shift induced by the empty cavity $\phi_{\text{cavity}} - \phi_{\text{drive}}$ can also be measured accurately. For this purpose, the heterodyne signal is recorded by a high bandwidth digitizer (Rohde&Schwarz RTO1024) while the probe laser is scanned over the cavity resonance during the time of a few seconds. The high bandwidth is important, since sidebands at 32 MHz are modulated on top of the probe laser. These serves as reference beams to detect any phase drift in the detection system during the scan. The result was already shown in Figure 3.6b. These measures permit to derive a well referenced phase measurement of $\phi_{\text{coupled}} - \phi_{\text{drive}}$, which indicates the total phase shift added by our coupled system. Furthermore, the referencing permits to compensate for non-negligible phase drifts (cf. Section 6.2.2) during the sequence-duration of around 250ms. As already described in Section 6.7.1, the phase of the probe interval is only considered if the amplitude during the neighboring cool intervals indicates a well coupled atom.

6.7.3. Qualification and Post-selection

As already mentioned in the previous section, the intensity of the transmitted probe laser during the cooling intervals can be used to post-select only those probe intervals, where the atom was well coupled to the probe beam inside the cavity. As the average transmission is directly linked to the temperature of the atom, this method is thus also a way of post-selecting on certain temperature classes. The selection process is depicted in Figure 6.17, where the probe and the qualification level are marked. The probe level is the intensity of the transmitted probe beam in the empty cavity case as set in the experimental control program. The qualification level defines the intensity which has to be undercut by the average value of the probe intensity in the neighboring cool intervals to take the measurement of the respective probe interval into account. The ratio of qualification and probe level results in the actual normalized qualification parameter, which is used for the post-selection process. Figure 6.18 shows a histogram of the number of intervals in which an atom was caught considering a certain qualification level (red). Every probe interval was binned to one qualification level interval spanning a width of 0.1% in order to derive the histogram. A total of close to 93,000 intervals have been evaluated to derive this figure.

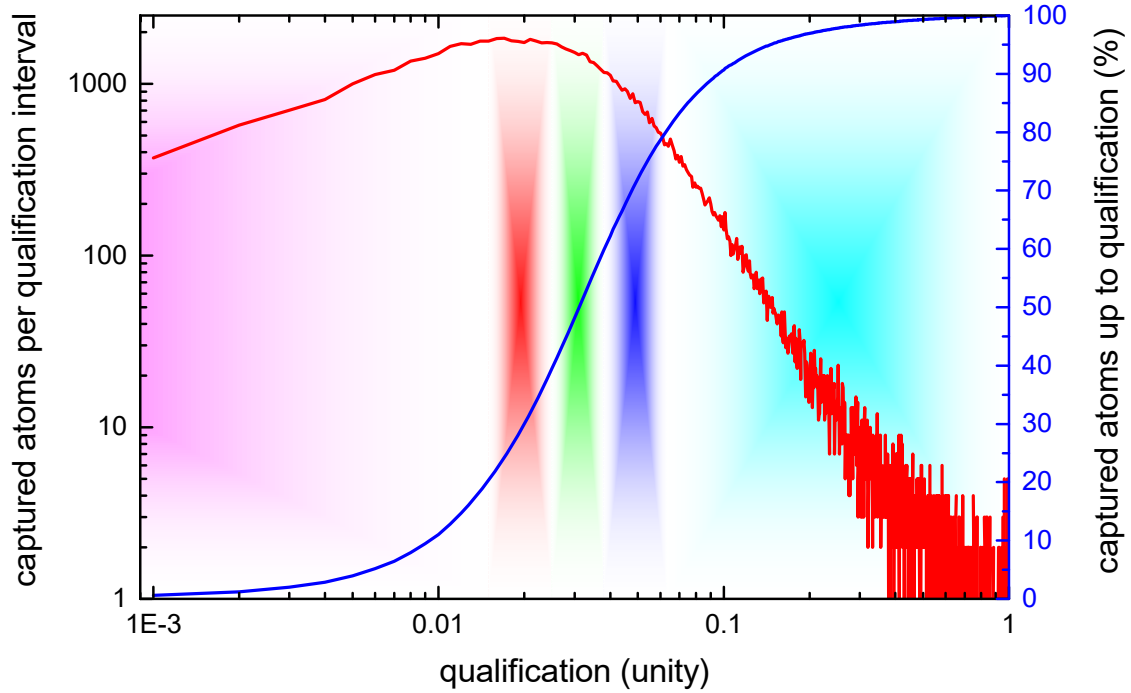


Figure 6.18: Number of captured atoms depending on qualification. The number of captured atoms per qualification interval is plotted in red. The overall fraction of atoms that are below a certain qualification setting are depicted in blue. The colors in the background specify certain ranges of qualifications levels as they will be used in the following. Magenta: 0% - 1.5%; red 1.5% - 2.5%; green: 2.5% - 3.8%; blue: 3.8% - 6.3% and cyan: 6.3% - 100%.

Despite the logarithmic scaling of the x-axis, it is important to note that each subdivisions of the histogram linearly spans a qualification range of 0.1%, i.e. intervals, where the qualification of the atom was e.g. between 1% and 1.1%. One can see a peak at a qualification value of 2% indicating that in most of the intervals the coupling of the atom to the cavity mode caused a suppression of the transmission by a factor of 50. The cumulative amount of intervals in which the atom was kept with qualification below a certain value is depicted by the blue line. As expected, this line continuously increases from 0% to 100%. As already mentioned previously, the qualification is a measure of the effective coupling of the atom to the cavity-mode. Post-selecting the data hence permits to extract different data-sets at various effective coupling strengths. In order to show the impact, all intervals have been grouped into 5 classes of different qualification-ranges each comprising the same number of intervals, i.e. 20% of the total amount. The borders of these classes are at 1.5%, 2.5%, 3.8% and 6.3%, respectively. The ranges are indicated by the magenta, red, green, blue and cyan background color in Figure 6.18. The corresponding normal-mode spectrum for each of the intervals within one of these qualification classes is plotted in Figure 6.19. The color-coding corresponds to the background color in the previous figure. The black solid line represents the theoretical value for an atom at rest, which is ideally coupled to the cavity-mode.

For these scans the atom-cavity detuning $\Delta_{ac}/2\pi = (\omega_a - \omega_c)/2\pi$ is set to -4MHz considering an ac-Stark shift of the dipole trap for well coupled atoms. The cooling intervals

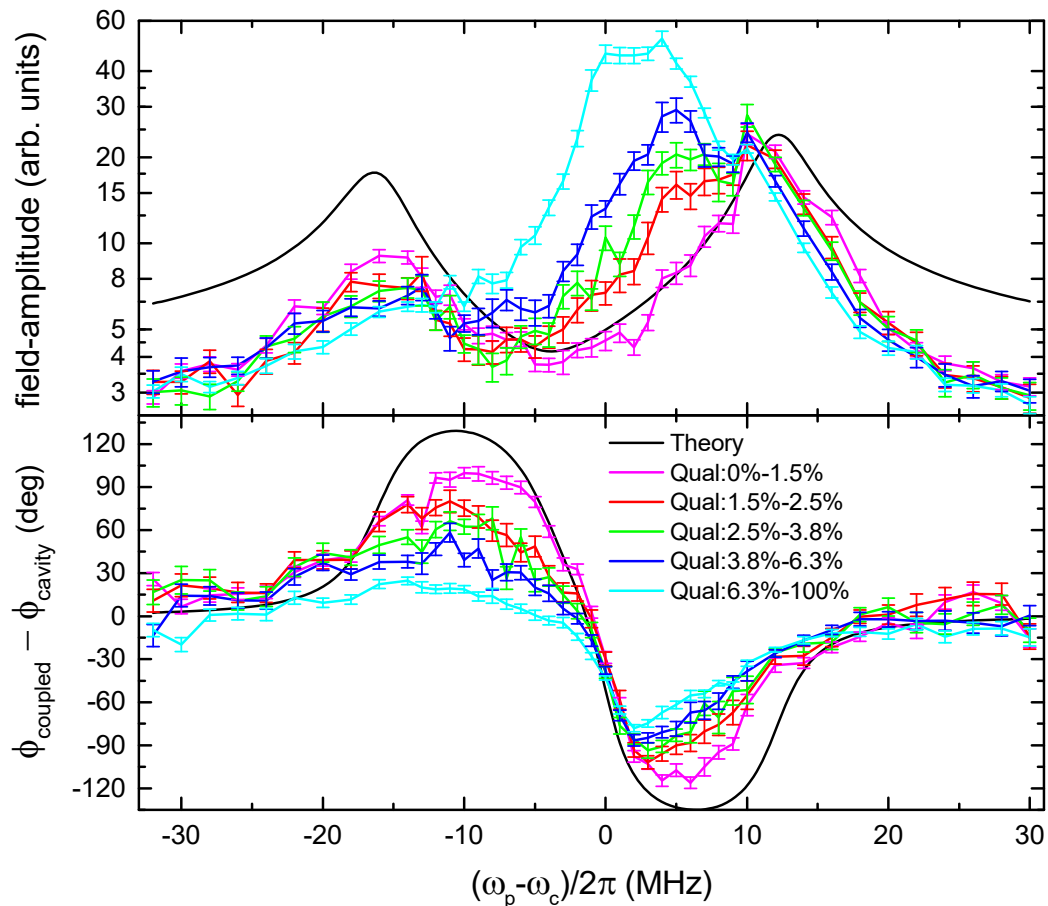


Figure 6.19: Normal-mode spectrum for different qualification intervals. The amplitude as well as the phase information of the heterodyne data are plotted for different probe-cavity detunings. The different-colored plots represent a post-selection of an ensemble of intervals in which the atom was captured with a qualification as indicated. The black line represents the theoretical prediction for an ideally coupled atom.

have a typical length of 5.5 ms and are interleaved with 0.5 ms long probe intervals. The frequency of the probe beam is scanned during the probe intervals and amplitude and phase information is extracted as described in the previous section. It is clearly visible that for the very-well coupled class of atoms (magenta line), the measured data lies closest to the theoretical value. Also, the amplitude plot shows two distinct and well-resolved normal-modes. They start to dissolve as weaker qualification factors are considered, and almost approaches the empty cavity case, as it can be recorded if no atom is present in the resonator, if only a very weak qualification is carried out. The phase is plotted with respect to empty cavity, showing the phase difference of the coupled systems to the bare cavity (cf. Section 6.7.2). It hence displays the influence the single atom has on the transmitted phase of the probe beam through the cavity. The details of this shape will be eluded in detail later. Here it is only important to notice that the same behavior as for the amplitude is apparent, i.e. that the well coupled atoms are close to the theory curve whereas the less well-coupled atoms approach a straight line of zero additional phase shift. This behavior is visualized in another way in Figure 6.20. Here, a color-coded two-dimensional histogram shows the unfiltered phase-shift data of every single recorded interval. The brightness determines the relative occurrence of events while the color-tones (i.e. red,

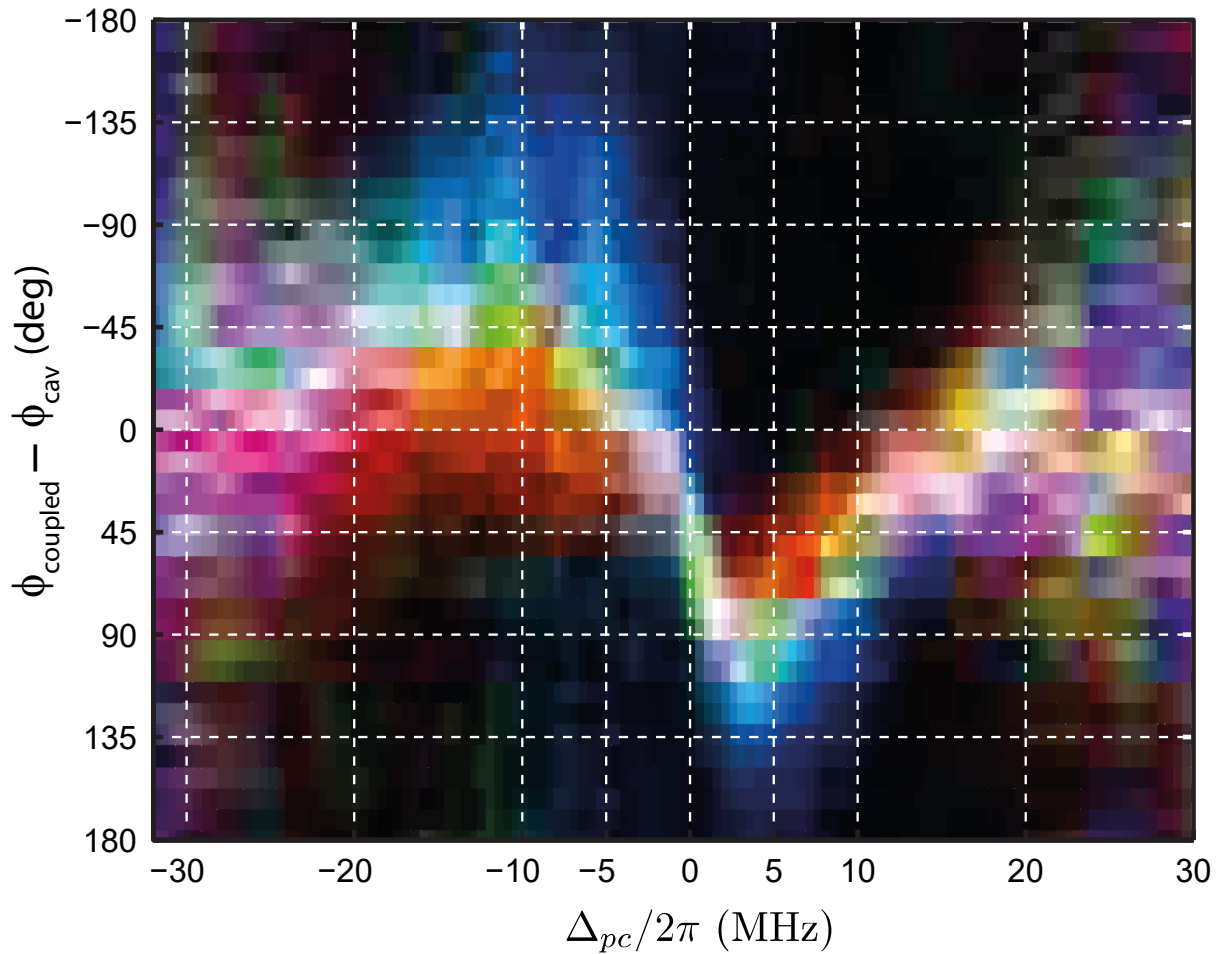


Figure 6.20: Phase shift induced by a single atom depending on its coupling to the cavity. A color-coded histogram of the raw data recorded for the phase shift induced by a single atom for different probe-cavity detunings is depicted. Intervals with weakly coupled atoms (qualification above 4.4%) are marked by an increasing amount of red color, medium coupled atoms (qualification 2.2% to 4.4%) by green color and well coupled atoms (qualification below 2.2%) add blue color.

green, blue) indicate the average qualification of the intervals yielding this data-point. Here red represents hot, i.e. weakly coupled, atoms, corresponding to a qualification of 4.4% and above, green to a qualification of 2.2% to 4.4% and blue represents cold, i.e. strongly coupled, atoms with a qualification below 2.2%.

In total, we have seen that post-selecting the data gives us an important tool to extract different effective coupling strengths. Choosing a very low qualification permits to only selected traces for further analysis were the atom was well coupled. In this case the relative coupling of the atom-cavity system is increased – approaching the theoretical value. In the further course of this thesis, the qualification will be employed and indicated as an important parameter to select well coupled atoms with a high coupling strength.

In the next section another feature of heterodyne measurements will be elaborated in detail before this switching measurement will be used to show atomic antiresonance in Chapter 7.

6.8. Super-Rabi Color Measurement

Retrieving information about the ‘color’, i.e. the actual frequency, of the emitted photons is one of the key features of any heterodyne measurement. However, until now, this feature has not been employed to its full extent. In the previous section heterodyning has only been used as a means to detect the phase of the transmitted probe beam. In Chapter 7.8.2 it will further be used to differentiate a signal of different beams transmitted simultaneously through the cavity. In this section we want to have a closer look at the frequency of the transmitted probe beam. In order to do so, we perform a measurement similar to the one described by Koch et. al. [152]. There strong driving of the coupled system was carried out at the normal modes and second and third order photon counting correlations have been employed to study the quantum dynamical properties of the system. Yet, this time, the photon counting mechanism is replaced by a heterodyne mechanism.

As for the previous measurements, the atoms are launched from underneath the cavity via an atomic fountain. This time, the detuning of the upper and lower MOT beams is set in such a way that the turning point of the ballistic flight of the cloud of the atoms is slightly above the cavity axis. This way around 15-40 atoms will pass the cavity every time a cloud is launched. The passage time for every atom through the cavity is on the order of 10-30 μs . The cavity is set to be on resonance with the $5S_{1/2}F=3 \rightarrow 5P_{3/2}F'=4$ transition of our atoms, yielding an atom-cavity detuning of $\Delta_{ac}=0$ MHz. The probe beam is set to a detuning of $\Delta_{pc}/2\pi = -8$ MHz with respect to the cavity. For atoms passing through the center of the cavity, the low power of the dipole trap of 150 μK yields an ac-Stark shift of 5 MHz. For typical atomic passages this value of the ac-Stark shift is reduced since only a fraction of the atoms passes through the center of the mode. The red detuning of the probe with respect to the cavity causes a low transmission of the probe beam when no atom is present in the cavity. Once an atom is coupled to the cavity mode, the normal-modes form, yielding an increase in transmission. In this case the probe beam is in the surrounding of the $|1, -\rangle$ normal mode.

The probe is set to a high value, corresponding to as much as 56 photons on the empty cavity resonance, which means $\eta = 7.5 \cdot \kappa$. This strong driving is necessary to observe nonlinear effects [153] such as Super-Rabi oscillations leading to a ‘‘color conversion’’ of the transmitted probe beam. The recorded spectrum of the transmitted probe beam is depicted as black curve in Figure 6.21. The spectrum was recorded with the AOM of the optical local oscillator set to 126.85 MHz in double pass configuration and the probe AOM set to 111.0 MHz, respectively. This causes a heterodyne beat frequency of 31.7 MHz. This heterodyne offset is subtracted from the spectral data shifting the unaltered signal peak to 0 MHz. The spectrum is derived by computing a 1024-point FFT of the input data sampled with 100 Msps whenever an atom has been detected. In order to select the corresponding parts of every trace, i.e. the timespan when an atom is coupled to the cavity, the heterodyne carrier at the probe frequency is extracted. The decision if an atom is detected is based on the transmitted probe intensity. An increase of the

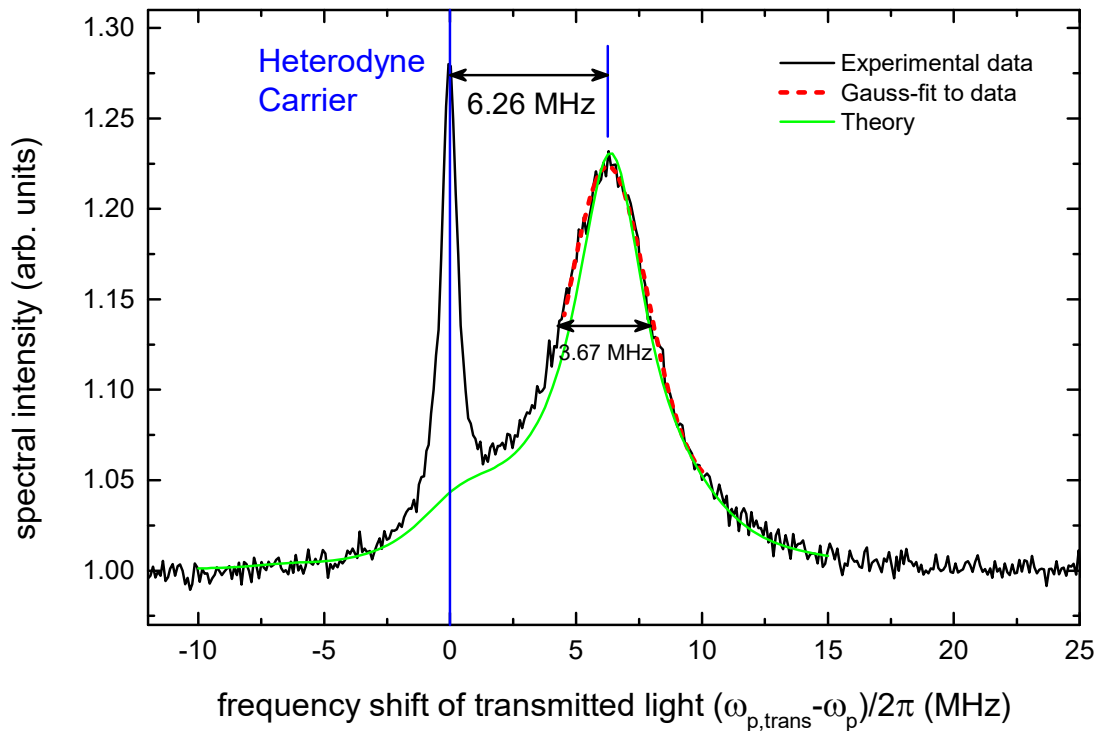


Figure 6.21: Nonlinear response of the atom-cavity system. The transmitted probe beam is recorded via a heterodyne measurement. The spectrum is computed via a Fourier transform. The spectral intensity is plotted as a function of the frequency shift referenced to the initial frequency of the probe beam. The experimental data is plotted in black. The red curve shows Gaussian fit to the peak at 6.3 MHz, which is caused by the high driving. The theoretical prediction of the transmitted spectrum is depicted as a green line.

transmission by a factor of 1.24 serves as threshold. The absolute values of the single frequency components of every FFT spectrum are summed up. The resulting spectrum is normalized to the absolute value of an FFT which is measured for the empty cavity. This permits to subtract a residual background still present in the data. The length of the FFT sets a limit to the frequency resolution of 98 kHz.

In the resulting spectrum in Figure 6.21 a clear and sharp peak at the input frequency of the probe beam is visible. This peak represents the increase in the transmission of the probe beam compared to the empty cavity case due to the resonance condition of the coupled atom-cavity system. The more intriguing part is the additional peak which appears 6.26 MHz blue-shifted from the probe beam used to excite the system. It is a clear sign of the nonlinear process which occurs in the system and leads to the emission of blue-shifted photons. One can attribute this additional peak to the Super-Rabi oscillation as described in [81], [152]. This Super-Rabi peak stems from the coherent exchange process of energy between the probing laser and the atom-cavity system and are a dynamic manifestation of the super-splitting of the vacuum Rabi resonance. In the low excitation regime, where the system can be described by a two-level model the expected Super-Rabi frequency amounts to:

$$\begin{aligned}
\Omega_{2\text{-level}} &= \sqrt{2}\eta \\
&= \sqrt{2} \cdot 7.5\kappa = 15.9 \text{ MHz}
\end{aligned}
\tag{6.5}$$

However, starting from a driving strength $\eta > 3\kappa$ deviations from this value are expected as transitions to the second order dressed state become important [81], [154]. A Gaussian fit of this peak (red curve) yields a FWHM of 3.7 MHz which agrees well with a theoretical computation (green curve). It has been derived by employing the quantum optics toolbox [94] using MATLAB. The deviation with the theory curve at 0 MHz is caused by the selection process and stems mainly from not ideally coupled atoms.

The big advantage of performing heterodyne measurements to observe nonlinear processes is the possibility to readily extract the full spectrum of the emitted photons. As it is required by heterodyne detection in comparison to homodyne detection, the carrier of the probe beam is offset from 0 Hz, normally at an RF frequency. This permits to iteratively measure both quadratures and hence retrieve further information to differentiate between red- and blue-shifting of photons, as it is not directly accessible in an intensity-based measurement.

7. Free-space Atomic Antiresonance

In this chapter we will examine the spectral behavior of the phase shift more closely. We will start by simulating the influence of the different parameters of our atom-cavity system and attribute the features in the spectrum to physical mechanisms. It will be shown that besides the well-known features of the normal-mode resonances, we can also identify an antiresonance whose intensity and phase response is exactly opposite to the one of a resonance and whose properties are – despite the strong coupling – only governed by the atomic resonance frequency. We will then compare our atom-cavity system to other macroscopic systems before the experimental data of the antiresonance is presented. In the end, possible applications of the technique will be eluded and an experimental realization of photonic phase switch will be given. Here saturation effects are employed to control the phase of a transmitted probe beam.

Part of the results presented in this section have been published in:

“*Antiresonance Phase Shift in Strongly Coupled Cavity QED*”

C. Sames, H. Chibani, C. Hamsen, P. Altin, T. Wilk, and G. Rempe; *Phys. Rev. Lett.* **112**, 043601 (2014)

7.1. Theoretical Perspective

The cavity transmission as well as the phase can be straightforwardly calculated within the framework of the Jaynes-Cummings model, extended to take into account driving and dissipation. In the limit of weak driving, this gives for the expectation value of the cavity field, represented by the photon annihilation operator \hat{a} :

$$\langle \hat{a} \rangle = \frac{\eta(\Delta_{pa} + i\gamma)}{(\Delta_{pa} + i\gamma)(\Delta_{pc} + i\kappa) - g^2} \quad (7.1)$$

where $\Delta_{pa} = \omega_p - \omega_a$ represents the probe-atom and $\Delta_{pc} = \omega_p - \omega_c$ the probe-cavity frequency detunings, respectively. The normal modes are the maxima of this function and occur where the denominator of Eqn. (7.1) is minimized, a condition which depends on all parameters of the coupled system [155]. Conversely, the antiresonance is the minimum of this function and occurs where the numerator is minimized. This is the case at $\Delta_{pa} = 0$ MHz. It is apparent from Eqn. (7.1) that the antiresonance depends only on the atomic parameters, ω_a and γ , and not on the cavity properties entering via κ or the coupling constant g . In particular, the antiresonance occurs at exactly the resonance frequency of the uncoupled atom ω_a and has a width equal to the bare atomic polarization decay rate γ , despite the strong coupling between atom and cavity. This behavior will be shown quantitatively in the following paragraphs. If the roles of atom and cavity are exchanged by driving the atom at the empty-cavity resonance, the steady state light field in the cavity reaches a magnitude equal to the drive, while the atom then remains in its ground state [156], [157].

7.2. Influence of Physical Parameters on the Spectrum

In Section 6.7.3 the phase shift induced by an atom strongly coupled to the cavity mode with respect to the empty cavity has been shown. Here we will have a closer look at the total phase shift of the transmitted probe beam which is caused by our atom-cavity system. This phase shift also corresponds to the intracavity phase of the probe beam [52]. We will examine the influence of the cavity amplitude decay rate κ , the atomic polarization decay rate γ as well as the atom-cavity detuning Δ_{ac} on the normal-mode spectrum of the phase. This helps to reveal a new feature in the normal-mode spectrum [13], [15], [155], [158] which is solely determined by the atomic resonance.

7.2.1. Cavity Amplitude and Atomic Polarization Decay Rate

First, the influence of the relevant decay rates involved in the system will be studied. The normal-mode spectrum of the phase is calculated analytically, as described in Section 7.1.

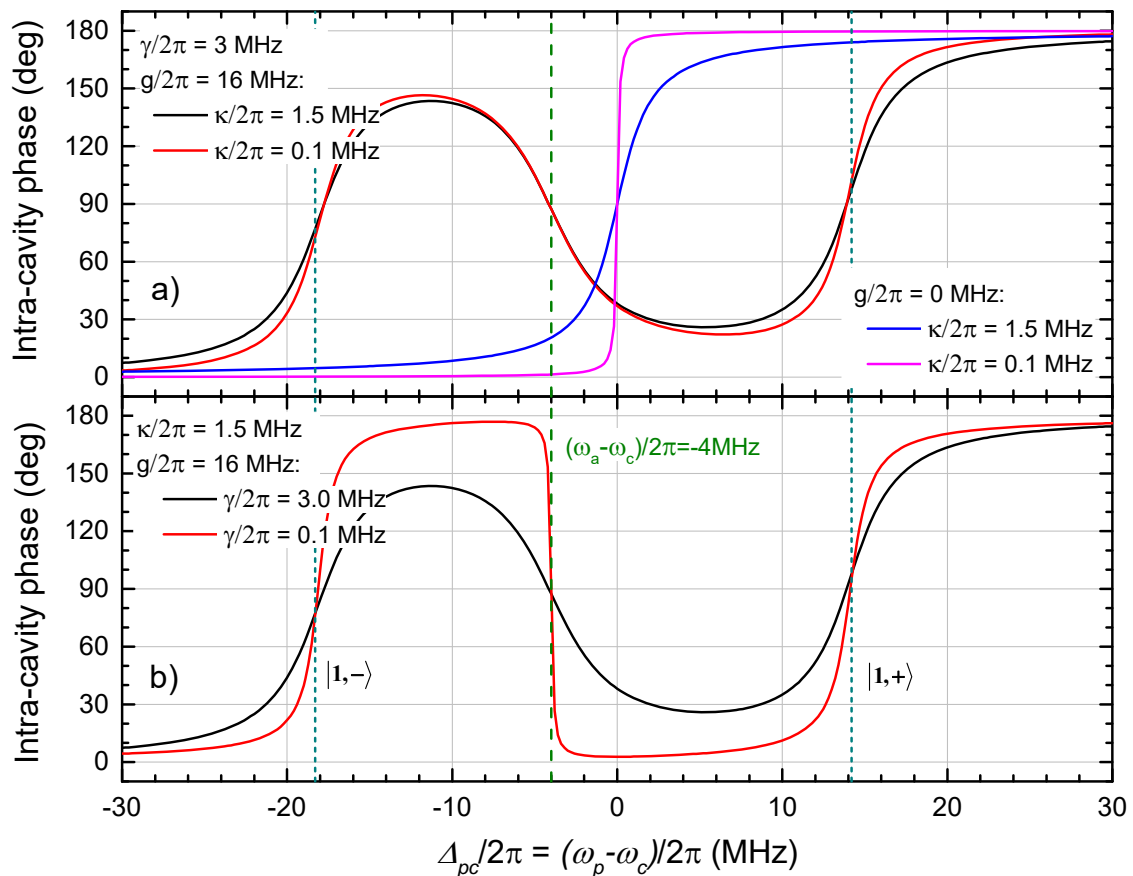


Figure 7.1: Influence of the relevant decay rates on the normal-mode spectrum. The intracavity phase of the probe beam is plotted as a function of the probe-cavity detuning. The black curve in both sub-plots represents the computed behavior for the actual experimental parameters. The influence of a significantly smaller cavity amplitude field decay rate is depicted in a) for the coupled system (black, red) as well as for the empty-cavity case (blue, magenta). Similarly, the influence of an assumed, significantly smaller atomic dipole transition linewidth is shown in b). The respective parameters are indicated in the graph.

The obtained behavior as a function of atom-cavity detuning is depicted in Figure 7.1. Part a) shows the influence of the field decay rate of the cavity $\kappa/2\pi$ and part b) shows the influence of the atomic polarization decay rate $\gamma/2\pi$. In part a) the phase shift in case of a strongly coupled atom (red, black) as well as the case of an empty cavity (blue, magenta) are plotted. For each case two different values of the cavity are chosen; once the actual value of our experimental system of $\kappa/2\pi = 1.5$ MHz (black, blue) as well as a significantly reduced value of only $\kappa/2\pi = 0.1$ MHz (red, magenta) are assumed. The remaining parameters correspond to the actual values in the experiment $\gamma/2\pi = 3$ MHz and $g/2\pi = 16$ MHz. As expected, the largest effect of the cavity decay rate is visible in case of the empty cavity, i.e. $g/2\pi = 0$ MHz. Here the decay rate directly translates into the width of the π phase shift at the cavity resonance. The spectrum becomes more complex for the coupled system. Two phase shifts of π at the positions of each of the normal modes, i.e. the resonances of the coupled system are visible (short-dashed vertical line). In between a phase shift of $-\pi$ can be observed (dashed vertical line). It is positioned at the atomic resonance frequency as it will be explained in the following sub-section. The width of the two normal modes in intensity and phase depends on cavity and atomic decay rate, hence a decrease in the cavity decay rate yields a sharper rise of the phase at the normal modes. The interesting part, however, is that the steepness of the drop in phase at the atomic resonance is independent of any change in the cavity decay rate. Subsequently, its width should solely depend on the atomic decay rate, as it is verified in part b). In this part of the plot the cavity decay rate is set to its actual experimental value and two different values for the atomic polarization decay rate are chosen. Once, the real value of the atomic polarization decay rate for the ^{85}Rb D2-line of $\gamma/2\pi = 3.0$ MHz (black) is used and once, a reduced value of $\gamma/2\pi = 0.1$ MHz (red) is assumed. The black curves are identical in both sub-plots, since they represent the actual experimental values. The red curve, however, varies significantly to the one in Figure 7.1 a). Similar to the situation studied above, the phase shift at the normal modes becomes steeper, caused by the dependency of the width of the normal modes on both decay channels, i.e. atom and cavity. A more pronounced behavior is found at the $-\pi$ phase shift at the atomic resonance. Here the phase shift now shows a steep drop. A more detailed view reveals that the width of the phase shift, as it is obtained from an inverse tangent fit, corresponds to the inverse phase shift of the free-space atomic resonance. This already hints on the presence of an anti-resonant atomic feature at this probe-cavity detuning.

7.2.2. Atom-Cavity Detuning

In order to better understand the anti-resonant behavior of the atom-cavity system, the intracavity field intensity as well as the phase for different atomic resonance frequencies need to be examined as well. The behavior as a function of the probe-cavity detuning is plotted in Figure 7.2 for different Δ_{ac} . Experimentally, the atomic resonance can be adjusted by changing the intracavity dipole-trap intensity and hence making use of the ac-Stark shift. Plots for

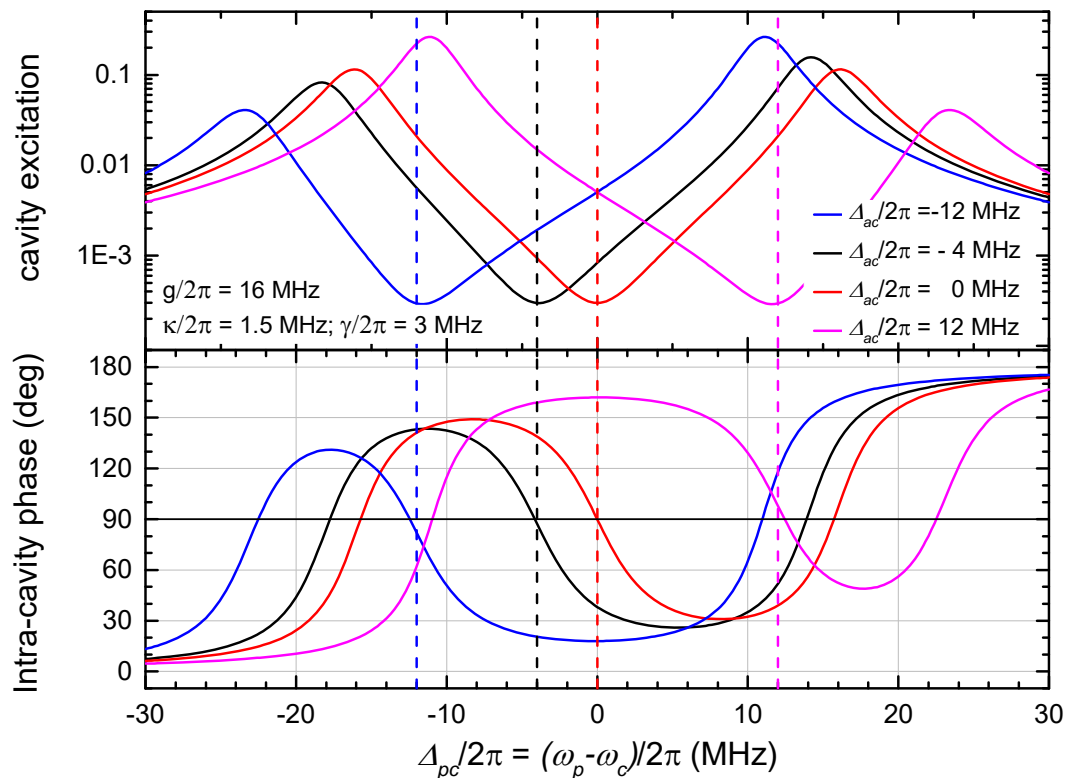


Figure 7.2: Influence of the atomic resonance frequency on the normal-mode spectrum. The transmitted intensity, i.e. the excitation of the cavity as well as the intracavity phase are plotted as a function of the probe-cavity detuning. Different atom-cavity detunings are shown in the plot. The respective parameters are indicated in the graph.

different atomic-cavity detunings of $\Delta_{ac}/2\pi = -12$ MHz (blue), $\Delta_{ac}/2\pi = -4$ MHz (black), $\Delta_{ac}/2\pi = 0$ MHz (red) as well as $\Delta_{ac}/2\pi = 12$ MHz (magenta) are shown.

The normal modes, i.e. the resonances of the coupled system, are evident as clear peaks in conjunction with a positive rise of almost π of the intracavity phase. A logarithmic scaling of the cavity excitation permits to unveil an additional feature, which is a pronounced dip. Despite the strong coupling of the system, this feature is positioned at the resonance frequency of the bare atom and shifts as the atomic resonance (dashed vertical lines in the respective color) is varied. In addition, this feature is also evident by a decrease in the phase by almost π . Here it shall be noted that the atomic excitation in combination with the phase of the emitted dipole radiation of the atom does show a different behavior, cf. [159], namely an overall increase of 2π with π at each normal mode. The feature observed here is called antiresonance, as its behavior shows the exactly opposite characteristic as expected for a resonance.

7.3. Pendulum Example

Antiresonances can be observed in a broad range of coupled systems. They can be intuitively understood by considering the analogy with a pair of strongly coupled pendula A and B. When driving A at a certain frequency between the two normal-mode resonances, the system reaches

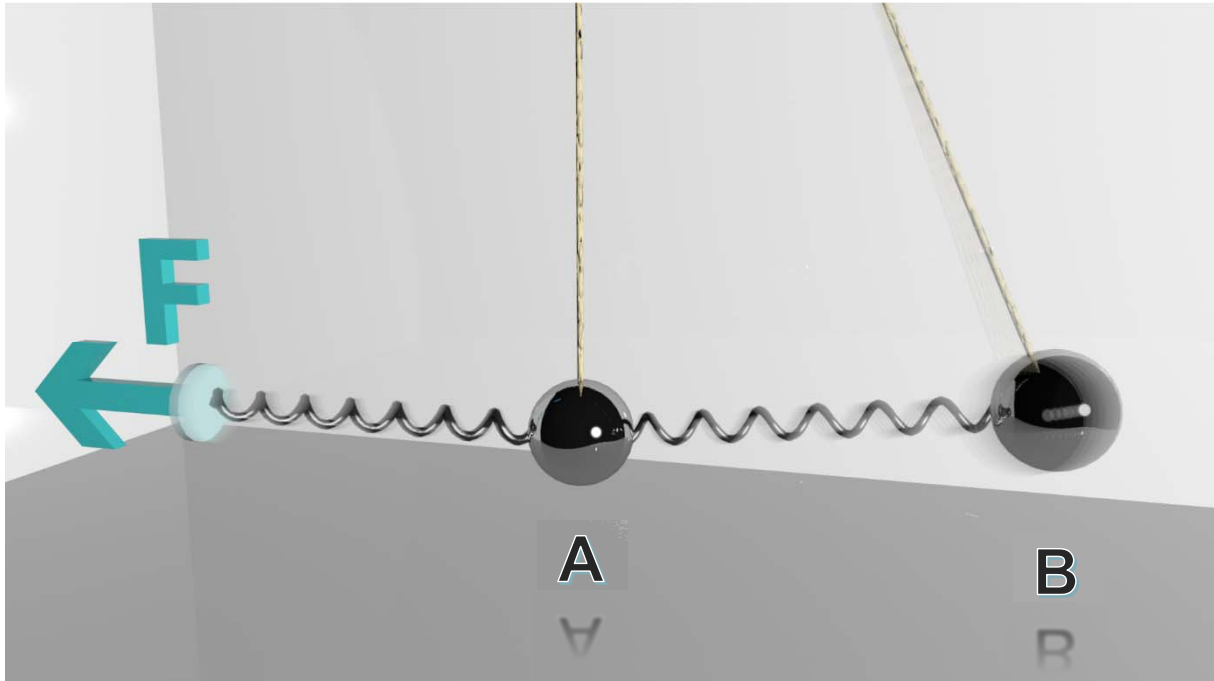


Figure 7.3: Artistic drawing of the antiresonance effect with two pendula. A sinusoidal altering force is acting via spring on the pendulum A on the left side. This pendulum itself is connected via a second spring to the pendulum B on the right side. The case is depicted in which the force oscillates with the resonance frequency of the pendulum B; here, the pendulum A remains at rest and the system is at its antiresonance.

a steady state in which pendulum B oscillates with a 180 degree phase shift to the drive. In steady state, the force exerted on A by the pendulum B exactly cancels the driving force, and the pendulum A ceases to oscillate. An artistic drawing is depicted in Figure 7.3. In contrast to a resonance, this leads to a minimum in the excitation spectrum of the pendulum A – hence the name antiresonance, and a corresponding phase shift. In case that the damping of the pendulum B fully reaches zero then the pendulum A will even completely stay at rest. The properties of the antiresonance are exclusively determined by the undriven oscillator, here pendulum B, independent of the coupling strength. This applies to the position of the antiresonance occurring at the natural frequency of the undriven oscillator as well as to its linewidth solely determined by the damping rate of the oscillating pendulum, B in our example.

The potential of antiresonances for disentangling the properties of sub-components in complex, strongly interacting systems is already exploited for macroscopic objects in mechanical engineering [160], [161]. This principle also finds its application in the largest buildings of the world, like skyscrapers and bridges. These fragile constructions require an ingenious design to withstand strong gusts and earthquakes. Since over a century tuned mass dampers have been employed here to harmonically absorb the structure’s kinetic energy at a certain vibrational mode and dispense it into dampers [162]–[167]. They consist of a large mass which is coupled elastically to a building in such a way that its resonance frequency is close to the one of the building. Kinetic energy of the building is then also partially transferred to the mass, where it is damped. This results in a splitting and reduction of the natural eigenfrequency of the building into two resonance peaks – previously described as normal modes. A prominent example where

this technique has been installed is the Taipei 101 in Taiwan. It possesses a 660 ton damper, which is held by wires between the 88th and 92nd floor and is visible to visitors. Despite its huge difference in size, the underlying principal, yet, is exactly that of an antiresonance.

7.4. Antiresonance in Cavity Quantum Electrodynamics

Our cavity QED system comprises a single atom with polarization decay rate γ resonantly coupled to a high-finesse optical resonator with field decay rate κ . The atom-cavity coupling constant g is large compared to the dissipation, $g \gg (\gamma, \kappa)$, and the cavity is driven weakly such that the driving strength $\eta \ll (g, \gamma, \kappa)$. This ensures that the average photon number in the cavity is too low to saturate the atom. In the weak driving regime, the system is formally equivalent to two strongly coupled harmonic oscillators. At the antiresonance, in analogy with the above classical picture, the field radiated by the atom interferes destructively with the field driving the cavity, giving rise to a transmission minimum. The measurement of the antiresonance is achieved by monitoring the phase of the light transmitted through the cavity. As predicted by Eqn. (7.1) and as it has already been shown in Section 7.2, a phase shift of $-\pi$ occurs for $g \gg (\gamma, \kappa)$ when the probe-atom detuning Δ_{pa} is changed from negative to positive values. This phase shift is as large as that induced by a resonance, e.g. a normal mode. A direct measurement of the dip in the intensity as it can be achieved by a simple photon counting measurement does not yield a sufficiently low noise floor. This makes the phase-measurement the only feasible way of observing the antiresonance. In cavity QED, this phase spectroscopy has so far only been performed in the limit $\kappa \gtrsim g$, and only modest phase shifts were observed [65], [66]. Phase changes due to strongly coupled atoms were seen in [168], but the antiresonance phase shift was not observed. The presence of a transmission dip at the atomic frequency (associated with the antiresonance) was noted in theoretical work in the intermediate-coupling, good-cavity limit ($\gamma > g > \kappa$) [169] and was referred to as cavity induced transparency²⁹. In contrast, in a strongly interacting system the coupling exceeds all decay rates, such that excitations are coherently exchanged between atom and cavity, leading to the formation of a new set of eigenstates. In this limit, the antiresonance occurs far from these new eigenstates, which impedes its observation via the intensity transmitted through the cavity [14], [15]. Here we overcome this limitation and reveal the antiresonance behavior through a measurement of the phase. Phase shifts on the transmitted beam of more than $3\pi/4$, mediated by a single atom, are observed. This is the highest phase shift yet observed from a single emitter [170]–[172]. The experimental results showing a clear antiresonance as well as the theoretical prediction are depicted in Figure 7.4.

²⁹ The work of Rice and Brecha links an absorption dip of a sideways driven atom in the intermediate-coupling, good-cavity regime to electromagnetically induced transparency (EIT). However, we note that the phase shift studied in this thesis cannot be observed on the light transmitted through an EIT medium, despite the apparent similarity between Eqn. (7.1) and the EIT susceptibility χ . This is because the phase acquired by light passing through an EIT medium is proportional to real part of χ (the refractive index), not to its argument. Here, we measure directly the phase of $\langle \hat{a} \rangle$.

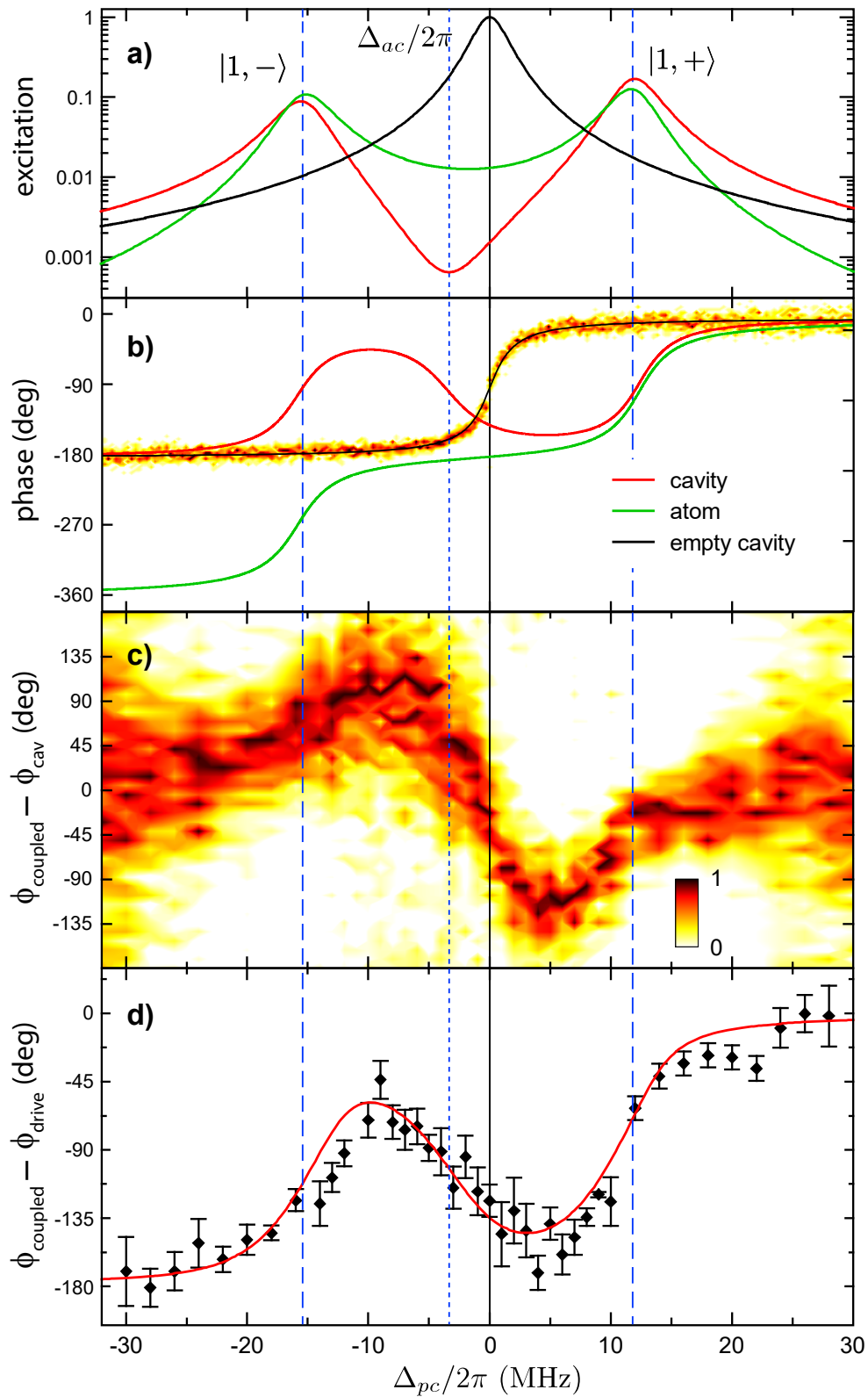


Figure 7.4: Phase spectroscopy of the strongly coupled system. a), b) Theoretical excitation probability a) and phase b) of the empty cavity (black) and the two constituents of the strongly coupled system, i.e., the atom (green) and the cavity (red), versus the probe-cavity detuning Δ_{pc} for our parameters. The experimentally measured phase shift induced by the empty cavity with respect to the driving field is also shown in b), as a histogram color-coded from white (no events) to black, which is normalized to the maximum number of events for each frequency setting. Vertical dashed lines mark the frequencies of the two normal modes and the short-dashed line at -3 MHz marks the frequency of the bare atom. c) Histogram of the additional phase shift caused by an atom strongly coupled to the cavity, referenced to the empty cavity. d) Measured overall phase shift of the coupled system, derived by adding b) and c). The red line is the result of a numerical simulation that includes atomic motion.

The theoretical amplitude and phase spectra for our atom-cavity parameters are shown in Part a) and b). The phase information is depicted relative to the phase of the driving probe beam. The black line in a) represents the Lorentzian frequency response of the empty cavity. This response changes significantly when an atom is strongly coupled to the cavity mode, resulting in the appearance of normal modes (denoted $|1,-\rangle$ and $|1,+\rangle$ as indicated by the dashed vertical lines) where the excitation is shared between the atom (green) and the cavity (red). In a logarithmic plot of the cavity excitation, a pronounced dip is evident at the resonance frequency of the bare atom. This is the antiresonance, which is marked by the short-dashed vertical line. No feature is apparent in either the atomic excitation or phase at this frequency, which demonstrates that the effect is not merely interference between the two normal modes. Around the antiresonance most of the energy from the drive is not able to enter the atom-cavity system. Nevertheless, the small amount which does enter the cavity is almost directly transferred to an atomic excitation, where the cavity is simply acting as a transfer medium. The excitation of the cavity only depends on the amount of energy which is transferred to the atom, e.g. due to its polarization decay. This explains the gross imbalance between the two excitations. The imbalance increases as the atomic decay rate is decreased, since – in this case – the needed energy to compensate for any damping reduces. Figure 7.4 b) and c) show the corresponding phase behavior of the transmitted light, as measured by heterodyne detection. The data presented here is a color-coded histogram of the raw-data for well coupled atoms, which satisfy the qualification criteria (cf. Section 6.7.3). The phase shift acquired by light transmitted through the empty cavity is overlaid onto the theory plot in part b), and shows the expected arctangent behavior, increasing by π as the probe laser is scanned over the resonance. Figure 7.4 c) shows the additional phase shift induced by a strongly coupled atom. A relatively soft qualification of 1.5% is chosen for the histogram; this causes more atoms to fulfill the requirements and hence increases the number of data-points, which are depicted, which is also the reason for a higher spread of the data. The sum of the empty cavity phase and the additional phase shift induced by the atom is the overall phase shift of the coupled system, shown in part d). In order to see a pronounced phase shift, the qualification was lowered to 0.6%, only considering atoms whose temperature is below 77 μK . Instead of a histogram, the data is shown here as points representing the mean phase shift deduced from fitting to the data a Gaussian distribution that is periodic in phase. The error bars represent the geometric mean of the statistical error and the uncertainty of the phase obtained from the fit. The solid red line is the result of a numerical simulation based on Eqn. (7.1) which includes effects due to residual atomic motion (cf. [81]). The normal-mode resonances can be clearly identified by sharp increases in phase. Between the normal modes, at the antiresonance, an inverse behavior is apparent, with the phase shift exhibiting a negative slope which is highest at the frequency of the uncoupled atom.

7.5. Optical Control of the Antiresonance Phase Shift

The ac-Stark shift induced by the dipole-trap light provides a simple way of altering the resonance frequency of the uncoupled atom. In order to verify the behavior described in the previous section, we perform phase measurements across the normal modes for different ac-Stark shifts (i.e. different dipole-trap intensities). Figure 7.5 a) shows a contour plot of the expected phase $\phi_{coupled} - \phi_{drive}$ as a function of the probe-cavity $\Delta_{pc} = \omega_p - \omega_c$ and atom-cavity $\Delta_{ac} = \omega_a - \omega_c$ detunings. The magnitude of the phase is color-coded from white zero to black -180 degrees. The diagonal line indicates where the probe is resonant with the atom $\omega_p = \omega_a$.

The horizontal dotted lines mark the atom's detunings at different dipole-trap intensities which are used in the subplots (b-d). For each plot, a vertical dashed arrow marks the effective atomic resonance frequency. The atom is red-detuned from the cavity resonance in b) $\Delta_{ac}/2\pi = -14$ MHz and c) $\Delta_{ac}/2\pi = -5$ MHz, whereas blue detuning is shown in d) $\Delta_{ac}/2\pi = 12$ MHz. In all scans, the two normal modes are recognizable as positive slopes in the phase on either side of $\Delta_{pc} = 0$ MHz. The interesting feature, however, is the negative slope of the antiresonance phase shift in between, which always occurs at the atom's resonance frequency (marked with a vertical arrow). This shows that the frequency of the antiresonance indeed directly reflects the properties of the uncoupled atom. The ac-Stark shift is directly linked to the dipole-trap intensity which is equivalent to the depth of the trapping potential in the probe intervals. The switching of the trap depth at the boundary from the cooling to the probe intervals increases or decreases the average temperature of the atom depending on whether the dipole-trap depth is increased or decreased, respectively [173]. In order to compensate for this effect, the subplots have been post-selected with different qualification settings of 0.9% in b), 0.7% in c) and 0.5% in d). This corresponds to temperatures of the atom at the end of the cool interval of 115 μ K, 77 μ K and 57 μ K, respectively.

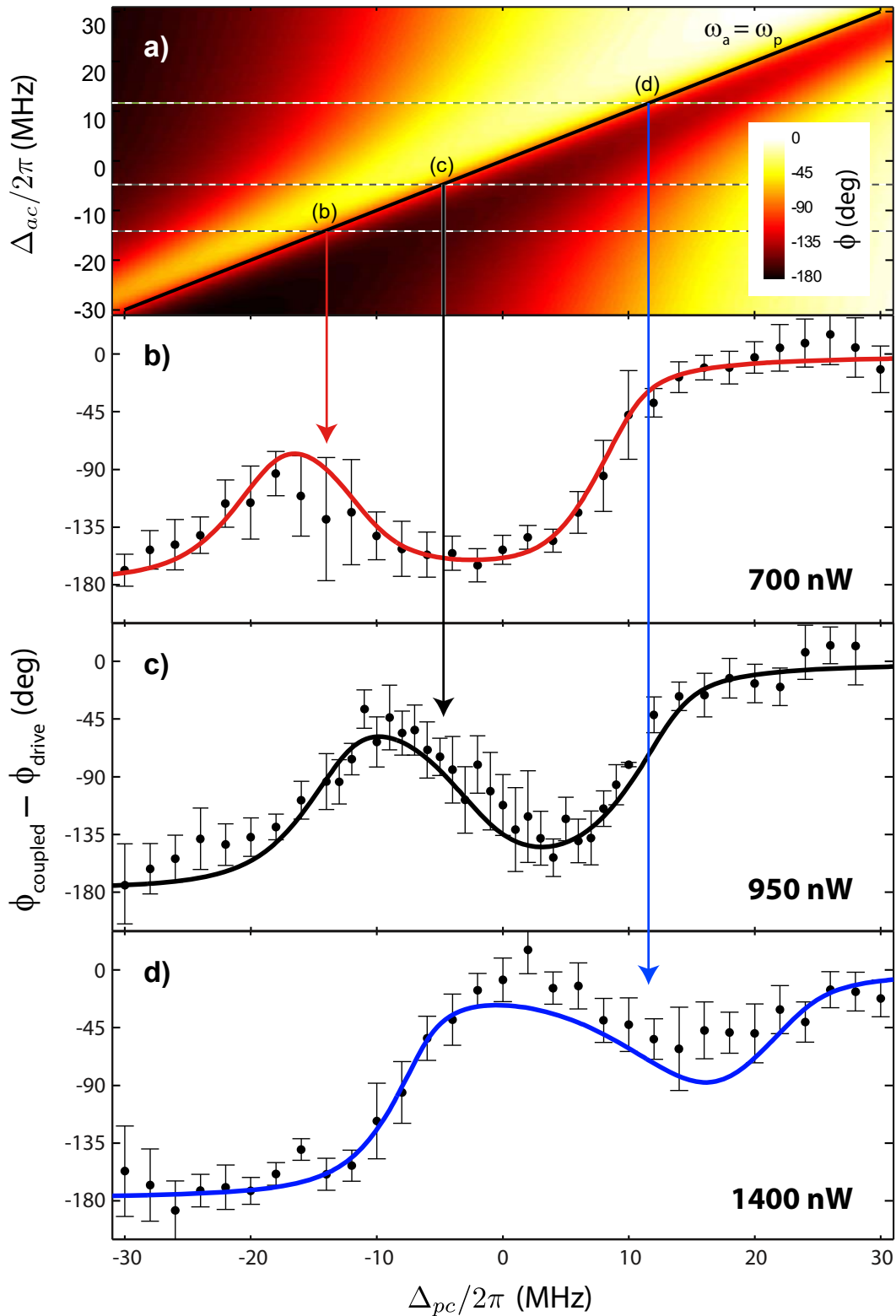


Figure 7.5: Tuning of the antiresonance phase shift via the ac-Stark effect. a) Theoretical phase shift of light transmitted through the strongly coupled system as a function of the probe-cavity Δ_{pc} (abscissa) and atom-cavity Δ_{ac} (ordinate) detuning. The diagonal black line indicates where the probe beam is on resonance with the atom. The horizontal dotted lines show the atom-cavity detuning for the scans depicted in the lower plots. Vertical arrows indicate the frequencies of the antiresonances. b)–d) Measured phase shift of the transmitted light for atom-cavity detunings of -14 (b), -5 (c), and 12 MHz (d), corresponding to dipole-trap laser powers of 700, 950, and 1400 nW, respectively. The solid lines are numerical simulations of the phase shift for each dipole trap laser power.

7.6. Bare Atomic Resonance in Strongly Coupled Systems

Since the frequency of the antiresonance is exclusively determined by the frequency of the uncoupled atom, the ac-Stark shift induced by the dipole trap can be used as an all-optical way to control the corresponding phase shift. We demonstrate this by measuring the phase shift of the probe light as the dipole power is varied between 450 nW and 1700 nW, yielding effective probe-atom detunings between -25 MHz and 25 MHz. The result is shown in Figure 7.6. During the measurement the probe laser is kept resonant to the empty cavity $\Delta_{pc} = 0$ MHz. As the atom moves across the cavity resonance, we observe a phase shift of 140° . This is the largest shift yet observed from a single emitter [65], [66], [170]–[172]. The theoretical maximum for our system, assuming no atomic motion and maximal coupling to the cavity, is 150° . An arctangent fit to the experimental data yields a width of (3.2 ± 0.3) MHz, which is in good agreement with the bare atom's decay rate of 3.0 MHz. This verifies that the atom alone, despite its strong coupling to the cavity, determines the characteristics of the antiresonance. The data used to generate Figure 7.6 is post-selected with a qualification of 1.9%.

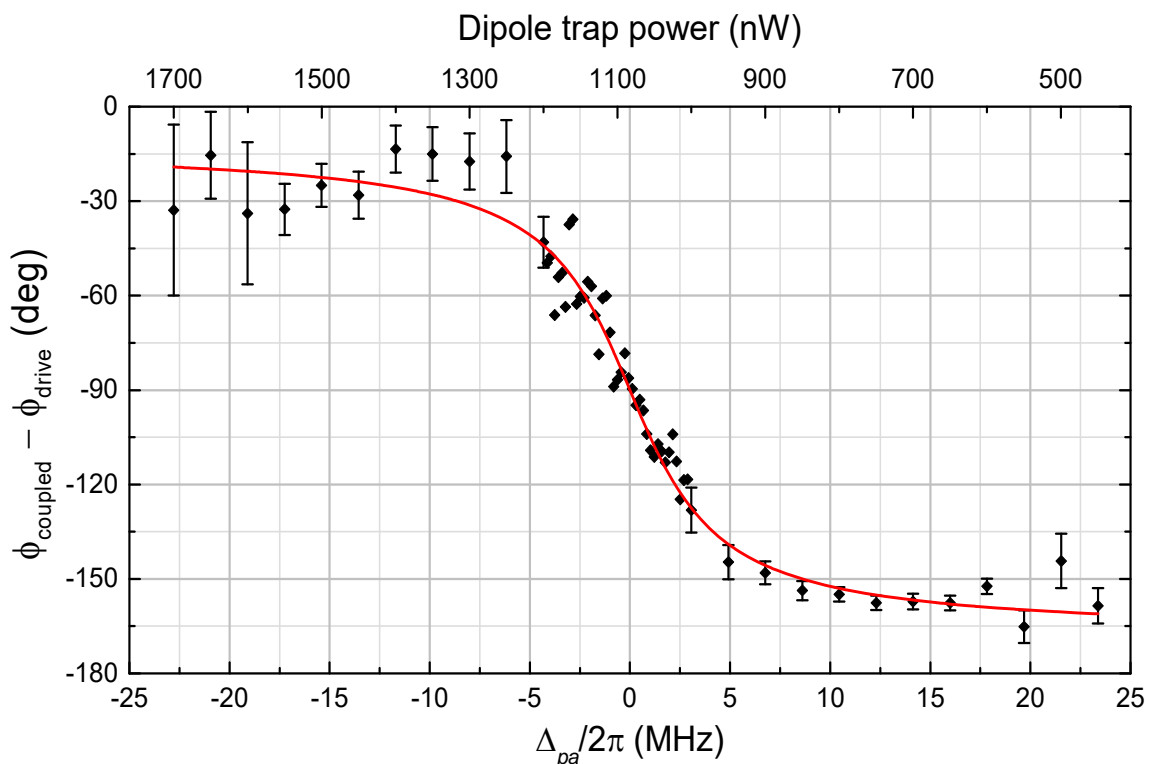


Figure 7.6: The phase shift induced by a single atom as a function of probe-atom detuning Δ_{pa} . The probe beam is kept on resonance with the cavity ($\Delta_{pc} = 0$) while the atomic resonance frequency is tuned via the ac-Stark effect induced by the intracavity dipole trap. The dipole-trap power is shown on the upper axis. This plot corresponds to a vertical scan in Figure 7.5 a). In the central region, error bars are small and omitted for clarity. The larger error bars for $\Delta_{pa} < 0$ are caused by the blue detuning of the atom with respect to the cavity, which causes cavity heating. The red line shows an arctangent fit, with a measured width of 3.2 ± 0.3 MHz that corresponds to the bare-atom decay rate.

7.7. Future Antiresonance Applications

The shown antiresonance phase shift can be used for the characterization of complex quantum circuits. Their utility stems from the general result that antiresonances represent what the resonances of the system would be, if the driven component was held unexcited [161]. This explains why the phase shift in our system occurs at the frequency of the atomic resonance and has its corresponding width, as we drive the cavity mode.

Consider a system of resonators or qubits coupled together in some arbitrary topology as sketched in Figure 7.7 a). The excitation spectrum of such a system exhibits a distinct behavior of resonances and antiresonances under driving, which is shown in Figure 7.7 b). The number of resonances corresponds to the number of constituents of the coupled system, while the number of antiresonances is one less. The resonances depend on the joint properties of all components and their couplings, and are independent of which component is driven. The antiresonances, however, depend on everything except the component being driven, and therefore provide information about how it affects the total system. By driving each component in turn and observing the response of the system by the same component, information about all of the individual subsystems can be obtained, despite the couplings between them.

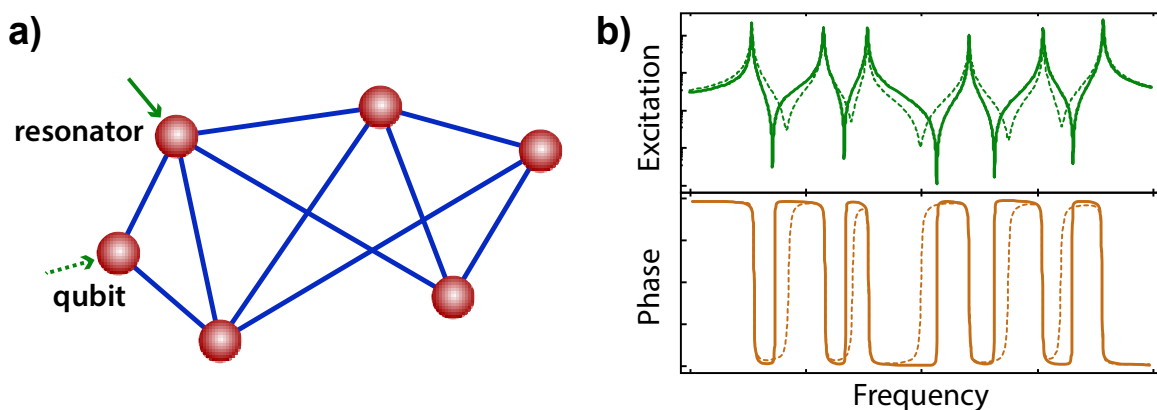


Figure 7.7: Antiresonance characterization of complex coupled systems. (a) A notional integrated quantum circuit: the red dots represent circuit components (e.g., qubits or cavities) and the blue lines show the couplings. (b) When driving different components, the system's resonances remain fixed while the positions and widths of the antiresonances change. Measuring the antiresonance phase shifts under different driving conditions therefore facilitates the characterization of the circuit.

As a simple example of this principle, let us suppose that one subsystem exhibits a much larger dissipation than the others, and it is desired to find the lossy component. The system resonances are of no help; their linewidths are an average of the decay rates of all components in the circuit, regardless of which we choose to drive. However, the antiresonances display properties of only the undriven components. Therefore, when the offending component is driven, the antiresonances become suddenly narrower, allowing it to be easily identified.

In conclusion, the experimental study conducted in Section 6.8 demonstrates a powerful spectroscopic technique that should prove useful in future experiments with interacting quantum systems. In addition, many other potential applications of antiresonances in quantum

systems can be envisaged. First, the ability to measure the properties of a single constituent in a strongly coupled system will be valuable in situations where probing the constituents in isolation is impractical, e.g. in solid-state cavity QED systems where the emitter and cavity are physically inseparable. Second, the grossly imbalanced distribution of energy among the system constituents at the antiresonance frequency could be useful for cavity cooling of molecules [174]–[176], since driving the molecules at the empty-cavity resonance frequency would limit their excitation and thus prevent optical pumping into unwanted molecular states. Third, using an emitter with a narrow linewidth may render the antiresonance phase shift useful for optical clock experiments, as it is immune to fluctuations of the cavity. Fourth, nonlinear effects like electromagnetically induced transparency could be incorporated in order to remove the opacity [177], [178]. The huge phase shift that can be imparted on a light beam by a single emitter might then find an application in quantum-information-processing devices [65]. Finally, our simulations predict giant intensity fluctuations at the cavity-driven antiresonance. Thus, one can expect large dipole fluctuations for an atom-driven antiresonance. It would be interesting to further explore the connection between these fluctuations and the anomalous atomic momentum diffusion noted by Murr et al. [179].

7.8. Saturation Measurements

The experiments with single atoms discussed so far require the use of very weak light fields. Increasing the strength of the light field beyond a certain threshold results in saturating the atomic transition. In this section we will employ saturation effects as a means to alter the phase response of the coupled system, which has been examined in detail in the previous section. As the resonator leads to a significant amplification of the light-field inside the cavity, weak intensities on the single intracavity photon level are sufficient to cause such saturation effects. The theoretical framework of saturation phenomena has already been elaborated in Section 2.1.7. One should point out that so far throughout this thesis it has always been avoided to enter the saturation regime and hence sufficiently small light levels have been chosen.

7.8.1. Saturation by High Probe Beam Intensity

Saturation effects become visible once the intensity of the probe beam increases over a certain threshold value. For cavity quantum electrodynamic systems this value is given by the dimensionless intracavity saturation photon number [180] and amounts to

$$n_s = \frac{\gamma^2}{2g^2} = 0.018 \text{ photons} \quad (7.2)$$

for our ideal experimental parameters of $g/2\pi = 16\text{MHz}$ and $\gamma/2\pi = 3\text{MHz}$. If the photon number inside the cavity rises above this level, the atom becomes saturated, resulting in a reduced splitting of the normal modes and excitation of higher order states [47], [181], [182]. Here we take a normal mode spectrum recorded by the heterodyne technique to observe this

effect; as in the previous section a switching measurement is executed. Due to the increased heating rate of the atom, a higher qualification factor of 8% is chosen, this time. The phase of the transmitted light at different power levels of the probe beam is recorded. The resulting plots are depicted in Figure 7.8. In the upper part the phase shift as a function of the probe-cavity detuning Δ_{pc} is plotted. The phase shift difference is measured as additional phase which is acquired by a strongly coupled atom to the cavity mode compared to the empty cavity case (cf. Figure 7.4 c)). In this representation, a phase shift close to zero hence corresponds to a very weakly coupled and saturated atom. The probe power level used for the phase scans is indicated in units of intracavity photons at the empty cavity resonance and is hence higher than the actual number of photons in the coupled system. The ratio between the indicated probe power and the actual probe power in the cavity mode corresponds to the cavity excitation as it is plotted in the lower part of the figure. As previously, the cavity is blue-detuned to the atomic resonance by $\Delta_{ac}/2\pi = -4$ MHz. Assuming an effective coupling constant of $g_{eff}/2\pi = 13$ MHz, this yields eigenmodes for low driving, i.e. below saturation intensity, at around $\Delta_{pc}/2\pi = -15$ MHz for the atom-like normal mode $|1-\rangle$ and $\Delta_{pc}/2\pi = 11$ MHz for the photon-like normal mode $|1+\rangle$. The excitation of the cavity mode is plotted in the lower part of Figure 7.8; the position of the normal modes as well as the empty cavity resonance are also marked in the upper plot by vertical dashed lines

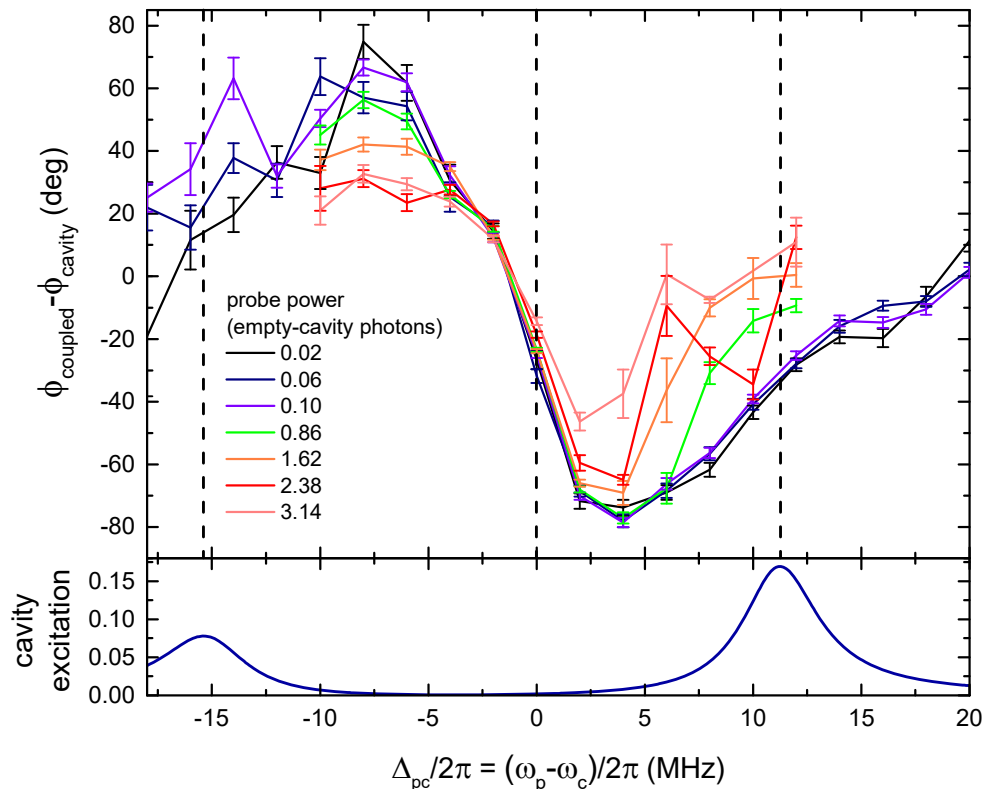


Figure 7.8: Normal-mode spectra recorded for different probe powers revealing saturation effects of the atom. The phase shift of the coupled atom-cavity system compared to an empty cavity is plotted. The data is recorded in a switching measurement with a qualification of 8%. The lower part of the plot shows the cavity excitation. The normal modes as well as the empty cavity resonance are also marked in the upper plot by vertical dashed lines

indicated by vertical dashed lines on the upper part of the plot. One can clearly see that the curves converge towards a typical behavior of the phase shift as indicated by the black curve when then power of the probe beam is lowered. This behavior changes as the probe power is continuously increased (going to red curve). Here, the interaction of the atom with the cavity is significantly reduced due to a saturation of the atom. The effect is strongest close to the normal modes where more light is able to enter the cavity, while only a weak effect is visible close to the empty cavity resonance.

In total, it can be seen that varying the intensity of the probe beam is a method of altering the phase shift of the beam transmitted through the atom-cavity system. For the selected parameters a phase control as large as 60 degrees is achieved at probe-cavity detuning of $\Delta_{pc}/2\pi = 5$ MHz. However, this technique is not a very useful method to control the phase of probe beam since it is directly linked to its intensity. In the next section a method will be shown which permits to overcome this limitation by adding a second beam which exclusively aims at saturating the atom.

7.8.2. Controlled Saturation by Separate Saturation Beam

In this section an additional, so-called saturation beam is introduced. It is exactly overlapped with the probe beam and only shifted in frequency by a few MHz. The overlap of the two beams is ensured by transferring them to the cavity in the same single mode fiber. They are generated by two independent AOM benches. This avoids unwanted sum and difference frequency generation as it would occur when driving one AOM with two frequencies. Since the stabilization of the probe and saturation beam is done after the fiber, where both beams are overlapped, a sample-and-hold technique has to be applied. Before the atoms are launched via the atomic fountain towards the cavity the probe beam PID control is used to sample the power level of the probe as well as the saturation beam independently and one after the other. During each of these gauging cycles the respective other beam is completely turned off. The determined output power values of the PID controller during this process are then stored by the experimental control system and can be activated during the experimental sequence when needed. Once an atom is captured, a similar switching measurement as described previously (cf. Section 6.7) is used. During the cool intervals the saturation beam is completely turned off and the intensity control of the probe beam is handled in the regular PID configuration. During the short probe intervals the previously stored intensity settings for the probe and saturation beam are activated and the otherwise applied feedback is switched off. After a certain number of repetitions of cool and probe intervals the atom is kicked out of the cavity. In the subsequent check and reference intervals the saturation beam as well as the probe beam are activated.

The additional saturation beam is used to independently saturate the atom inside the cavity from the probe beam and hence acts as if the coupling of the atom and the cavity is dynamically controlled. A low power of the probe beam is chosen such that the atom is not saturated by this beam. The saturation beam is positioned frequency wise close to one of the normal modes of the atom enabling saturation even at lower powers. The actual frequency relative to the coupled

system is depicted in the inset of Figure 7.9. As done in the previous section, the probe beam is scanned in frequency and the phase of the coupled system compared to the empty cavity is measured. The data in the plot has been post-selected with a qualification of 20%. Scans for three different power levels of the saturation beam are depicted. The indicated power levels are referenced to the empty cavity photon number, which is around one order of magnitude larger than the actual photon number at the position of the saturation beam for the coupled system. The scan at low saturation power (blue line) does not show any significant deviation from a scan without saturation beam. This is expected since the intensity of the beam is still slightly below the saturation photon number of the atom. The situation changes clearly for higher intensity levels as depicted by the green and red curve. Here, the atom is saturated leading to a clear reduction of the phase shift.

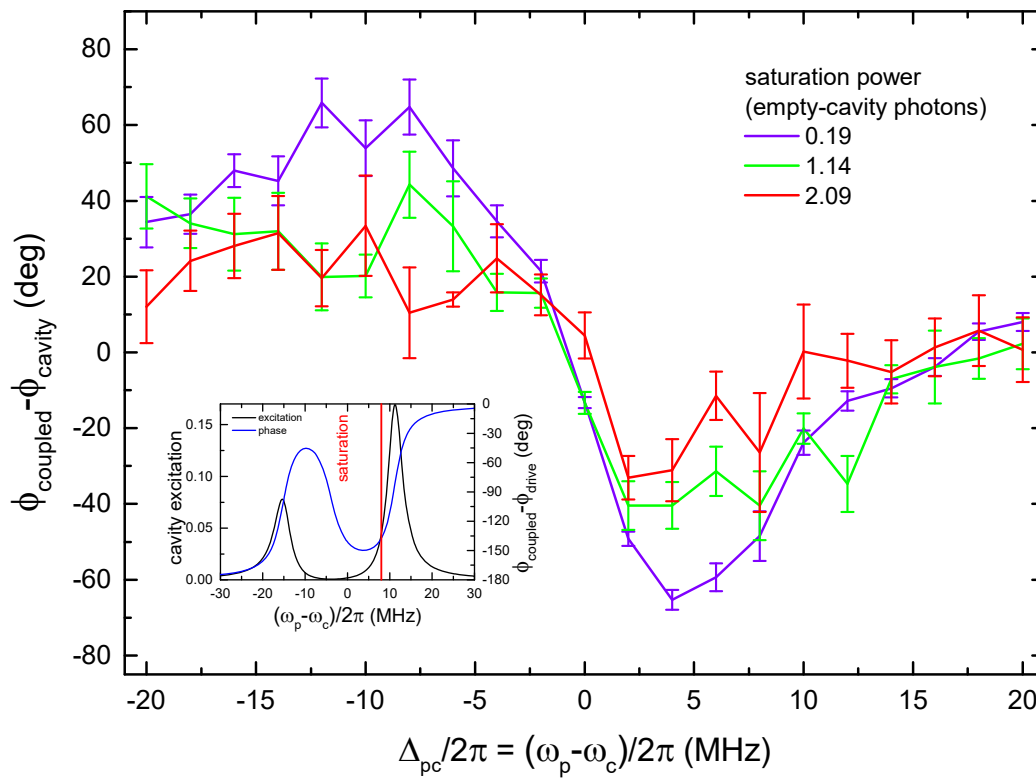


Figure 7.9: Influence of saturation beam on the normal-mode spectrum. Normal-mode spectra for various intensity settings of the saturation beam are depicted. A switching measurement of the phase shift of the coupled system with respect to the empty cavity is carried out. A qualification of 20% is chosen. The inset shows the position of the saturation beam in a theoretically computed spectrum.

The change in the phase of the transmitted probe beam depending on the power of the saturation beam can also be employed as an efficient means to control the phase of the transmitted beam with a weak saturation beam. A phase scan where the detuning of the probe as well as the saturation beam is fixed is plotted in Figure 7.10. Here only the intensity of the saturation beam is altered. The detuning of the two beams relative to the cavity resonance can be seen in the inset. The frequency of the saturation beam is again chosen close to the position of one of the

normal mode to efficiently saturate the atom $\Delta_{pc}/2\pi = 12$ MHz. The probe beam is set a few MHz above the empty cavity resonance. Here the phase shift of the coupled system compared to the empty cavity is largest. The power of the saturation beam results from an actual measurement of the transmitted power obtained from the heterodyne data taken during the reference intervals at the end of the sequence. The values are scaled to their respective empty cavity value. The power region around 0.01 empty cavity photons was hard to probe since the PID is not aligned to function properly for such small light intensities; in the case the set-point was adjusted to such power levels the output of the PID produced an output, which corresponds to around 0.001 empty cavity photons. Readjusting the PID to work in this power regime would significantly limit its frequency response to values in the few kHz region or cause a saturation of the PID at higher trap powers.

In Figure 7.10 the phase dependency of the transmitted probe beam as a function of the power of the saturation beam is shown. For this plot a qualification of 3% is used to post-select the data. A logarithmic scaling is chosen for the x-axis of the plot. It illustrates nicely saturation effects as they occur for the single atom. An exponential decay serves can be fitted to the negative experimental values of the phase shift measured at higher intensities of the saturation beam, i.e. above 0.05 empty cavity photons. The result is shown as diagonal red line. A

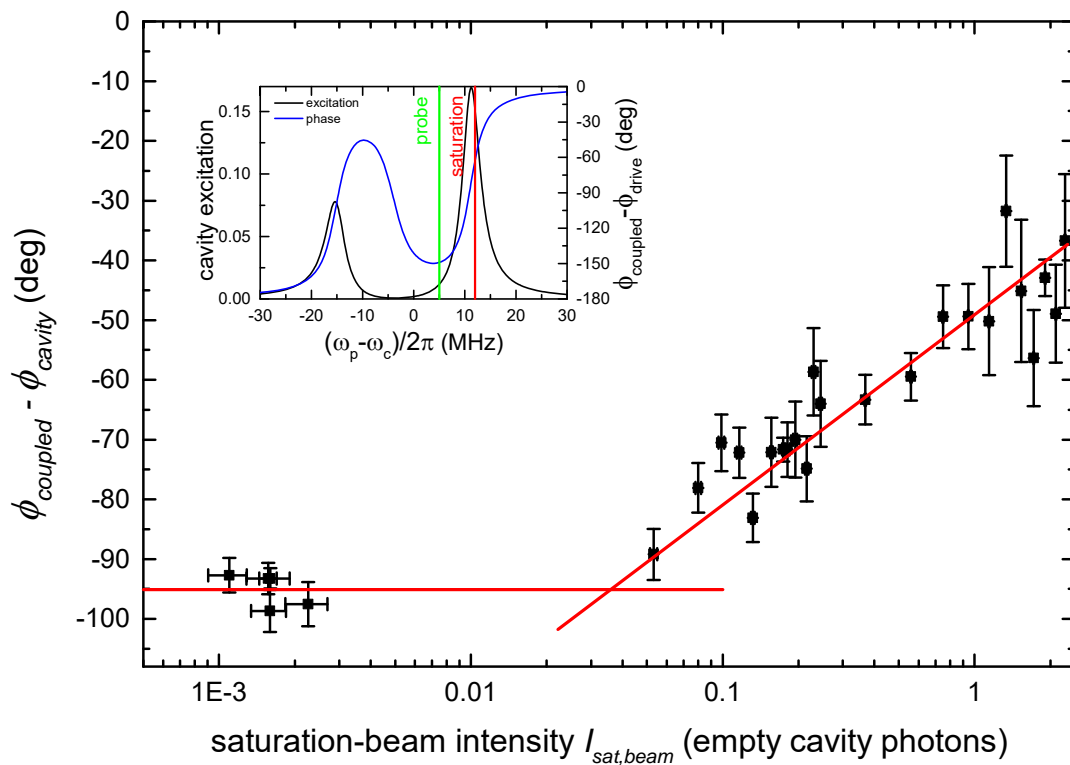


Figure 7.10: Controlling the phase of the transmitted probe beam by the saturation beam intensity. The phase shift of the transmitted probe beam for the coupled system with respect to the empty cavity is plotted as a function of the saturation beam intensity (logarithmic scaling). The intensity of the saturation beam is measured behind the cavity and plotted in units of the empty cavity photon number.

horizontal red line marks the value of -95 degrees, measured for the unsaturated atom. For an effective coupling of $g_{\text{eff}}/2\pi = 13$ MHz the saturation intensity amounts to 0.027 intracavity photons. For the selected experimental parameters this value corresponds to a saturation beam intensity of 0.18. Here the phase of the transmitted probe beam also shows a clear increase in the experimental data. The measured phase shift varies from values below -95 degrees for a very weak saturation beam to values above -35 degrees for high saturation. The saturation beam thus enables to shift the phase of the probe beam by more than 60 degrees. While this phase shift is achieved for a very low intensity level of the saturation beam, it still does not permit to generate phase control with just a single photon. The main reason for this is the incoupling efficiency of the beam into the cavity at the respective detuning which is below 10% in combination with the missing phase matching with the light in the cavity. However, this phase measurement shows the implementation of a nonlinear process on the few photon level.

8. Summary and Outlook

A new experimental apparatus for investigating the fundamental interaction of a single atom strongly coupled to the single mode of a resonator has been set up³⁰. The new system comprises an asymmetric cavity, which is formed out of two mirrors with different reflectivity, enhancing the photon flux on the outcoupling side while still guaranteeing strong coupling. In addition, it features a vastly improved side access compared to its forerunner experiment, and hence permits to focus side-ways beams through the cavity. By having access to the atom on all direction, three dimensional cooling schemes [110], [183], [184] can be transferred to strongly coupled systems in the future. In the current system, one of the mirrors is furthermore mounted on an inch-worm motor. This permits, for the first time, to macroscopically alter the cavity length while it remains in the vacuum and thus vastly enhances the flexibility in the choice of the resonant wavelength. This gives rise to consider the experimental realization of more complex schemes where one atom is interacting strongly with two resonant cavity modes simultaneously [185]–[187]; due to this nature this system is also referred to as N-type scheme.

Along with the new apparatus a new electronic control and processing system has been introduced. The new system features field programmable gate arrays (FPGAs). These devices permit to embed experimental data acquisition, real-time processing and feedback tasks in hardware and feature deterministic and fast execution. This technology enables the implementation of more advanced feedback routines, real-time heterodyne data processing as well as an improved cavity lock. The significant speed improvements go hand in hand with a special and hardware close way of programming. The increased computational power paves the way for complex processing algorithms, which in the future could enable real-time hardware-in-the-loop simulations of the atom-cavity system or feedback routines based on the system's quantum properties and thus introducing a real quantum-feedback process [188]–[191].

An analysis of the time evolution of the transmitted probe beam intensity permits to gain information about the atomic motion. In addition, a time and position depended force can be exerted on the atom via the dipole-trap intensity, enabling to implement a feedback loop. This implementation permits to increase the storage time of the atom in the cavity and also leads to a cooling [58]. In this thesis a new real-time feedback strategy on the motion of the atom has been studied. Compared to previous feedback algorithms, which only considered sub-oscillation timescales of the radial motion transverse to the cavity axis, the history of the atomic trajectory over typically one to three oscillation periods is taken into account. This requires providing ab-initio values of the system and by doing so increases the efficiency of how the information from the system can be used; it hence more than doubles the average storage time of an atom captured in the cavity – extending it to above 2 seconds. This new routine, which accounts for the parametric oscillation of the atoms and applies a phase-shifted, counter-acting

³⁰ The new system has been set-up together with M. Koch. Hence, some of the new features of the system have already been described in [81].

force, allows to extend the feedback algorithm even to the two orders of magnitude faster oscillation of the atom along the cavity axis. In this case, despite the fact that the feedback algorithm bases its decision on as little as one photon per oscillation period, a clear influence on the atomic motion is visible. The advances in the feedback process promote this mechanism as standard tool for atom-cavity experiments, especially when the side access is limited. Its extension to the axial direction marks a clear step towards full three-dimensional feedback. In this case an additional higher-order, blue-detuned dipole trap [192], breaking the radial symmetry of the current dipole-trap mode, would be needed [57].

During this thesis a heterodyne detection has been built and the previously mentioned feedback algorithms have been adapted. This enabled to record the amplitude and phase dependency as the probe-cavity detuning is scanned. Besides the two normal modes, which are also visible in intensity measurements, a new feature starts to appear. In case of driving and observing the cavity mode of a strongly coupled system, it is positioned at the free-space frequency of the atom and its features are solely determined by the properties of the atom. The behavior in amplitude and phase, however, is opposite to that at the resonance, hence the name antiresonance. The strong coupling of our atom-cavity system enabled to observe a phase shift of 140° imprinted on the probing beam, at the position of the antiresonance. To-date this is the highest phase shift yet observed from a single oscillator [170]–[172]. In an ideal case phase shifts as large as 150° can be realized with the current system. As a single atom shows strong nonlinear effects even on the single-photon level [80], [193], effects like electromagnetically induced transparency [177], [178] can be incorporated. The resulting huge phase shift imprinted on a light beam by the single emitter can be used, in addition, to build quantum gates, thus rendering antiresonances applicable for quantum computation systems [65], [194].

A spectral scan reveals – despite the strong coupling – the linewidth of the bare atomic transition and verifies that the effect is mediated only by the single atom. This promotes antiresonance phase shifts to be employed in the future to characterize complex quantum systems. Their utility stems from the general result that antiresonances represent what the resonances of the system would be, if the driven component was held unexcited [161]. The ability to measure the properties of single components in a strongly coupled system is particularly valuable in situations where probing the constituents in isolation is impractical, e.g. in solid-state cavity QED systems where the emitter and cavity are physically inseparable. As the antiresonance is immune to fluctuations of the cavity, using an emitter with a narrow linewidth may render the antiresonance phase shift useful for optical clock experiments. The antiresonance furthermore causes a grossly imbalanced distribution of energy among the system constituents, which could be useful for cavity cooling of molecules [174]–[176] in the future, since driving the molecules at the empty-cavity resonance frequency would limit their excitation and thus prevent optical pumping into unwanted molecular states.

Besides enabling phase-sensitive measurements of the transmitted light, heterodyning also paves the way to detect the absolute frequency of the transmitted beam. While this is useful to separate multiple probing beams passing the system at once, it also permits to uncover slight

shifts in the frequency of the transmitted beam. By doing so, Super-Rabi oscillations [81], [152], caused by the coherent exchange of energy between the atom-cavity system and the probe laser, directly became visible. These oscillations can also be derived by correlation measurements [152], in this case, however, no information about the direction of the shift, i.e. red- or blue-shifted, can be inferred. Hence, the heterodyne detection built provides an excellent tool to gain further insights into the nonlinear processes on the single emitter level.

9. List of Own Publications

- A. Kubanek, M. Koch, C. Sames, A. Ourjoumtsev, P. W. H. Pinkse, K. Murr, and G. Rempe, “*Photon-by-photon feedback control of a single-atom trajectory*,” *Nature*, vol. 462, no. 7275, pp. 898–901, Dec. 2009. [doi:10.1038/nature08563](https://doi.org/10.1038/nature08563)
- M. Koch, C. Sames, A. Kubanek, M. Apel, M. Balbach, A. Ourjoumtsev, P. Pinkse, and G. Rempe, “*Feedback Cooling of a Single Neutral Atom*,” *Phys. Rev. Lett.*, vol. 105, no. 17, p. 173003, Oct. 2010. [doi:10.1103/PhysRevLett.105.173003](https://doi.org/10.1103/PhysRevLett.105.173003)
- C. Sames, M. Balbach, M. Koch, A. Kubanek, P. W. H. Pinkse, and G. Rempe, “*FPGA-based Feedback Control of a Single Atom Trajectory*,” in *Virtuelle Instrumente in der Praxis 2010, Erste Aufl.*, Vde-Verlag, 2010, p. 578.
- A. Kubanek, M. Koch, C. Sames, A. Ourjoumtsev, T. Wilk, P. W. H. Pinkse, and G. Rempe, “*Feedback control of a single atom in an optical cavity*,” *Appl. Phys. B*, vol. 102, no. 3, pp. 433–442, Feb. 2011. [doi:10.1007/s00340-011-4410-x](https://doi.org/10.1007/s00340-011-4410-x)
- A. Ourjoumtsev, A. Kubanek, M. Koch, C. Sames, P. W. H. Pinkse, G. Rempe, and K. Murr, “*Observation of squeezed light from one atom excited with two photons*,” *Nature*, vol. 474, no. 7353, pp. 623–6, Jun. 2011. [doi:10.1038/nature10170](https://doi.org/10.1038/nature10170)
- M. Koch, C. Sames, M. Balbach, H. Chibani, A. Kubanek, K. Murr, T. Wilk, and G. Rempe, “*Three-Photon Correlations in a Strongly Driven Atom-Cavity System*,” *Phys. Rev. Lett.*, vol. 107, no. 2, pp. 2–5, Jul. 2011. [doi:10.1103/PhysRevLett.107.023601](https://doi.org/10.1103/PhysRevLett.107.023601)
- C. Sames, H. Chibani, C. Hamsen, P. Altin, T. Wilk, and G. Rempe, “*Antiresonance Phase Shift in Strongly Coupled Cavity QED*,” *Phys. Rev. Lett.*, vol. 112, no. 4, p. 043601, Jan. 2014. [doi:10.1103/PhysRevLett.112.043601](https://doi.org/10.1103/PhysRevLett.112.043601)
- C. Sames, C. Hamsen, H. Chibani, P. A. Altin, T. Wilk, and G. Rempe, “*Continuous parametric feedback cooling of a single atom in an optical cavity*,” *Phys. Rev. A*, vol. 97, no. 5, p. 53404, 2018. [doi:10.1103/PhysRevA.97.053404](https://doi.org/10.1103/PhysRevA.97.053404)

Awards



Own Publications Prior to this Thesis

- R. W. Newson, J. M. Ménard, C. Sames, M. Betz, and H. M. Van Driel, “*Coherently controlled ballistic charge currents injected in single-walled carbon nanotubes and graphite,*” *Nano Lett.*, vol. 8, no. 6, pp. 1586–1589, 2008. [doi:10.1021/nl0733051](https://doi.org/10.1021/nl0733051)
- C. Sames, J. M. Ménard, M. Betz, A. L. Smirl, and H. M. Van Driel, “*All-optical coherently controlled terahertz ac charge currents from excitons in semiconductors,*” *Phys. Rev. B - Condens. Matter Mater. Phys.*, vol. 79, no. 4, 2009. [doi:10.1103/PhysRevB.79.045208](https://doi.org/10.1103/PhysRevB.79.045208)
- M. Betz, C. Ruppert, S. Thunich, R. Newson, J. M. Ménard, C. Sames, G. Abstreiter, A. Fontcuberta i Morral, A. W. Holleitner, and H. M. van Driel, “*Coherent control of electrical currents in semiconductor nanowires/-tubes,*” *Phys. Status Solidi Curr. Top. Solid State Phys.*, vol. 8, no. 4, pp. 1224–1226, 2011. [doi:10.1002/pssc.201000819](https://doi.org/10.1002/pssc.201000819)

10. Appendix

10.1. Mirror Specifications

Two highly reflective mirrors are used to build the cavity. Both mirrors have been ordered from Research Electro-Optics, Inc. and the shipment arrived on the 26th October 2001. The following specifications have been supplied with the mirrors.

Mirror 1 (taken from box 50, position 2):

- Specified transmission at 780 nm: 25 ppm
- Radius of curvature: 1 cm
- REO; LN#41; Coning No; LT# 60-0604-01
- Coating Run: L6-262=25PPM
- Additional anti-reflection coating: OX1618=AR

The transmissivity was measured and is depicted in Figure 10.1. While the graph is not capable of showing the high reflectivity at 780nm, the broad range of low transmission and the fringes already advert to the high number of layers.

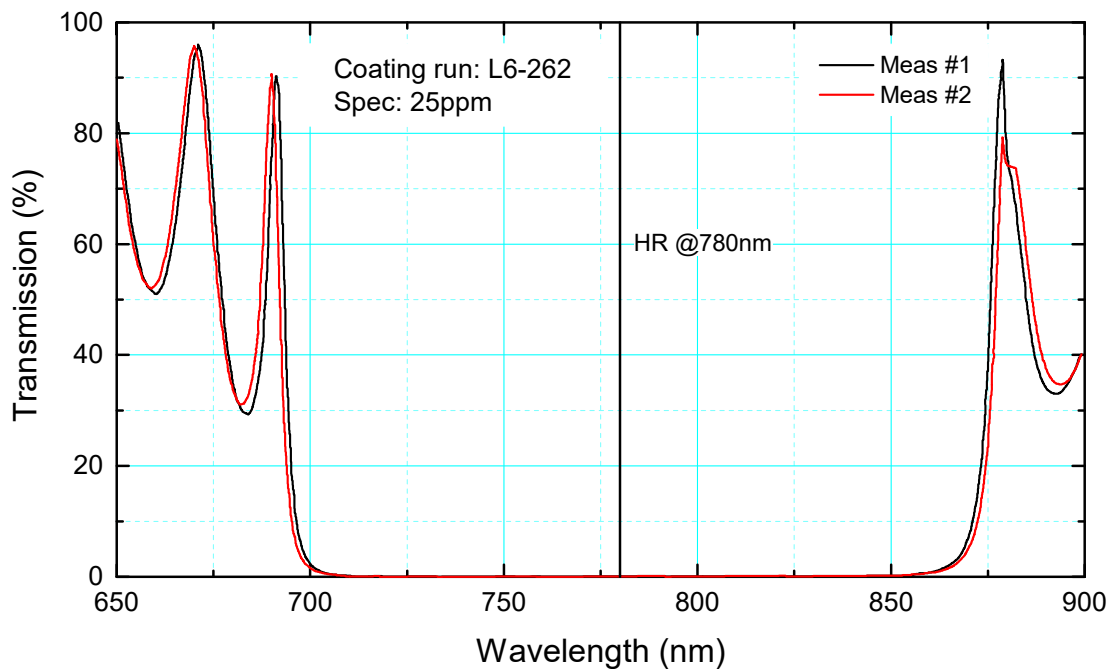


Figure 10.1: Transmission of coating run L6-262. Spectrum of the high reflectivity coating as provided by REO. The two measurements are expected to be the TE and TM polarized mode. The transmission is measured on normal incidence.

Reflections from the back-face of the mirror need to be avoided. Hence this is coated with an anti-reflection coating at the desired wavelength of 780 nm. A measurement of the reflectivity is shown in Figure 10.2. Here, a clear minimum of the reflectivity of around 100 ppm becomes visible at the desired wavelength.

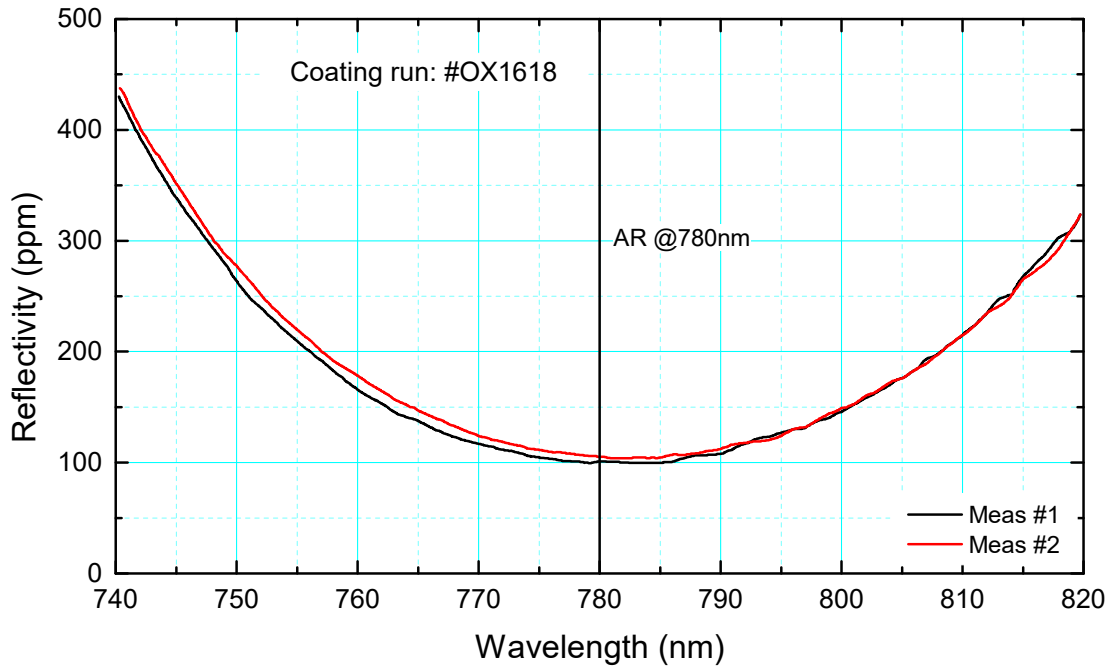


Figure 10.2: Reflectivity measurement of anti-reflection coating run #OX1618.

Mirror 2:

- Specified transmission at 780 nm: 4ppm
- Radius of curvature: 20 cm
- Coating run: L6-261 HR@780nm

The transmission recorded and supplied with this mirror is depicted in Figure 10.3. As this is the higher reflective incoupling mirror, an anti-reflection coating on back-face is not necessary.

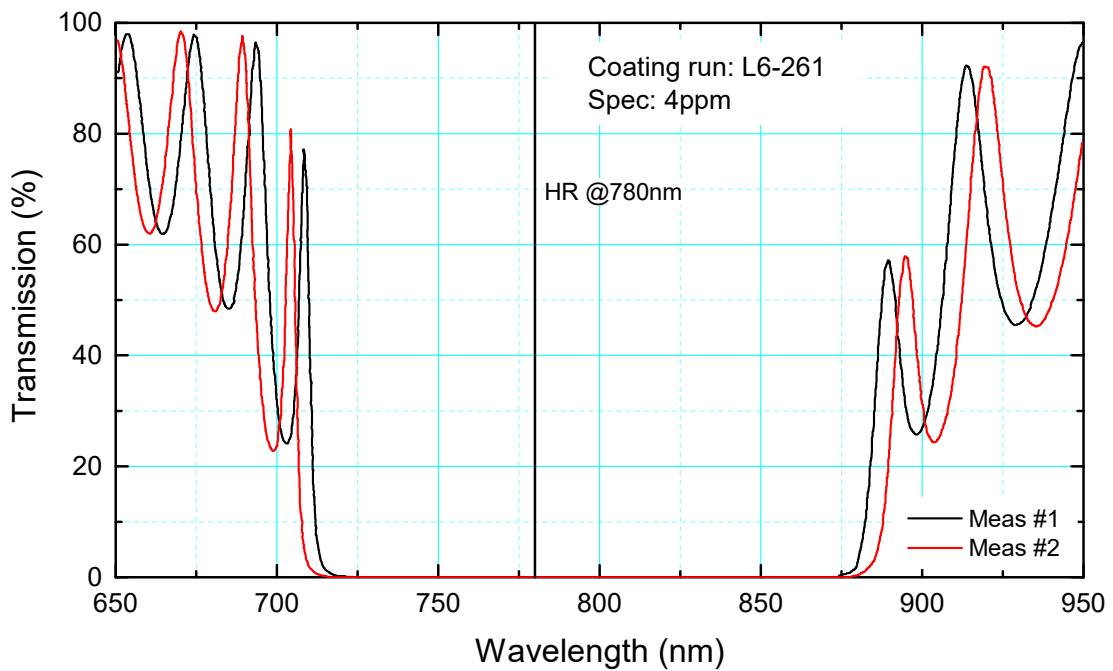


Figure 10.3: Transmission of coating run L6-261.

10.2. Photon Counting Socketed CLIP

```

ISERDES_NODELAY_master : ISERDES_NODELAY
  generic map (
    BITSLLIP_ENABLE => TRUE,
    DATA_RATE => "DDR",
    DATA_WIDTH => 8,
    INTERFACE_TYPE => "NETWORKING",
    NUM_CE => 2,
    SERDES_MODE => "MASTER"
  )
  port map (
    Q1 => data_out_ISERDES(7),
    Q2 => data_out_ISERDES(6),
    Q3 => data_out_ISERDES(5),
    Q4 => data_out_ISERDES(4),
    Q5 => data_out_ISERDES(3),
    Q6 => data_out_ISERDES(2),
    SHIFTOUT1 => iserdes_shift1,
    SHIFTOUT2 => iserdes_shift2,
    BITSLLIP => '0',
    CE1 => pll_locked,
    CE2 => pll_locked,
    CLK => GClk_fast,
    CLKB => GClk_fast_n,
    CLKDIV => GClk_div,
    D => input_iserdes,
    OCLK => '0',
    RST => reset_iserdes,
    SHIFTTIN1 => '0',
    SHIFTTIN2 => '0'
  );

ISERDES_NODELAY_slave : ISERDES_NODELAY
  generic map (
    BITSLLIP_ENABLE => TRUE,
    DATA_RATE => "DDR",
    DATA_WIDTH => 8,
    INTERFACE_TYPE => "NETWORKING",
    NUM_CE => 2,
    SERDES_MODE => "SLAVE"
  )
  port map (
    Q1 => open,
    Q2 => open,
    Q3 => data_out_ISERDES(1),
    Q4 => data_out_ISERDES(0),
    Q5 => open,
    Q6 => open,
    SHIFTOUT1 => open,
    SHIFTOUT2 => open,
    BITSLLIP => '0',
    CE1 => pll_locked,
    CE2 => pll_locked,
    CLK => GClk_fast,
    CLKB => GClk_fast_n,
    CLKDIV => GClk_div,
    D => '0',
    OCLK => '0',
    RST => reset_iserdes,
    SHIFTTIN1 => iserdes_shift1,
    SHIFTTIN2 => iserdes_shift2
  );

```

Figure 10.4: VHDL code of deserialization. The in- and output pins of the two iserdes primitives are connected to the respective signals. The primitives are configured in the respective “generic map” part.

The acquisition of the photon clicks by an FPGA has already been described previously (cf. Section 4.4). Here the core of the VHDL code, which consists of the actual deserialization and processing of the photon clicks, is displayed.

As shown in Figure 10.4, two *ISERDES_NODELAY* primitives, one configured as master the other as slave, are employed for the deserialization. This is required as the number of deserialization channels surpasses six. Both are configured in DDR (double data rate) mode to permit reliable operation at high clock speeds of up to one GS/s. In this mode the input data is sampled on the rising and falling edge of a clock signal; hence a 500 MHz clock (*GClk_fast*) as well as its phase inverted facsimile are provided (*GClk_fast_n*). The data is output synchronously to a phase-locked 125 MHz clock (*GClk_div*).

The processing of the deserialized photon click stream is displayed in Figure 10.5. The process is running synchronously to the same 125 MHz clock used for the deserialization. In this process a 61-bit timestamp with 1 ns resolution is generated for every photon click on each detector channel. It is composed of a 61-bit counter running at 125 MHz (*counter_125MHz_61bit*) and the information where in the deserialized data a rising edge occurs (*LUT_3bit_count_var*). The highest order bits are not used as they will be used later on in the processing to store stream relevant information. In addition, an *arbiter_data* signal is issued, which

provides information in which order photon clicks arrived on the different detector channels; this signal will be used for the sorting of the photon clicks.

```

process(GCLK_div)
  VARIABLE LUT_var: std_logic_vector(7 downto 0);
  VARIABLE FIFO_in_tempvar: std_logic_vector(63 downto 0);
  VARIABLE LUT_3bit_count_var: std_logic_vector(2 downto 0);
BEGIN
  if(rising_edge(GCLK_div)) then
    MSB_LAST_ISERDES <= data_out_ISERDES(7);

    LUT_var(0) := (not MSB_LAST_ISERDES) and data_out_ISERDES(0);
    LUT_var(1) := (not data_out_ISERDES(0)) and data_out_ISERDES(1);
    LUT_var(2) := (not data_out_ISERDES(1)) and data_out_ISERDES(2);
    LUT_var(3) := (not data_out_ISERDES(2)) and data_out_ISERDES(3);
    LUT_var(4) := (not data_out_ISERDES(3)) and data_out_ISERDES(4);
    LUT_var(5) := (not data_out_ISERDES(4)) and data_out_ISERDES(5);
    LUT_var(6) := (not data_out_ISERDES(5)) and data_out_ISERDES(6);
    LUT_var(7) := (not data_out_ISERDES(6)) and data_out_ISERDES(7);

    LUT_3bit_count_var(0) := LUT_var(7) or LUT_var(5) or LUT_var(3) or LUT_var(1);
    LUT_3bit_count_var(1) := LUT_var(7) or LUT_var(6) or LUT_var(3) or LUT_var(2);
    LUT_3bit_count_var(2) := LUT_var(7) or LUT_var(6) or LUT_var(5) or LUT_var(4);

    timestamp_event_ch1 <= LUT_var(7) or LUT_var(6) or LUT_var(5) or LUT_var(4) or LUT_var(3) or LUT_var(2) or LUT_var(1) or LUT_var(0);

    FIFO_in_tempvar := x"0" & counter_125MHz_61bit(56 downto 0) & LUT_3bit_count_var(2 downto 0);
    timestamp_ch1_hi <= FIFO_in_tempvar(63 downto 32);
    timestamp_ch1_low <= FIFO_in_tempvar(31 downto 0);

    arbiter_event <= LUT_var(7) or LUT_var(6) or LUT_var(5) or LUT_var(4) or LUT_var(3) or LUT_var(2) or LUT_var(1) or LUT_var(0)
      or LUT_var_2(7) or LUT_var_2(6) or LUT_var_2(5) or LUT_var_2(4) or LUT_var_2(3) or LUT_var_2(2) or LUT_var_2(1) or LUT_var_2(0)
      or LUT_var_3(7) or LUT_var_3(6) or LUT_var_3(5) or LUT_var_3(4) or LUT_var_3(3) or LUT_var_3(2) or LUT_var_3(1) or LUT_var_3(0)
      or LUT_var_4(7) or LUT_var_4(6) or LUT_var_4(5) or LUT_var_4(4) or LUT_var_4(3) or LUT_var_4(2) or LUT_var_4(1) or LUT_var_4(0);

    arbiter_data <= (LUT_var_4(7) or LUT_var_4(6) or LUT_var_4(5) or LUT_var_4(4) or LUT_var_4(3) or LUT_var_4(2) or LUT_var_4(1) or LUT_var_4(0))
      & not LUT_3bit_count_var_4
      & (LUT_var_3(7) or LUT_var_3(6) or LUT_var_3(5) or LUT_var_3(4) or LUT_var_3(3) or LUT_var_3(2) or LUT_var_3(1) or LUT_var_3(0))
      & not LUT_3bit_count_var_3
      & (LUT_var_2(7) or LUT_var_2(6) or LUT_var_2(5) or LUT_var_2(4) or LUT_var_2(3) or LUT_var_2(2) or LUT_var_2(1) or LUT_var_2(0))
      & not LUT_3bit_count_var_2
      & (LUT_var(7) or LUT_var(6) or LUT_var(5) or LUT_var(4) or LUT_var(3) or LUT_var(2) or LUT_var(1) or LUT_var(0))
      & not LUT_3bit_count_var;

    if count_reset = '1' then
      counter_125MHz_61bit <= "0000000000000000000000000000000000000000000000000000000000000000";
    else
      counter_125MHz_61bit <= counter_125MHz_61bit + 1;
    end if;
  end if;
END PROCESS;

```

Figure 10.5: VHDL code of photon click processing.

10.3. FPGA Photon Counting Protocol

The timestamps acquired from the digital pulses of the SPCMs are temporarily stored in 4 separate FIFOs. Another FIFO holds in addition the data from the arbiter, which signals in which order the clicks from the separate channels were recorded. This redundant data is necessary to ensure proper operation of the FPGA even at high clock rates. In order to transfer the acquired data to the host PC and store them on the hard disk, they need to be merged into a single stream. The LabVIEW FPGA routine merging the individual streams is depicted in Figure 10.6.

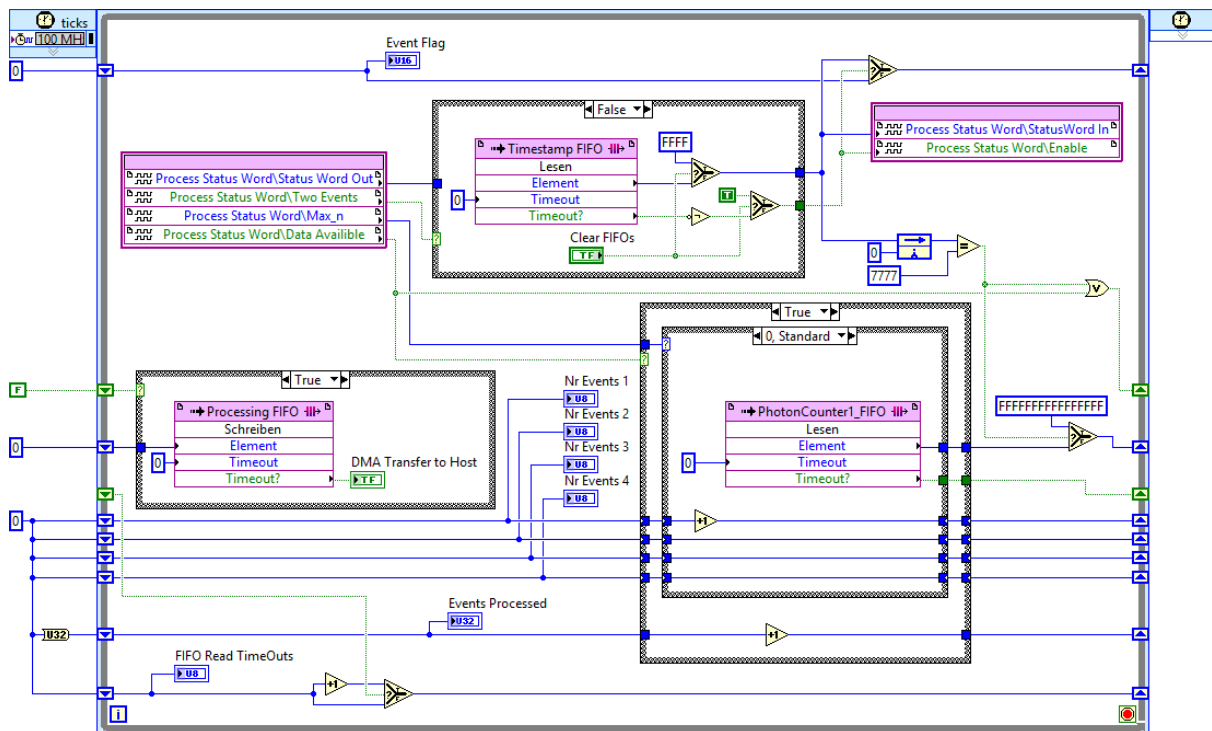


Figure 10.6: Sorting of the clicks of the individual photon counters into a single data stream. Depending on the data from the arbiter (*Timestamp_FIFO*), the photon clicks from the various channels are merged.

New data from the arbiter (*Timestamp_FIFO*) – if not already processed, i.e. the FIFO is empty – is read. The respective element is passed to an external VHDL code (*Process Status Word*) where it is processed, see Figure 10.7; this ensures that the netlist of the FPGA can be generated supporting clock speeds of 100 MHz. The VHDL code outputs the number of the digital channel where the next click occurred and if another channel recorded a click in the same 8 ns interval. The timestamp from this channel is then read and saved into an output FIFO (*Processing_FIFO*). If the atom is lost, the hexadecimal code $0x7777$ is written into the arbiter-stream. In this case $0xffffffff$ signals the end of the current photon counting stream. In order to save disk space and to ensure the possibility to add additional control data later-on, the data is sorted into a specific protocol. The protocol definition is shown in Table 10.1.

```

entity ProcessStatusWord is
  port (
    clk           : in std_logic;
    aReset        : in std_logic;
    cStatusW      : in std_logic_vector(15 downto 0);
    cEnable       : in std_logic;
    cStatusWout   : out std_logic_vector(15 downto 0) := x"0000";
    cMax_nOut     : out std_logic_vector(7 downto 0) := x"00";
    cTwoEvents    : out std_logic := '0';
    cAvailable    : out std_logic
  );
end ProcessStatusWord;

architecture rtl of ProcessStatusWord is
begin
  process(aReset, clk)
    variable vC1,vC2,vc3,vc4: std_logic_vector(3 downto 0);
    variable vMax12, vMax34, vMax1234: std_logic_vector(3 downto 0);
    variable vMax_nOut_12, vMax_nOut_34: std_logic;
    variable vMax_nOut_temp: std_logic_vector(1 downto 0);
  begin
    if(aReset = '1') then
      cStatusWout <= x"0000";
      cMax_nOut <= x"00";
    else
      if(rising_edge(clk)) then
        vC1 := cStatusW(3 downto 0);
        vC2 := cStatusW(7 downto 4);
        vC3 := cStatusW(11 downto 8);
        vC4 := cStatusW(15 downto 12);
        if vC1>vC2 then
          vMax12 := vC1;
          vMax_nOut_12 := '0';
        else
          vMax12 := vC2;
          vMax_nOut_12 := '1';
        end if;
        if vC3>vC4 then
          vMax34 := vC3;
          vMax_nOut_34 := '0';
        else
          vMax34 := vC4;
          vMax_nOut_34 := '1';
        end if;
        if vMax12>vMax34 then
          vMax_nOut_temp := '0' & vMax_nOut_12;
        else
          vMax_nOut_temp := '1' & vMax_nOut_34;
        end if;
        cMax_nOut <= "000000" & vMax_nOut_temp;
        cTwoEvents <= (cStatusW(3) and cStatusW(7)) or (cStatusW(3) and cStatusW(11))
          or (cStatusW(3) and cStatusW(15)) or (cStatusW(7) and cStatusW(11))
          or (cStatusW(7) and cStatusW(15)) or (cStatusW(11) and cStatusW(15));
        case vMax_nOut_temp is
          when "00" =>
            cStatusWout <= cStatusW and x"FFF7";
          when "01" =>
            cStatusWout <= cStatusW and x"FF7F";
          when "10" =>
            cStatusWout <= cStatusW and x"F7FF";
          when "11" =>
            cStatusWout <= cStatusW and x"7FFF";
          when others =>
            cStatusWout <= x"0000";
        end case;
        cAvailable <= cEnable and (cStatusW(15) or cStatusW(11) or cStatusW(7) or cStatusW(3));
      end if;
    end process;
  end rtl;
end architecture;

```

Figure 10.7: VHDL code processing the arbiter data.

The protocol requires the 61-bit long timestamp of the individual photon counters to be shortened to 58-bit, which ensures an efficient and optimized handling of the data. Furthermore, each of these photon click timestamps needs to be divided into two parts of 29 bits each. This way the high bit part only needs to be updated with a frequency of once around every half a second, while the lower part holds the specific information about the channel and the detailed timing information.

Bit 31	Bit 30-29	Bit 28-0
0 data	channel (0-3)	count [ns] ($max. 2^{29} ns = 0.537 s$)
1 status	00 overflow	hi-count [$2^{29} ns = 0.537 s$] ($max. 2^{58} ns = 9.13 years$)
	01 HS-marker	high-speed marker not yet implemented
	10 LS-marker	low-speed marker not yet implemented
	11 EOF	0b11111111111111111111111111111111

Table 10.1: Protocol of the photon counting data stream. The first three bits are selecting the basic information while the remaining 29 bits contain the actual data.

The application of this protocol to the photon stream data is shown in Figure 10.8. Here the current timestamp is read. Its higher 29 bits are compared to the ones of the last timestamp, which has been processed. If they differ, the binary code *0b100* followed by the 29 bits is stored in a second FIFO (*DRAM_Transfer_FIFO*). If they are equal, a binary *0b0* followed by the 2-bit channel number and the lower 29 bits of the timestamp are stored. The loop runs at a clock speed of 100 MHz which permits a synchronous data transfer to the integrated DDR2 memory.

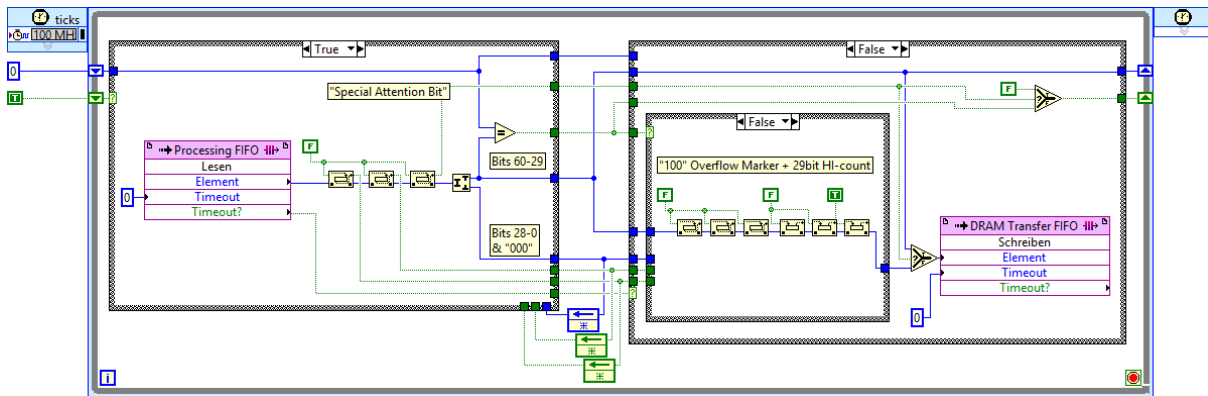


Figure 10.8: Application of protocol to common data stream. The sorted data stream from the SPCMs is stored into a uniform stream according to a predefined protocol; this permits to directly store the data on a hard disk.

10.4. Simple FPGA-VGA Connector

The deterministic timing and fast processing of the FPGAs permit to embed an integrated and very simple graphics adaptor in the chip. This enables to graphically display the acquired data in real-time and is an easy way to align the setup. The inherent parallelism of FPGAs guarantees that the actual data acquisition and processing tasks are in no way impacted.

	Screen 1	Screen 2
Resolution	800x600 @ 60 Hz	1280x1024 @ 60 Hz
Color-Depth	3-bit (8 colors)	3-bit (8 colors)
Pixel-Clock	40 MHz	108 MHz

Table 10.2: Technical specification of the two VGA ports.

The FPGA responsible for the photon counting has two screens attached. An overview of the technical specification is given in Table 10.2. Each screen is only capable of depicting a maximum of 8 colors, as for simplicity each primary color is directly connected to a digital output pin. In total 5 output pins are required, two for the vertical and horizontal display sync, respectively and 3 for the color data signal. The matching to the required voltage level to the VGA standard is achieved via resistors as shown in Figure 10.9.

DIO-Channels in 3.3V configuration (50 Ω) (NI 6581)

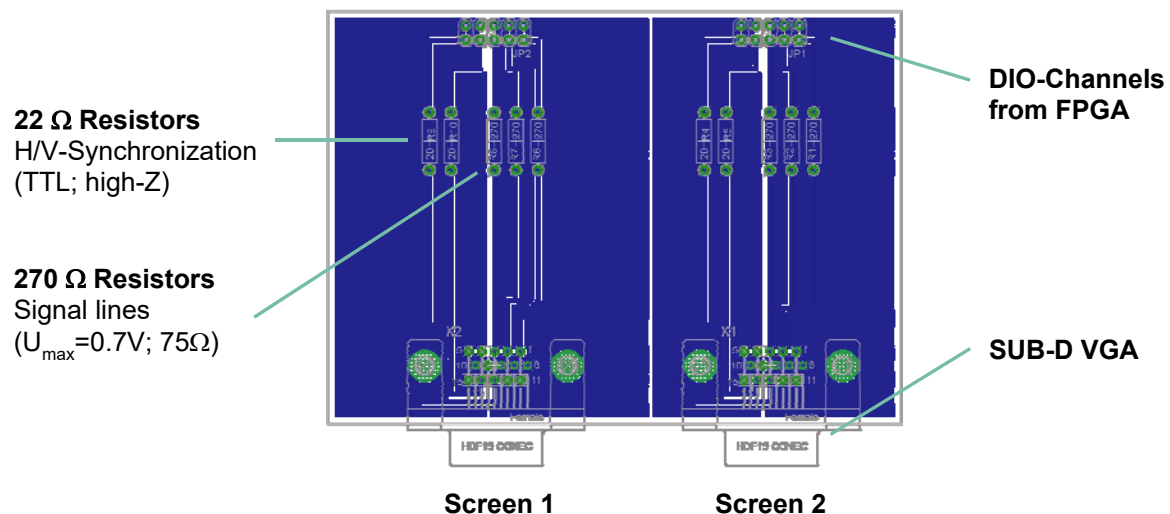


Figure 10.9: Electronic schematics of the VGA board. The digital pins of the FPGA supply 3.3V in 50 Ω configuration. The required power levels according to the VGA standard are attained by inserting resistors. 1-bit depth per color is achieved.

The DIO channels are capable of outputting 3.3V into 50 Ω . As full color is defined to be 0.7V into 75 Ω , the voltage level on the VGA connector is lowered by employing 270 Ω resistors. As the horizontal and vertical synchronization channels are high impedance TTL logic, 22 Ω resistors are only used to prevent overshoots.

The display output used for photon counting is shown in Figure 10.10. It consists of a text-mode part, which is capable of dynamically displaying text and numbers, a graphics part, showing multiple plots and a triggering info, showing information of the data processing.



Figure 10.10: Displayed output of the VGA interface. The output is divided into a text, a graphics and a triggering part.

The underlying LabVIEW FPGA code is depicted in Figure 10.10. A single cycled timed loop runs with the required pixel clock. Based on loop counters, the horizontal and vertical synchronization are generated. The text mode features two memory elements, one storing the actual ASCII data and one containing the font. The graphs and triggers are generated from separate memory elements addressed by the horizontal pixel number.

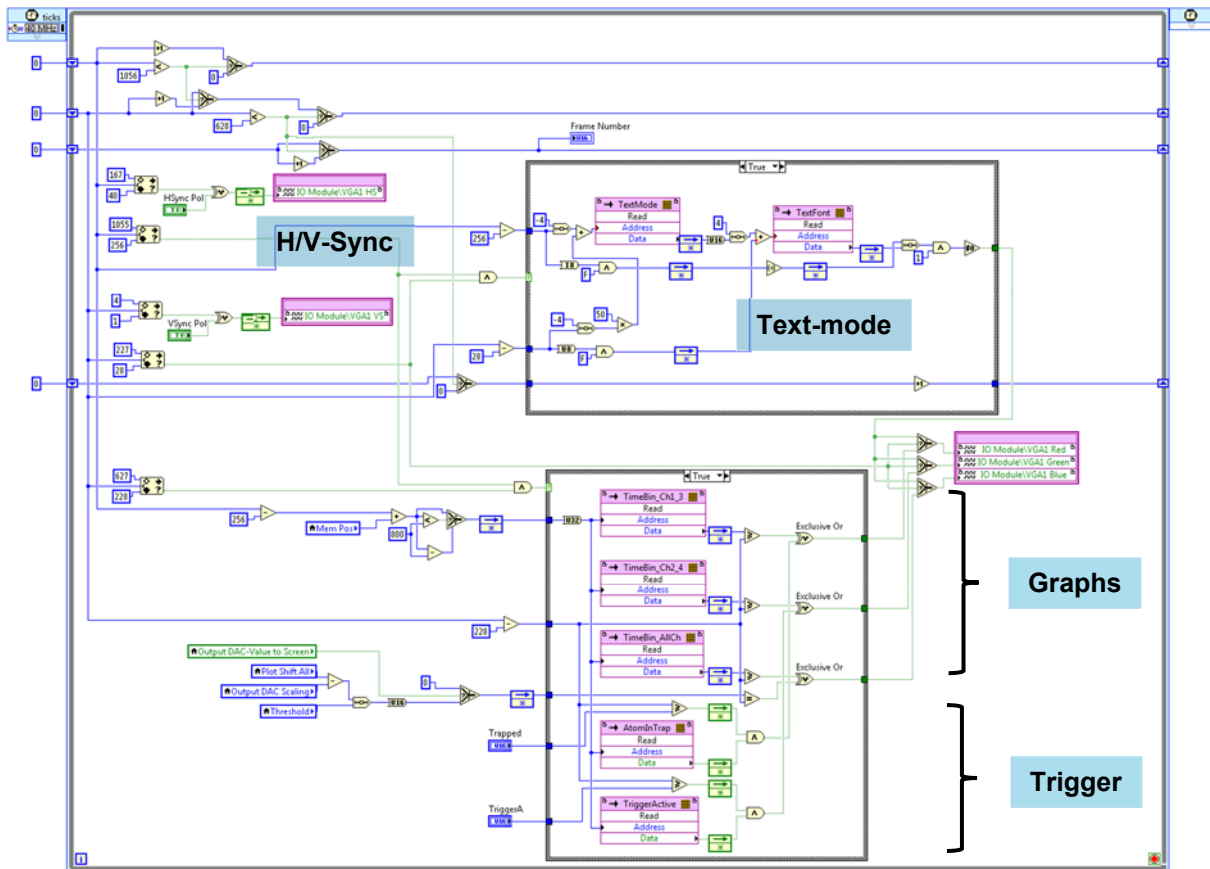


Figure 10.11: LabVIEW FPGA code switching digital channels to generate screen output.

10.5. High-Speed FPGA Digital-to-Analog-Converter

The parametric feedback requires a fast digital-to-analog conversion (DAC). As the Virtex FPGAs do not have DACs on board, an external solution is added. This is achieved by employing an Analog Devices AD9744 IC. Its 14 digital input bits as well as the clock signal are connected to the FPGA pins. The schematics and a rendering are displayed in Figure 10.12.

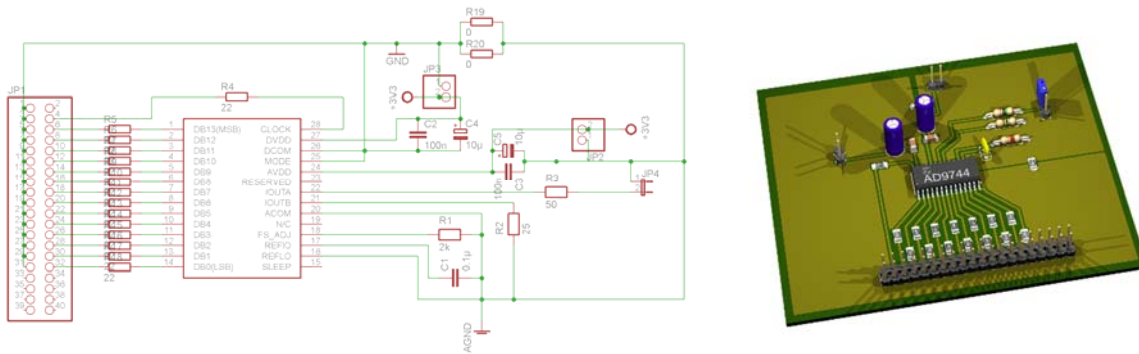


Figure 10.12: Schematics and rendering of digital-to-analog conversion board.

In order to prevent overshoots in the digital signal, 22Ω resistors are inserted. A supply voltage of 3.3V for the digital and analog domain of the DAC is applied via an external stable power supply. The maximum clock frequency is specified at 210 MHz. Here, we employ the phase-locked 125 MHz clock, also used for the photon counting, to permit synchronous data exchange. The single cycled timed loop clocking the DAC and updating its values is depicted in Figure 10.13. This permits an easy integration into the existing FPGA project.

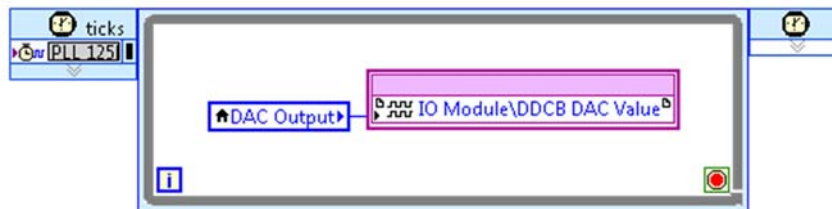


Figure 10.13: Data transfer to DAC. Integration of a SCTL running at 125 MHz to clock and the DAC and updates its values.

10.6. Heterodyne Detection

The heterodyning process has already been described in detail in Chapter 5.6. Here additional aspects of the heterodyne detection and how it is implemented will be eluded.

10.6.1. Spectral Filtering of Signal

Heterodyne detection relies on a spectral filtering of input data. Spectral filtering is a very powerful mechanism for extracting very weak signals, which are superimposed by a significant amount of noise. This is exemplified in Figure 10.14.

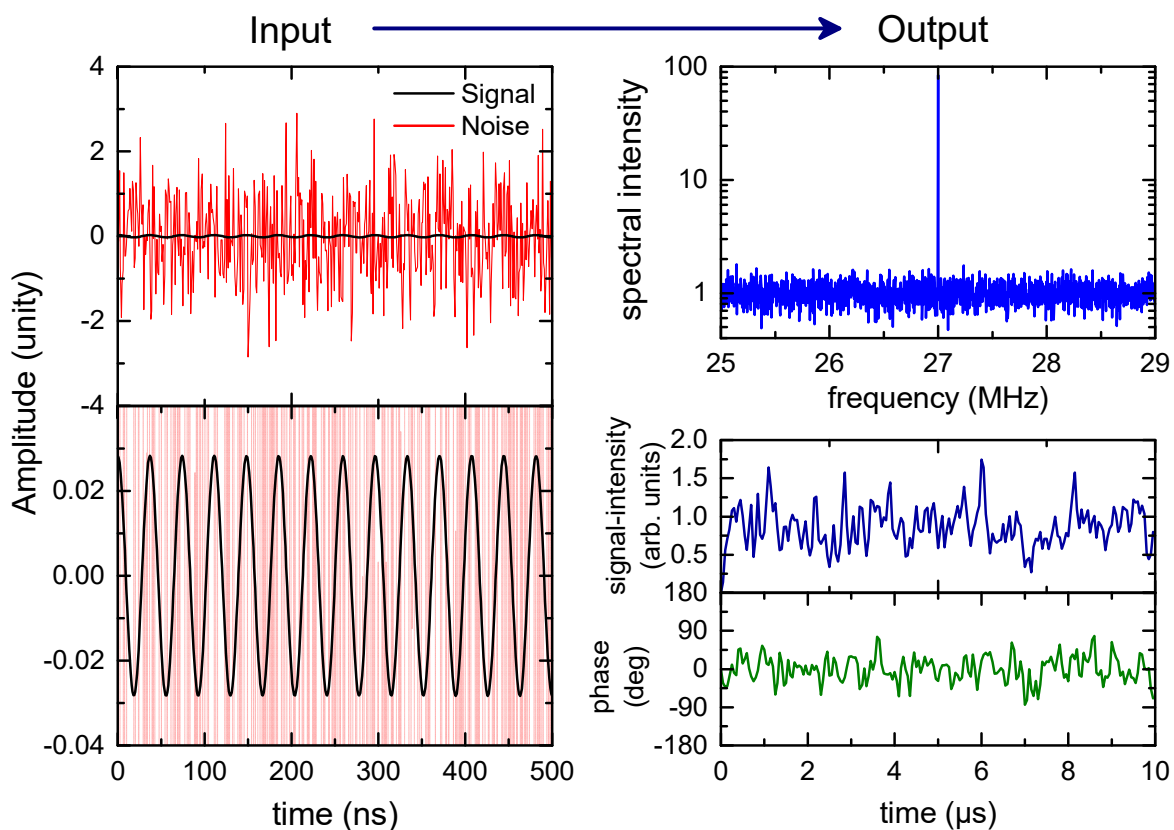


Figure 10.14: Spectral filtering of heterodyne data. The upper left side of the illustration shows the input waveform. A small signal (black) is superimposed by a large amount of noise (red). The lower left part shows a zoom-in. The right side of the illustration depicts the derived output after a frequency analysis. The upper part shows the FFT spectrum, where the carrier of the signal is clearly visible. The lower part shows the magnitude (blue) and phase (green) information extracted after digitally down-converting the signal.

On the left-hand, the actual signal (black) as well as the background noise (red) are plotted. In order to show the shear difference in amplitude, two plots with different vertical scaling are presented. The spectral power density of the superimposed signals is depicted in the upper right graph. Despite the high amount of noise, a clear peak at 27 MHz is visible. In the lower two graphs the spectrally filtered magnitude (blue) and phase (green) information of the carrier at 27 MHz is extracted. The shown simulated signal with the high amount of background noise is similar to the actual heterodyne carrier, which is the beat between the transmitted probe beam

and the local oscillator. Despite these adversities, spectral filtering is a powerful tool to extract information out of these signals as it has been shown in the upper Figure.

10.6.2. Resolution and Video Bandwidth

In Section 6.2.1 two different bandwidth notions were introduced. At first glance, the fundamental difference of low-passing the signal either in the complex baseband or after the rectangular-to-polar conversion is not directly visible; however, a look at the mathematical formulas shows an evident difference. As mentioned previously, the low-pass filter is implemented as a simple moving average filter. If we consider a digital signal sampled with the frequency f_s , then an integration of the signal over a time T_{int} corresponds to averaging over the last $n_{int} = T_{int} \cdot f_s$ samples. Assuming that $S_{I,n}$ and $S_{Q,n}$ are the n -th value of the I/Q signal in the complex plane before the low-pass filter is applied, then the magnitude obtained after the polar conversion gives

$$A_{Hd,n} = \sqrt{S_I'^2 + S_Q'^2} = \frac{1}{n_{int}} \sqrt{\left(\sum_{n_{int}} S_{I,n} \right)^2 + \left(\sum_{n_{int}} S_{Q,n} \right)^2}. \quad (7.3)$$

In this equation $S_{I,n}'$ and $S_{Q,n}'$ are the low-passed I/Q amplitudes before the polar conversion. Nevertheless, low-passing A_{Hd} by using a moving average filter after the conversion to polar coordinates gives

$$A'_{Hd,n} = \frac{1}{n_{int}} \sum_{n_{int}} \sqrt{A_{Hd,n}} = \frac{1}{n_{int}} \sum_{n_{int}} \sqrt{S_I^2 + S_Q^2}. \quad (7.4)$$

Mathematically the difference between (7.3) and (7.4), which consists in a summation before or after the polar conversion, is evident. It is also known that a summation carried out before the absolute value is taken yields smaller values than the opposite case. Here, however, it is also important to understand the different physical influence depending on where the signal is filtered.

This influence can be visualized by considering a carrier at typical heterodyne frequencies at 27 MHz with amplitude modulated sidebands at 500 kHz and 1 kHz. The signal is superimposed with white noise, which is uncorrelated in time and hence produces a spectrally flat background. The spectrum of the resulting signal is visualized in Figure 10.15 a) and b).

This signal – similar to the processing of the heterodyne signal – is multiplied by a local oscillator at 27 MHz as well as its -90° phase-shifted facsimile, producing the complex I/Q baseband amplitude. They are low-passed individually by a moving average filter with a -3dB bandwidth of 664 kHz and afterwards converted to polar coordinates. Its temporal behavior is shown in Figure 10.15 c). One can clearly identify both modulations at oscillation frequencies of 1 kHz and 500 kHz, respectively (corresponding to periods of 1 ms and 2 μ s, respectively).

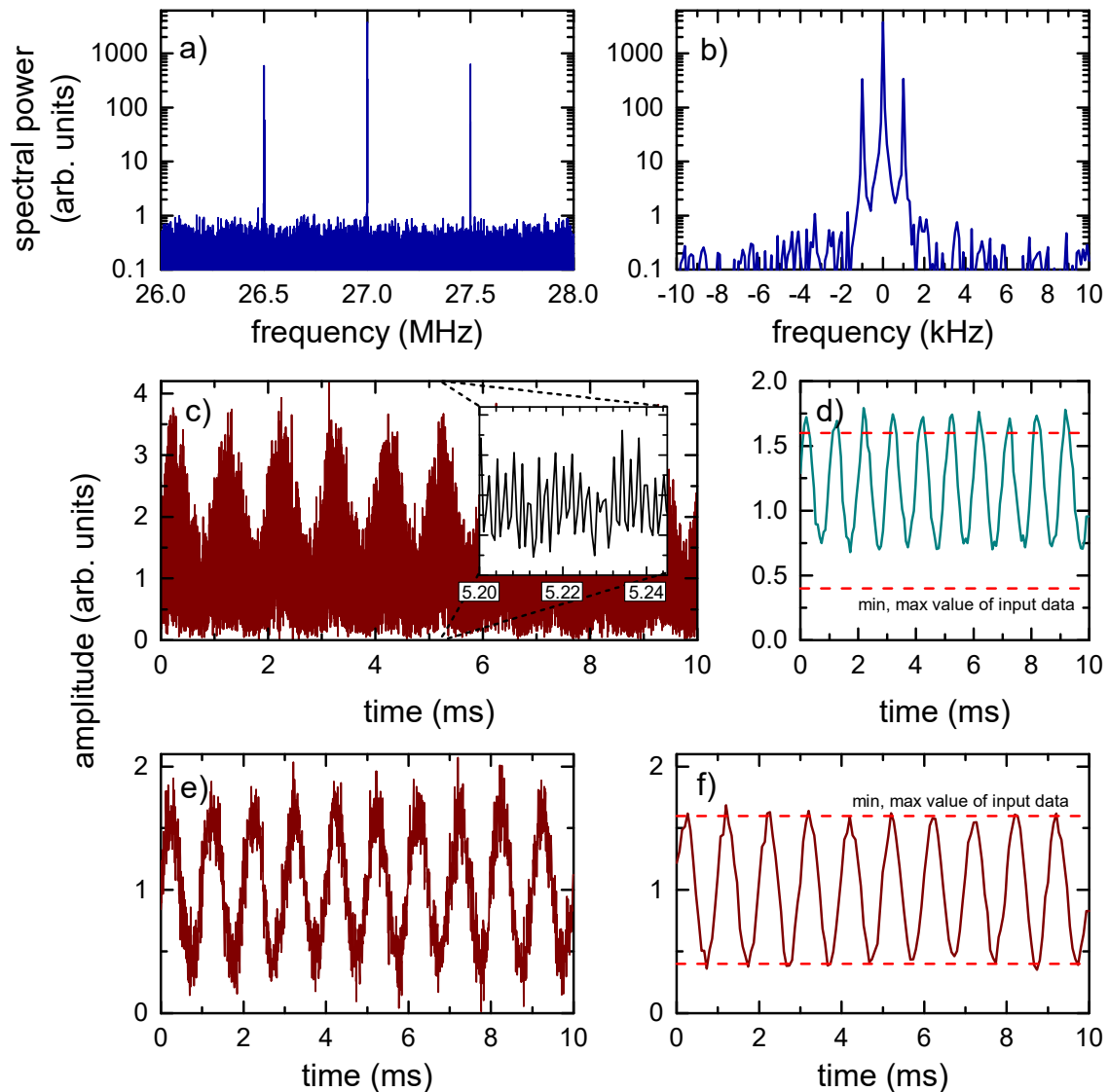


Figure 10.15: Visualization of the difference between resolution and video bandwidth. The frequency spectrum of signal with the AM sidebands at 500 kHz and 1 kHz is shown in a) and b). The temporal evolution of the signal with a 664 kHz RBW filter applied is depicted in c). Part d) applies an additional 6.6 kHz VBW filter to the signal of c). A 66.4 kHz and 6.6 kHz RBW filter to the original data is applied in e) and f), respectively. In d) and f) the upper and lower limit of the oscillating original signal are indicated by dashed red lines. In f) compared to d) no VBW filtering occurred.

The filtering in the complex baseband reduces the spectral width of the data before it is passed to the polar converter. Spectral features which are above the filters cut-off frequency are hence eliminated. This filtering bandwidth is hence termed resolution bandwidth (RBW), since it is responsible for the spectral resolution of the output data. This is also the reason, why the 500kHz signal is still clearly visible in the inset. A second filtering of the amplitude after the polar conversion smoothens the displayed data. The effect of this low-passing is depicted in Figure 10.15 d). Here only the slower oscillation survives. However, the filter after polar conversion does not eliminate spectral features but rather only smoothens the data. This leads to an overall increased offset in the data, which in our case mainly results from the 500kHz oscillation as well as the noisy background. The original amplitude of the modulation as it was

generated is also depicted as dashed red lines. This bandwidth associated with this filtering process is hence termed video bandwidth (VBW) and only reduces the bandwidth of the displayed data. The different effect of the filters becomes visible if one changes their parameters. The same data plotted with RBW of 66.4kHz is plotted in Figure 10.15 e). Here the disappearance of the oscillation at 500 kHz is evident. The result, if the RBW filter is further reduced to 6.6 kHz is depicted in f). This signal has the same overall bandwidth as the one obtained by the VBW filter at 6.6 kHz. The main difference is the missing offset since higher frequency components are not smoothed out but are rather fully rejected. This is also the reason, why the data stretches exactly to the minimum and maximum values of the original data.

In this section the difference between the RBW and the VBW was emphasized. It is important to keep in mind that only low-passing the data in the complex baseband eliminated spectral features without artefacts. This is the reason why in this thesis – except if noted otherwise – the VBW was set to match the RBW. In this configuration all filtering is hence characterized by the RBW.

10.6.3. Filter Response in the Time and Frequency Domain

In Section 10.6.2 the difference between the resolution and the video bandwidth was explained. Here we will have a closer look at the actual digital implementation of the filter; the spectral as well as temporal characteristics will be elaborated on.

10.6.3.1. Rectangular Moving Average Filter

One of the simplest filters one can imagine is to simply average data of a given length. Assuming that data is sampled at a sampling frequency f_s then this corresponds to summing over the last N values and dividing by the number of summands. The filter outputs a new value for every sampled point. This “motion” of the averaging process also causes its name “moving average filter”. In an FPGA this filter can very easily and efficiently be integrated by starting with the sum of the past N values and adding the most up to date value while subtracting the value which was sampled N -cycles ago. In our case, the FPGA clock corresponds to the sampling frequency of the ADC and amounts to $f_s = 100\text{Ms} / \text{s}$. The spectral power response of a moving average filter of length $N = 200$ samples is depicted in Figure 10.16; this is equivalent to an integration time of $2 \mu\text{s}$.

The behavior of the filter for the full spectral range of the input data is shown in part a). The spectral power response is the square of the amplitude response. An analytic expression of this amplitude response is found by integrating the complex amplitudes at the desired frequency over one full period $T_0 = N/f_s$.

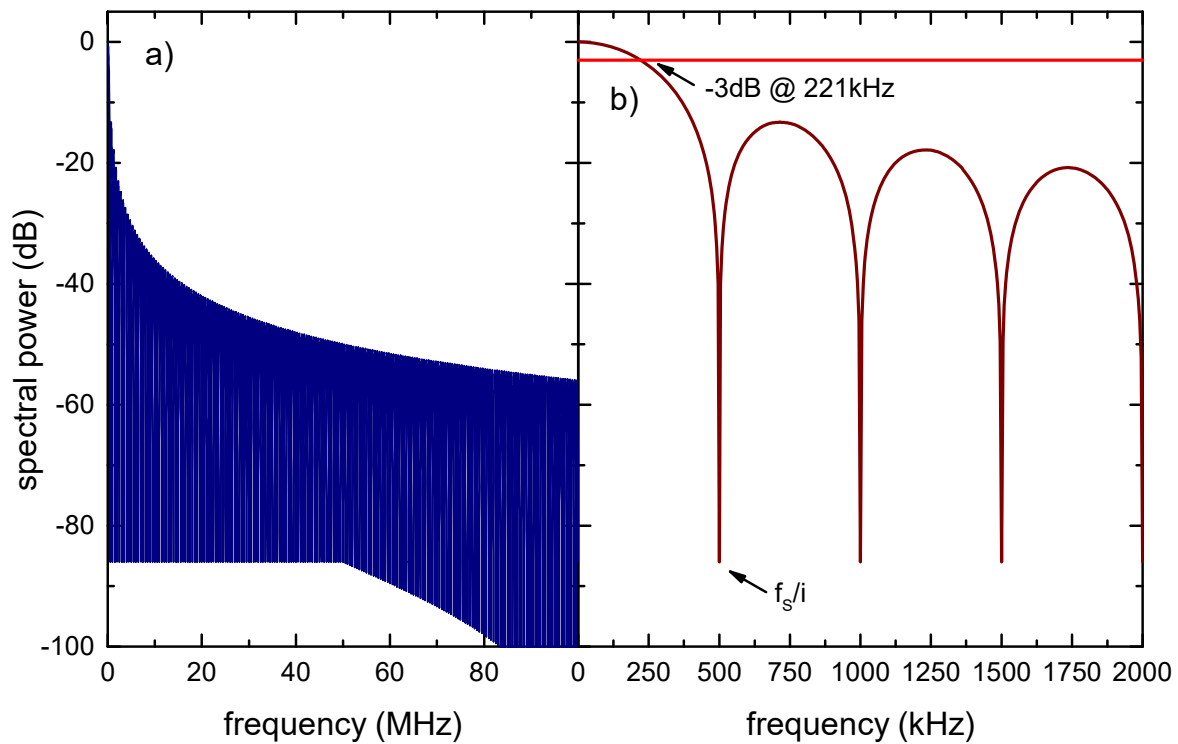


Figure 10.16: Simulation of the spectral filtering of a moving average filter. a) shows the full spectral power response from DC frequency to the sampling frequency of the input data. b) shows a zoom-in to the region where the pattern of the filter becomes visible.

$$R(f) = \frac{\int_{T=0}^{T_0} e^{i2\pi fT} dT}{T_0} = \frac{\sqrt{2 - 2\cos(2\pi fT_0)}}{2\pi fT_0} \quad (7.5)$$

Over the full spectrum a drop in the response of almost -60 dB approaching the sampling frequency of the data is visible. A closer view as it is presented in part b) reveals the structure of the main and side lobes which are separated by sharp drops, so-called “nulls”. These sharp drops at integer multiples of f_s/N can be understood by considering that averaging over a full period of a sine wave results in zero signal ($-\infty$ dB). The finite values as they are displayed in Figure 10.16 b) are caused by numeric artefacts. The -3 dB bandwidth, i.e. the bandwidth where the power of the signal is attenuated to half its value, can be computed by evaluating, where Eqn. (7.5) drops to one half. The resulting bandwidth is hence given by:

$$f_{rect}^{3dB} = 0.4429 \cdot T_0^{-1} = f_{mov-avg}^{3dB} \quad (7.6)$$

The implementation of the moving average filter with the computed value obtained in Eqn. (7.5) is verified experimentally. In order to do so, a function generator performs a frequency sweep around the carrier frequency of 31 MHz. The signal is input into the FPGA, which is

responsible for the heterodyning and is set to an integration time of 4000 samples, which corresponds to $T_0 = 40\mu s$. The result is plotted in Figure 10.17.

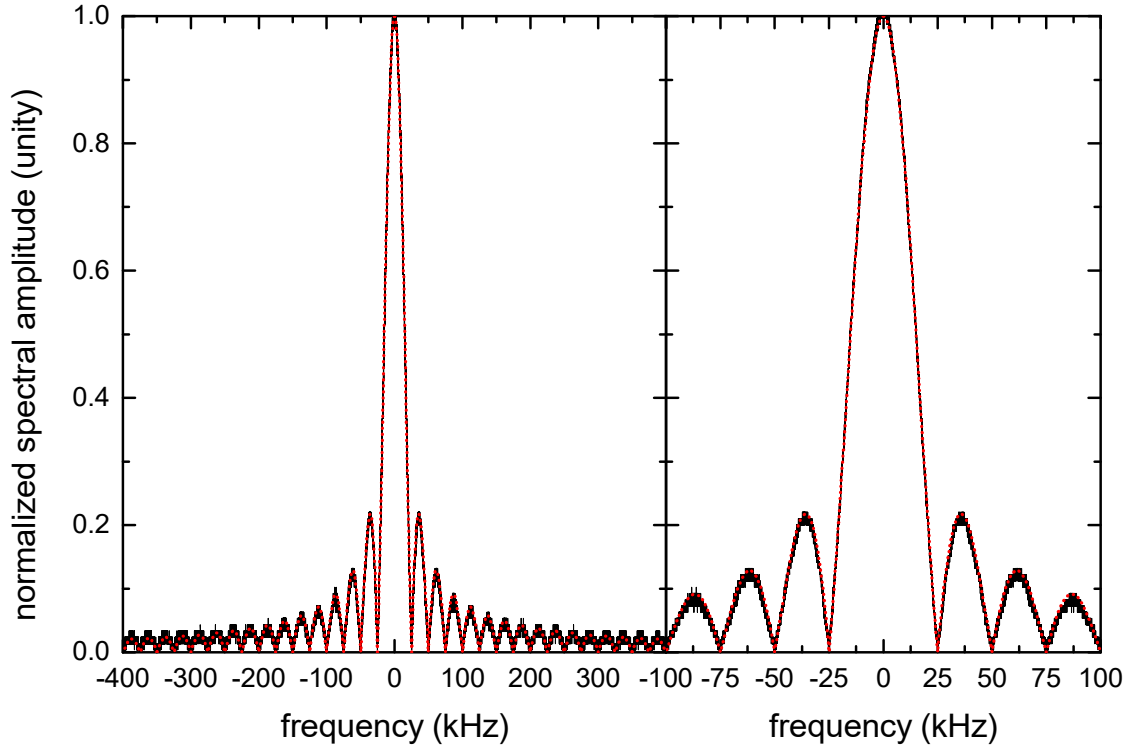


Figure 10.17: Implementation of the moving average filter into the FPGA. The experimental data is shown as black curve. The computed values are depicted as red dotted curve. The right side is a horizontal zoom into the center region shown on the left side.

The black curve represents the experimental data. The lobes and “nulls” are clearly visible. The data shows excellent agreement with the computed values, as they are plotted as reference as red dotted line. This confirms the proper implementation and working principle of the filter in the FPGA.

10.6.3.2. Custom FIR Filter

In this section more advanced filters will be presented and their performance will be compared to the simple moving average filter. The term FIR stands for finite impulse response and refers to the finite response character of the filter. A discrete-time FIR filter of length N is the weighted sum of the previous $N+1$ samples. Filtering a discrete signal with the samples S_n with the FIR coefficients b_i will give the output

$$S'_n = \sum_{i=0}^N b_i \cdot S_{n-i} . \quad (7.7)$$

A moving average filter as it was described in the previous section is in this sense also a special case of FIR filter. As one can see by Eqn. (7.7), real-time FIR filtering with arbitrary filters can easily be realized on an FPGA by making use of its inherent parallelism. The step response, i.e. the response if a Heaviside function is applied as input, of different FIR filters are plotted in Figure 10.18.

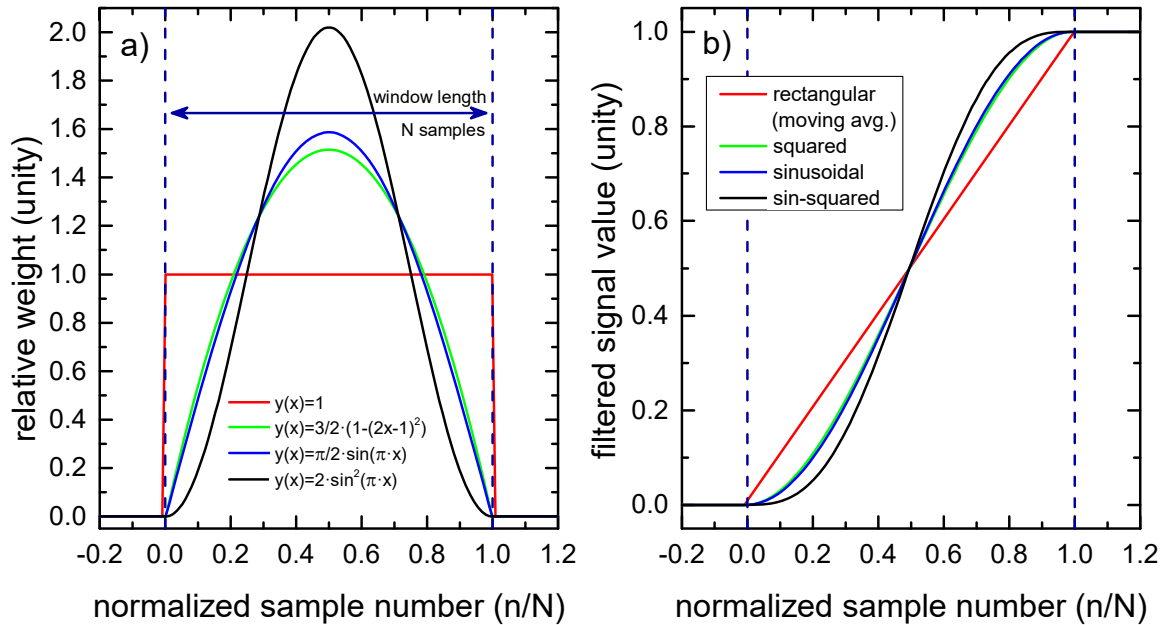


Figure 10.18: Step response of various FIR filters. a) shows a plot of the FIR coefficients. The samples are normalized to the length of the FIR filter N . The functional description of the filters is given by the equations. b) shows the step response of the different FIR filters, if a Heaviside function is used as input. The data rises from 0 to 1 over the length of the FIR filter N .

Part a) shows the weighting of single samples normalized to the whole summation region. This weighting curve corresponds to the discrete FIR coefficients. All filters are normalized to one. In case of the moving average filter (red), the weighting simply corresponds to a rectangular function, where all the samples within the interval have equal weight. In green a second order polynomial weighting function is considered. The blue and the green curve show different sinusoidal weightings. The functional dependency of the separate filters is given by

$$\begin{aligned}
 y_{rect}(n/N) &= 1 \\
 y_{sq}(n/N) &= \frac{3}{2} \cdot (1 - (2x - 1)^2) \\
 y_{sin}(n/N) &= \frac{\pi}{2} \cdot \sin(\pi \cdot x) \\
 y_{sin-sq}(n/N) &= 2 \cdot \sin^2(\pi \cdot x)
 \end{aligned} \tag{7.8}$$

Figure 10.18 b) shows the respective step response of each of the considered filters. One can see that while the moving average filter has the fastest response in the beginning, it is surpassed by the other filters in the second half. As it was done in the previous section, the spectral power response for each filter is determined. As done in Eqn. (7.5), the dependency is computed by

integration over the period at a given frequency. As an example, the spectral response of the sinusoidal filter amounts to

$$R_{\text{sin}}(f) = \frac{\int_{T=0}^{T_0} \frac{\pi}{2} \cdot \sin(\pi \cdot T/T_0) e^{i2\pi fT} dT}{T_0} = \frac{\sqrt{2}}{2} \frac{\sqrt{1 + \cos(2\pi fT_0)}}{4f^2T_0 - 1}. \quad (7.9)$$

The spectral response in Eqn. (7.9) is plotted along with the other three filters in Figure 10.19.

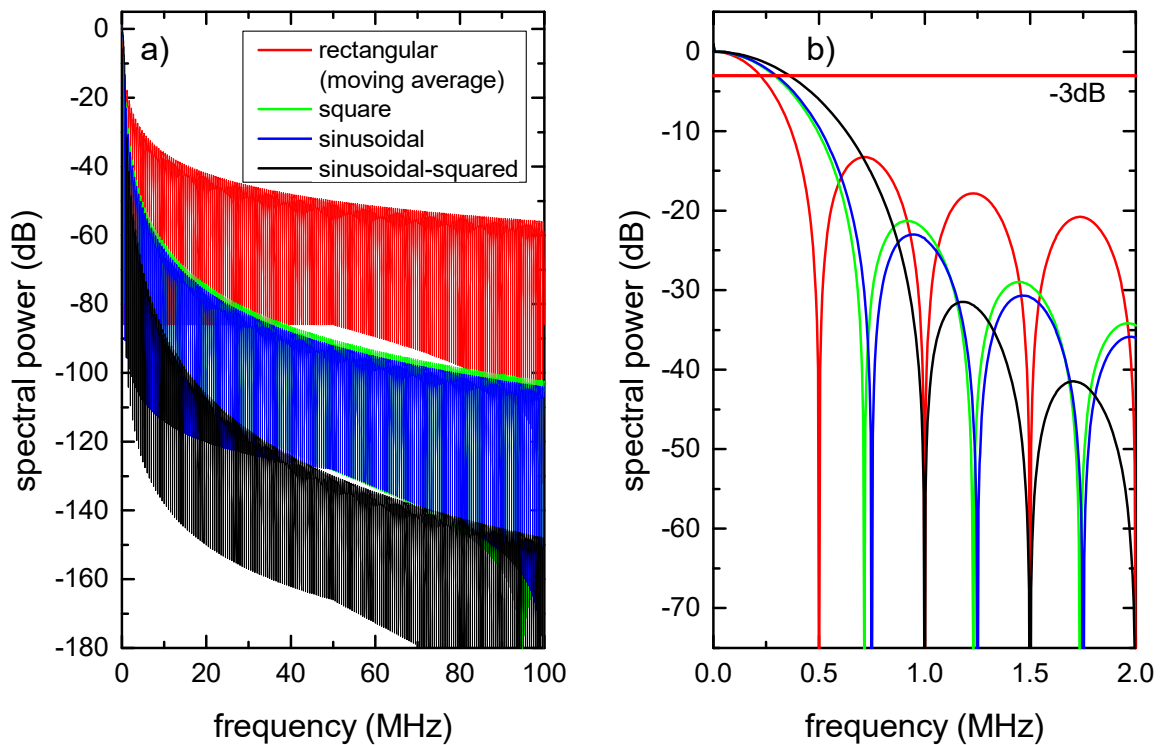


Figure 10.19: Spectral response of different FIR filters. a) shows the full spectral power response from DC frequency to the sampling frequency of the input data. The response of four different FIR filters are depicted. b) shows a zoom-in to the region where the lobes and “nulls” of the FIR filters become visible.

As previously the length of the filtering interval was set to $N=200$ samples. Part a) shows the full spectral power response from DC frequency to the sampling frequency. Here a big disadvantage of the moving average filter, which is its poor suppression for higher frequencies, becomes evident. As an example, the side lobes of the sinusoidal-squared filter yield an attenuation of almost -130 dB at 50 MHz, while the moving average filter does not even reach the -50 dB mark. A zoom-in of the data, showing the 3dB bandwidth is depicted in Figure 10.19 b). This plot reveals another property of the moving average filter, which is given by the narrow width of the main lobe, and hence gives rise to a small 3dB bandwidth. An overview of the -3 dB bandwidth of all filters is given in Eqn. (7.10).

$$\begin{aligned}
 f_{rect}^{3dB} &= 0.4429 \cdot T_0^{-1} = f_{mov-avg}^{3dB} \\
 f_{sq}^{3dB} &= 0.5777 \cdot T_0^{-1} \\
 f_{sin}^{3dB} &= 0.5945 \cdot T_0^{-1} \\
 f_{sin^2}^{3dB} &= 0.7203 \cdot T_0^{-1}
 \end{aligned}
 \tag{7.10}$$

Comparing the 3dB bandwidth of a filter with sinusoidal squared weighting to a moving average filter of equal length yields $f_{sin^2}^{3dB} = 1.63 \cdot f_{rect}^{3dB}$. This means that filtering signals with equal bandwidth requires a sinusoidal squared filter whose integration time is increased by a factor of 1.63. The effect this has on the signal response will be analyzed in the following.

Figure 10.20 shows a moving average filter as well as a filter with sinusoidal squared weighting both having a 3dB bandwidth of 221kHz as it can be seen in subplot c). The moving average filter sums over 200 samples recorded with 100 MS/s while the sinusoidal squared filter takes the weighted sum of 325 samples. This significantly delays the step response by roughly 30% as displayed in subplot a). Part b) shows the attenuation for the whole spectrum, which shows the poor suppression of higher frequencies of the moving average filter.

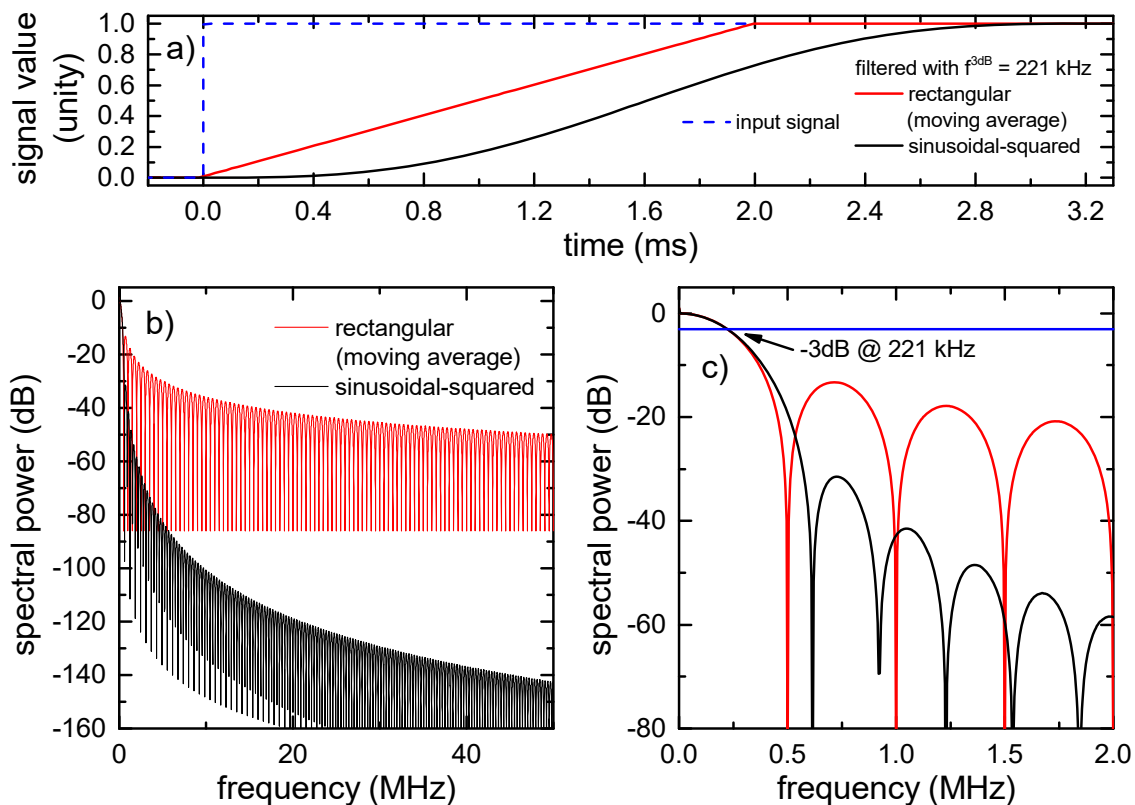


Figure 10.20: Response time for different filters with the same 3db bandwidth. a) shows the step response of a moving average as well as a sinusoidal-squared filter with a 3dB bandwidth of 221kHz. The spectral response over the full spectrum as well as for small frequencies is plotted in b) and c), respectively.

In total one can see that the FIR coefficients, which determine the weighting, have a significant impact on the step response, the -3dB bandwidth as well as the attenuation at higher frequencies. Since the heterodyne detection is also responsible for the feedbacking, a filter which offers a faster response at a reasonably small 3dB bandwidth is chosen. This is why a moving average filters is employed in the FPGA for real-time filtering.

10.6.4. Visibility

In heterodyning the local oscillator beam is responsible to down-mix the probe beam. At typical intensity-level any nonlinearity of the air is way too weak to mediate an interaction between these two beams in the detection setup. Due to this, the actual down-mixing occurs during the detection process with a square-law detector, i.e. a photodiode [148]. This requires that the wave-functions of the two beams are mode-matched, i.e. polarization of probe and local oscillator as well as their wave-fronts exactly overlap at the position of the photodiodes. While matching of the polarization can easily be achieved by $\lambda/2$ and $\lambda/4$ waveplates, an alignment of the wave-fronts is a more challenging task. Besides a proper alignment of the position and the size of the two beams, their incident angle and focal length also need to match. In order to examine the alignment, the probe and local oscillator beam are balanced, i.e. brought to equal intensity. The normalized difference in intensity of their destructive and constructive interference then yields what is called the visibility.

It is measured by recording the intensity of balanced probe and local oscillator which are offset in frequency by only a few tens of Hertz. The frequency difference corresponds to a slow drift in the relative phase between them. This hence causes the two beams to interfere once destructively and once constructively yielding the respective intensity levels $I_{v;\min}$ and $I_{v;\max}$.

The visibility is a measure for the overlap of the beams. It is given by

$$\eta_{vis} = \frac{I_{v;\max} - I_{v;\min}}{I_{v;\max} + I_{v;\min}} \quad (7.11)$$

and ranges between 0% and 100%. The recorded data is displayed in Figure 10.21.

The voltage level was measured with an oscilloscope and corresponds to the optical intensity at the photodiode. Only one arm of the heterodyne detection was used for this measurement. Since using the difference of the two arms, as it is regularly done in heterodyning, would not permit to measure the absolute value of the interference signal. For the present setup we were able to achieve a mode matching quality corresponding to a visibility of 82% ($\eta_{vis} = 0.82$). The underlying intensity levels are indicated by the two red lines in Figure 10.21. The baseline, which needs to be subtracted from every value is given by the orange line at around 3mV.

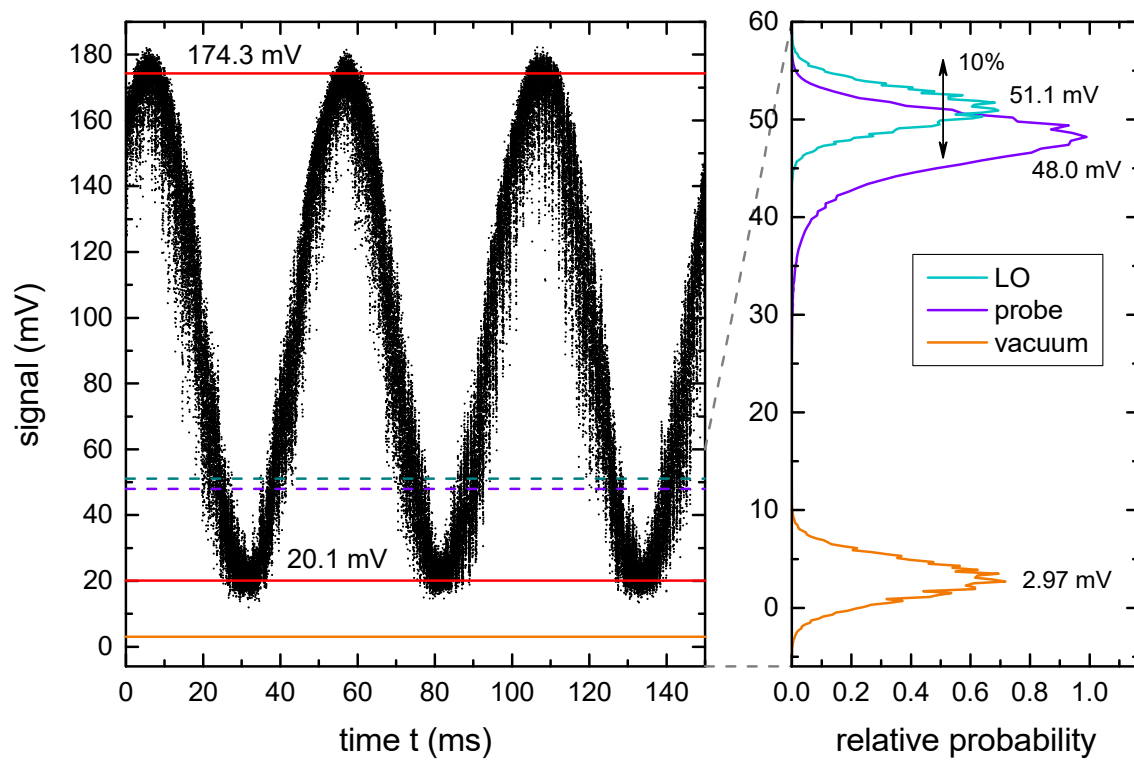


Figure 10.21: Visibility measurement of the heterodyne detection. On the left side the recorded data is displayed. The power levels of the local oscillator (cyan), the probe beam (purple), the base value (orange) as well as the two values for constructive and destructive interference (red) are indicated by vertical lines. The right side shows the histogram of the power level distribution of the individual beams.

10.7. Coupled Electronic Oscillators

The coupling of light and matter was studied throughout this thesis. As both constituents of this system can also be seen as simple oscillators, similar effects can be demonstrated by coupling two electric oscillators. As depicted in Figure 10.22, the two oscillators consist of an inductance and a capacity each. The coupling is achieved by bringing the inductances close to each other or even inserting one of the coils into the other.

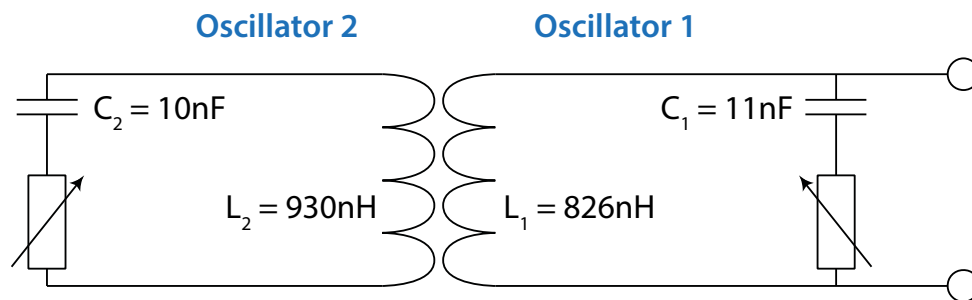


Figure 10.22: Schematics of the coupled electric oscillators. Each oscillatory circuit comprises an inductance L and a capacitance C . The coupling is achieved by spatially overlapping the field of the inductances.

A picture of a realization of this very simple system is found in Figure 10.23. The system is connected to the Rohde und Schwarz network analyzer ZVR 9kHz-4GHz. This device is responsible for exciting the system as well as probing the received oscillatory behavior.

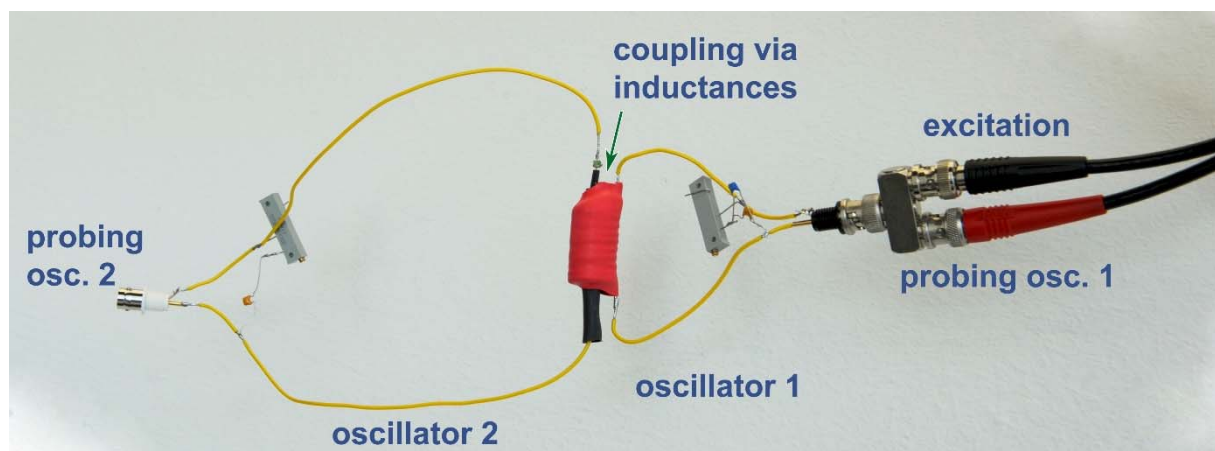


Figure 10.23: Picture of the coupled electric oscillators. Both oscillatory circuits possess a BNC connector through which they are excited and probed. The inductances consist of a small coil which is isolated on the outside. This ensures that only the field of the inductances can couple and no electric contact is established, when the coils are close to each other.

As a first test both oscillators are connected separately and their respective spectral response is measured. The result is recorded with the network analyzer and is depicted in Figure 10.24. A Lorentz profile can be fitted to the two oscillators yielding resonance frequencies of 1.67 MHz and 1.65 MHz for oscillator 1 and oscillator 2, respectively.

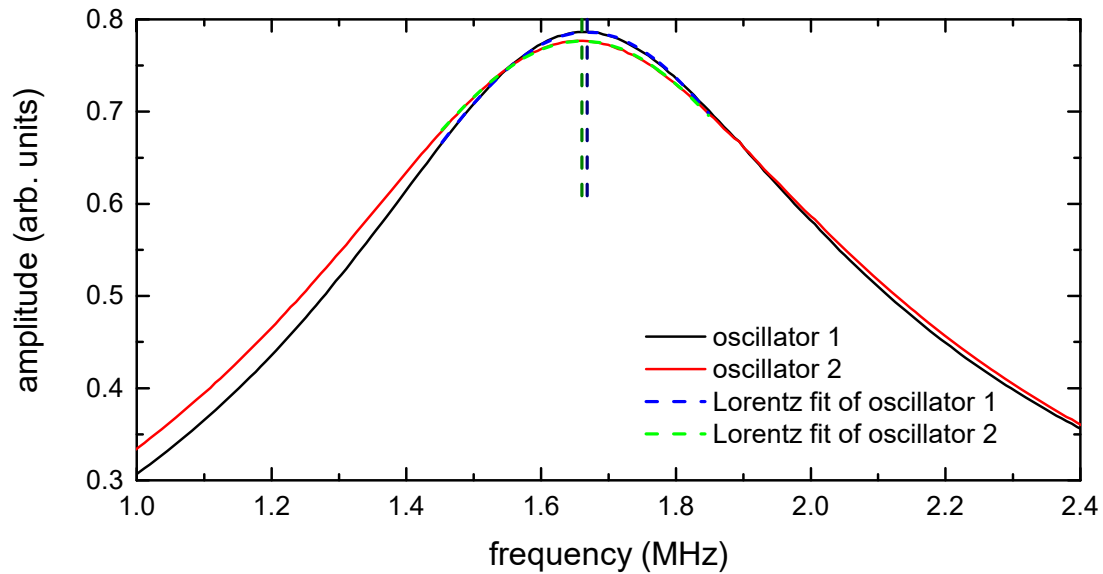


Figure 10.24: Resonance of uncoupled oscillators. The frequency is scanned and the received amplitude is measured via a network analyzer.

As a next step the two resonators are coupled. In that case oscillator 1 is used to excite and probe the system. The coupling is achieved by moving the inductive coil of oscillator 2 into the one of oscillator 1. By this means it is possible to achieve a variable coupling strength. Four different settings have been examined and are depicted in Figure 10.25.

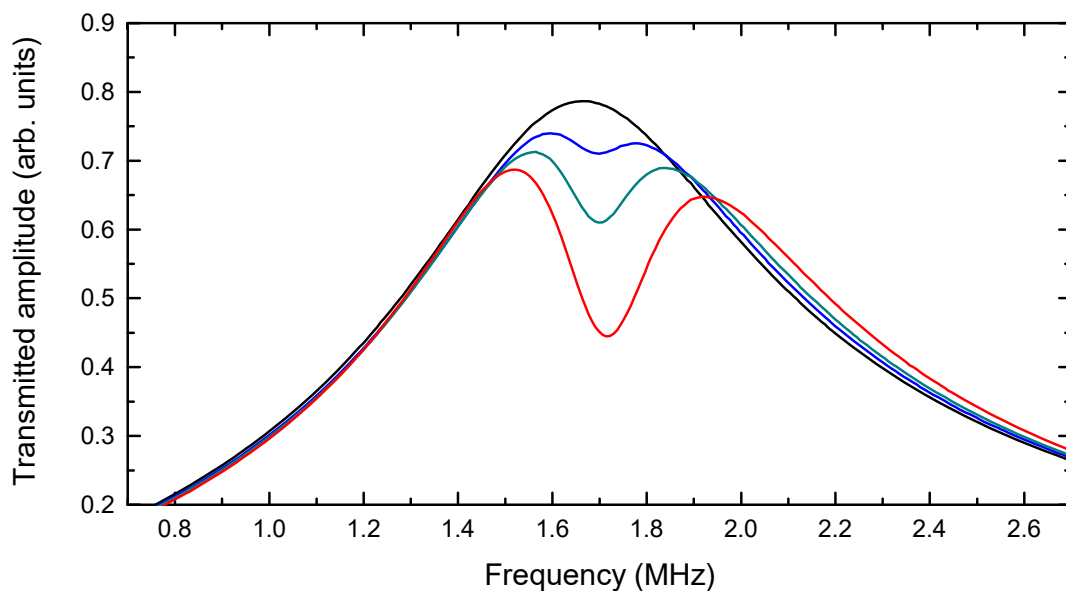


Figure 10.25: Coupled electric oscillators. The coupling constant is varied by changing the spatial overlap of the two inductivities.

In case of the black curve, inductance 2 is far away from inductance 1 resulting in a negligible coupling. On the other end does the red curve depict the case in which both resonators are

ideally coupled. In that case, a clear normal-mode splitting becomes visible, which is comparable to the splitting visible in case of the previously shown atom-cavity system.

Network analyzers also permit to carry out a phase sensitive measurement and hence permit to detect the phase shift from the received compared to the output frequency. The result is plotted in Figure 10.26. Here the amplitude and phase information are depicted. The behavior of the curves resembles the one of the heterodyne measurement. In this case the coupling, however, is weaker and hence the separation of the normal modes is not as pronounced. Due to this a clear antiresonance cannot be observed. The basic shift in the phase of 180 degrees as one scans across a coupled system, yet, remains the same.

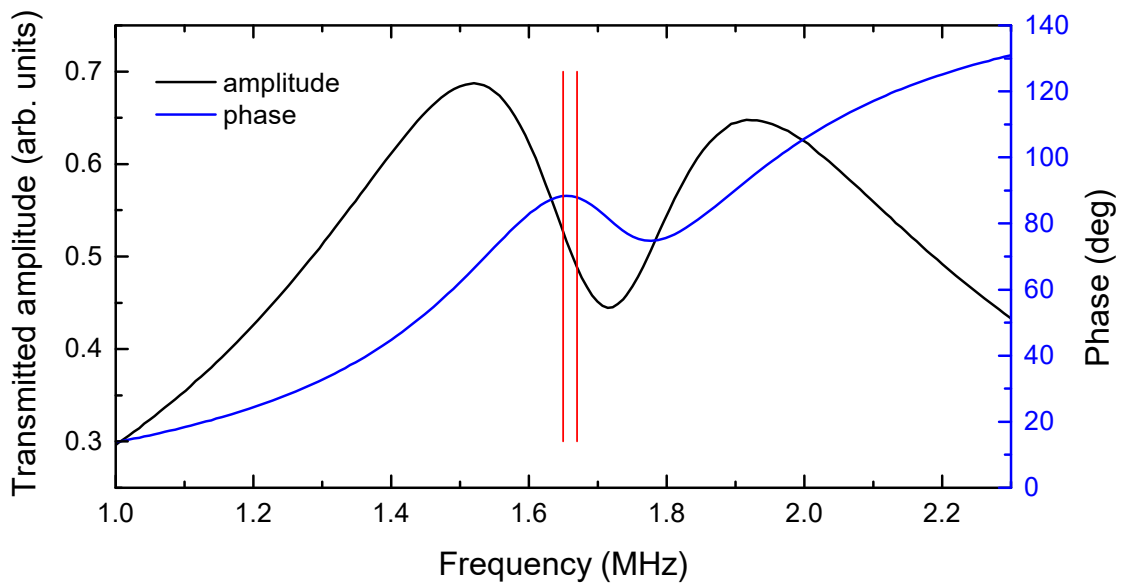
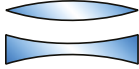
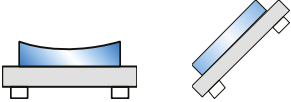
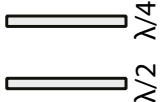
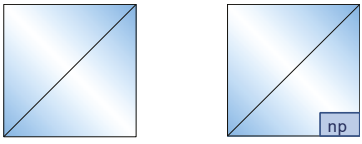






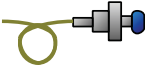


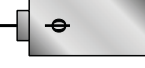


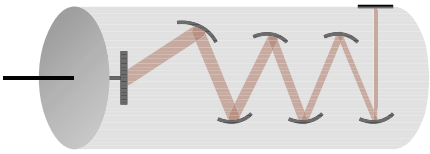
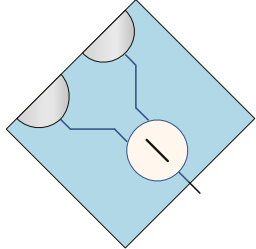

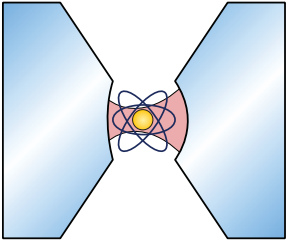
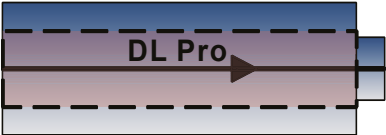
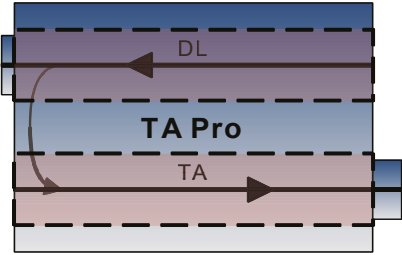
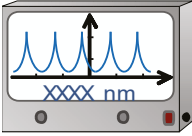
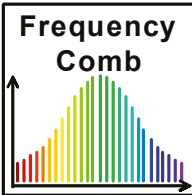


Figure 10.26: Amplitude and phase of coupled electric oscillators. The individual resonance frequencies of the two oscillators are marked by the two vertical red lines.

10.8. Symbols Used in Drawings

Throughout this thesis symbols have been used for a variety optical elements. In the below table an overview of their representation is given.

	Concave and convex lens
	Concave and planar mirror
	Lambda-quarter and lambda-half waveplate
	Polarizing and non-polarizing beam cubes/splitters (PBS/ NPBS)
	Polarizer
	Interference filter (band pass filter)
	Neutral density filter
	Neutral density filter wheel
	Pinhole
	Beam blocker
	Fiber coupler with attached lens and fiber
	Acousto-optic modulator (AOM)
	Electro-optic amplitude modulator (EOAM)
	Electro-optic phase modulator EOPM
	(Positive intrinsic negative) Photodiode (PIN PD)
	Single photon counting module (SPCM)
	Photomultiplier tube (PM)

	<p>Balanced photodiode (including balancing and difference amplifier)</p>
	<p>Rubidium vapor cell</p>
	<p>Atom-cavity system</p>
	<p>Diode laser (DL)</p>
	<p>Diode laser with tapered amplifier (TA)</p>
	<p>Wavemeter</p>
	<p>Frequency comb</p>

11. References

- [1] M. Faraday, “VIII. Experimental researches in electricity. — Thirteenth series,” *Philos. Trans. R. Soc. London*, vol. 128, pp. 125–168, 1838.
- [2] L. Boltzmann, “Über die Beziehung zwischen dem Zweiten Hauptsatze der mechanischen Wärmetheorie und der Wahrscheinlichkeitsrechnung respektive den Sätzen über das Wärmegleichgewicht,” *Sitzungsber. Kais. Akad. Wiss. Wien Math. Naturwiss.*, vol. 2, no. 76, pp. 373–435, 1877.
- [3] L. Boltzmann, “Weitere Studien über das Wärmegleichgewicht unter Gasmolekülen,” *Sitzungsber. Kais. Akad. Wiss. Wien Math. Naturwiss.*, vol. 66, pp. 275–370, 1872.
- [4] H. Hertz, “Über einen Einfluss des ultravioletten Lichtes auf die elektrische Entladung,” *Ann. Phys.*, vol. 267, no. 8, pp. 983–1000, 1887.
- [5] M. Planck, “Über das Gesetz der Energieverteilung im Normalspektrum,” *Annalen der Physik Physik*, vol. 4, pp. 553–563, 1901.
- [6] A. Einstein, “Über einen die Erzeugung und Verwandlung des Lichtes betreffenden heuristischen Gesichtspunkt,” *Annalen der Physik*, vol. 17, no. 6, pp. 132–148, 1905.
- [7] W. Heisenberg, “Über quantentheoretische Umdeutung kinematischer und mechanischer Beziehungen,” *Zeitschrift für Phys.*, vol. 33, no. 1, pp. 879–893, 1925.
- [8] M. Born, W. Heisenberg, and P. Jordan, “Zur Quantenmechanik. II.,” *Zeitschrift für Phys.*, vol. 35, no. 8–9, pp. 557–615, 1926.
- [9] M. Born and P. Jordan, “Zur Quantenmechanik,” *Zeitschrift für Phys.*, vol. 34, no. 1, pp. 858–888, 1925.
- [10] E. T. Jaynes and F. W. Cummings, “Comparison of quantum and semiclassical radiation theories with application to the beam maser,” *Proc. IEEE*, vol. 51, no. 1, 1963.
- [11] G. Rempe, H. Walther, and N. Klein, “Observation of quantum collapse and revival in a one-atom maser,” *Phys. Rev. Lett.*, vol. 58, no. 4, pp. 353–356, 1987.
- [12] M. Brune, F. Schmidt-Kaler, A. Maali, J. Dreyer, E. Hagley, J.-M. Raimond, and S. Haroche, “Quantum Rabi Oscillation: A Direct Test of Field Quantization in a Cavity,” *Phys. Rev. Lett.*, vol. 76, no. 11, pp. 1800–1803, 1996.
- [13] R. J. Thompson, G. Rempe, and H. J. Kimble, “Observation of normal-mode splitting for an atom in an optical cavity,” *Phys. Rev. Lett.*, vol. 68, no. 8, pp. 1132–1135, 1992.
- [14] A. Boca, R. Miller, K. Birnbaum, A. Boozer, J. McKeever, and H. J. Kimble, “Observation of the Vacuum Rabi Spectrum for One Trapped Atom,” *Phys. Rev. Lett.*, vol. 93, no. 23, p. 233603, Dec. 2004.

References

- [15] P. Maunz, T. Puppe, I. Schuster, N. Syassen, P. W. H. Pinkse, and G. Rempe, “Normal-Mode Spectroscopy of a Single-Bound-Atom–Cavity System,” *Phys. Rev. Lett.*, vol. 94, no. 3, p. 033002, Jan. 2005.
- [16] M. Khudaverdyan, W. Alt, T. Kampschulte, S. Reick, A. Thobe, A. Widera, and D. Meschede, “Quantum jumps and spin dynamics of interacting atoms in a strongly coupled atom-cavity system,” *Phys. Rev. Lett.*, vol. 103, no. 12, pp. 1–4, 2009.
- [17] R. Gehr, J. Volz, G. Dubois, T. Steinmetz, Y. Colombe, B. L. Lev, R. Long, J. Estève, and J. Reichel, “Cavity-based single atom preparation and high-fidelity hyperfine state readout,” *Phys. Rev. Lett.*, vol. 104, no. 20, pp. 1–4, 2010.
- [18] D. J. Alton, N. P. Stern, T. Aoki, H. Lee, E. Ostby, K. J. Vahala, and H. J. Kimble, “Strong Interactions of Single Atoms and Photons near a Dielectric Boundary,” *Nat. Phys.*, vol. 7, no. 2, p. 8, 2010.
- [19] J. P. Reithmaier, G. Sek, A. Löffler, C. Hofmann, S. Kuhn, S. Reitzenstein, L. V Keldysh, V. D. Kulakovskii, T. L. Reinecke, and A. Forchel, “Strong coupling in a single quantum dot-semiconductor microcavity system,” *Nature*, vol. 432, no. 7014, pp. 197–200, Nov. 2004.
- [20] E. Peter, P. Senellart, D. Martrou, A. Lemaître, J. Hours, J. M. Gérard, and J. Bloch, “Exciton-photon strong-coupling regime for a single quantum dot embedded in a microcavity,” *Phys. Rev. Lett.*, vol. 95, no. 6, pp. 1–4, 2005.
- [21] K. Hennessy, A. Badolato, M. Winger, D. Gerace, M. Atature, S. Gulde, S. Falt, E. L. Hu, and A. Imamoglu, “Quantum nature of a strongly-coupled single quantum dot-cavity system,” vol. 445, no. February, p. 14, 2006.
- [22] A. Laucht, F. Hofbauer, N. Hauke, J. Angele, S. Stobbe, M. Kaniber, G. Böhm, P. Lodahl, M. C. Amann, and J. J. Finley, “Electrical control of spontaneous emission and strong coupling for a single quantum dot,” *New J. Phys.*, vol. 11, 2009.
- [23] T. Yoshie, A. Scherer, J. Hendrickson, G. Khitrova, H. M. Gibbs, G. Rupper, C. Ell, O. B. Shchekin, and D. G. Deppe, “Vacuum Rabi splitting with a single quantum dot in a photonic crystal nanocavity,” *Nature*, vol. 432, no. November, pp. 200–203, 2004.
- [24] A. Wallraff, D. I. Schuster, A. Blais, and L. Frunzio, “Strong coupling of a single photon to a superconducting qubit using circuit quantum electrodynamics,” *Nature*, vol. 431, no. September, p. 162, 2004.
- [25] I. Chiorescu, P. Bertet, K. Semba, Y. Nakamura, C. J. P. M. Harmans, and J. E. Mooij, “Coherent dynamics of a flux qubit coupled to a harmonic oscillator,” *Nature*, vol. 431, no. 7005, pp. 159–162, 2004.
- [26] K. B. Cooper, M. Steffen, R. McDermott, R. W. Simmonds, S. Oh, D. A. Hite, D. P. Pappas, and J. M. Martinis, “Observation of Quantum Oscillations between a Josephson Phase Qubit and a Microscopic Resonator Using Fast Readout,” *Phys. Rev. Lett.*, vol. 93, no. 18, pp. 2–5, 2004.

- [27] F. Deppe, M. Mariani, E. P. Menzel, A. Marx, S. Saito, K. Kakuyanagi, H. Tanaka, T. Meno, K. Semba, H. Takayanagi, E. Solano, and R. Gross, “Two-photon probe of the Jaynes-Cummings model and symmetry breaking in circuit QED,” vol. 4, no. September, p. 8, 2008.
- [28] J. I. Cirac and P. Zoller, “Quantum Computations with Cold Trapped Ions,” *Physical Review Letters*, vol. 74, no. 20. pp. 4091–4094, 1995.
- [29] T. Pellizzari, S. Gardiner, J. I. Cirac, and P. Zoller, “Decoherence, Continuous Observation, and Quantum Computing: A Cavity QED Model,” *Physical Review Letters*, vol. 75, no. 21. pp. 3788–3791, 1995.
- [30] J. I. Cirac, P. Zoller, H. J. Kimble, and H. Mabuchi, “Quantum state transfer and entanglement distribution among distant nodes in a quantum network,” *Phys. Rev. Lett.*, vol. 78, p. 3221, 1997.
- [31] A. S. Parkins, P. Marte, P. Zoller, and H. J. Kimble, “Synthesis of arbitrary quantum states via adiabatic transfer of Zeeman coherence,” *Phys. Rev. Lett.*, vol. 71, no. 19, pp. 3095–3098, 1993.
- [32] W. Neuhauser, M. Hohenstatt, P. E. Toschek, and H. Dehmelt, “Localized visible Ba⁺ mono-ion oscillator,” *Phys. Rev. A*, vol. 22, no. 3, pp. 1137–1140, 1980.
- [33] D. J. Wineland and W. M. Itano, “Spectroscopy of a single Mg⁺ ion,” *Physics Letters A*, vol. 82, no. 2. pp. 75–78, 1981.
- [34] W. D. Phillips, “Laser cooling and trapping of neutral atoms,” *Rev. Mod. Phys.*, vol. 70, no. 3, pp. 721–741, 1998.
- [35] C. N. Cohen-Tannoudji, “Manipulating Atoms with Photons,” *Rev. Mod. Phys.*, vol. 70, no. 3, pp. 707–719, 1998.
- [36] V. S. Letokhov and V. G. Minogin, “Laser radiation pressure on free atoms,” *Physics Reports*, vol. 73, no. 1. pp. 1–65, 1981.
- [37] S. Chu, “The manipulation of neutral particles,” *Rev. Mod. Phys.*, vol. 70, no. 3, pp. 685–706, 1998.
- [38] Z. Hu and H. J. Kimble, “Observation of a single atom in a magneto-optical trap,” *Opt. Lett.*, vol. 19, no. 22, p. 1888, 1994.
- [39] F. Ruschewitz, D. Bettermann, Peng J. L., and W. Ertmer, “Statistical investigations on single trapped neutral atoms,” *Eur. Lett.*, vol. 34, no. 9, pp. 651–656, 1996.
- [40] D. Haubrich, H. Schadwinkel, F. Strauch, B. Ueberholz, R. Wynands, and D. Meschede, “Observation of individual neutral atoms in magnetic and magneto-optical traps,” *Eur. Lett.*, vol. 34, no. 9, pp. 663–668, 1996.

References

- [41] D. Frese, B. Ueberholz, S. Kuhr, W. Alt, D. Schrader, V. Gomer, and D. Meschede, “Single atoms in an optical dipole trap: towards a deterministic source of cold atoms,” *Phys. Rev. Lett.*, vol. 85, no. 18, pp. 3777–3780, 2000.
- [42] N. Schlosser, G. Reymond, I. Protsenko, and P. Grangier, “Sub-poissonian loading of single atoms in a microscopic dipole trap,” *Nature*, vol. 411, no. 6841, pp. 1024–1027, 2001.
- [43] H. Mabuchi, Q. A. Turchette, M. S. Chapman, and H. J. Kimble, “Real-time detection of individual atoms falling through a high-finesse optical cavity,” *Opt. Lett.*, vol. 21, no. 17, pp. 1393–1395, 1996.
- [44] J. A. Sauer, K. M. Fortier, M. S. Chang, C. D. Hamley, and M. S. Chapman, “Cavity QED with optically transported atoms,” *Phys. Rev. A - At. Mol. Opt. Phys.*, vol. 69, no. 5 A, pp. 051804-1, 2004.
- [45] P. Münstermann, T. Fischer, P. W. H. Pinkse, and G. Rempe, “Single slow atoms from an atomic fountain observed in a high-finesse optical cavity,” *Opt. Commun.*, vol. 159, no. 1–3, pp. 63–67, Jan. 1999.
- [46] G. Rempe, “One atom in an optical cavity: Spatial resolution beyond the standard diffraction limit,” *Appl. Phys. B Laser Opt.*, vol. 60, no. 2–3, pp. 233–237, 1995.
- [47] C. J. Hood, M. S. Chapman, T. W. Lynn, and H. J. Kimble, “Real-Time Cavity QED with Single Atoms,” *Phys. Rev. Lett.*, vol. 80, no. 19, pp. 4157–4160, May 1998.
- [48] P. Münstermann, T. Fischer, P. Maunz, P. W. H. Pinkse, and G. Rempe, “Dynamics of Single-Atom Motion Observed in a High-Finesse Cavity,” *Phys. Rev. Lett.*, vol. 82, no. 19, pp. 3791–3794, May 1999.
- [49] P. W. H. Pinkse, T. Fischer, P. Maunz, and G. Rempe, “Trapping an atom with single photons,” *Nature*, vol. 404, no. 6776, pp. 365–368, Mar. 2000.
- [50] C. J. Hood, “The Atom-Cavity Microscope: Single Atoms Bound in Orbit by Single Photons,” *Science*, vol. 287, no. 5457, pp. 1447–1453, Feb. 2000.
- [51] T. Fischer, P. Maunz, P. W. H. Pinkse, T. Puppe, and G. Rempe, “Feedback on the Motion of a Single Atom in an Optical Cavity,” *Phys. Rev. Lett.*, vol. 88, no. 16, p. 163002, Apr. 2002.
- [52] T. Fischer, “Controlling the motion of an atom in an optical cavity,” Technische Universität München, 2002.
- [53] P. Horak, H. Ritsch, T. Fischer, P. Maunz, T. Puppe, P. W. H. Pinkse, and G. Rempe, “Optical kaleidoscope using a single atom,” *Phys. Rev. Lett.*, vol. 88, no. 4, p. 043601, 2002.
- [54] T. Puppe, P. Maunz, T. Fischer, P. W. H. Pinkse, and G. Rempe, “Single-Atom Trajectories in Higher-Order Transverse Modes of a High-Finesse Optical Cavity,” *Phys. Scr.*, vol. T112, no. 1, p. 7, 2004.

- [55] P. Maunz, T. Puppe, T. Fischer, P. W. H. Pinkse, and G. Rempe, “Emission pattern of an atomic dipole in a high-finesse optical cavity.,” *Opt. Lett.*, vol. 28, no. 1, pp. 46–8, Jan. 2003.
- [56] A. Kubanek, M. Koch, C. Sames, A. Ourjoumtsev, P. W. H. Pinkse, K. Murr, and G. Rempe, “Photon-by-photon feedback control of a single-atom trajectory.,” *Nature*, vol. 462, no. 7275, pp. 898–901, Dec. 2009.
- [57] A. Kubanek, M. Koch, C. Sames, A. Ourjoumtsev, T. Wilk, P. W. H. Pinkse, and G. Rempe, “Feedback control of a single atom in an optical cavity,” *Appl. Phys. B*, vol. 102, no. 3, pp. 433–442, Feb. 2011.
- [58] M. Koch, C. Sames, A. Kubanek, M. Apel, M. Balbach, A. Ourjoumtsev, P. W. H. Pinkse, and G. Rempe, “Feedback Cooling of a Single Neutral Atom,” *Phys. Rev. Lett.*, vol. 105, no. 17, p. 173003, Oct. 2010.
- [59] C. Sames, M. Balbach, M. Koch, A. Kubanek, P. W. H. Pinkse, and G. Rempe, “FPGA-based Feedback Control of a Single Atom Trajectory,” in *Virtuelle Instrumente in der Praxis 2010*, Erste Aufl., Vde-Verlag, 2010, p. 578.
- [60] C. Sames, C. Hamsen, H. Chibani, P. A. Altin, T. Wilk, and G. Rempe, “Continuous parametric feedback cooling of a single atom in an optical cavity,” *Phys. Rev. A*, vol. 97, no. 5, p. 53404, 2018.
- [61] J. V. L. Hogan, “The Heterodyne Receiver,” *Electr. J.*, vol. 18, p. 116, 1921.
- [62] R. A. Fessenden, “Wireless Signaling,” US706740 A, 1902.
- [63] R. A. Fessenden, “Electric signaling apparatus,” US 1050441 A, 1913.
- [64] R. A. Fessenden, “Method of signaling,” US1050728 A, 1913.
- [65] Q. A. Turchette, C. J. Hood, W. Lange, H. Mabuchi, and H. J. Kimble, “Measurement of conditional phase shifts for quantum logic,” *Phys. Rev. Lett.*, vol. 75, no. 25, pp. 4710–4713, 1995.
- [66] I. Fushman, D. Englund, A. Faraon, N. Stoltz, P. Petroff, and J. Vucković, “Controlled phase shifts with a single quantum dot.,” *Science*, vol. 320, no. 5877, pp. 769–772, May 2008.
- [67] H. J. Carmichael, “Photon antibunching and squeezing for a single atom in a resonant cavity,” *Phys. Rev. Lett.*, vol. 55, no. 25, pp. 2790–2793, 1985.
- [68] M. G. Raizen, L. A. Orozco, M. Xiao, T. L. Boyd, and H. J. Kimble, “Squeezed-state generation by the normal modes of a coupled system,” *Phys. Rev. Lett.*, vol. 59, no. 2, pp. 198–201, 1987.
- [69] G. T. Foster, L. A. Orozco, H. M. Castro-Beltran, and H. J. Carmichael, “Quantum state reduction and conditional time evolution of wave-particle correlations in cavity QED.,” *Phys. Rev. Lett.*, vol. 85, no. 15, pp. 3149–52, Oct. 2000.

References

- [70] J. E. Reiner, W. P. Smith, G. T. Foster, L. A. Orozco, H. J. Carmichael, and P. R. Rice, "Time evolution and squeezing of the field amplitude in cavity QED," *J. Opt. Soc. Am. B*, vol. 18, no. 12, pp. 1911–1921, 2001.
- [71] A. Ourjoumtsev, A. Kubanek, M. Koch, C. Sames, P. W. H. Pinkse, G. Rempe, and K. Murr, "Observation of squeezed light from one atom excited with two photons," *Nature*, vol. 474, no. 7353, pp. 623–6, Jun. 2011.
- [72] D. Smithey, M. Beck, M. Raymer, and A. Faridani, "Measurement of the Wigner distribution and the density matrix of a light mode using optical homodyne tomography: Application to squeezed states and the vacuum," *Phys. Rev. Lett.*, vol. 70, no. 9, pp. 1244–1247, 1993.
- [73] K. Vogel and H. Risken, "Determination of quasiprobability distributions in terms of probability distributions for the rotated quadrature phase," *Phys. Rev. A*, vol. 40, no. 5, pp. 2847–2849, 1989.
- [74] M. Armen, "Bifurcations in single atom cavity QED," *PhD Thesis*, vol. 2009, 2009.
- [75] C. Sames, H. Chibani, C. Hamsen, P. A. Altin, T. Wilk, and G. Rempe, "Antiresonance Phase Shift in Strongly Coupled Cavity QED," *Phys. Rev. Lett.*, vol. 112, no. 4, p. 043601, Jan. 2014.
- [76] P. Maunz, T. Puppe, I. Schuster, N. Syassen, P. W. H. Pinkse, and G. Rempe, "Cavity cooling of a single atom," *Nature*, vol. 428, no. 6978, pp. 50–2, Mar. 2004.
- [77] P. Maunz, "Cavity cooling and spectroscopy of a bound atom-cavity system," Technische Universität München, 2004.
- [78] T. Puppe, "Trapping and observing single atoms in the dark," Technische Universität München, 2007.
- [79] A. Fuhrmanek, "Multiphoton transitions in a strongly-coupled atom-cavity system," Technische Universität München, 2008.
- [80] I. Schuster, "Nonlinear spectroscopy of a single-atom-cavity system," Technische Universität München, 2008.
- [81] M. Koch, "Classical and Quantum Dynamics of a Strongly Coupled Atom-Cavity System," Technische Universität München, 2011.
- [82] P. R. Berman, *Cavity Quantum Electrodynamics (Volume 2 in Advances in Atomic, Molecular and Optical Physics: Supplement)*. Academic Press, Inc., New York, 1994.
- [83] M. O. Scully and M. S. Zubairy, *Quantum optics*. Cambridge University Press, 1997.
- [84] S. M. Dutra, "Cavity quantum electrodynamics: the strange theory of light in a box," 2005.

- [85] R. P. Feynman, *QED: The Strange Theory of Light and Matter*, no. pg. 96. Princeton University Press, 1985.
- [86] H. J. Carmichael, *An open systems approach to quantum optics: lectures presented at the Université libre de Bruxelles, October 28 to November 4, 1991*. Springer, 1993.
- [87] D. F. Walls and G. J. Milburn, *Quantum optics*, 2nd ed. Springer-Verlag, 2008.
- [88] C. W. Gardiner and P. Zoller, *Quantum noise: a handbook of Markovian and non-Markovian quantum stochastic methods with applications to quantum optics*. 2004.
- [89] M. Tavis and F. W. Cummings, “Approximate solutions for an N-molecule-radiation-field Hamiltonian,” *Phys. Rev.*, vol. 99, no. 1953, pp. 692–695, 1969.
- [90] M. Tavis, “A Study of an N Molecule-Quantized Radiation Field-Hamiltonian,” *arXiv*, vol. quant-ph, no. 1206.0078v1, p. 104, 2012.
- [91] R. Graham, *Quantum Statistics in Optics and Solid-State Physics*, vol. 66. Springer-Verlag Berlin, Heidelberg, New York, 1973.
- [92] S. A. Gardiner, “Quantum Measurement, Quantum Chaos, and Bose-Einstein Condensates,” Leopold-Franzens-Universität Innsbruck, 2000.
- [93] H. J. Carmichael, R. J. Brecha, and P. R. Rice, “Quantum interference and collapse of the wavefunction in cavity QED,” *Opt. Commun.*, vol. 82, no. 1–2, pp. 73–79, Apr. 1991.
- [94] S. Tan, “A quantum optics toolbox for Matlab 5,” *J. Opt. B Quantum Semiclass. Opt*, 1999.
- [95] G. Hechenblaikner, M. Gangl, P. Horak, and H. Ritsch, “Cooling an atom in a weakly driven high-Q cavity,” *Phys. Rev. A*, vol. 58, no. 4, pp. 3030–3042, Oct. 1998.
- [96] H. J. Metcalf and P. Van der Straten, *Laser cooling and trapping*, 1st ed. Springer-Verlag New York, 1999.
- [97] W. Demtroeder, *Laserspektroskopie: Grundlagen und Techniken*, 4th editio. Springer, 2000.
- [98] S. Dürr, “Skript zur Vorlesung: Ultrakalte Quantengase I und II,” 2010.
- [99] P. Kok and B. W. Lovett, *Optical Quantum Information Processing*. Cambridge University Press, 2010.
- [100] A. Ourjoumtsev, “Homodyne spectroscopy of a coupled cavity-atom system,” Munich, 2010.
- [101] A. Kubanek, “Two-photon gateway and feedback control of a single atom in a cavity,” Technische Universität München, 2010.

References

- [102] P. Münstermann, “Dynamik einzelner Atome in einem optischen Resonator höchster Finesse,” Universität Konstanz, 1999.
- [103] D. R. Lide, *CRC handbook of chemistry and physics*, 93rd ed., vol. 75, no. 2005. 2012.
- [104] D. A. Steck, “Rubidium 85 D Line Data,” 2012.
- [105] T. Rieger and T. Volz, “Doppler-Free Saturation Spectroscopy,” Max-Planck-Institut für Quantenoptik, 2004.
- [106] C. J. Hood, H. J. Kimble, and J. Ye, “Characterization of high-finesse mirrors: Loss, phase shifts, and mode structure in an optical cavity,” *Phys. Rev. A*, vol. 64, no. 3, pp. 1–7, Aug. 2001.
- [107] B. E. A. Saleh, M. C. Teich, and B. E. Saleh, *Fundamentals of photonics*, vol. 22. Wiley Online Library, 1991.
- [108] J. Almer, “Aufbau und Charakterisierung eines längenveränderbaren optischen Hoch-Finesse-Resonators,” Technische Universität München, 2006.
- [109] A. E. Siegman, *Lasers*. Univ Science Books, 1986.
- [110] S. Nußmann, K. Murr, M. Hijlkema, B. Weber, A. Kuhn, and G. Rempe, “Vacuum-stimulated cooling of single atoms in three dimensions,” *Nat. Phys.*, vol. 1, no. 2, pp. 122–125, Oct. 2005.
- [111] A. C. Eckl, “High-Resolution Imaging of a Single Atom Strongly Coupled to a Cavity,” Ludwig-Maximilians Universität, 2013.
- [112] M. W. Fleming and A. Mooradian, “Spectral Characteristics of External-Cavity,” *Quantum Electron. IEEE J. ...IEEE J.*, vol. 17, no. 1, pp. 44–59, 1981.
- [113] C. J. Hawthorn, K. P. Weber, and R. E. Scholten, “Littrow configuration tunable external cavity diode laser with fixed direction output beam,” *Rev. Sci. Instrum.*, vol. 72, no. 12, p. 4477, 2001.
- [114] K. Liu and M. G. Littman, “Novel geometry for single-mode scanning of tunable lasers,” *Opt. Lett.*, vol. 6, no. 3, pp. 117–118, 1981.
- [115] R. W. P. Drever, J. L. Hall, F. V. Kowalski, J. Hough, G. M. Ford, a. J. Munley, and H. Ward, “Laser phase and frequency stabilization using an optical resonator,” *Appl. Phys. B Photophysics Laser Chem.*, vol. 31, no. 2, pp. 97–105, Jun. 1983.
- [116] S. Chu, J. E. Bjorkholm, A. Ashkin, and A. Cable, “Experimental observation of optically trapped atoms,” *Phys. Rev. Lett.*, vol. 57, 1986.
- [117] J. D. Miller, R. A. Cline, and D. J. Heinzen, “Far-off-resonance optical trapping of atoms,” *Phys. Rev. A*, vol. 47, no. 6, p. R4567, 1993.

- [118] J. Ye, D. W. Vernooy, and H. J. Kimble, “Trapping of single atoms in cavity QED,” *Phys. Rev. Lett.*, vol. 83, p. 4987, 1999.
- [119] R. Holzwarth, T. Udem, T. W. Hänsch, J. Knight, W. J. Wadsworth, and P. S. Russell, “Optical frequency synthesizer for precision spectroscopy,” *Phys. Rev. Lett.*, vol. 85, no. 11, pp. 2264–7, Sep. 2000.
- [120] J. Bochmann, “Coherent Dynamics and State Detection of Single Atoms in a Cavity,” Technische Universität München, 2010.
- [121] J. Bochmann, M. Mücke, G. Langfahl-Klabes, C. Erbel, B. Weber, H. Specht, D. Moehring, and G. Rempe, “Fast Excitation and Photon Emission of a Single-Atom-Cavity System,” *Phys. Rev. Lett.*, vol. 101, no. 22, p. 223601, Nov. 2008.
- [122] B. Bernhardt, T. W. Hänsch, and R. Holzwarth, “Implementation and characterization of a stable optical frequency distribution system,” *Opt. Express*, vol. 17, no. 19, pp. 904–909, 2009.
- [123] S. Chu, L. Hollberg, J. E. Bjorkholm, A. Cable, and A. Ashkin, “Three-dimensional viscous confinement and cooling of atoms by resonance radiation pressure,” *Phys. Rev. Lett.*, vol. 55, pp. 48–51, 1985.
- [124] W. D. Phillips, a. L. Migdall, and H. J. Metcalf, “Laser-cooling and electromagnetic trapping of neutral atoms,” *AIP Conf. Proc.*, vol. 146, no. 1986, pp. 362–365, 1986.
- [125] W. D. Phillips and H. J. Metcalf, “Cooling and trapping atoms,” *Sci. Am.*, vol. 256, no. March, p. 36, 1987.
- [126] C. N. Cohen-Tannoudji and W. D. Phillips, “New Mechanisms for Laser Cooling,” *Phys. Today*, vol. 43, no. 10, p. 33, 1990.
- [127] S. Chu, “Laser manipulation of atoms and particles,” *Science*, vol. 253, pp. 861–866, 1991.
- [128] J. Dalibard and C. N. Cohen-Tannoudji, “Laser cooling below the Doppler limit by polarization gradients: simple theoretical models,” *J. Opt. Soc. Am. B*, vol. 6, no. 11, p. 2023, 1989.
- [129] D. S. Weiss, E. Riis, Y. Shevy, P. J. Ungar, and S. Chu, “Optical molasses and multilevel atoms: experiment,” *J. Opt. Soc. Am. B*, vol. 6, no. 11, p. 2072, 1989.
- [130] V. S. Letokhov, “Cooling and capture of atoms and molecules by a resonant light field,” *Sov. J. ...*, vol. 54, no. 1949, pp. 698–705, 1977.
- [131] B. Hagemann, “Vibration isolation and spectroscopy of a high-finesse optical resonator,” Technische Universität München, 2008.
- [132] M. Apel, “Aufbau eines Cavity-QED-Experiments der nächsten Generation,” Ludwig-Maximilians-Universität München, 2009.

References

- [133] T. Savard, K. O'Hara, and J. Thomas, "Laser-noise-induced heating in far-off resonance optical traps," *Phys. Rev. A*, vol. 56, no. 2, pp. R1095–R1098, Aug. 1997.
- [134] M. Balbach, "Characterization of Quantum States via Photon-Correlation and Field Measurements," Technische Universität München, 2010.
- [135] M. Clive, *The Design Warrior's Guide to FPGAs*, 1st ed. Elsevier Inc., 2004.
- [136] Xilinx Inc., *Xilinx UG190 Virtex-5 FPGA User Guide*, UG190 (v5., vol. 190. Xilinx Inc., 2012.
- [137] G. Kell, A. Bülter, M. Wahl, and R. Erdmann, " τ -SPAD: a new red sensitive single-photon counting module," *Proc. SPIE*, vol. 8033, no. Advanced Photon Counting Techniques V, p. 803303, May 2011.
- [138] Xilinx Inc., *Virtex-5 FPGA Data Sheet : DC and Switching Characteristics*, DS202 (v5., vol. 202. Xilinx Inc., 2010.
- [139] N. Strauß, I. Ernsting, S. Schiller, A. Wicht, P. Huke, and R.-H. Rinkleff, "A simple scheme for precise relative frequency stabilization of lasers," *Appl. Phys. B*, vol. 88, no. 1, pp. 21–28, May 2007.
- [140] B. Kedem, "On frequency detection by zero-crossings," *Signal Processing*, vol. 10, pp. 303–306, 1986.
- [141] M. Dechambre and J. Lavergnat, "Frequency determination of a noisy signal by zero-crossings counting," *Signal Processing*, vol. 8, pp. 93–105, 1985.
- [142] R. Grimm, M. Weidemüller, and Y. B. Ovchinnikov, "Optical dipole traps for neutral atoms," *Adv. At. Mol. Opt. Phys.*, vol. 42, pp. 95–170, Feb. 2000.
- [143] W. B. Case, "The pumping of a swing from the standing position," *Am. J. Phys.*, vol. 64, no. 3, p. 215, 1996.
- [144] E. Vetsch, D. Reitz, G. Sagué, R. Schmidt, S. T. Dawkins, and A. Rauschenbeutel, "Optical interface created by laser-cooled atoms trapped in the evanescent field surrounding an optical nanofiber," *Phys. Rev. Lett.*, vol. 104, no. 20, pp. 1–4, 2010.
- [145] B. Dayan, A. S. Parkins, T. Aoki, E. P. Ostby, K. J. Vahala, and H. J. Kimble, "A photon turnstile dynamically regulated by one atom," *Science*, vol. 319, no. February, pp. 1062–1065, 2008.
- [146] L. W. Couch, *Digital and Analog Communication Systems*, Fifth edit. Prentice Hall, Inc, 1996.
- [147] R. W. Boyd, *Nonlinear optics*, 3rd revise. Academic Press, Inc., New York, 2008.
- [148] R. Paschotta, "Optical Heterodyne Detection," *Own webpage*. [Online]. Available: http://www.rp-photonics.com/optical_heterodyne_detection.html. [Accessed: 01-Aug-2015].

- [149] D. F. Walls, "Squeezed states of light," *Nature*, vol. 306, p. 141, 1983.
- [150] H. P. Yuen and V. W. S. Chan, "Noise in homodyne and heterodyne detection," *Opt. Lett.*, vol. 8, no. 3, pp. 177–179, 1983.
- [151] J. F. Holmes and B. J. Rask, "Optimum optical local-oscillator power levels for coherent detection with photodiodes," *Appl. Opt.*, vol. 34, no. 6, pp. 927–933, 1995.
- [152] M. Koch, C. Sames, M. Balbach, H. Chibani, A. Kubanek, K. Murr, T. Wilk, and G. Rempe, "Three-Photon Correlations in a Strongly Driven Atom-Cavity System," *Phys. Rev. Lett.*, vol. 107, no. 2, pp. 2–5, Jul. 2011.
- [153] L. S. Bishop, J. M. Chow, J. Koch, a. a. Houck, M. H. Devoret, E. Thuneberg, S. M. Girvin, and R. J. Schoelkopf, "Nonlinear response of the vacuum Rabi resonance," *Nat. Phys.*, vol. 5, no. 2, p. 6, 2008.
- [154] J. Claudon, a. Zazunov, F. W. J. Hekking, and O. Buisson, "Rabi-like oscillations of an anharmonic oscillator: Classical versus quantum interpretation," *Phys. Rev. B - Condens. Matter Mater. Phys.*, vol. 78, no. 18, pp. 1–8, 2008.
- [155] M. Raizen, R. Thompson, and R. Brecha, "Normal-mode splitting and linewidth averaging for two-state atoms in an optical cavity," *Phys. Rev. Lett.*, vol. 63, no. 3, pp. 240–243, 1989.
- [156] S. Zippilli, J. Asboth, G. Morigi, and H. Ritsch, "Forces and spatial ordering of driven atoms in a resonator in the regime of fluorescence suppression," *Appl. Phys. B*, vol. 79, no. 8, pp. 969–978, Nov. 2004.
- [157] P. M. Alsing, D. A. Cardimona, and H. J. Carmichael, "Suppression of fluorescence in a lossless cavity," *Phys. Rev. A*, vol. 45, no. 3, pp. 1793–1803, 1992.
- [158] J. J. Childs, K. An, M. S. Otteson, R. R. Dasari, and M. S. Feld, "Normal Mode Line Shapes for Atoms in Standing-Wave Optical Resonators.," *Phys. Rev. Lett.*, vol. 77, no. 14, pp. 2901–2904, Sep. 1996.
- [159] Y. S. Joe, A. M. Satanin, and C. S. Kim, "Classical analogy of Fano resonances," *Phys. Scr.*, vol. 74, no. 2, pp. 259–266, Aug. 2006.
- [160] P. Sjövall and T. Abrahamsson, "Substructure system identification from coupled system test data," *Mech. Syst. Signal Process.*, vol. 22, no. 1, pp. 15–33, Jan. 2008.
- [161] F. Wahl, G. Schmidt, and L. Forrai, "On the Significance of Antiresonance Frequencies in Experimental Structural Analysis," *J. Sound Vib.*, vol. 219, no. 3, pp. 379–394, Jan. 1999.
- [162] H. Frahm, "Device for damping vibrations of bodies," US19090525455, 1911.
- [163] J. Ormondroyd and J. P. Den Hartog, "Theory of the dynamic vibration absorber," *Trans. Am. Soc. Mech. Eng.*, vol. 50, pp. 9–22, 1928.

References

- [164] J. E. Brock, “A note on the damped vibration absorber,” *J. Appl. Mech.*, vol. 68, p. A-284, 1946.
- [165] J. P. Den Hartog, *Mechanical Vibrations*. Courier Corporation, 1985.
- [166] R. Rana, “Response control of structures by TMD and their generalizations,” *Eleventh World Conference on Earthquake Engineering*. 1996.
- [167] J. J. Connor, *Introduction to Structural Motion Control*. Upper Saddle River, N.J.: Prentice Hall Pearson Education, 2003.
- [168] H. Mabuchi, J. Ye, and H. J. Kimble, “Full observation of single-atom dynamics in cavity QED,” *Appl. Phys. B*, vol. 68, pp. 1095–1108, 1999.
- [169] P. R. Rice and R. J. Brecha, “Cavity induced transparency,” *Opt. Commun.*, vol. 126, no. May, pp. 230–235, 1996.
- [170] S. A. Aljunid, M. K. Tey, B. Chng, T. Liew, G. Maslennikov, V. Scarani, and C. Kurtsiefer, “Phase Shift of a Weak Coherent Beam Induced by a Single Atom,” *Phys. Rev. Lett.*, vol. 103, no. 15, p. 153601, Oct. 2009.
- [171] M. Pototschnig, Y. Chassagneux, J. Hwang, G. Zumofen, A. Renn, and V. Sandoghdar, “Controlling the Phase of a Light Beam with a Single Molecule,” *Phys. Rev. Lett.*, vol. 107, no. 6, p. 063001, Aug. 2011.
- [172] A. Jechow, B. G. Norton, S. Händel, V. Blüms, E. W. Streed, and D. Kielpinski, “Controllable optical phase shift over one radian from a single isolated atom,” *Phys. Rev. Lett.*, vol. 110, no. March, p. 113605, 2013.
- [173] W. Alt, D. Schrader, S. Kuhr, M. Müller, V. Gomer, and D. Meschede, “Single atoms in a standing-wave dipole trap,” *Phys. Rev. A*, vol. 67, no. 3, pp. 1–7, Mar. 2003.
- [174] G. Morigi, P. W. H. Pinkse, M. Kowalewski, and R. De Vivie-Riedle, “Cavity Cooling of Internal Molecular Motion,” *Phys. Rev. Lett.*, vol. 99, no. 7, p. 073001, Aug. 2007.
- [175] V. Vuletic and S. Chu, “Laser cooling of atoms, ions, or molecules by coherent scattering,” *Phys. Rev. Lett.*, vol. 84, no. 17, pp. 3787–3790, Apr. 2000.
- [176] P. Horak, G. Hechenblaikner, K. M. Gheri, H. Stecher, and H. Ritsch, “Cavity-Induced Atom Cooling in the Strong Coupling Regime,” *Phys. Rev. Lett.*, vol. 79, no. 5, pp. 4974–4977, 1997.
- [177] M. Mücke, E. Figueroa, J. Bochmann, C. Hahn, K. Murr, S. Ritter, C. J. Villas-Boas, and G. Rempe, “Electromagnetically induced transparency with single atoms in a cavity,” *Nature*, vol. 465, no. 7299, pp. 755–758, Jun. 2010.
- [178] T. Kampschulte, W. Alt, S. Brakhane, M. Eckstein, R. Reimann, A. Widera, and D. Meschede, “Optical Control of the Refractive Index of a Single Atom,” *Phys. Rev. Lett.*, vol. 105, no. 15, p. 153603, Oct. 2010.

- [179] K. Murr, P. Maunz, P. W. H. Pinkse, T. Puppe, I. Schuster, D. Vitali, and G. Rempe, “Momentum diffusion for coupled atom-cavity oscillators,” *Phys. Rev. A*, vol. 74, no. 4, p. 043412, Oct. 2006.
- [180] J. R. Buck, “Cavity QED in Microsphere and Fabry-Perot Cavities,” California Institute of Technology; Pasadena, California, 2003.
- [181] D. Englund, A. Faraon, I. Fushman, N. Stoltz, P. Petroff, and J. Vucković, “Controlling cavity reflectivity with a single quantum dot,” *Nature*, vol. 450, no. December, pp. 857–861, Dec. 2007.
- [182] K. Srinivasan and O. Painter, “Linear and nonlinear optical spectroscopy of a strongly coupled microdisk-quantum dot system,” *Nature*, vol. 450, no. December, pp. 862–865, 2007.
- [183] S. Nußmann, “Kühlen und Positionieren eines Atoms in einem optischen Resonator,” Technische Universität München, 2006.
- [184] K. Murr, S. Nußmann, T. Puppe, M. Hijlkema, B. Weber, S. Webster, A. Kuhn, and G. Rempe, “Three-dimensional cavity cooling and trapping in an optical lattice,” *Phys. Rev. A*, vol. 73, no. 6, p. 063415, Jun. 2006.
- [185] W. Chen, K. M. Beck, R. Bucker, M. Gullans, M. D. Lukin, H. Tanji-Suzuki, and V. Vuletic, “All-Optical Switch and Transistor Gated by One Stored Photon,” *Science*, vol. 341, no. 6147, pp. 768–770, 2013.
- [186] M. Albert, A. Dantan, and M. Drewsen, “Cavity electromagnetically induced transparency and all-optical switching using ion Coulomb crystals,” *Nature Photonics*, vol. 5, no. 10, pp. 633–636, 2011.
- [187] A. Imamoglu, H. Schmidt, G. Woods, and M. Deutsch, “Strongly Interacting Photons in a Nonlinear Cavity,” *Phys. Rev. Lett.*, vol. 79, no. 8, pp. 1467–1470, Aug. 1997.
- [188] W. P. Smith, J. E. Reiner, L. A. Orozco, S. Kuhr, and H. M. Wiseman, “Capture and release of a conditional state of a cavity QED system by quantum feedback,” *Phys. Rev. Lett.*, vol. 89, no. 13, p. 133601, 2002.
- [189] R. Van Handel, J. K. Stockton, and H. Mabuchi, “Modelling and feedback control design for quantum state preparation,” *J. Opt. B Quantum Semiclassical Opt.*, vol. 7, no. 10, pp. S179–S197, 2005.
- [190] S. Deléglise, I. Dotsenko, C. Sayrin, J. Bernu, M. Brune, J.-M. Raimond, and S. Haroche, “Reconstruction of non-classical cavity field states with snapshots of their decoherence,” *Nature*, vol. 455, no. 7212, pp. 510–4, Sep. 2008.
- [191] R. Vijay, C. Macklin, D. H. Slichter, S. J. Weber, K. W. Murch, R. Naik, A. N. Korotkov, and I. Siddiqi, “Stabilizing Rabi oscillations in a superconducting qubit using quantum feedback,” *Nature*, vol. 490, no. 7418, pp. 77–80, Oct. 2012.

References

- [192] T. Puppe, I. Schuster, A. Grothe, A. Kubanek, K. Murr, P. W. H. Pinkse, and G. Rempe, “Trapping and Observing Single Atoms in a Blue-Detuned Intracavity Dipole Trap,” *Phys. Rev. Lett.*, vol. 99, no. 1, p. 013002, Jul. 2007.
- [193] I. Schuster, A. Kubanek, A. Fuhrmanek, T. Puppe, P. W. H. Pinkse, K. Murr, and G. Rempe, “Nonlinear spectroscopy of photons bound to one atom,” *Nat. Phys.*, vol. 4, no. 5, pp. 382–385, Apr. 2008.
- [194] D. E. Chang, A. S. Sørensen, E. A. Demler, and M. D. Lukin, “A single-photon transistor using nanoscale surface plasmons,” *Nat. Phys.*, vol. 3, no. 11, pp. 807–812, Aug. 2007.

Danksagung

Zum Schluss dieser Arbeit möchte ich die Chance nutzen, mich bei all denjenigen Personen zu bedanken, die direkt oder indirekt zum Gelingen dieser Arbeit beigetragen haben.

Zunächst möchte ich an dieser Stelle meinem Doktorvater, Gerhard Rempe, meinen Dank aussprechen. Er gab mir die Chance, an einem spannenden Thema und Experiment in einem tollen Team zu arbeiten. In allen Phasen meiner Doktorarbeit konnte ich mich auf seine Unterstützung und seinen Rat verlassen; darüber hinaus war er stets für Anregungen, neue Ideen sowie Diskussionen offen und hat mir somit ein ideales, motivierendes und kreatives Arbeitsumfeld eröffnet.

Mein besonderer Dank gilt auch meinen Teamkollegen Tatjana Wilk, Markus Koch, Haytham Chibani sowie Christoph Hamsen für eine klasse Zusammenarbeit. Mit ihrer Hilfe war es möglich, ein Experiment dieser Komplexität innerhalb weniger Jahre von einem leeren Tisch ausgehend komplett aufzubauen, stets zu verbessern, täglich am Laufen zu halten sowie neue, spannende Erkenntnisse zu gewinnen. Ein Dank gebührt hierbei auch unseren Diplomanden Borys Hagemann, Matthias Apel sowie Maximilian Balbach, die hierzu ebenfalls ihren erheblichen Beitrag geleistet haben.

Auch der „alten Riege“ des „Cavity-QED Teams“ („Cavies“) möchte ich meinen Dank aussprechen, angefangen von Peter Maunz, Thomas Puppe über Ingrid Schuster und Alexander Kubanek sowie den Postdocs Pepijn Pinkse, Alexei Ourjoumtsev und Karim Murr. Bereits während erster Praktika konnte ich von ihrem Wissen und ihrer Erfahrung profitieren. Dies setzte sich während meiner Promotion fort. So konnten wir zusammen – als der neue Aufbau noch in Konstruktion war – bereits experimentelle Daten am Vorgängeraufbau sammeln und interessante Erkenntnisse gewinnen.

Ein besonderes Lob für seinen wesentlichen Beitrag möchte ich auch Josef Bayerl aussprechen. Er hat den mechanischen Aufbau des Experimentes nach unseren Vorstellungen am Computer entworfen und auch die Fertigung sichergestellt. In diesem Zusammenhang geht mein Dank auch an Thomas Wiesmeier für seine Unterstützung bei Fragen zur Elektronik sowie an Franz Denk und Helmuth Stehbeck für zahlreiche Lösungen zu technischen Problemen.

Bei der gesamten Quantendynamik-Abteilung, die ich an dieser Stelle nicht alle persönlich erwähnen kann, möchte ich mich für die sehr angenehme, freundschaftliche sowie hilfsbereite Atmosphäre bedanken. Hierdurch ging der Spaß an der Arbeit nie verloren.

Neben meinem Team am Max-Planck-Institut für Quantenoptik habe ich auch große Unterstützung seitens Steffen Glaser, Thomas Schulte-Herbrüggen sowie Simone Lieser im Rahmen des Doktorandenkollegs QCCC (Quantum Computing Control and Communication) des Elite Netzwerk Bayerns erfahren; ihnen möchte ich ebenfalls meinen Dank aussprechen.

Danksagung

Erwähnen möchte ich an dieser Stelle auch die Firma National Instruments. Im Rahmen der Implementierung der verschiedenen FPGAs stand Sie stets kollaborativ zur Seite. Dies mündete ferner in einer gemeinsamen Partnerschaft innerhalb eines EU Förderprogrammes.

Mein größter Dank geht jedoch an mein privates Umfeld, das mir diese Chance erst ermöglichte.